Title

Numerical Study of 3D Magnetohydrodynamic Flows Towards Liquid Metal Blankets, Including Complex Geometry and Buoyancy Effects

Author

Rhodes, Tyler James

Publication Date

2019

Peer reviewed|Thesis/dissertation

UNIVERSITY OF CALIFORNIA

Los Angeles

Numerical Study of 3D Magnetohydrodynamic Flows Towards Liquid Metal Blankets, Including Complex Geometry and Buoyancy Effects

A dissertation submitted in partial satisfaction

of the requirements for the degree

Doctor of Philosophy in Mechanical Engineering

by

Tyler James Rhodes

2019

ABSTRACT OF THE DISSERTATION

Numerical Study of 3D Magnetohydrodynamic Flows Towards Liquid Metal Blankets, Including Complex Geometry and Buoyancy Effects

by

Tyler James Rhodes

Doctor of Philosophy in Mechanical Engineering

University of California, Los Angeles, 2019

Professor Mohamed Abdou, Chair

Understanding magnetohydrodynamic (MHD) phenomena associated with complex duct geometries and buoyancy effects is required to effectively design liquid metal (LM) blankets for fusion reactors. These topics are investigated in the present work by numerically simulating 3D LM MHD flow using HIMAG (HyPerComp Incompressible MHD solver for Arbitrary Geometry), a code developed by HyPerComp with support from UCLA. In Part I of this dissertation, the simulated geometry is a manifold consisting of a rectangular feeding duct which abruptly expands along the applied magnetic field direction to distribute LM into several parallel channels. As a first step in qualifying the flow, a magnitude of the curl of the induced Lorentz force is used to distinguish between inviscid, irrotational core flows and boundary and internal shear layers where inertia and/or viscous forces are important. Scaling laws are obtained which characterize the 3D MHD pressure drop and flow balancing as a function of the flow parameters and the manifold geometry. Associated Hartmann (*Ha*) and Reynolds (*Re*) numbers in the computations are ~10^3 and ~10^1-10^3 respectively while the expansion ratio is varied from 4 to 12. An accurate model for the pressure drop is developed for the first time for inertial-electromagnetic and

viscous-electromagnetic regimes based on 96 computed cases. Analysis shows that increasing the distance between the manifold inlet and the entrances of the parallel channels can improve flow balance by utilizing the effect of flow transitioning to a quasi-two-dimensional state in the expansion region of the manifold. Lastly, a Resistor Network Model is developed to describe the effect of the length of the poloidal channels on flow balancing in LM manifold. As the poloidal channels lengthen, the flow balance improves.

The simulated geometry in Part II consists of a straight, vertical duct which runs perpendicular to a strong, fringing applied magnetic field. There is also a region of applied heating as the primary goal of Part II is to explore buoyancy effects in MHD duct flows. The unsteady 3D MHD equations are solved using HIMAG. Results are presented for both upwards and downwards flows in electrically conducting (wall conductance ratio c_w=0.12) and nonconducting ducts for a range of Ha~10^2, Re~10^3-10^4, and Grashof (Gr) numbers~10^7-10^8. While increasing Gr or decreasing Re increases buoyancy effects, increasing Ha was shown to increase maximum temperature by enhancing flow stability. The extent to which the flow is quasi-2D is analyzed and buoyant effects, in competition with Joule dissipation, are shown to bring about 3D flow features and newly discovered MHD mixed convection phenomena. Steeply diminishing volumetric heating, which approximates nuclear heating, is applied to the vertical MHD flows for comparison to flows with surface heating only. Surface heating generates stronger buoyancy effects than volumetric heating of the same total power; however, many of the same phenomena occur. Therefore, surface heating, the only option for lab experiments, can be useful in exploring the effects of volumetric heating in MHD flows. Lastly, the results of a surface heating case are presented for the purpose of comparison with other codes and experiments, especially the MaPLE-U experiment that is currently is underway at UCLA.

The dissertation of Tyler James Rhodes is approved.

J. John Kim

Jeff D. Eldredge

Xiaolin Zhong

Sergey Y. Smolentsev

Mohamed A. Abdou, Committee Chair

University of California, Los Angeles

2019

For my little brother, Kyle Rhodes;

sic itur ad astra.

TABLE OF CONTENTS

Chapter 1: Introduction 1

1.1 Liquid Metal Blankets for Fusion Power Reactors 1

1.2 MHD Duct Flows 3

1.3 MHD Flows in Complex Geometries 4

1.4 MHD Duct Flows with Buoyancy Effects 8

Part I: MHD Flows in Manifolds 13

Chapter 2: Physical and Mathematical Model of MHD Flows in Manifolds 14

Chapter 3: Results of Manifold Simulations and Discussion 18

3.1 Comparison to Previous Results 18

3.2 Mesh Refinement Study 19

3.3 Characteristic Features of MHD Manifold Flow 21

3.4 Pressure Analysis 31

3.5 Flow Distribution Analysis 35

3.5.A Effect of the length of the Expansion Region 35

3.5.B Effect of the Length of the Parallel Channels 43

3.6 Example of Application of the Derived Pressure Model to a Fusion Blanket 50

Chapter 4: Conclusions and Future Studies for MHD Flows in Manifolds 52

Part II: MHD Duct Flows with Buoyancy Effects 56

Chapter 5: Physical and Mathematical Model of MHD Duct Flows with Buoyancy Effects 57

Chapter 6: Results of MHD Duct Flow Simulations with Buoyancy Effects and Discussion 66

6.1 Mesh Refinement Study 66
6.2 Characteristic Features of MHD Mixed Convection Flows in a Vertical Duct 68
6.3 Parametric Study of MHD Mixed Convection Flows in a Conducting Duct 75
6.3.A Downward Flows 78
6.3.B Upward Flows 84
6.4 Balance of X-direction Forces 90
6.5 3D Flow Features 101
6.6 Volumetric Heating 131
6.6.A Results of Volumetric Heating Comparison 136
6.6.A.i Downward flow with conducting walls: 137
6.6.A.ii Upward flow with conducting walls: 140
6.6.A.iii Downward flow with nonconducting walls: 142
6.6.A.iv Upward flow with nonconducting walls: 144
6.6.B Comparison to Surface Heating Scenarios 146
6.7 Results for Comparison 149
6.7.A Calculating Velocity Via Electric Potential Measurements 151
6.7.B Simulation Results for Direct Comparison 154
6.7.C Direct Comparison with Results From COMSOL 164
Chapter 7: Conclusions and Future Studies for MHD Duct Flows with Buoyancy Effects 168
References 173
Appendix A: Dimensionless Figures 178

LIST OF FIGURES

FIG. 1. A prototypic manifold geometry for numerical simulation. Fully developed flow enters the feeding duct, spreads out into the expansion region, is sorted into multiple parallel channels, and collects in the common outlet where it becomes fully developed before exiting the duct. 13

FIG. 2. An example computational mesh with 2.05 million cells for a manifold geometry with 3 channels, $L_{exp}/b=0.5$, $L_{chan}/b=2$, $r_{exp}=4$, and $s_c=0.3$. 17

FIG. 3. A comparison of present simulation results with previous numerical and experimental work [17]. Here flow distribution is reported as the percentage of flow through each of three channels. Ha=2190, Re=250, $r_{exp}=4$, $L_{chan}/b=2$, $L_{exp}/b=1$, $s_c=0.3$. 19

FIG. 4. Results of a mesh refinement study. Axial pressure gradient is plotted along the y=z=0 centerline of a manifold without multiple channels for three meshes: coarse, medium and fine. Fully developed flow Shercliff solution is also shown. Zooming in on the sudden expansion at x/b=0.5 reveals differences between the meshes. Here, Ha=4380, Re=100, $r_{exp}=8$. 20

FIG. 5. Electric currents circulate in an MHD manifold flow. The currents become 3D near changes in the flow geometry. $r_{exp}=4$, $L_{exp}/b=2$, $L_{chan}/b=2$, $s_c=0.3$, and n=3 channels for Ha=1465 and Re=50. 21

FIG. 6. Electric potential and currents on the y=0 center plane. Axial currents are generated near the sudden expansion at x/b=0.5 and then close upstream and downstream of the expansion. Ha=5475, Re=50, and $r_{exp}=10$. 22

FIG. 7. (Bottom) Non-dimensional pressure is plotted for the centerlines of the center (solid red) and side (dashed blue) channels over a top-down view (xy) of a manifold with $r_{exp}=4$, $L_{exp}/b=2$, $L_{chan}/b=2$, $s_c=0.3$, and n=3 channels for Ha=1465 and Re=50. The vertical grey lines labeled (a) through (i) correspond to the 9 axial velocity profiles shown above. (Top) Non-dimensional axial component of velocity, u/U, is plotted for yz cross-sections at 9 locations along the manifold. ..23

FIG. 8. (a) Electric currents and contours of z-direction Lorentz force at the z/a=.94 plane in the side layer. (b) Velocity streamlines and pressure contours at z/a=.94 plane in the side layer. The dashed lines are streamlines which intersect the Hartmann walls at reattachment points and define a reattachment length. r_{exp}=10, Ha=5475, and Re=50. 25

FIG. 9. Velocity streamlines in the y=0 center xz-plane of an insulating duct with a sudden expansion at x/b=0.5. r_{exp}=8, Ha=3400, and Re=500, 1000, 1500, and 2000 for (a), (b), (c), and (d) respectively. The contours are of x-direction velocity. 26

FIG. 10. Contours of the log of the magnitude of $\nabla \times \boldsymbol{J} \times \boldsymbol{B}$ are shown on the y=0 xz-plane (a) and the z=0 xy-plane (b) indicating that most of the manifold flow can be classified as a core flow except for special subdomains at the sudden expansion, entry to and exit from the parallel channels, as well as boundary layers where rotational hydrodynamic forces are important. Here, r_{exp}=4, L_{exp}/b=2, L_{chan}/b=2, s_c=0.3, and n=3 channels for Ha=1465 and Re=50. 28

FIG. 11. The length of the vertical dashed line at the sudden expansion is defined as the 3D MHD pressure drop in the hydraulic scale. The two dot-dashed black lines have slopes equal to the local fully developed Shercliff pressure gradient. Here, r_{exp}=10, Ha=5475, and Re=50.....30

FIG. 12. Centerline pressure of manifold simulations with either 1 or 3 channels, r_{exp}=4. For the cases with 3 channels, L_{exp}/b=1, L_{chan}/b=2, and s_c=0.3. The flow with Re=50 is in the VE regime and the Re=500 flow is in the IE regime. Sudden expansion at x/b=1. 32

FIG. 13. Proposed pressure model for MHD flows in a nonconducting manifold. (a) For the IE regime ($Ha^{3/2}/N > 3$) the RMSD and R2 is 76.08 and 0.9980 respectively. (b) For the VE regime ($Ha^{3/2}/N < 3$) the RMSD and R2 for the fit is 540.9 and 0.9989 respectively. 34

FIG. 14. Velocity streamlines are plotted with pressure contour lines on the sidewall (z/a=0.98) for two manifold geometries. Ha=1465, Re=50, r_{exp}=4, L_{chan}/b=2, s_c=0.3, and L_{exp}/b=0.5 or 2 for (a) and (b) respectively. 36

FIG. 15. Percentage of flow through the center channel of manifolds with three channels is plotted for various Ha, N, and L_{exp}. For these simulations, r_{exp}=4, and L_{chan}/b=2.....37
FIG. 16. Percentage of flow through the center channel of manifolds with three channels and manifolds without multiple channels is plotted for various L_{exp} = L. For these simulations, r_{exp}=4 and, for simulations with channels, L_{chan}/b=2.....39
FIG. 17. Percentage of flow through the center virtual channel of manifolds with three virtual channels is plotted for various distances L/b into the expansion region for four choices of Ha. Here, r_{exp}=8 and Re=1000.....40
FIG. 18. Percentage of flow through the center virtual channel of manifolds with three virtual channels is plotted for various distances L/b into the expansion region and at multiple Re. Here, r_{exp}=10 and Ha=5475. 41
FIG. 19. The parameters A, B, and C plotted versus r_{exp} for the exponential functions describing the percentage of flow through the center virtual channel versus L for manifolds with 3, 10, and 12 virtual channels. Ha=547.5r_{exp} and Re=2000.....42
FIG. 20. The balancing length is plotted versus r_{exp} for manifolds with 3, 10, and 12 virtual channels. Ha=547.5r_{exp} and Re=2000.....43
FIG. 21. Percentage of the total flowrate carried by each of the three channels vs length of channels. Ha=1465, Re=100, r_{exp}=4, L_{exp}/b=0.5, and s_c=0.3 for six choices of L_{chan}/b=2, 10, 20, 30, 40, and 50.....44
FIG. 22. A Resistor Network Model of the prototypical manifold in Fig.1. 45
FIG. 23. An RNM is fit to the numerical results for (%center). The smaller plot shows the modelled behavior of the flow distribution for much larger channel length. The flowrate carried by the center channel approaches 1/3 of the total flowrate as L_{chan} increases. The circles are results for Ha=1465, Re=100, r_{exp}=4, L_{exp}/b=0.5, and s_c=0.3 for six choices of L_{chan}/b=2, 10, 20, 30, 40, and 50.....47

FIG. 24. Resistor values are plotted against the sum of each pair of channel lengths used for the calculations. 48
FIG. 25. Two RNMs, each with the highest or lowest values of resistors R1 and R2, are compared to numerical values of the percentage of total flowrate carried by the center channel. 49
FIG. 26. Crosscut of one of the 16 toroidal sectors in the FNSF with the IB and OB blankets. The arrows show the PbLi flow path in the poloidal ducts. 51
FIG. 27. A test blanket submodule geometry for numerical simulation. The origin for the coordinate system is at the center of the duct's cross-section in the center of the heated region. Uniform flow enters the duct in a zero-magnetic field region. The flow continues into a region with a fringing, y-direction magnetic field which is uniform for 80cm along the duct. Inside the uniform magneticfield region, the flow encounters a 60cm region where heating is applied either as volumetric heating in the fluid or as surface heating on the $z=-a-t_w$ sidewall. The flow exits the duct, fully developed, through a region of zero-magnetic field. The final 40cm of the duct has artificially high viscosity for numerical reasons. 56
FIG. 28. An example magnetic field plotted using Eq. (21) with B_o=0.5 T. The vertical dashed lines mark the bounds of the uniform magnetic field region. The vertical dotted line marks where the magnetic field strength goes to zero.....60
FIG. 29. An example computational mesh with 1510400 cells. Due to the large aspect ratio of x:z, only a small segment of the x-axis is included.....62
FIG. 30. (a) Time-averaged mean temperature of fluid cross-sections along x are plotted for each computational mesh. (b) The instantaneous mean pressure of fluid cross-sections along x are plotted for each computational mesh.....67
FIG. 31. (a) The instantaneous centerline temperature is plotted for each of the computational meshes. (b) Instantaneous centerline temperature, zoomed in on x= [-0.6 m, 0.1 m].....67
FIG. 32. Instantaneous axial velocity contours and profiles on the y=0 center-plane. Surface heating q_o''=0.20 MW/m^2, B_o=0.5 T, U=0.02 m/s, and ΔT=350.5^{o}C (Ha=220, Re=2027,

Gr=1.44x10^8). (a, b) c_w=0.12, (c, d) c_w~0. (a, c) Downward flow, (b, d) upward flow. The z-axis is stretched compared to the x-axis by a factor of 5 to more easily view the entire flow field. The dashed red lines space every 13.3 cm are the zero lines for the profiles which are solid red lines. The black dashed lines ark the bounds of the heated region. 69

FIG. 33. Instantaneous temperature contours and profiles on the y=0 center-plane. Surface heating q_o''=0.20 MW/m^2, B_o=0.5 T, U=0.02 m/s, and ΔT=350.5^{o}C (Ha=220, Re=2027, Gr=1.44x10^8). (a, b) c_w=0.12, (c, d) c_w~0. (a, c) Downward flow, (b, d) upward flow. The z-axis is stretched compared to the x-axis by a factor of 5 to more easily view the entire flow field. The dashed, red lines spaced every 13.3 cm are the zero lines for the profiles which are solid red lines. The dashed, black lines mark the bounds of the heated region. 72

FIG. 34. Instantaneous time-averaged axial velocity contours and profiles on the y=0 m center-plane. Downward flow with surface heating q_o''=0.20 MW/m^2, B_o=0.5 T, U=0.02 m/s, and ΔT=350.5^{o}C (Ha=220, Re=2027, Gr=1.44x10^8). (a) c_w=0.12, (b) c_w~0. The z-axis is stretched compared to the x-axis by a factor of 5 to more easily view the entire flow field. The dashed, red lines spaced every 13.3 cm are the zero lines for the profiles which are solid red lines. The dashed, black lines mark the bounds of the heated region. 74

FIG. 35. Contours of instantaneous axial velocity on the y=0 center-plane for the case of downward flow at Ha = 220, Gr = 1.44x10^8 and c_w=0.12. (a) Re = 2027, (b) Re = 5067, (c) Re = 10135, (d) Re = 15201, and (e) Re = 20270. The z-axis is stretched relative to the x-axis by a factor of 5 to more easily show the entire flow domain. 79

FIG. 36. Contours of instantaneous temperature on the y=0 center-plane for the case of downward flow at Ha = 220, Gr = 1.44x10^8 and c_w=0.12. (a) Re = 2027, (b) Re = 5067, (c) Re = 10135, (d) Re = 15201, and (e) Re = 20270. The z-axis is stretched relative to the x-axis by a factor of 5 to more easily show the entire flow domain. 79

FIG. 37. Profiles of (a) time-averaged axial velocity, and (b) time-averaged temperature along the z-direction at x/b = -4.35 and y/b = 0 for Ha = 220, Gr = $1.44x10^8$, c_w = 0.12, Re=2027 ,5067, 10135, 15203, and 20270, and downward flow. 80

FIG. 38. Contours of instantaneous axial velocity on the y=0 center-plane for the case of downward flow at Re = 2027, Gr = $1.44x10^8$ and c_w = 0.12. (a) Ha = 110, (b) Ha = 220, (c) Ha = 440, (d) Ha = 880. The z-axis is stretched relative to the x-axis by a factor of 5 to more easily show the entire flow domain. 81

FIG. 39. Contours of instantaneous temperature on the y=0 center-plane for the case of downward flow at Re = 2027, Gr = $1.44x10^8$ and c_w = 0.12. (a) Ha = 110, (b) Ha = 220, (c) Ha = 440, (d) Ha = 880. The z-axis is stretched relative to the x-axis by a factor of 5 to more easily show the entire flow domain. 82

FIG. 40. Profiles of (a) time-averaged axial velocity, and (b) time-averaged temperature along the z-direction at x/b = -4.35 and y/b = 0 for Re = 2027, Gr = $1.44x10^8$ and c_w = 0.12. Ha = 110, 220, 440, and 880. 82

FIG. 41. Results of the numerical simulations performed at Ha = 220, Re = 2027, and c_w = 0.12 for downward flow. (a, c) Gr = $1.44x10^8$, (b, d) Gr = $3.6x10^8$. Contours on the y=0 center-plane are plotted for (a, b) instantaneous streamwise velocity, and (c, d) instantaneous temperature. The z-axis is stretched relative to the x-axis by a factor of 5 to more easily show the entire flow domain. 83

FIG. 42. Profiles of (a) time-averaged axial velocity, and (b) time-averaged temperature along the z-direction at x/b = -4.35 and y/b = 0 for Ha = 220, Re = 2027, and c_w = 0.12 for downward flow. Gr = $1.44x10^8$, $3.6x10^8$. 84

FIG. 43. Contours of instantaneous axial velocity along the y=0 center-plane for the case of upward flow at Ha = 220, Gr = $1.44x10^8$ and c_w = 0.12. (a) Re = 2027, (b) Re = 5067, (c) Re = 10135, (d) Re = 15201, and (e) Re = 20270. The z-axis is stretched relative to the x-axis by a factor of 5 to more easily show the entire flow domain. 85

FIG. 44. Contours of instantaneous temperature on the y=0 center-plane for the case of upward flow at Ha = 220, Gr = 1.44×10^8 and c_w = 0.12. (a) Re = 2027, (b) Re = 5067, (c) Re = 10135, (d) Re = 15201, and (e) Re = 20270. The z-axis is stretched relative to the x-axis by a factor of 5 to more easily show the entire flow domain. 85

FIG. 45. Profiles of (a) time-averaged axial velocity, and (b) time-averaged temperature along the z-direction at x/b = -4.35 and y/b = 0. Ha = 220, Gr = 1.44×10^8 and c_w = 0.12. Re=2027, 5067, 10135, 15203, and 20270. 86

FIG. 46. Contours of instantaneous axial velocity on the y=0 center-plane for the case of upward flow at Re = 2027, Gr = 1.44×10^8 and c_w = 0.12. (a) Ha = 110, (b) Ha = 220, (c) Ha = 880. The z-axis is stretched relative to the x-axis by a factor of 5 to more easily show the entire flow domain. 87

FIG. 47. Contours of instantaneous temperature on the y=0 center-plane for the case of upward flow at Re = 2027, Gr = 1.44×10^8 and c_w = 0.12. (a) Ha = 110, (b) Ha = 220, (c) Ha = 880. The z-axis is stretched relative to the x-axis by a factor of 5 to more easily show the entire flow domain. 87

FIG. 48. Profiles of (a) time-averaged axial velocity, and (b) time-averaged temperature along the z-direction at x/b = -4.35 and y/b = 0 for Ha = 220, Re = 2027, and c_w = 0.12 for upward flow. Ha = 110, 220, and 880. 88

FIG. 49. Results of the numerical simulations performed at Ha = 220, Re = 2027, and c_w = 0.12 for downward flow. (a, c) Gr = 1.44×10^8, (b, d) Gr = 3.6×10^8. Contours on the y=0 center-plane are plotted for (a, b) instantaneous streamwise velocity, and (c, d) instantaneous temperature. The z-axis is stretched relative to the x-axis by a factor of 5 to more easily show the entire flow domain. 89

FIG. 50. Profiles of (a) time-averaged axial velocity, and (b) time-averaged temperature along the z-direction at x/b = -4.35 and y/b = 0 for Ha = 220, Re = 2027, and c_w = 0.12 for upward flow. Gr = 1.44×10^8, 3.6×10^8. 89

FIG. 51. Instantaneous pressure at y=0 for 5 values of z is plotted along the x-axis for each of 4 cases with surface heating and variable flow orientation (upwards or downwards) and wall conductivity (c_w=0.12 or ~0). q_o''=0.20 MW/m^2, B_o=0.5 T, U=0.02 m/s, and ΔT=350.5^{o}C (Ha=220, Re=2027, Gr=1.44x10^8). 91

FIG. 52. The instantaneous mean pressure of each fluid cross-section is plotted along x for each of 4 cases with surface heating and variable flow orientation (upwards or downwards) and wall conductivity (c_w=0.12 or ~0). q_o''=0.20 MW/m^2, B_o=0.5 T, U=0.02 m/s, and ΔT=350.5^{o}C (Ha=220, Re=2027, Gr=1.44x10^8). The integraded buoyant force is also plotted for each case. Here, "integrated buoyancy" refers to the integral from 1.4m to x of the instantaneous bouyancy force, -ρgβ(T-T_o), averaged on fluid cross-section. g>0 for downward flows and g<0 for upward flows. 92

FIG. 53. The instantaneous mean pressure of each fluid cross-section is plotted along x for each of 4 cases with surface heating and variable flow orientation (upwards or downwards) and wall conductivity (c_w=0.12 or ~0). q_o''=0.20 MW/m^2, B_o=0.5 T, U=0.02 m/s, and ΔT=350.5^{o}C (Ha=220, Re=2027, Gr=1.44x10^8). The integraded EM+buoyancy is also plotted for each case. Here, "integrated EM+Buoyancy" refers to the integral from 1.4m to x of the sum of the instantaneous bouyancy force and axial Lorentz force, -ρgβ(T-T_o)-J_zB, averaged on fluid cross-sections. g>0 for downward flows and g<0 for upward flows. 93

FIG. 54. The contribution of hydrodynamic forces to the mean pressure distribution is plotted for each of 4 cases with surface heating and variable flow orientation (upwards or downwards) and wall conductivity (c_w=0.12 or ~0). q_o''=0.20 MW/m^2, B_o=0.5 T, U=0.02 m/s, and ΔT=350.5^{o}C (Ha=220, Re=2027, Gr=1.44x10^8). This contribution is the difference between the instantaneous mean pressure of each fluid cross-section and the sum of integrated EM+Buoyancy forces. Here, "integrated EM+Buoyancy" refers to the integral from 1.4m to x of the sum of the instantaneous bouyancy force and axial Lorentz force, -ρgβ(T-T_o)-J_zB, averaged on fluid cross-sections. g>0 for downward flows and g<0 for upward flows. 94

FIG. 55. The instantaneous mean pressure gradient of each fluid cross-section is plotted along with the instantaneous mean values of buoyant force, axial Lorentz force, and the sum of axial hydrodynamic forces on each fluid cross-section. q_o''=0.20 MW/m^2, B_o=0.5 T, U=0.02 m/s, and ΔT=350.5^{o}C (Ha=220, Re=2027, Gr=1.44x10^8). c_w=0.12, downward flow with surface heating.95
FIG. 56. The instantaneous mean pressure gradient of each fluid cross-section is plotted along with the instantaneous mean values of buoyant force, axial Lorentz force, and the sum of axial hydrodynamic forces on each fluid cross-section. q_o''=0.20 MW/m^2, B_o=0.5 T, U=0.02 m/s, and ΔT=350.5^{o}C (Ha=220, Re=2027, Gr=1.44x10^8). c_w=0.12, upward flow with surface heating. 96
FIG. 57. The instantaneous mean pressure gradient of each fluid cross-section is plotted along with the instantaneous mean values of buoyant force, axial Lorentz force, and the sum of axial hydrodynamic forces on each fluid cross-section. q_o''=0.20 MW/m^2, B_o=0.5 T, U=0.02 m/s, and ΔT=350.5^{o}C (Ha=220, Re=2027, Gr=1.44x10^8). c_w~0, downward flow with surface heating. 97
FIG. 58. The instantaneous mean pressure gradient of each fluid cross-section is plotted along with the instantaneous mean values of buoyant force, axial Lorentz force, and the sum of axial hydrodynamic forces on each fluid cross-section. q_o''=0.20 MW/m^2, B_o=0.5 T, U=0.02 m/s, and ΔT=350.5^{o}C (Ha=220, Re=2027, Gr=1.44x10^8). c_w~0, downward flow with surface heating. 98
FIG. 59. The instantaneous pressure gradient is plotted along with instantaneous values of buoyant force, axial Lorentz force, and the sum of axial hydrodynamic forces at y=0m, x=0m. q_o''=0.20 MW/m^2, B_o=0.5 T, U=0.02 m/s, and ΔT=350.5^{o}C (Ha=220, Re=2027, Gr=1.44x10^8), surface heating only, (a, c) downward flow, (b, d) upward flow, (a, b) c_w=0.12, (c, d) c_w~0.....99
FIG. 60. The instantaneous pressure gradient is plotted along with instantaneous values of buoyant force, axial Lorentz force, and the sum of axial hydrodynamic forces at z=0 m, x=0 m. q_o''=0.20 MW/m^2, B_o=0.5 T, U=0.02 m/s, and ΔT=350.5^{o}C (Ha=220, Re=2027, Gr=1.44x10^8), surface heating only, (a, c) downward flow, (b, d) upward flow, (a, b) c_w=0.12, (c, d) c_w~0.....100
FIG. 61. y-nonuniformity of the instantaneous axial velocity field on fluid cross-sections for each of 4 cases with surface heating and variable flow orientation (upwards or downwards) and wall

conductivity (c_w=0.12 or ~0). q_o''=0.20 MW/m^2, B_o=0.5 T, U=0.02 m/s, and ΔT=350.5^{o}C (Ha=220, Re=2027, Gr=1.44x10^8). The locations where y-nonuniformity is maximum are marked by black dotted lines (a)-(d) for (a) downward flow in a conducting duct, (b) downward flow in a nonconducting duct, (c) upward flow in a conducting duct, and (d) upward flow in a nonconducting duct. 102

FIG. 62. y-nonuniformity of the time-averaged axial velocity field on fluid cross-sections for each of 4 cases with surface heating and variable flow orientation (upwards or downwards) and wall conductivity (c_w=0.12 or ~0). q_o''=0.20 MW/m^2, B_o=0.5 T, U=0.02 m/s, and ΔT=350.5^{o}C (Ha=220, Re=2027, Gr=1.44x10^8). 103

FIG. 63. 2D profiles of the time-averaged axial velocity field on duct cross-sections at x= -0.3m, -0.225m, -0.15m, -0.075m, 0m, 0.075m, 0.15m, 0.225m, 0.3m for downward flow with surface heating, q_o''=0.20 MW/m^2, B_o=0.5 T, U=0.02 m/s, and ΔT=350.5^{o}C (Ha=220, Re=2027, Gr=1.44x10^8). c_w=0.12. 104

FIG. 64. 2D profiles of the time-averaged axial velocity field on duct cross-sections at x= -0.3m, -0.225m, -0.15m, -0.075m, 0m, 0.075m, 0.15m, 0.225m, 0.3m for downward flow with surface heating, q_o''=0.20 MW/m^2, B_o=0.5 T, U=0.02 m/s, and ΔT=350.5^{o}C (Ha=220, Re=2027, Gr=1.44x10^8). c_w~0. 105

FIG. 65. 2D profiles of the time-averaged axial velocity field on duct cross-sections at x= -0.3m, -0.225m, -0.15m, -0.075m, 0m, 0.075m, 0.15m, 0.225m, 0.3m for upward flow with surface heating, q_o''=0.20 MW/m^2, B_o=0.5 T, U=0.02 m/s, and ΔT=350.5^{o}C (Ha=220, Re=2027, Gr=1.44x10^8). c_w=0.12. 106

FIG. 66. 2D profiles of the time-averaged axial velocity field on duct cross-sections at x= -0.3m, -0.225m, -0.15m, -0.075m, 0m, 0.075m, 0.15m, 0.225m, 0.3m for upward flow with surface heating, q_o''=0.20 MW/m^2, B_o=0.5 T, U=0.02 m/s, and ΔT=350.5^{o}C (Ha=220, Re=2027, Gr=1.44x10^8). c_w~0. 107

FIG. 67. 2D profiles of the time-averaged temperature field on duct cross-sections at x= -0.3m, -0.225m, -0.15m, -0.075m, 0m, 0.075m, 0.15m, 0.225m, 0.3m for downward flow with surface heating, q_o''=0.20 MW/m^2, B_o=0.5 T, U=0.02 m/s, and ΔT=350.5^{o}C (Ha=220, Re=2027, Gr=1.44x10^8). c_w=0.12. 108

FIG. 68. 2D profiles of the time-averaged temperature field on duct cross-sections at x= -0.3m, -0.225m, -0.15m, -0.075m, 0m, 0.075m, 0.15m, 0.225m, 0.3m for downward flow with surface heating, q_o''=0.20 MW/m^2, B_o=0.5 T, U=0.02 m/s, and ΔT=350.5^{o}C (Ha=220, Re=2027, Gr=1.44x10^8). c_w~0. 109

FIG. 69. 2D profiles of the time-averaged temperature field on duct cross-sections at x= -0.3m, -0.225m, -0.15m, -0.075m, 0m, 0.075m, 0.15m, 0.225m, 0.3m for upward flow with surface heating, q_o''=0.20 MW/m^2, B_o=0.5 T, U=0.02 m/s, and ΔT=350.5^{o}C (Ha=220, Re=2027, Gr=1.44x10^8). c_w=0.12. 110

FIG. 70. 2D profiles of the time-averaged temperature field on duct cross-sections at x= -0.3m, -0.225m, -0.15m, -0.075m, 0m, 0.075m, 0.15m, 0.225m, 0.3m for upward flow with surface heating, q_o''=0.20 MW/m^2, B_o=0.5 T, U=0.02 m/s, and ΔT=350.5^{o}C (Ha=220, Re=2027, Gr=1.44x10^8). c_w~0. 111

FIG. 71. 2D profiles of the time-averaged temperature field on duct cross-sections where the y-nonuniformity is maximum for q_o''=0.20 MW/m^2, B_o=0.5 T, U=0.02 m/s, and ΔT=350.5^{o}C (Ha=220, Re=2027, Gr=1.44x10^8), surface heating, (a, c) c_w=0.12, (b, d) c_w~0, and (a, b) downward flow, (c, d) upward flow. 112

FIG. 72. 2D profiles of the time-averaged velocity field on duct cross-sections where the y-nonuniformity is maximum for q_o''=0.20 MW/m^2, B_o=0.5 T, U=0.02 m/s, and ΔT=350.5^{o}C (Ha=220, Re=2027, Gr=1.44x10^8), surface heating, (a, c) c_w=0.12, (b, d) c_w~0, and (a, b) downward flow, (c, d) upward flow. 113

FIG. 73. 2D profiles of the instantaneous velocity field on duct cross-sections where the y-nonuniformity is maximum for q_o''=0.20 MW/m^2, B_o=0.5 T, U=0.02 m/s, and ΔT=350.5^{o}C

(Ha=220, Re=2027, Gr=1.44x10^8), surface heating, (a, c) c_w=0.12, (b, d) c_w~0, and (a, b) downward flow, (c, d) upward flow. 115

FIG. 74. 2D profiles of the instantaneous temperature field on duct cross-sections where the y-nonuniformity is maximum for q_o''=0.20 MW/m^2, B_o=0.5 T, U=0.02 m/s, and ΔT=350.5^{o}C (Ha=220, Re=2027, Gr=1.44x10^8), surface heating, (a, c) c_w=0.12, (b, d) c_w~0, and (a, b) downward flow, (c, d) upward flow. 117

FIG. 75. Total kinetic energy and components of kinetic energy are calculated for fluid cross-sections along the x-direction for downward flow with surface heating, q_o''=0.20 MW/m^2, B_o=0.5 T, U=0.02 m/s, and ΔT=350.5^{o}C (Ha=220, Re=2027, Gr=1.44x10^8), and c_w=0.12. The kinetic energy calculations do not include the mean axial flowrate. 118

FIG. 76. Velocity streamlines on the y=0 center-plane for downward flow with surface heating, q_o''=0.20 MW/m^2, B_o=0.5 T, U=0.02 m/s, and ΔT=350.5^{o}C (Ha=220, Re=2027, Gr=1.44x10^8). c_w=0.12. 119

FIG. 77. Total kinetic energy and components of kinetic energy are calculated for fluid cross-sections along the x-direction for downward flow with surface heating, q_o''=0.20 MW/m^2, B_o=0.5 T, U=0.02 m/s, and ΔT=350.5^{o}C (Ha=220, Re=2027, Gr=1.44x10^8), and c_w~0. The kinetic energy calculations do not include the mean axial flowrate. 121

FIG. 78. Velocity streamlines on the y=0 center-plane for downward flow with surface heating, q_o''=0.20 MW/m^2, B_o=0.5 T, U=0.02 m/s, and ΔT=350.5^{o}C (Ha=220, Re=2027, Gr=1.44x10^8). c_w~0. 122

FIG. 79. 2D profiles of the instantaneous velocity field on duct cross-sections at x= -0.3m, -0.225m, -0.15m, -0.075m, 0m, 0.075m, 0.15m, 0.225m, 0.3m for downward flow with surface heating, q_o''=0.20 MW/m^2, B_o=0.5 T, U=0.02 m/s, and ΔT=350.5^{o}C (Ha=220, Re=2027, Gr=1.44x10^8). c_w=0.12. 124

FIG. 80. 2D profiles of the instantaneous velocity field on duct cross-sections at x= -0.3m, -0.225m, -0.15m, -0.075m, 0m, 0.075m, 0.15m, 0.225m, 0.3m for downward flow with

surface heating, q_o''=0.20 MW/m^2, B_o=0.5 T, U=0.02 m/s, and ΔT=350.5^{o}C (Ha=220, Re=2027, Gr=1.44x10^8). c_w~0. 125

FIG. 81. 2D profiles of the instantaneous velocity field on duct cross-sections at x= -0.3m, -0.225m, -0.15m, -0.075m, 0m, 0.075m, 0.15m, 0.225m, 0.3m for upward flow with surface heating, q_o''=0.20 MW/m^2, B_o=0.5 T, U=0.02 m/s, and ΔT=350.5^{o}C (Ha=220, Re=2027, Gr=1.44x10^8). c_w=0.12. 126

FIG. 82. 2D profiles of the instantaneous velocity field on duct cross-sections at x= -0.3m, -0.225m, -0.15m, -0.075m, 0m, 0.075m, 0.15m, 0.225m, 0.3m for upward flow with surface heating, q_o''=0.20 MW/m^2, B_o=0.5 T, U=0.02 m/s, and ΔT=350.5^{o}C (Ha=220, Re=2027, Gr=1.44x10^8). c_w~0. 127

FIG. 83. 2D profiles of the instantaneous temperature field on duct cross-sections at x= -0.3m, -0.225m, -0.15m, -0.075m, 0m, 0.075m, 0.15m, 0.225m, 0.3m for downward flow with surface heating, q_o''=0.20 MW/m^2, B_o=0.5 T, U=0.02 m/s, and ΔT=350.5^{o}C (Ha=220, Re=2027, Gr=1.44x10^8). c_w=0.12. 128

FIG. 84. 2D profiles of the instantaneous temperature field on duct cross-sections at x= -0.3m, -0.225m, -0.15m, -0.075m, 0m, 0.075m, 0.15m, 0.225m, 0.3m for downward flow with surface heating, q_o''=0.20 MW/m^2, B_o=0.5 T, U=0.02 m/s, and ΔT=350.5^{o}C (Ha=220, Re=2027, Gr=1.44x10^8). c_w~0. 129

FIG. 85. 2D profiles of the instantaneous temperature field on duct cross-sections at x= -0.3m, -0.225m, -0.15m, -0.075m, 0m, 0.075m, 0.15m, 0.225m, 0.3m for upward flow with surface heating, q_o''=0.20 MW/m^2, B_o=0.5 T, U=0.02 m/s, and ΔT=350.5^{o}C (Ha=220, Re=2027, Gr=1.44x10^8). c_w=0.12. 130

FIG. 86. 2D profiles of the instantaneous temperature field on duct cross-sections at x= -0.3m, -0.225m, -0.15m, -0.075m, 0m, 0.075m, 0.15m, 0.225m, 0.3m for upward flow with surface heating, q_o''=0.20 MW/m^2, B_o=0.5 T, U=0.02 m/s, and ΔT=350.5^{o}C (Ha=220, Re=2027, Gr=1.44x10^8). c_w~0. 131

FIG. 87. Volumetric heating profiles. Both heating distributions have the same total heating per axial length Q'=.01 MW/m when integrated over the fluid cross-section. The heating is uniform along the y-direction.....133
FIG. 88. Volumetric heating profiles. All three heating distributions have the same total heating per axial length Q'=.01 MW/m when integrated over the fluid cross-section. The heating is uniform along the y-direction.....135
FIG. 89. (a) Time-averaged axial velocity, (b) instantaneous axial velocity, (c) time-averaged temperature, and (d) instantaneous temperature contours and profiles on the y=0 center-plane. B_o=0.5 T, U=0.02 m/s, and ΔT=381°C (Ha=220, Re=2027, Gr=1.57x10^8). c_w=0.12, downward flow with exponential heating. The flow enters from the top in the direction of gravity. The z-axis is stretched compared to the x-axis by a factor of 5 to more easily view the entire flow field. The dashed, red lines spaced every 13.3cm are the zero lines for the profiles which are solid red lines. The dashed, black lines mark the bounds of the heated region.....137
FIG. 90. (a) Time-averaged axial velocity, (b) instantaneous axial velocity, (c) time-averaged temperature, and (d) instantaneous temperature contours and profiles on the y=0 center-plane. B_o=0.5 T, U=0.02 m/s, and ΔT=381°C (Ha=220, Re=2027, Gr=1.57x10^8). c_w=0.12, downward flow with nuclear heating. The flow enters from the top in the direction of gravity. The z-axis is stretched compared to the x-axis by a factor of 5 to more easily view the entire flow field. The dashed, red lines spaced every 13.3cm are the zero lines for the profiles which are solid red lines. The dashed, black lines mark the bounds of the heated region. 138
FIG. 91. (a) Time-averaged axial velocity, (b) instantaneous axial velocity, (c) time-averaged temperature, and (d) instantaneous temperature contours and profiles on the y=0 center-plane. B_o=0.5 T, U=0.02 m/s, and ΔT=381°C (Ha=220, Re=2027, Gr=1.57x10^8). c_w=0.12, upward flow with exponential heating. The flow enters from the bottom opposite the direction of gravity. The z-axis is stretched compared to the x-axis by a factor of 5 to more easily view the entire flow field.

The dashed, red lines spaced every 13.3cm are the zero lines for the profiles which are solid red lines. The dashed, black lines mark the bounds of the heated region.....140
FIG. 92. (a) Time-averaged axial velocity, (b) instantaneous axial velocity, (c) time-averaged temperature, and (d) instantaneous temperature contours and profiles on the y=0 center-plane. B_o=0.5 T, U=0.02 m/s, and ΔT=381°C (Ha=220, Re=2027, Gr=1.57x10^8). c_w=0.12, upward flow with nuclear heating. The flow enters from the bottom opposite the direction of gravity. The z-axis is stretched compared to the x-axis by a factor of 5 to more easily view the entire flow field. The dashed, red lines spaced every 13.3cm are the zero lines for the profiles which are solid red lines. The dashed, black lines mark the bounds of the heated region.....141
FIG. 93. (a) Time-averaged axial velocity, (b) instantaneous axial velocity, (c) time-averaged temperature, and (d) instantaneous temperature contours and profiles on the y=0 center-plane. B_o=0.5 T, U=0.02 m/s, and ΔT=381°C (Ha=220, Re=2027, Gr=1.57x10^8). c_w~0, downward flow with exponential heating. The flow enters from the top in the direction of gravity. The z-axis is stretched compared to the x-axis by a factor of 5 to more easily view the entire flow field. The dashed, red lines spaced every 13.3cm are the zero lines for the profiles which are solid red lines. The dashed, black lines mark the bounds of the heated region.....142
FIG. 94. (a) Time-averaged axial velocity, (b) instantaneous axial velocity, (c) time-averaged temperature, and (d) instantaneous temperature contours and profiles on the y=0 center-plane. B_o=0.5 T, U=0.02 m/s, and ΔT=381°C (Ha=220, Re=2027, Gr=1.57x10^8). c_w~0, downward flow with nuclear heating. The flow enters from the top in the direction of gravity. The z-axis is stretched compared to the x-axis by a factor of 5 to more easily view the entire flow field. The dashed, red lines spaced every 13.3cm are the zero lines for the profiles which are solid red lines. The dashed, black lines mark the bounds of the heated region. 143
FIG. 95. (a) Time-averaged axial velocity, (b) instantaneous axial velocity, (c) time-averaged temperature, and (d) instantaneous temperature contours and profiles on the y=0 center-plane. B_o=0.5 T, U=0.02 m/s, and ΔT=381°C (Ha=220, Re=2027, Gr=1.57x10^8). c_w~0, upward flow with

exponential heating. The flow enters from the bottom opposite the direction of gravity. The z-axis is stretched compared to the x-axis by a factor of 5 to more easily view the entire flow field. The dashed, red lines spaced every 13.3cm are the zero lines for the profiles which are solid red lines. The dashed, black lines mark the bounds of the heated region. 144
FIG. 96. (a) Time-averaged axial velocity, (b) instantaneous axial velocity, (c) time-averaged temperature, and (d) instantaneous temperature contours and profiles on the y=0 center-plane. B_o=0.5 T, U=0.02 m/s, and ΔT=381°C (Ha=220, Re=2027, Gr=1.57x10^8). c_w~0, upward flow with exponential heating. The flow enters from the bottom opposite the direction of gravity. The z-axis is stretched compared to the x-axis by a factor of 5 to more easily view the entire flow field. The dashed, red lines spaced every 13.3cm are the zero lines for the profiles which are solid red lines. The dashed, black lines mark the bounds of the heated region. 145
FIG. 97. A comparison of time-averaged velocity profiles at x=y=0m for flows with exponential volumetric heating in the fluid domain or surface heating applied to the outside surface of the duct wall at z=-t_w-a. In all cases, the total heating is the same. B_o=0.5 T, U=0.02 m/s (Re=2027, Ha=220). c_w=0.12 or ~0, Gr=1.57x10^8 for volumetric heating scenarios and Gr=1.44x10^8 for surface heating scenarios. 146
FIG. 98. A comparison of time-averaged velocity profiles at x=y=0m for flows with nuclear volumetric heating in the fluid domain or surface heating applied to the outside surface of the duct wall at z=-t_w-a. In all cases, the total heating is the same. B_o=0.5 T, U=0.02 m/s (Re=2027, Ha=220). c_w=0.12 or ~0, Gr=1.57x10^8 for volumetric heating scenarios and Gr=1.44x10^8 for surface heating scenarios. 147
FIG. 99. A comparison of time-averaged temperature profiles at x=y=0m for flows with exponential volumetric heating in the fluid domain or surface heating applied to the outside surface of the duct wall at z=-t_w-a. In all cases, the total heating is the same. B_o=0.5 T, U=0.02 m/s (Re=2027, Ha=220). c_w=0.12 or ~0, Gr=1.57x10^8 for volumetric heating scenarios and Gr=1.44x10^8 for surface heating scenarios. 147

FIG. 100. A comparison of time-averaged velocity profiles at x=y=0m for flows with nuclear volumetric heating in the fluid domain or surface heating applied to the outside surface of the duct wall at z=-t_w-a. In all cases, the total heating is the same. B_o=0.5 T, U=0.02 m/s (Re=2027, Ha=220). c_w=0.12 or ~0, Gr=1.57x10^8 for volumetric heating scenarios and Gr=1.44x10^8 for surface heating scenarios. 148

FIG. 101. Instantaneous axial velocity profiles at (a) x=-0.3 m and (b) x=0 m. Downward flow with surface heating. B_o=0.5 T, U=0.03 m/s, q_o''=0.04 MW/m^2 (Ha=220, Re=3041, Gr=2.88x10^7). c_w=0.12. 152

FIG. 102. Contours of instantaneous electric potential on duct cross-sections at (a) x=-0.3 m and (b) x=0 m. Downward flow with surface heating. B_o=0.5 T, U=0.03 m/s, q_o''=0.04 MW/m^2 (Ha=220, Re=3041, Gr=2.88x10^7). c_w=0.12. 153

FIG. 103. Instantaneous axial velocity profiles at y=0m, x=-0.3m, 0m. Using Eq. 35, velocity profiles are constructed with electric potential data from (a) y=0.025m and (b) y=0m. Downward flow with surface heating. B_o=0.5 T, U=0.03 m/s, q_o''=0.04 MW/m^2 (Ha=220, Re=3041, Gr=2.88x10^7). c_w=0.12. 154

FIG. 104. The instantaneous bulk temperature for downward flow and surface heating for B_o=0.5 T, U=0.03 m/s, q_o''=0.04 MW/m^2 (Ha=220, Re=3041, Gr=2.88x10^7). c_w=0.12. 155

FIG. 105. Time-averaged velocity at y=0m, x= -0.25 m, -0.15 m, -0.05 m, 0.05 m, 0.15 m, and 0.25 m. Downward flow with surface heating. B_o=0.5 T, U=0.03 m/s, q_o''=0.04 MW/m^2 (Ha=220, Re=3041, Gr=2.88x10^7). c_w=0.12. 156

FIG. 106. Time-averaged velocity at z=0m, x= -0.25 m, -0.15 m, -0.05 m, 0.05 m, 0.15 m, and 0.25 m. Downward flow with surface heating. B_o=0.5 T, U=0.03 m/s, q_o''=0.04 MW/m^2 (Ha=220, Re=3041, Gr=2.88x10^7). c_w=0.12. 156

FIG. 107. Time-averaged temperature at y=0 m, x= -0.25 m, -0.15 m, -0.05 m, 0.05 m, 0.15 m, and 0.25 m. Downward flow with surface heating. B_o=0.5 T, U=0.03 m/s, q_o''=0.04 MW/m^2 (Ha=220, Re=3041, Gr=2.88x10^7). c_w=0.12. 157

FIG. 108. Time-averaged temperature at z=0 m, x= -0.25 m, -0.15 m, -0.05 m, 0.05 m, 0.15 m, and 0.25 m. Downward flow with surface heating. B_o=0.5 T, U=0.03 m/s, q_o''=0.04 MW/m^2 (Ha=220, Re=3041, Gr=2.88x10^7). c_w=0.12. 157

FIG. 109. Time-averaged temperature on the outer surface of the wall at z=-0.025 m, x=-0.3 m, -0.2 m, -0.1 m, 0 m, 0.1 m, 0.2 m, and 0.3 m. Downward flow with surface heating. B_o=0.5 T, U=0.03 m/s, q_o''=0.04 MW/m^2 (Ha=220, Re=3041, Gr=2.88x10^7). c_w=0.12. 158

FIG. 110. Time-averaged temperature on the outer surface of the wall at z=0.025 m, x=-0.3 m, -0.2 m, -0.1 m, 0 m, 0.1 m, 0.2 m, and 0.3 m. Downward flow with surface heating. B_o=0.5 T, U=0.03 m/s, q_o''=0.04 MW/m^2 (Ha=220, Re=3041, Gr=2.88x10^7). c_w=0.12.....158

FIG. 111. Time-averaged temperature on the outer surface of the wall at y=0.025 m, x=-0.3 m, -0.2 m, -0.1 m, 0 m, 0.1 m, 0.2 m, and 0.3 m. Downward flow with surface heating. B_o=0.5 T, U=0.03 m/s, q_o''=0.04 MW/m^2 (Ha=220, Re=3041, Gr=2.88x10^7). c_w=0.12.....159

FIG. 112. Time-averaged temperature on the outer surface of the wall at y=-0.025 m, x=-0.3 m, -0.2 m, -0.1 m, 0 m, 0.1 m, 0.2 m, and 0.3 m. Downward flow with surface heating. B_o=0.5 T, U=0.03 m/s, q_o''=0.04 MW/m^2 (Ha=220, Re=3041, Gr=2.88x10^7). c_w=0.12. 159

FIG. 113. Instantaneous electric potential on the outer surface of the wall at z=0.025 m, x=-0.3 m, -0.2 m, -0.1 m, 0 m, 0.1 m, 0.2 m, and 0.3 m. Downward flow with surface heating. B_o=0.5 T, U=0.03 m/s, q_o''=0.04 MW/m^2 (Ha=220, Re=3041, Gr=2.88x10^7). c_w=0.12. 160

FIG. 114. Instantaneous electric potential on the outer surface of the wall at z=-0.025 m, x=-0.3 m, -0.2 m, -0.1 m, 0 m, 0.1 m, 0.2 m, and 0.3 m. Downward flow with surface heating. B_o=0.5 T, U=0.03 m/s, q_o''=0.04 MW/m^2 (Ha=220, Re=3041, Gr=2.88x10^7). c_w=0.12. 161

FIG. 115. Instantaneous electric potential on the outer surface of the wall at y=0.025 m, x=-0.3 m, -0.2 m, -0.1 m, 0 m, 0.1 m, 0.2 m, and 0.3 m. Downward flow with surface heating. B_o=0.5 T, U=0.03 m/s, q_o''=0.04 MW/m^2 (Ha=220, Re=3041, Gr=2.88x10^7). c_w=0.12. 161

FIG. 116. Instantaneous electric potential on the outer surface of the wall at y=-0.025 m, x=-0.3 m, -0.2 m, -0.1 m, 0 m, 0.1 m, 0.2 m, and 0.3 m. Downward flow with surface heating. B_o=0.5 T, U=0.03 m/s, q_o''=0.04 MW/m^2 (Ha=220, Re=3041, Gr=2.88x10^7). c_w=0.12. 162
FIG. 117. (a) Time-averaged velocity contours and profiles on the y=0 center-plane. (b) Time-averaged temperature contours and profiles on the y=0 center-plane. Downward flow with surface heating. B_o=0.5 T, U=0.03 m/s, q_o''=0.04 MW/m^2 (Ha=220, Re=3041, Gr=2.88x10^7). c_w=0.12. The z-axis is stretched compared to the x-axis by a factor of 5 to more easily view the entire flow field. The dashed, red lines spaced every 0.1 m are the zero lines for the profiles which are solid red lines. The dashed, black lines mark the bounds of the heated region. 163
FIG. 118. COMSOL Multiphysics results. (a) Time-averaged velocity contours and profiles on the y=0 center-plane. (b) Time-averaged temperature contours and profiles on the y=0 center-plane. Downward flow with surface heating. B_o=0.5 T, U=0.03 m/s, q_o''=0.04 MW/m^2 (Ha=220, Re=3041, Gr=2.88x10^7). c_w=0.12. The z-axis is stretched compared to the x-axis by a factor of 5 to more easily view the entire flow field. The dashed, red lines spaced every 0.1m are the zero lines for the profiles which are solid red lines. The dashed, black lines mark the bounds of the heated region.....165
FIG. 119. Time-averaged velocity at y=0m, x= -0.25 m, -0.15 m, -0.05 m, 0.05 m, 0.15 m, and 0.25 m. Downward flow with surface heating. B_o=0.5 T, U=0.03 m/s, q_o''=0.04 MW/m^2 (Ha=220, Re=3041, Gr=2.88x10^7). c_w=0.12. Results from HIMAG are solid lines while results from COMSOL are dashed lines. 166
FIG. 120. Time-averaged temperature at y=0m, x= -0.25 m, -0.15 m, -0.05 m, 0.05 m, 0.15 m, and 0.25 m. Downward flow with surface heating. B_o=0.5 T, U=0.03 m/s, q_o''=0.04 MW/m^2 (Ha=220, Re=3041, Gr=2.88x10^7). c_w=0.12. Results from HIMAG are solid lines while results from COMSOL are dashed lines. 167
FIG. 121. Instantaneous axial velocity contours and profiles on the y=0 center-plane. Ha=220, Re=2027, Gr=1.44x10^8, surface heating only. (a, b) c_w=0.12, (c, d) c_w~0. (a, c) Downward flow,

(b, d) upward flow. The z-axis is stretched compared to the x-axis by a factor of 5 to more easily view the entire flow field. The dashed, red lines spaced every 5.78 characteristic lengths are the zero lines for the profiles which are solid red lines. The dashed, black lines mark the bounds of the heated region. 179
FIG. 122. Instantaneous temperature contours and profiles on the y=0 center-plane. Ha=220, Re=2027, Gr=1.44x10^8, surface heating only. (a, b) c_w=0.12, (c, d) c_w~0. (a, c) Downward flow, (b, d) upward flow. The z-axis is stretched compared to the x-axis by a factor of 5 to more easily view the entire flow field. The dashed, red lines spaced every 5.78 characteristic lengths are the zero lines for the profiles which are solid red lines. The dashed, black lines mark the bounds of the heated region. 180
FIG. 123. Time-averaged axial velocity contours and profiles on the y=0 center-plane. Ha=220, Re=2027, Gr=1.44x10^8, surface heating only. (a, b) c_w=0.12, (c, d) c_w~0. (a, c) Downward flow, (b, d) upward flow. The z-axis is stretched compared to the x-axis by a factor of 5 to more easily view the entire flow field. The dashed, red lines spaced every 5.78 characteristic lengths are the zero lines for the profiles which are solid red lines. The dashed, black lines mark the bounds of the heated region. 181
FIG. 124. Time-averaged temperature contours and profiles on the y=0 center-plane. Ha=220, Re=2027, Gr=1.44x10^8, surface heating only. (a, b) c_w=0.12, (c, d) c_w~0. (a, c) Downward flow, (b, d) upward flow. The z-axis is stretched compared to the x-axis by a factor of 5 to more easily view the entire flow field. The dashed, red lines spaced every 5.78 characteristic lengths are the zero lines for the profiles which are solid red lines. The dashed, black lines mark the bounds of the heated region. 182
FIG. 125. (a) Time-averaged axial velocity, (b) instantaneous axial velocity, (c) time-averaged temperature, and (d) instantaneous temperature contours and profiles on the y=0 center-plane. Ha=220, Re=2027, Gr=1.57x10^8, c_w=0.12, downward flow with exponential heating. The flow enters from the top in the direction of gravity. The z-axis is stretched compared to the x-axis by a

factor of 5 to more easily view the entire flow field. The dashed, red lines spaced every 5.78 characteristic lengths are the zero lines for the profiles which are solid red lines. The dashed, black lines mark the bounds of the heated region. 183
FIG. 126. (a) Time-averaged axial velocity, (b) instantaneous axial velocity, (c) time-averaged temperature, and (d) instantaneous temperature contours and profiles on the y=0 center-plane. Ha=220, Re=2027, Gr=1.57x10^8, c_w=0.12, downward flow with nuclear heating. The flow enters from the top in the direction of gravity. The z-axis is stretched compared to the x-axis by a factor of 5 to more easily view the entire flow field. The dashed, red lines spaced every 5.78 characteristic lengths are the zero lines for the profiles which are solid red lines. The dashed, black lines mark the bounds of the heated region. 184
FIG. 127. (a) Time-averaged axial velocity, (b) instantaneous axial velocity, (c) time-averaged temperature, and (d) instantaneous temperature contours and profiles on the y=0 center-plane. Ha=220, Re=2027, Gr=1.57x10^8, c_w=0.12, upward flow with exponential heating. The flow enters from the bottom opposite the direction of gravity. The z-axis is stretched compared to the x-axis by a factor of 5 to more easily view the entire flow field. The dashed, red lines spaced every 5.78 characteristic lengths are the zero lines for the profiles which are solid red lines. The dashed, black lines mark the bounds of the heated region. 185
FIG. 128. (a) Time-averaged axial velocity, (b) instantaneous axial velocity, (c) time-averaged temperature, and (d) instantaneous temperature contours and profiles on the y=0 center-plane. Ha=220, Re=2027, Gr=1.57x10^8, c_w=0.12, upward flow with nuclear heating. The flow enters from the bottom opposite the direction of gravity. The z-axis is stretched compared to the x-axis by a factor of 5 to more easily view the entire flow field. The dashed, red lines spaced every 5.78 characteristic lengths are the zero lines for the profiles which are solid red lines. The dashed, black lines mark the bounds of the heated region. 186
FIG. 129. (a) Time-averaged axial velocity, (b) instantaneous axial velocity, (c) time-averaged temperature, and (d) instantaneous temperature contours and profiles on the y=0 center-plane.

Ha=220, Re=2027, Gr=1.57x10^8, c_w~0, downward flow with exponential heating. The flow enters from the top in the direction of gravity. The z-axis is stretched compared to the x-axis by a factor of 5 to more easily view the entire flow field. The dashed, red lines spaced every 5.78 characteristic lengths are the zero lines for the profiles which are solid red lines. The dashed, black lines mark the bounds of the heated region. 187

FIG. 130. (a) Time-averaged axial velocity, (b) instantaneous axial velocity, (c) time-averaged temperature, and (d) instantaneous temperature contours and profiles on the y=0 center-plane. Ha=220, Re=2027, Gr=1.57x10^8, c_w~0, downward flow with nuclear heating. The flow enters from the top in the direction of gravity. The z-axis is stretched compared to the x-axis by a factor of 5 to more easily view the entire flow field. The dashed, red lines spaced every 5.78 characteristic lengths are the zero lines for the profiles which are solid red lines. The dashed, black lines mark the bounds of the heated region.....188

FIG. 131. (a) Time-averaged axial velocity, (b) instantaneous axial velocity, (c) time-averaged temperature, and (d) instantaneous temperature contours and profiles on the y=0 center-plane. Ha=220, Re=2027, Gr=1.57x10^8, c_w~0, upward flow with exponential heating. The flow enters from the bottom opposite the direction of gravity. The z-axis is stretched compared to the x-axis by a factor of 5 to more easily view the entire flow field. The dashed, red lines spaced every 5.78 characteristic lengths are the zero lines for the profiles which are solid red lines. The dashed, black lines mark the bounds of the heated region. 189

FIG. 132. (a) Time-averaged axial velocity, (b) instantaneous axial velocity, (c) time-averaged temperature, and (d) instantaneous temperature contours and profiles on the y=0 center-plane. Ha=220, Re=2027, Gr=1.57x10^8, c_w~0, upward flow with exponential heating. The flow enters from the bottom opposite the direction of gravity. The z-axis is stretched compared to the x-axis by a factor of 5 to more easily view the entire flow field. The dashed, red lines spaced every 5.78 characteristic lengths are the zero lines for the profiles which are solid red lines. The dashed, black lines mark the bounds of the heated region. 190

LIST OF TABLES

Table 1. Mesh Refinement Details. 20

Table 2. The Dimensionless Blanket Parameters and the Computed 3D MHD Pressure Drop in the Manifold. 51

Table 3: Material Properties 59

Table 4. Simulation Matrix.....65

Table 5. Mesh Refinement Details. 66

Table 6. Simulation Matrix for Parametric Survey.....76

Table 7. Simulation Parameters for Case 16.....150

ACKNOWLEDGEMENTS

I want to thank Professor Mohamed Abdou for the opportunity to study fusion and to pursue a doctoral degree at UCLA. I much appreciate the support he has provided me as my graduate supervisor.

I also want to thank Dr. Sergey Smolentsev for his dedication as my mentor and advisor and for his infectious enthusiasm for science.

I would like to express my appreciation for Dr. Gautam Pulugundla who's friendly guidance greatly accelerated my early progress in simulating MHD mixed convection flows. Furthermore, he provided me with simulation results for 17 cases (Table 6) towards the parametric study in section 6.3.

I am also grateful to Yi Yan for his comradery and insight as well as the numerical results he provided for comparison in section 6.7.C.

The members of my doctoral committee also hold my appreciation and I am honored to have learned from these men: Prof. Jeff Eldredge, Prof. Jon Kim, Prof. Xiaolin Zhong, Dr. Smolentsev, and Prof. Abdou.

Many thanks to Dr. Ramakanth Munipalli and Dr. Peter Huang of Hypercomp Inc. for their help in using HIMAG, the numerical solver which I used extensively throughout my research. Dr. Huang solved many technical issues that would have precluded my research progress.

I am very grateful to my colleagues at Fusion Science and Technology Center: Dr. Alice Ying, Dr. Neil Morley, Tom Sketchley, Dr. Christian Di Sanzo, Dr. Hongjie Zhang, Dr. Gautam Pulugundla, Dr. Jack Young, Dr. Sheida Saeidi, Damien Sutevski, Dr. Jon Van Lew, Dr. Mahmoud Mohammed, Dr. Charlie Kawczynski, Yi Yan, Marco Riva, Dr. Cyril Courtessol. I consider many of the members of my research group to be close friends and I cherish the experiences we've shared. I also deeply appreciate the kind support of the staff: Esther Martinez, Erica Suh, Emily Hoffmann, and Arnoud Larousse.

I am fortunate to have made a number of lifelong friends in Los Angeles, without whom I would have enjoyed this time in my life much less. Of these, I would especially like to thank Francis Turney for the many conversations we've had regarding my research.

This work was performed with support from US Department of Energy, Office of Fusion Energy Sciences, under Grant No. DE-FG02-86ER52123.

The numerical efforts in Part I of this research used computational and storage services associated with the Hoffman2 Shared Cluster provided by UCLA Institute for Digital Research and Education's Research Technology Group.

The numerical efforts in Part II of this research used resources of the National Energy Research Scientific Computing Center (NERSC), a U.S. Department of Energy Office of Science User Facility operated under Contract No. DE-AC02-05CH11231.

Finally, I am immensely grateful for my family to whom I owe all that I have achieved. I want to thank my Mom and Dad for cultivating my early interest in science and for wholly investing themselves in my life, Ryan and Kyle for the deep companionship and brotherhood we share, Poppy and Gramz for the weekly phone calls and their loving encouragement during my graduate program, my uncle Jim for our many scientific debates, and Grandma and Papa for the happy memories. Lastly, I wish to express my deepest gratitude to my loving wife, Hannah, who proofread the entirety of this dissertation. For her determination and love and support of me, I am extremely grateful.

VITA

University of California, Santa Barbara, Santa Barbara, CA
Bachelor of Science - Mechanical Engineering, 2009-2013

University of California, Los Angeles, Los Angeles, CA
Master of Science - Mechanical Engineering, September 2013-March 2015
Doctor of Philosophy - Mechanical Engineering, September 2013-present
(Advanced to Candidacy March 16, 2018)

JOURNAL PUBLICATIONS

G. Pulugundla, S. Smolentsev, **T. Rhodes**, C. Kawczynski, and M. Abdou, Transition to a Quasi-Fully Developed MHD Flow in an Electrically Conducting Pipe under a Transverse Non-Uniform Magnetic Field, Fus. Sci. Tech. 68.3 (2015) 684-689.

S. Smolentsev, M. Abdou, C. Courtessole, G. Pulugundla, F-C. Li, N. Morley, R. Munipalli, P. Huang, C. Kaczynski, J. Young, **T. Rhodes**, Y. Yan, REVIEW OF RECENT MHD ACTIVITIES FOR LIQUID METAL BLANKETS IN THE US, Magnetohydrodynamics (0024-998X) 53.2 (2017).

T. Rhodes, S. Smolentsev, M. Abdou, Effect of the Length of the Poloidal Ducts on Flow Balancing in a Liquid Metal Blanket, Submitted to Fus. Eng. Des., 2017.

S. Smolentsev, **T. Rhodes**, G. Pulugundla, C. Courtessole, M. Abdou, S. Malang, M. Tillack, C. Kessel, MHD thermohydraulics analysis and supporting R&D for DCLL blanket in the FNSF, Fus. Eng. Des.,135 (2018) 314-323.

T. Rhodes, S. Smolentsev, M. Abdou, Magnetohydrodynamic pressure drop and flow balancing of liquid metal flow in a prototypic fusion blanket manifold, Physics of Fluids 30(5), (2018) 057101.

CONFERENCE PRESENTATIONS

International Symposium for Fusion Nuclear Technology, Kyoto, Japan. September 27, 2017
Poster: Effect of the length of the poloidal ducts on flow balancing in a liquid metal blanket
Authors: T. Rhodes*, S. Smolentsev, M. Abdou

Chapter 1: Introduction

1.1 Liquid Metal Blankets for Fusion Power Reactors

To make clear the importance of studying the physics and phenomena of MHD duct flows in the context of fusion power reactors, a brief introduction to fusion reactor theory is provided. The goal of all power fusion reactors is to sustainably produce electrical power by harnessing the energy made available through fusing atomic nuclei. There are several research paths towards achieving this goal but the most promising of these aim to fuse the hydrogen isotopes deuterium and tritium ($^{2}_{1}H + {}^{3}_{1}H \rightarrow {}^{4}_{2}He + {}^{1}_{0}n + 17.6MeV$) which produces an alpha particle at 3.5 MeV and a neutron at 14.1 MeV per reaction. Typically, a plasma of deuterium and tritium will be heated to extremely high temperatures (~100 million ^{o}C) and pressure such that the fuel "ignites" and the fusion reactions become self sustaining. Super-conducting magnets are commonly utilized in reactor designs to help facilitate the reaction; not only will the magnetic field exert pressure on the plasma fuel, the magnetic field also prevents the exceedingly hot plasma from touching the walls of the core region in a scheme known as magnetic confinement. The 3.5 MeV alpha particles produced by fusion are also confined by the magnetic field along with the rest of the plasma. As these particles accelerate, they heat the surface of the reactor's first wall via bremsstrahlung radiation. The 14.1 MeV neutrons produced by fusion do not interact with the magnetic field and so they exit the plasma and the core region and penetrate the first wall to be absorbed in the breeding blankets.

Breeding blankets are an integral part of Deuterium-Tritium fusion power reactors [1]. Surrounding the core region, blankets are responsible for shielding the outer components (e.g. the magnets), collecting and transporting heat to be used in electrical power generation, and producing tritium to fuel the reactor. It should be noted that while deuterium is common in sea water, tritium does not exist naturally on Earth as it undergoes beta-decay with a short half-life of only 12.3 years.

Therefore, it must be produced via nuclear reactions. In blanket designs, a liquid metal (LM) or solid breeder material is situated near the first wall to interact with the flux of neutrons emanating from the reactor's core. The breeder material always contains lithium which reacts with neutrons to produce the tritium needed to fuel the reactor. LM breeder blanket designs are attractive due to the high thermal conductivity (~10 W/mK) of the LM, low susceptibility to radiation damage, and the designs' capacity to provide a sufficient tritium breeding ratio. However, there are some additional challenges associated with LM breeders. For instance, because the strong, plasma-confining magnetic field permeates the blanket and LM has high electrical conductivity (~10^6 S/m), LM blanket flows are highly magnetohydrodynamic (MHD). MHD flows are characterized by significant electromagnetic Lorentz forces which, among other effects, tend to dampen or modify turbulence, smoothen axial velocity profiles, and significantly increase the pressure drop when the applied magnetic field is transverse to the flow direction (as in LM blankets for fusion power reactors). Efforts to design LM blankets require more research towards predicting the behavior of MHD flows in fusion blanket conditions. Such efforts are made even more challenging by complex blanket duct geometries (e.g. expansions and manifolds) and by the strong buoyant effects produced by the steep volumetric heating in the LM from neutron radiation and surface heating at the first wall [2]. These challenges are addressed in the numerical studies of the present work. In Part I of this dissertation, 3D numerical simulations of MHD flow in manifolds are used to characterize large 3D MHD pressure drops occurring where ducts undergo expansion to feed multiple channels. Then, flow balancing among multiple channels is analyzed with respect to the dimensionless parameters and aspects of the duct geometry. In Part II, buoyancy effects in vertical MHD duct flows are analyzed using 3D numerical simulations of many scenarios including one-sided surface heating, steep volumetric heating, electrically conducting and nonconducting walls, upward flows, and downward flows, as well as several combinations of dimensionless parameters.

1.2 MHD Duct Flows

Much has been written on the subject of MHD duct flows. The simplest configurations of such flows have been solved analytically by the likes of Shercliff (1953) [3], who studied the case of electrically nonconducting duct walls, Uflyand (1961) [4] and Chang and Lundgren (1961) [5], who studied ducts with perfectly conducting walls, and Hunt (1965) [6], who solved several cases with various configurations of perfectly conducting walls and walls with arbitrary conductivity. Exact analytic solutions were determined for steady flow in straight rectangular ducts with uniform applied magnetic fields that are perpendicular to the flow. These authors analyzed fully developed flow, i.e. when all flow variables except pressure do not change along the flow direction and the pressure gradient is also uniform and constant, which reduces the problem to 2D since the axial direction has no variation. The solutions presented in these early works, expressed exactly as Fourier series, were the first of two types of analytical solutions of 2D MHD flows. The second type of solutions are asymptotic solutions which are derived using the simplifying assumption that electromagnetic forces are characteristically much larger than viscous forces and or inertia. These assumptions are often expressed using nondimensional numbers Ha, $N>>1$ where the Hartmann number squared Ha^2 represents the ratio of electromagnetic to viscous forces, and the interaction parameter N represents the ratio of electromagnetic to inertial forces.

Hartmann (1937) [7] derived exact 1D solutions to MHD flows prior to Shercliff's 2D derivations. Hartmann analyzed the case of fully developed laminar MHD flow between infinite parallel plates in a uniform magnetic field that is perpendicular to both the plates and the flow direction. Hartmann found that as Ha was made sufficiently large, the velocity profile became uniform except for very thin boundary layers attached to the no-slip plates. These so-called Hartmann boundary layers appear in duct flows along walls which are not parallel to the applied magnetic field and are therefore called Hartmann walls.

When Shercliff published his exact solution for fully developed MHD duct flows in 1953, he also included an analysis of the resulting velocity field. In addition to the Hartmann boundary layer, Shercliff observed a second layer attached to the sidewalls (i.e. walls parallel to the magnetic field) which behaved differently. This second MHD boundary layer came to be known as the Shercliff layer or, as in the present work, the side layer. A decade later, Hunt and Stewartson (1965) [8] used a boundary layer technique to study fully developed MHD duct flow at high *Ha* with insulated Hartmann walls (i.e. walls normal to the magnetic field) and perfectly conducting Shercliff walls (i.e. walls parallel to the magnetic field). They observed the thickness of the two MHD boundary layers to scale with Ha^{-1} and $Ha^{-1/2}$ for the Hartmann and side layers respectively. The bulk of the flow, called the core, is outside the boundary layers and is characterized by the paucity of viscous and inertial forces when $Ha, N >> 1$.

1.3 MHD Flows in Complex Geometries

Any LM blanket of a power fusion reactor exhibits a variety of complex geometry flows, including flows in bends, contractions, expansions, elbows, etc., where a liquid metal breeder circulates in the presence of a strong plasma-confining magnetic field for tritium breeding and possibly cooling and power conversion. Among them, manifolds are the key 3D elements as they are responsible for distributing the liquid inside the blanket. In blankets of toroidal *tokamak* reactors for example, such manifolds distribute LM flow from a radial feeding pipe at the blanket inlet to several poloidal channels and, collect the liquid from the poloidal flows to an exit pipe at the blanket outlet. Though these manifolds are small compared to the full length of the liquid metal circuit, they are the main contributors to the total pressure drop in the blanket due to 3D magnetohydrodynamic (MHD) effects that occur near sudden changes in the blanket geometry [2]. Reducing the pressure drop of the circulating breeder is one of the most fundamental practical goals of the blanket design and analysis. Additionally, it is important that the LM is distributed evenly throughout the blanket as areas with low flowrate are prone to overheating. Therefore, it is important to understand and

quantify the 3D effects in the manifold flows relating to MHD pressure drop and flow distribution. These 3D MHD effects are associated with 3D induced electric currents that close their circuit mostly in the axial direction. The electromagnetic Lorentz forces associated with the 3D currents are responsible for complex 3D flow patterns, formation of boundary and internal MHD layers, 3D pressure gradients, and ultimately, high, extra pressure losses.

3D MHD effects are known to be caused by non-uniform applied magnetic fields and, as in the present work, by axial variations of the flow geometry [2]. By comparison, 2D MHD effects are associated with 2D electric currents that circulate in the cross-sectional plane perpendicular to the main flow direction. The 2D effects are typical of fully developed MHD flows in which the velocity field does not change with the axial coordinate while the pressure varies linearly in the axial direction without variation within the cross-sectional plane. A number of analytic solutions (e.g. [3], [6]) are available for predicting 2D MHD flows, whereas 3D MHD flows are much more complicated such that the flow behavior must be studied experimentally or via numerical modeling.

Branover and Lielausis (1962) [9] and Branover, Vasil'ev, and Gel'fgat (1967) [10] performed experiments which featured a liquid metal flow in an electrically nonconducting duct that expanded suddenly in the plane of a transverse applied magnetic field. They observed large velocity jets in the side layers which carried nearly all the flow near the sudden expansion. The latter experiment also provided data on the pressure drop across the expansion which fit reasonably well to a correlation in the form $\Delta P_{3D}=\zeta(0.5)\rho U^2$, where ζ, the local pressure drop coefficient, is proportional to N. In an effort to explain the formation of jets in the side layers (M-shaped velocity profile) in the previously mentioned experiments with sudden expanding ducts, Gel-fgat and Kit (1971) [11] pointed out that in such regions where the duct width along the magnetic field direction changes, the Lorentz force is rotational and so could not be balanced by pressure gradients alone. Their conclusion was that the occurrence of side layer jets near expansions could be explained by the

necessity for hydrodynamic forces to arise in order to balance the rotational Lorentz force. This effect is also observable in flow through fringing magnetic fields and flows with other geometries that change along the flow direction. For example, MHD flow through nonuniform magnetic fields was studied asymptotically by Holroyd and Walker (1978) [12] who observed formation of side layer jets in the vicinity of the fringe.

Around the same time, while studying MHD flow over 2D obstacles, Ludford (1960) [13] observed a new type of internal layer which spread out along magnetic field lines from the obstacle. When Hunt and Leibovich (1967) [14] observed internal layers in their asymptotic analysis of 2D duct flows with diverging walls, they coined the term “Ludford layer” to describe such internal layers that span the flow at locations where the walls not parallel to the magnetic field have sufficiently high curvature for large *Ha* and *N*. Their 2D asymptotic analysis of Ludford layers suggested the existence of essentially three possible flow regimes which are characterized by the forces that balance the pressure gradient inside the Ludford layer: (i) the viscous-electromagnetic (VE) regime which holds for $N>>Ha^{3/2}$, (ii) the inertial-electromagnetic (IE) regime for $N<<Ha^{3/2}$, and a third regime (iii) where all three forces (IVE) are balanced for $N\sim Ha^{3/2}$ [15].

Hunt and Ludford (1968) [16] studied 3D MHD flow over obstacles inside ducts that have diverging walls and observed how the shear layer changes when the obstacle is conducting versus nonconducting. In that paper, they approximated solutions to the 3D governing equations using asymptotic analysis, taking the limit of dimensionless numbers such as Reynolds number *Re*, *Ha,* and, *N* approaching infinity. As a sequel to that paper, Walker, Ludford, and Hunt (1971) [17] studied 3D MHD duct flows with diverging walls using the analysis developed in the previous paper and observed three cases: the first case having the top and bottom walls diverge with the sidewalls remaining parallel, the second case having the sidewalls diverge while the Hartmann walls remain parallel, and a final case where both sets of walls diverged. In the first case, they found that velocity jets occurred near the sidewalls while the second case’s velocity profile was

conventional. When both walls diverged, the velocity profile included much larger velocities near the sidewalls which even reversed direction depending on the geometry. A third paper in the series was published by Walker, Ludford, and Hunt (1972) [18] which used the same 3D analysis of the first two papers to study diverging duct flow, this time with electrically nonconducting walls. They found large velocity jets in the side layers which carry most of the flow when the duct expands into the magnetic field direction. They also found that the disturbance caused by the expansion decays exponentially upstream.

Aitov, Kalyutik, and Tananaev (1983) [19] used numerical methods to solve for the entire flow field of 3D MHD flow through a suddenly expanding duct, as did Myasnikov and Kalyutik (1997) [20] and Bühler (2003) [21]. The latter used an asymptotic numerical method which neglected inertial force and demonstrated that without inertia, the flow becomes discontinuous at a sudden expansion, and even in gradual but short expansions, indicating the existence of a region near expansions where inertial forces are non-negligible. The former two studies were restricted to small *Ha* (10 and 40 respectively) due to the relatively high computational costs associated with higher *Ha*. All three of the above studies confirmed that side layer jets quickly form in the regions leading up to sudden expansions in electrically nonconducting ducts.

Another noteworthy numerical work is that of Molokov (1994) [22] who studied 3D MHD flow through a variety of complex geometries including expansion, manifolds, u-bends, elbows, and others. Citing the arguments of Hunt and Leibovich (1967) [14] and Tsinober and Stern (1964) [23], Molokov posited that the pressure drop (in the MHD scale [$p^*=p/\sigma UB^2b$]) across a sudden expansion in an insulated MHD duct flow would scale as $Ha^{-1/2}$ and $N^{-1/3}$. Later, Stiegletz, Barleon, Bühler, and Molokov (1996) [24] published a study on MHD flow through elbows that indicated a similar scaling for the pressure drop across the shear layer that occurred when the duct turned in the magnetic field direction.

In her thesis, Mistrangelo (2006) [25] numerically simulated the full 3D MHD equations in an electrically conducting duct featuring a sudden expansion in the plane of a uniform magnetic field. She observed many phenomena at *Ha* up to 1000 which are consistent with the present work (though the present work features insulating walls) including recirculation in the side layers downstream of the sudden expansion.

Other experimental studies of MHD flows through ducts featuring sudden expansions include Evtushenko, Sidorenkov and Shishko (1992) [26], Bühler, Horanyi and Arbogast (2007) [27], and Messadek and Abdou (2009) [28]. The latter featured multiple parallel channels which the flow entered downstream of the expansion. Surprisingly, it was observed that the flow balance among the parallel channels became less balanced as *Ha* increased.

Another numerical study which is relevant to the present work was performed by Mistrangelo and Bühler (2014) [29] who simulated an insulated MHD manifold flow which also featured an elbow to better match fusion blanket geometry. The flow distribution data they provide matches trends which are studied in more detail in the present work. They also demonstrated that a significant MHD pressure drop occurs across the expansion, the proper scaling of which is a major topic of the present work.

1.4 MHD Duct Flows with Buoyancy Effects

The volumetric nuclear heating induced by neutrons in LM fusion blankets is highly non-uniform along the radial direction with the majority of the heating occurring near the first wall [30]. The heating decreases rapidly moving outwards along the radius of the reactor as the neutron flux is attenuated by the LM. Such high radial gradient in heating is bound to produce temperature gradients which will in turn give rise to buoyant forces. Buoyant force is oriented opposite to the direction of gravity and the orientation of the LM blanket flows will vary along the perimeter of the reactor's core [1], so the possible buoyant effects have a wide spectrum of phenomena with many

important particular cases to study. Moreover, there is the simultaneous effect of the strong magnetic field to consider, the strength of which also varies by location inside the reactor. Depending on the flowrate, magnetic field, and relative strength of buoyant effects, the flow regime may be that of MHD forced flow, weakly unsteady MHD mixed convection, or strongly unsteady MHD mixed convection. In addition to *Ha* and *Re*, such flows are also characterized by the Grashof number *Gr* which represents a ratio of buoyant force to viscous force.

While many studies have been performed for MHD duct flows in the context of fusion research and development, relatively few studies have included the combined effect of buoyancy and MHD simultaneously as in the present work.

Bühler (1998) [31] performed asymptotic analysis on buoyancy driven flows in long vertical ducts with transverse magnetic fields and various heating modes. His analysis, which assumes $Ha^4 >> Gr$, suggests the inviscid core does not necessarily behave two-dimensionally and that large jets attached to the sidewalls will carry most of the flow for conducting walls. The problem was revisited by Mistrangelo and Bühler (2011) [32] using numerical methods, confirming the previous conclusions and validating their numerical approach.

Zikanov, Thess, and Sommeria (1998) [33] performed DNS type simulation of a vertical duct flow with periodic axial boundaries driven by uniform axial temperature gradients. The focus of their study was on elevator modes: antiparallel vertical jets which grow due to buoyant effect. They found the elevator modes to be stabilized by an axial applied magnetic field to enhance vertical heat transfer.

There have been experimental efforts to study MHD mixed convection duct flows. Experiments in Russia by Melnikov et al. (2013) [34] as part of the MPEI – JIHT RAS MHD-facility showed significant low frequency, high magnitude, temperature fluctuations in downward flow of mercury in a round tube heated on one side via radiation. Experiment on a rectangular duct in the same

facility by Kirillov et al. (2016) [35] also showed periodic temperature fluctuations but also included velocity data which indicated significant asymmetry due to buoyant effects in downward MHD flow of mercury. Belyaev et al. (2018) [36] studied MHD mixed convection in a vertical pipe with transverse magnetic field and uniform surface heating using the more recent HELM Experimental Facility at the JIHT RAS. The experimental results indicated that the magnetic field promoted high amplitude temperature fluctuations at moderate *Ha* (300-350) but suppressed fluctuations at higher *Ha* (>500) for *Re* on the order of 10^4 and *Gr* on the order 10^7. As of recently, the MaPLE-U experiment is underway at UCLA. The present dissertation provides numerical comparison for future results of this experiment which consists of vertically driven PbLi in a square duct with one-sided surface heating and a region of uniform, transverse magnetic field.

In the past few decades, there have been substantial numerical efforts to explore the combined effects of MHD and buoyancy in vertical MHD mixed convection duct flows with transverse magnetic fields and applied heating. However, in order to reduce the cost of computations, researchers mostly limited their investigations to 2D flows, either by studying the fully developed flow, or by assuming the flow is quasi-2D. The former assumes that the velocity does not change along the flow direction while the latter assumes that the velocity does not change along the magnetic field direction (outside of the boundary layers).

Fully developed downward flows in vertical ducts were studied by several researchers: Sposito and Ciofalo (2008) [37] studied fully developed downward flow with an analytic temperature solution and numerical velocity and electric potential solutions for vertical square ducts with variable wall conductivity and applied magnetic field and uniform volumetric heating. Smolentsev et al. (2008) [38] found solutions of fully developed flow in insulated vertical ducts with exponential volumetric heating and transverse magnetic field using a newly developed analytical solution in addition to a numerical Q2D approach. The results of the two approaches showed good agreement and indicated the occurrence of flow reversal in buoyancy opposed MHD flows for the

first time. The flow reversal was also characterized by the steepness of the heating curve and a ratio of the parameters *Ha*, *Re*, and *Gr*. Based on Smolentsev's prediction of flow reversal in buoyancy opposed MHD flows, blanket designs are recommended to avoid having downward flows in channels closest to the first wall. Saleh and Hashim (2010) [39] studied fully developed downward flow in electrically nonconducting ducts numerically. Mistrangelo and Bühler (2012) [40] numerically investigated the effects of changing the transverse magnetic field direction relative to the applied surface heating and changing the electrical conductivity of the walls by considering fully developed flows. Chutia and Deka (2012) [41] studied fully developed flow using MATLAB with low parameters *Gr, Ha*~10^2 and *Re*=1. Zhang and Zikannov [42] used a Q2D model to study turbulent convection in horizontal pipes in 2015. Later, in 2018 [43] they studied instability and flow reversal in vertical MHD flows with applied heating and a transverse magnetic field. All studies featuring downward flows with strong buoyancy effects reported considerable flow reversal.

Liu and Zikanov (2015) [44] numerically simulated vertical MHD mixed convection duct flow with a transverse magnetic field and a heated wall using a quasi-2D formulation to observe stable elevator modes.

Some efforts to model fully 3D flows have been made for the purpose of studying MHD mixed convection flow phenomena in the context in fusion blankets. Vetcha (2012) [45] studied the instability of buoyancy assisted and buoyancy opposed flows in his thesis which included fully 3D numerical simulation of MHD mixed convection flow. His study begins with linear stability analysis and DNS of MHD inflectional instabilities and then continues with Q2D numerical investigation of MHD mixed convection upward flows with volumetric heating for various *Gr* up to 10^9, *Re* up to 10^4 and *Ha* up to 500. Steady, weak turbulence, and strong turbulence regimes were characterized based on the dimensionless parameters. Lastly, fully 3D numerical modeling using HIMAG was performed for the sake of comparison with buoyancy assisted duct flow solutions

from Q2D models and analytic solutions for fully developed flow [38]. Zikanov and Listartov (2016) [46] simulated the test section geometry of Melnikov et al. (2013) [34] which included a vertical pipe flow with transverse magnetic field and one-sided heating. From the results, they identified the mechanism behind temperature fluctuations observed in experiment and they explain the mechanism as “the growth and breakdown of elevator convection modes”. Listratov et al. (2018) [47] simulated horizontal pipe flow with a transverse magnetic field and one-sided uniform heating from below to study the effect of *Ha*, *Re*, and *Gr* on high amplitude temperature fluctuations from buoyant effects.

The studies on the combined effects of MHD and buoyancy in the present work reveal new phenomena which may influence many aspects of blanket design including thermomechanical fatigue and corrosion of the duct walls, tritium permeation, and heat transfer for power generation. Moreover, the results presented in this dissertation (Part II) will be valuable for the development of future numerical tools and validation of new experimental results.

Part I: MHD Flows in Manifolds

In Part I, 3D numerical analysis of MHD flows were performed in a simplified model of an inlet manifold subject to a transverse magnetic field (Fig.1).

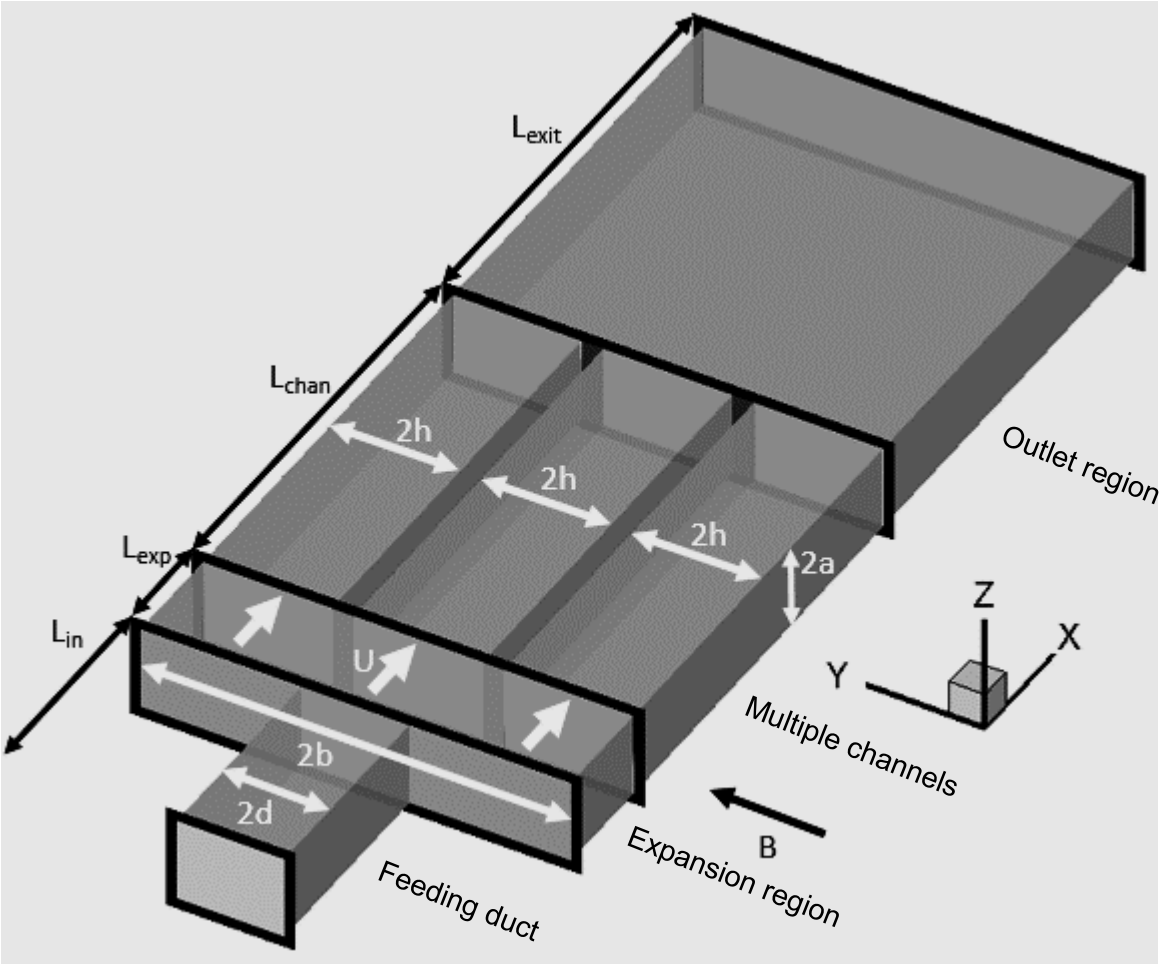

FIG. 1. A prototypic manifold geometry for numerical simulation. Fully developed flow enters the feeding duct, spreads out into the expansion region, is sorted into multiple parallel channels, and collects in the common outlet where it becomes fully developed before exiting the duct.

In this prototypic model, flow enters the manifold of height 2*a* through the feeding duct of width 2*d* and length L_{in} before entering the expansion region, which has length L_{exp}, width 2*b*, and average velocity *U*. From the expansion region, the flow proceeds into three or more identical parallel channels of the width 2*h* and length L_{chan} and exits through a common outlet of width 2*b* and length L_{exit}. These dimensions have a strong effect on the flow distribution and the pressure drop and are subject to optimization. In the present study, some of the dimensions are used as

computational parameters to address the effect of the manifold design on the flow. The flow in the manifold occurs in a uniform transverse magnetic field *B*, which is also used as a parameter in the computational study. In this study, only nonconducting manifolds are considered such that all induced electric currents are closed inside the flow domain.

Part I of this dissertation is organized as follows: Chapter 2 contains a description of the problem formulation and numerical methods used; Chapter 3 contains a brief comparison to experimental results, a mesh refinement study, a discussion of the physics and phenomena of MHD manifold flows, a discussion of the developed 3D MHD pressure drop model, a discussion of the flow distribution in manifolds, an analysis of a Resistor Network Model for describing flow distribution, and an example application of the developed pressure model to a dual coolant lead lithium (DCLL) blanket; Chapter 4 contains a summary of conclusions.

Chapter 2: Physical and Mathematical Model of MHD Flows in Manifolds

To study 3D MHD manifold flow behavior sketched in Fig. 1, a well-verified MHD solver developed by HyPerComp/UCLA, HIMAG [48], is used to simulate the laminar flow of liquid metal of kinematic viscosity *v*, electrical conductivity σ and density ρ through an electrically insulated manifold in a strong transverse magnetic field *B*. Such a flow is characterized by the following key dimensionless parameters: the Hartmann number, $Ha = bB\sqrt{\sigma/\nu\rho}$; the Reynolds number, $Re = \frac{bU}{\nu}$; the expansion ratio, $r_{exp} = b/d$; the dimensionless length of the expansion region, L_{exp}/b; the dimensionless length of the parallel channels, L_{chan}/b; and the channel size parameter, $s_c = h/b$. In addition to *Re* and *Ha*, the interaction parameter, $N = \frac{Ha^2}{Re}$, which characterizes the ratio of electromagnetic to inertia forces, is another important parameter. The half width *b* of the expansion region was chosen as a length scale in the definition of *Ha*, *Re*, and *N*, to best

characterize the 3D MHD effects which exist primarily in the expansion region. Furthermore, the expansion region is also where the flow is redistributed and where stationary vortex tubes may exist. For the same reasons, the average velocity in the expansion region *U* was chosen as the velocity scale. However, because the flow in the expansion region is electrically coupled with the flow in the inlet via 3D currents, the expansion ratio r_{exp} is required in order to fully characterize the flow. Physical properties were chosen to equal those of eutectic lead-lithium alloy (PbLi) at 500ºC. The applied magnetic field *B* is varied to control *Ha. U* was chosen such that the inlet velocity U^*r_{exp}=0.01m/s is the same for all the simulations and $\frac{a}{d} = 0.8$ for every simulation.

The HIMAG code solves the full incompressible MHD equations, shown below (1-4), using an electric potential formulation with the assumption that the induced magnetic field is small enough to be neglected compared to the applied one. Equations (1-4) are the modified form of the Navier-Stokes-Maxwell equations written in the inductionless approximation, which include the continuity equation, momentum equation with the Lorenz force term on the right-hand-side, Ohm's law to compute the induced electric current, and the electric potential equation respectively:

$$\nabla \cdot \mathbf{u} = 0, \tag{1}$$

$$\frac{\partial \mathbf{u}}{\partial t} + \mathbf{u} \cdot \nabla \mathbf{u} = -\frac{1}{\rho}\nabla \mathrm{p} + \nu \nabla^2 \mathbf{u} + \frac{1}{\rho}\mathbf{J} \times \mathbf{B}, \tag{2}$$

$$\mathbf{J} = \sigma(-\nabla \phi + \mathbf{u} \times \mathbf{B}), \tag{3}$$

$$\nabla \cdot (\sigma \nabla \phi) = \nabla \cdot (\sigma \mathbf{u} \times \mathbf{B}). \tag{4}$$

Here, **u**, **J**, and **B** are the velocity, electric current density, and magnetic field vectors respectively and p and ϕ are the pressure and electric potential. Equation (4) is obtained by taking the divergence of Eq. (3) while stipulating that electric current is continuous ($\nabla \cdot \mathbf{J} = 0$). To consider both the liquid and the surrounding solid wall, which may have different electrical conductivity, the electrical conductivity σ is put inside the derivatives in Eq. (4).

HIMAG (HyPerComp Incompressible MHD solver for Arbitrary Geometry) is a three-dimensional, unstructured grid based MHD flow solver developed over the last decade by a US software company named HyPerComp, with support from UCLA. The numerical approach is based on finite-volume discretization using a collocated arrangement (all unknowns are located at the cell centers) with second-order accuracy in space and time. The mass conservation is satisfied, and the pressure field is evaluated using a four-step projection method with semi-implicit Crank–Nicolson formulation for the convective and diffusion terms. A charge conserving consistent scheme developed in [49, 50] is applied to accurately compute the electric potential and the electric current density at high Hartmann numbers. Given the unstructured nature of the solver, multiple strategies are employed to account for mesh skewness and non-orthogonality. Finally, the solver algorithms are parallelized using MPI architecture, thereby making the solver capable of being run on large computational clusters. Additional details regarding the formulation and validation of the HIMAG code can be found elsewhere (e.g. [51]).

Equations (1-4) are solved numerically on non-uniform rectangular meshes (Fig. 2). In making each mesh, I ensured that there are at least 5 nodes inside all Hartmann layers on the walls perpendicular to the magnetic field and 12 nodes inside each side layer on the wall parallel to the magnetic field. Also, higher mesh resolution was used in the liquid next to the back wall of the expansion region, which is perpendicular to the axial direction, and at the beginning and end of the multiple channels.

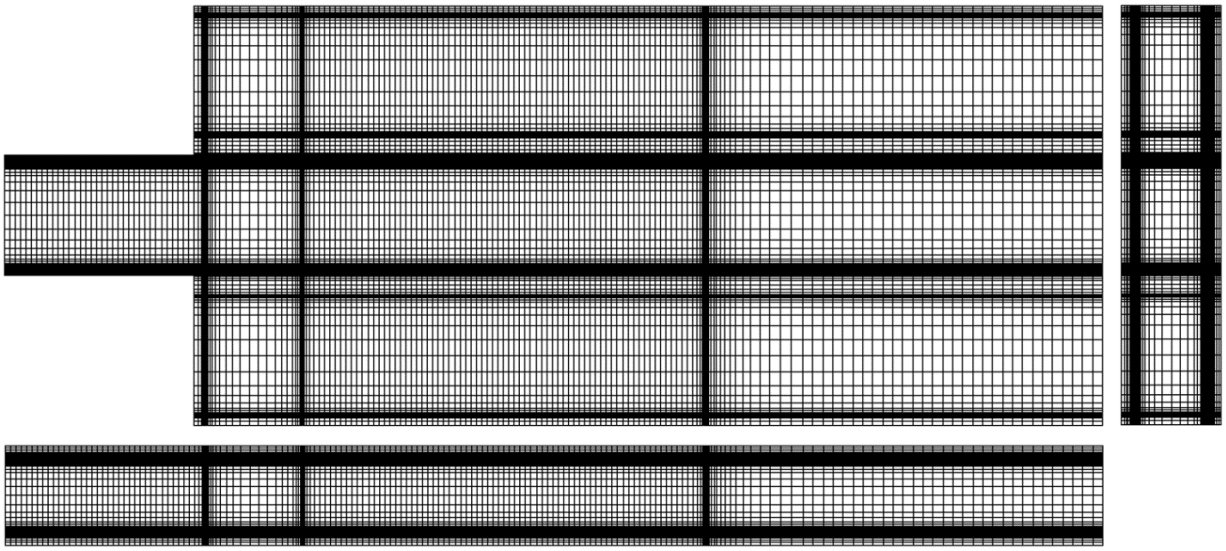

FIG. 2. An example computational mesh with 2.05 million cells for a manifold geometry with 3 channels, $L_{exp}/b=0.5$, $L_{chan}/b=2$, $r_{exp}=4$, and $s_c=0.3$.

Shercliff flow [3] is used at the inlet boundary condition for both the pressure gradient and the velocity profile in the feeding duct and a fully developed flow outlet boundary condition in the form $\frac{\partial}{\partial \mathrm{x}} = 0$ is used at the exit. The pressure is set to zero at the outlet and the fluid-wall boundaries have Neumann pressure conditions $\left(\frac{dp}{dn} = 0\right)$. The no slip and no flow-through conditions are enforced at fluid-wall interfaces $(\mathbf{u_{wall}} = \mathbf{0})$. Normal components of electric current density are set to zero at the outer domain boundary $\left(\frac{d\phi}{dn} = (\mathbf{u} \times \mathbf{B}) \cdot \hat{\boldsymbol{n}}\right)$. Since this study deals with a nonconducting manifold, the wall electrical conductivity is set to zero. Simulations were started with initially uniform flow conditions with a time step size of $\Delta t=10^{-4}$ s. Using the Hoffman2 computer cluster at UCLA, each simulation was run in parallel on 64 or 128 nodes until steady state solutions were reached as determined by the L2 norm of the residuals reaching the order of 10^{-10}. The L2 norms of residuals were calculated according to Eqs. (5) and (6):

$$|\mathbf{r}| = \sqrt{\sum \mathrm{r_i^2}}, \tag{5}$$

$$\mathrm{r_i} = \mathrm{F_i^{m+1}} - \mathrm{F_i^m}. \tag{6}$$

Here the L2 norm $|\mathbf{r}|$ of residuals r_i is calculated for each of the flow variables F for time step m. The subscript i is the cell index. Many simulations varying by geometry and *Ha* were started simultaneously. Once each simulation converged, the converged solutions were used as initial conditions for subsequent simulations at higher values of the flow parameters to reduce the computational time. Totally, 130 cases have been computed. The minimal computational time was half a day and the longest simulations ran for a month, depending on the flow parameters and manifold geometry. Generally, computational time increased as *Re* was increased.

Chapter 3: Results of Manifold Simulations and Discussion

3.1 Comparison to Previous Results

Present simulation results show superior agreement with the experimental measurements and demonstrate significant improvement compared to the previous computations of flow distribution in an MHD manifold. Fig. 3 shows the flow distribution for a manifold that feeds three channels as determined by experimental work by Messadek et al. at UCLA [28], numerical work by Morley et al. [52], and the present numerical work.

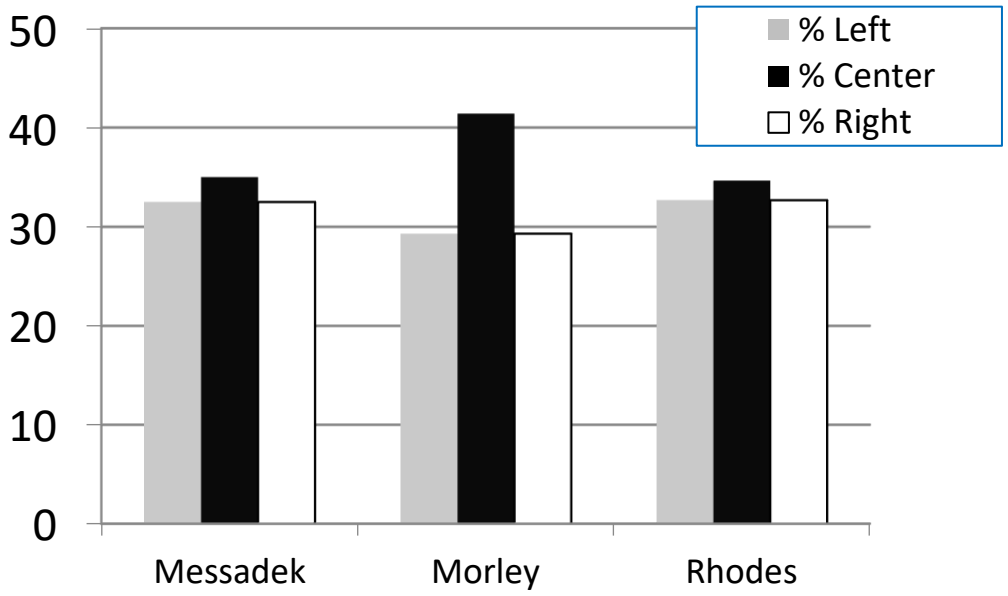

FIG. 3. A comparison of present simulation results with previous numerical and experimental work [17]. Here flow distribution is reported as the percentage of flow through each of three channels. Ha=2190, Re=250, r_{exp}=4, L_{chan}/b=2, L_{exp}/b=1, s_c=0.3.

The computations of the present study show just a small imbalance among three parallel channels (for the given set of the parameters). This is very similar to the earlier experiments but different from the computational predictions in [52]. The recent improvement in the computations of the manifold flows is attributed solely to the addition of a common outlet region with length L_{exit} so that the use of the uniform pressure boundary condition (p=0) is more appropriate. In the previous computations in [52], the outlet section was not included such that the flow at the manifold exit was artificially forced to agree with uniform pressure boundary condition.

3.2 Mesh Refinement Study

Prior to the main computations, a mesh sensitivity study was performed using an electrically nonconducting manifold without multiple channels at *Ha*=4380, *Re*=100 and r_{exp}=8, on three computational meshes of ~10^6 cells each in order to quantify the discretization error, including "coarse", "medium" and "fine" meshes. Each consecutive mesh featured approximately twice as many cells as the previous mesh. The number of cells in each mesh is shown in Table 1.

Table 1. Mesh Refinement Details.

Mesh	# of cells along x	# of cells along y	# of cells along z	Total # of cells
Coarse	110	154	33	490776
Medium	139	191	40	932040
Fine	174	240	50	1832500

The manifold's centerline axial pressure gradient obtained in the mesh sensitivity study for the three meshes is plotted in Fig. 4 along with the pressure gradient of fully developed flow (Shercliff solution [3]).

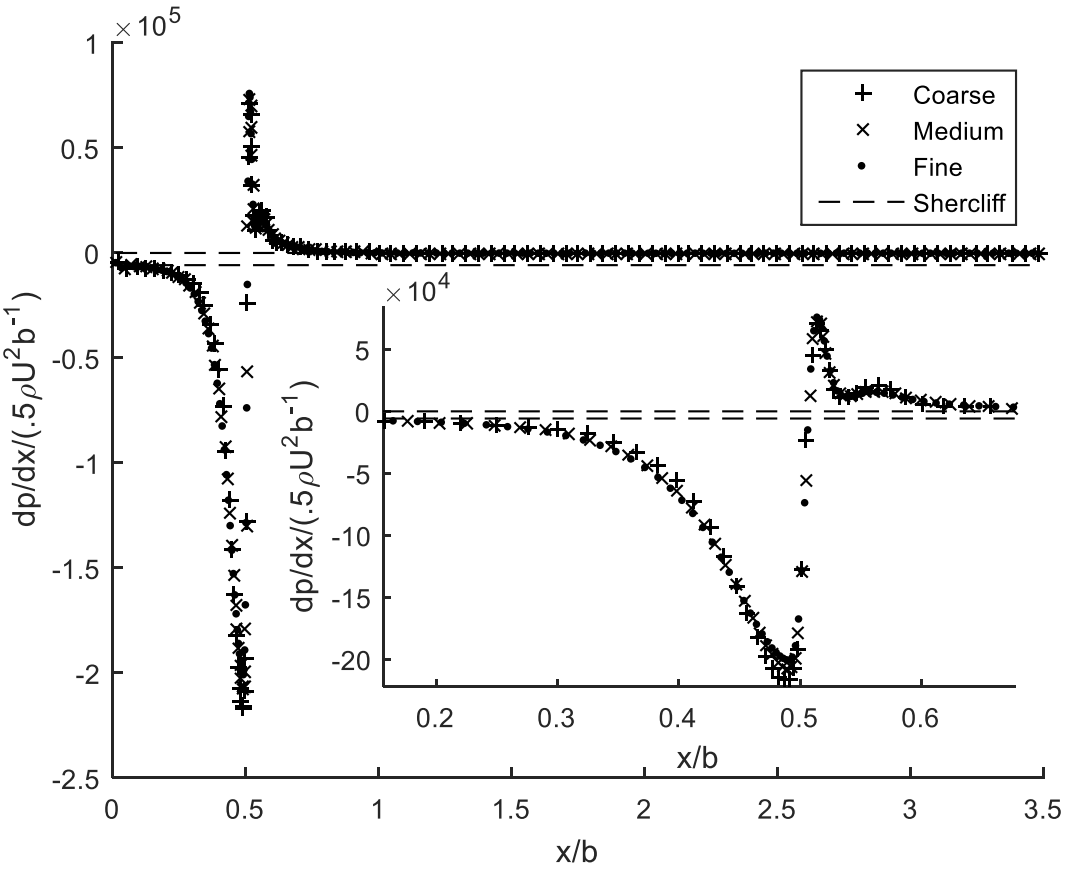

FIG. 4. Results of a mesh refinement study. Axial pressure gradient is plotted along the y=z=0 centerline of a manifold without multiple channels for three meshes: coarse, medium and fine. Fully developed flow Shercliff solution is also shown. Zooming in on the sudden expansion at x/b=0.5 reveals differences between the meshes. Here, Ha=4380, Re=100, r_{exp}=8.

The difference in pressure drop between the medium mesh and the coarse mesh is 2.55%. The difference in pressure drop between the fine mesh and the medium mesh is 0.027%. For all other computations in the present work, meshes similar to the fine mesh are used.

3.3 Characteristic Features of MHD Manifold Flow

Before going into details of the proposed pressure model and flow distribution analysis, the most important flow features are summarized here to describe the fundamental manifold flow physics. The discussion is based on the present computations for electrically nonconducting manifolds as shown in Fig. 1 in a range of flow parameters relevant to a fusion blanket at $Ha \sim 10^3$, $r_{exp} \geq 4$, and $Re \sim 10^1\text{-}10^3$. In this parameter space, the computed flows are laminar, symmetrical with respect to the symmetry planes y=0 and z=0, and steady. The most characteristic flow feature, as observed in all the computations, is the appearance of induced 3D (axial) currents as shown in Fig. 5 and related 3D MHD effects that manifest themselves through abrupt variations in the velocity and pressure field where the flow geometry changes.

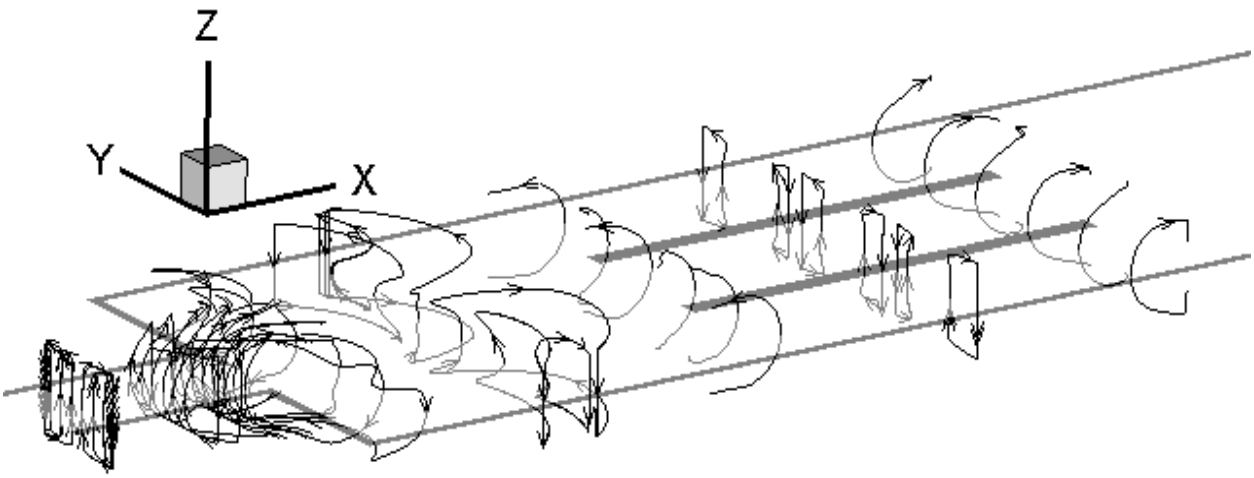

FIG. 5. Electric currents circulate in an MHD manifold flow. The currents become 3D near changes in the flow geometry. r_{exp}=4, L_{exp}/b=2, L_{chan}/b=2, s_c=0.3, and n=3 channels for Ha=1465 and Re=50.

Sources for the 3D MHD effects exist at three locations along the flow path (see the sketch in Fig. 1): first where the liquid enters the expansion region, then where it is distributed into parallel

channels, and finally near the exit of the channels where the liquid is collected before exiting the manifold. The generation of such 3D currents at these three locations can be explained through Ohm's law. Namely, the average velocity changes due to continuity as the flow geometry changes. These changes in the mean velocity (while the applied magnetic field doesn't change) cause axial variations in the electric potential distribution which in turn drive an axial electric current whose circuit is closed upstream and downstream of each cross-sectional variation. This phenomenon is illustrated in detail for the sudden expansion in Fig. 6.

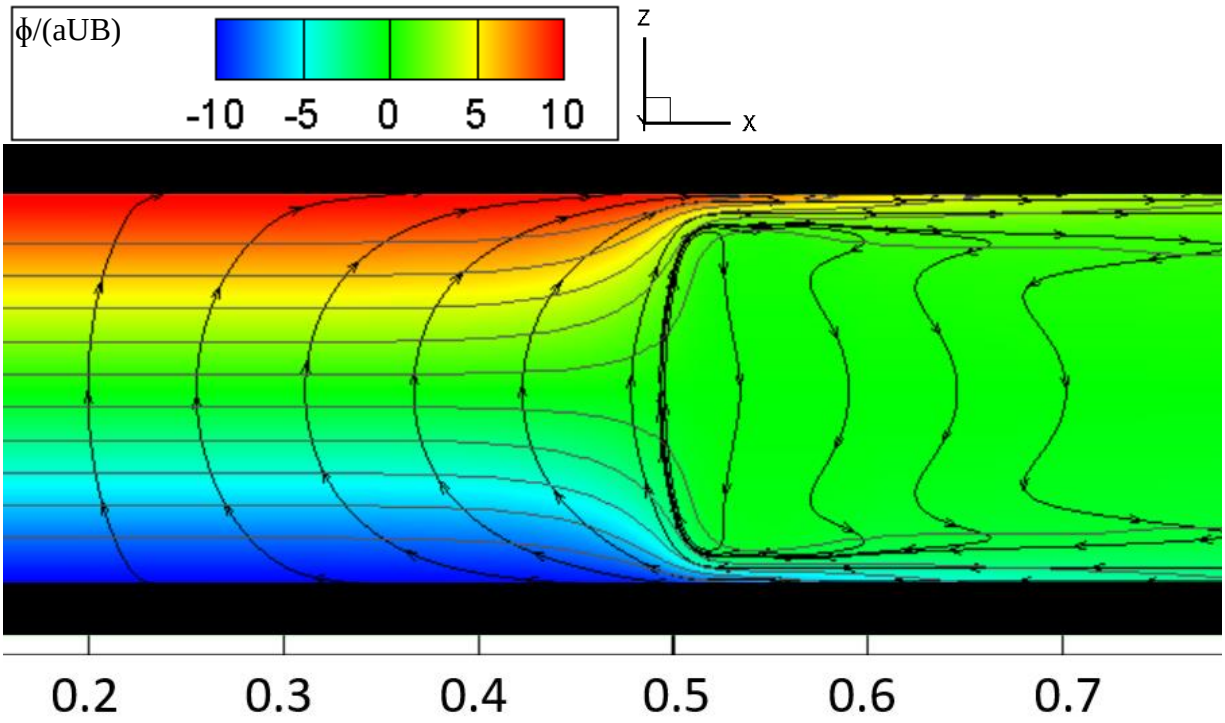

FIG. 6. Electric potential and currents on the y=0 center plane. Axial currents are generated near the sudden expansion at x/b=0.5 and then close upstream and downstream of the expansion. Ha=5475, Re=50, and r_{exp}=10.

Such 3D circulations are shown to occur where the mean velocity decreases across the sudden expansion, increases into each individual parallel channel, and then decreases again into the outlet region. Compared to 2D currents, which are limited by the resistance of the Hartmann layers where they close, 3D currents mostly close inside the bulk of the fluid. As a result, even small changes in cross-section cause bulk current densities that are much greater than the 2D

circulations which occur in the feeding duct near the inlet, in the middle of the parallel channels, and near the end of the outlet region as shown in Fig. 5.

The observed 3D and 2D current circuits and associated Lorentz forces have a strong impact on the flow and the pressure field as illustrated in Fig. 7, which shows velocity profiles at nine selected locations along the flow path as well as the axial pressure distribution.

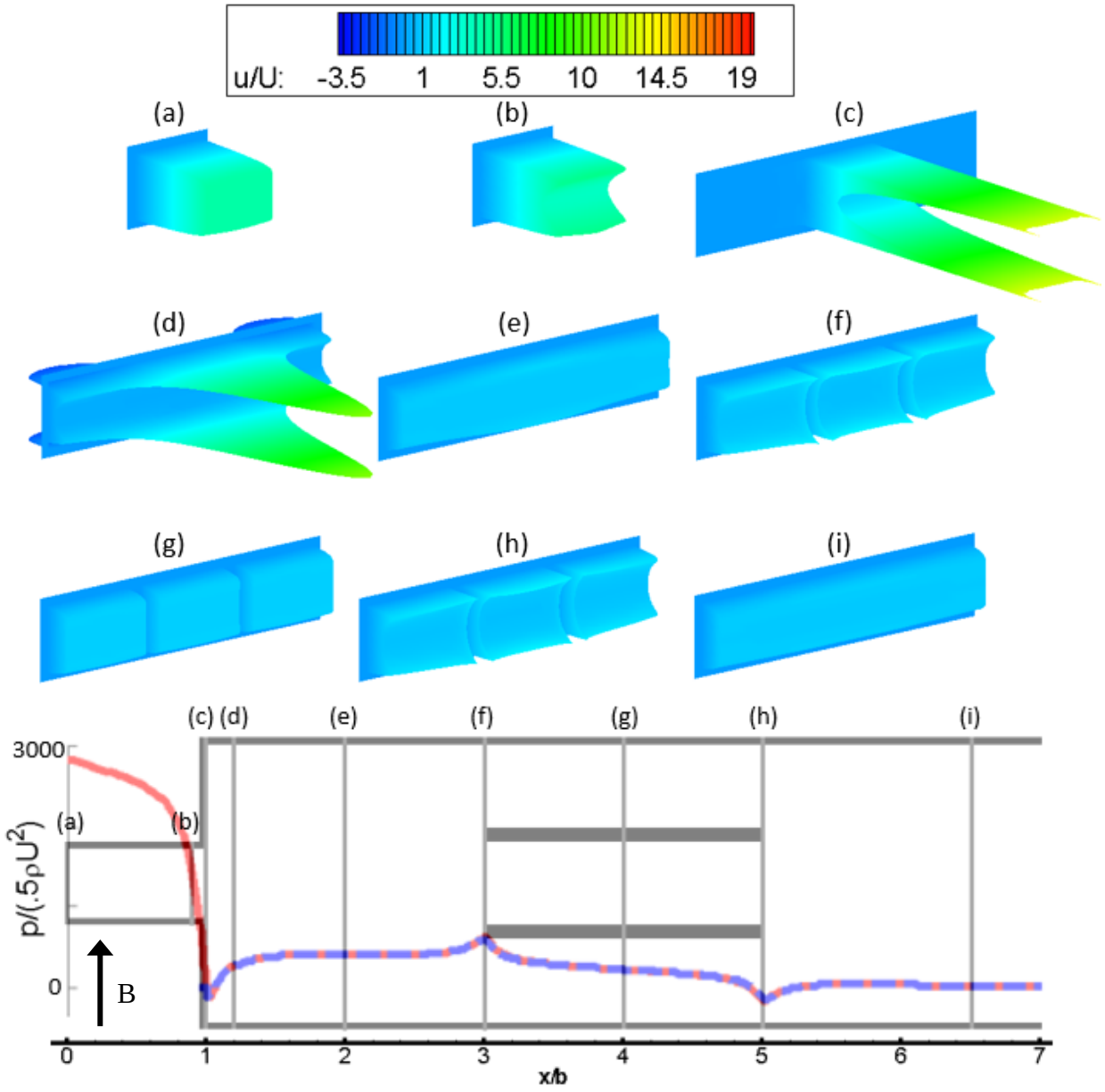

FIG. 7. (Bottom) Non-dimensional pressure is plotted for the centerlines of the center (solid red) and side (dashed blue) channels over a top-down view (xy) of a manifold with r_{exp}=4, L_{exp}/b=2, L_{chan}/b=2, s_c=0.3, and n=3 channels for Ha=1465

and Re=50. The vertical grey lines labeled (a) through (i) correspond to the 9 axial velocity profiles shown above. (Top) Non-dimensional axial component of velocity, u/U, is plotted for yz cross-sections at 9 locations along the manifold.

Inside the feeding duct, the 3D MHD effects are responsible for smoothly transitioning the flow from a fully developed Shercliff velocity profile at the inlet [location (a) in Fig. 7] to an M-shaped profile [location (b)]. The trend of forming the M-shaped velocity profile accelerates rapidly between locations (b) and (c) and falls off just as quickly downstream of the expansion. Inside the expansion region, a complex M-shaped flow structure [location (d)] quickly changes to a nearly uniform flow, evenly distributed in the transverse direction [location (e)], owing to the tendency of MHD duct flows in a strong transverse magnetic field to become quasi-2D. The 3D effects reappear at locations (f) and (h) at the entry to at the exit from the parallel channels. Inside the parallel channels, between locations (f) and (h), the flow is almost fully developed as seen from the linear pressure distribution and Shercliff-type velocity profiles at location (g). Once exiting the parallel channels, the flow in the outlet region quickly becomes fully developed [location (i)].

The flow downstream of the sudden expansion [between locations (c) and (e)] is particularly complex and warrants further discussion. Flow enters the expansion region with the majority of the flow localized near the sidewalls parallel to the magnetic field (Fig. 7c). In the side layers, y-direction pressure gradients force flow outwards toward the periphery of the channel. The y-direction pressure gradients are induced by axial electric currents as follows: axial currents exist near the sidewalls as seen in Fig. 8a which cause z-direction Lorentz force in the expansion region; according to the direction of the axial currents here, these forces are positive near the center and negative near sides (at $|y|>0$); as the core pressure is uniform along the y-direction, the sidewall pressure will be greater near the center and lesser near the sides compared to the core pressure due to the z-direction Lorentz forces. The pressure on the sidewall gradually becomes uniform as the axial current density approaches zero away from the expansion. The resulting pressure distribution near the sidewalls causes liquid to return to the back wall of the expansion region in a manner that also distributes it along the y-direction as illustrated in Fig. 8b.

Once the fluid reaches the internal layer along the back wall, it drops out of the side layers to enter the Q2D core.

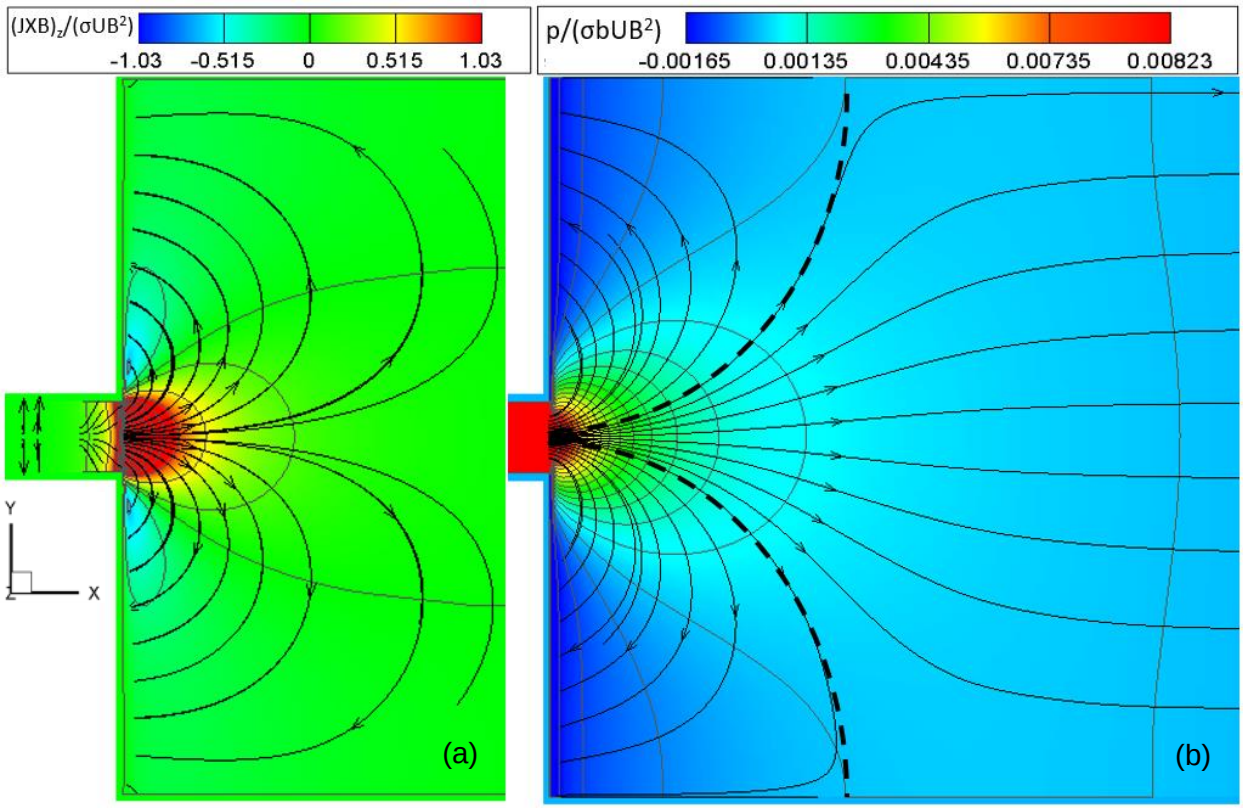

FIG. 8. (a) Electric currents and contours of z-direction Lorentz force at the z/a=.94 plane in the side layer. (b) Velocity streamlines and pressure contours at z/a=.94 plane in the side layer. The dashed lines are streamlines which intersect the Hartmann walls at reattachment points and define a reattachment length. r_{exp}=10, Ha=5475, and Re=50.

The present observations of reverse flow in the side layers is consistent with those of Bühler [21], who first observed reverse flow in MHD sudden expansions, and of Mistrangelo [25], who studied the reverse flow in more detail. Mistrangelo also defined the reattachment length as the distance between a sudden expansion and a limiting streamline which bounds the reverse flow. She noted that the reattachment length shrinks with stronger applied magnetic field, scaling with $N^{-1/3}$. The electromagnetically driven 3D flow structure in the expansion region allows the core to become Q2D after a very short distance into the expansion region (note the evenly distributed core flow in Fig. 7d). Past the reattachment length, the entire flow in the expansion region becomes Q2D. The above description of the flow structure in the expansion region is typical for the entire parameter

space of the present simulations; however, at large enough *Re*, additional complexity enters the flow in the expansion region as stationary vortex tubes are observed to form (see Fig. 9).

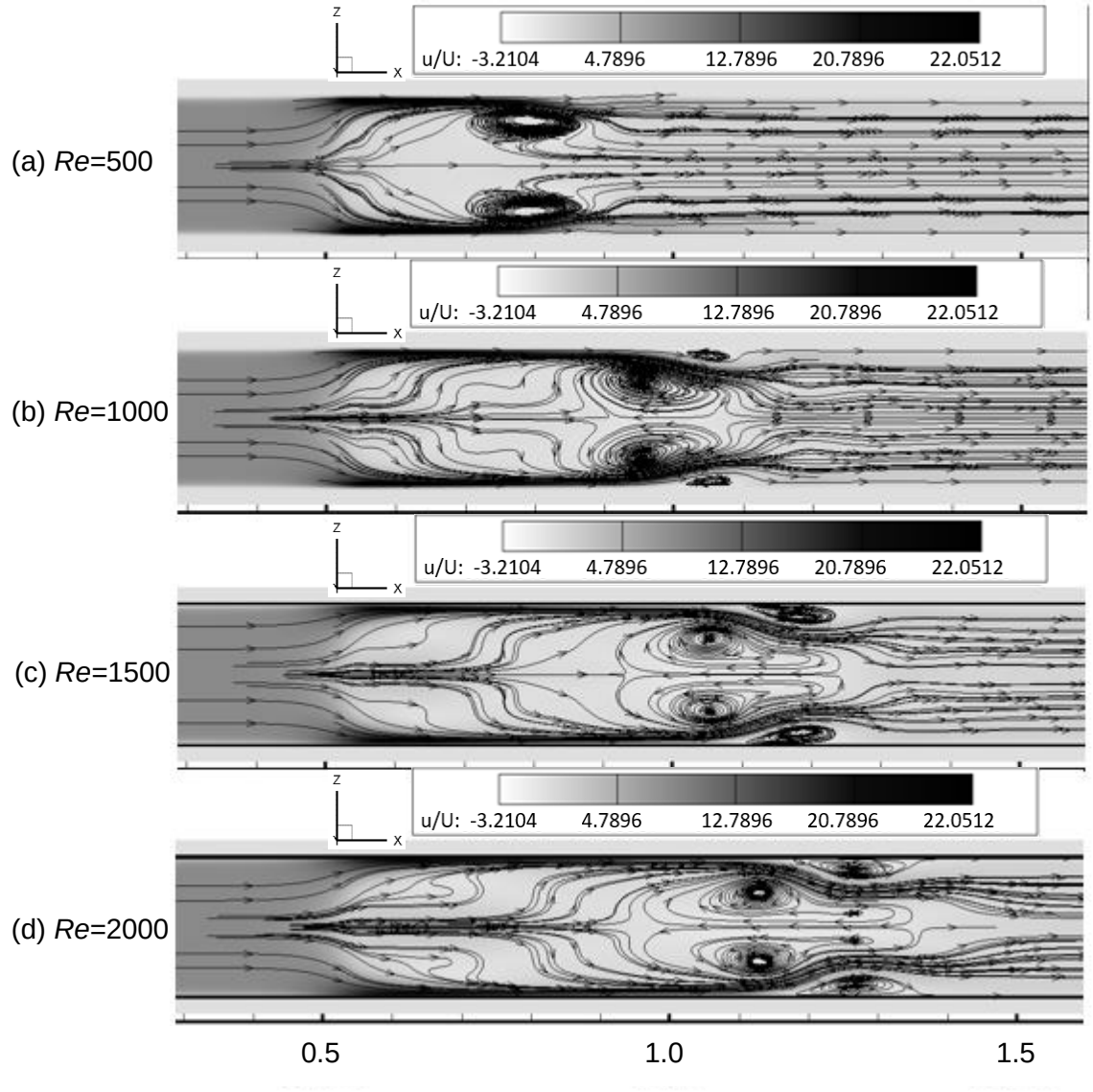

FIG. 9. Velocity streamlines in the y=0 center xz-plane of an insulating duct with a sudden expansion at x/b=0.5. r_{exp}=8, Ha=3400, and Re=500, 1000, 1500, and 2000 for (a), (b), (c), and (d) respectively. The contours are of x-direction velocity.

In the course of computations, the vortices were observed to travel downstream until a steady state was achieved. The equilibrium axial position of the vortices is observed to increase with *Re*. The number of vortices also increases as *Re* increases. The vortex tubes span the duct along

magnetic field lines, confirming that the Q2D flow regime is dominant in the bulk of the flow despite the complexity.

Apart from the above considerations that refer to 2D versus 3D flow features, it is useful to look at the structure of MHD flows in the manifold from the point of view of the magnitude of curl of the Lorentz force. As shown below, a high magnitude of $\nabla \times \mathbf{J} \times \mathbf{B}$ indicates special flow subdomains, where inertial and/or viscous forces are important [53]. To begin, we note that in the fusion relevant parameter space, N>>1 and Ha>>1 so that the flow is essentially inertialess and inviscid and pressure gradients tend to balance electromagnetic forces wherever possible. Such flow subdomains where viscous and inertia forces can be neglected are usually referred to as “core flows” [54]. However, there can be subdomains where the Lorentz force cannot be fully balanced by the pressure gradients because pressure gradients are always curl free while the Lorentz force can include a rotational component. Thus, in such subdomains where its curl is non-zero, rotational hydrodynamic forces must exist to balance Lorentz force. For instance, in fully developed MHD flows, the Lorentz force is curl free everywhere except for inside the Hartmann boundary layers at the walls perpendicular to the magnetic field and Shercliff layers at the duct walls parallel to the magnetic field, where viscous forces are very important. In uniform magnetic fields, $\nabla \times \mathbf{J} \times \mathbf{B}$ reduces to $(\mathbf{B} \cdot \nabla)\mathbf{J}$ so curl of Lorentz force can be interpreted as a measure of nonuniformity of current density along the B-field direction. Thus, we can predict that Lorentz force will be strongly rotational at expansions and contractions that occur in the plane parallel to **B** (as in the present case) because variation in current density is expected to occur along the B-field. The same cannot be said for expansions and contractions that are perpendicular to **B**.

Plots of the magnitude of $\nabla \times \mathbf{J} \times \mathbf{B}$ in Fig. 10 confirm this prediction and reveal thin internal layers at the sudden expansion and contractions where viscous and inertial forces must be significant to balance electromagnetic forces. According to the 2D Ludford layer theory [14], and also as confirmed for 3D flows by Bühler [21] and Mistrangelo [25], the thickness δ of the internal layer

scales with $Ha^{-1/2}$ if the flow regime is viscous-electromagnetic for $N>>Ha^{3/2}$ and with $N^{-1/3}$ in the inertial-electromagnetic regime for $N<<Ha^{3/2}$. In the literature, the internal layer is also sometimes referred to as the expansion layer, a term coined by Bühler to differentiate the 3D phenomenon from the 2D Ludford layer. Here, these layers are referred to as internal layers. Fig. 10 clearly demonstrates formation of thin internal layers at the sudden expansion and at the entrance to and exit from the parallel channels. Hartmann and Shercliff boundary layers, where viscous forces are dominant, are also visible.

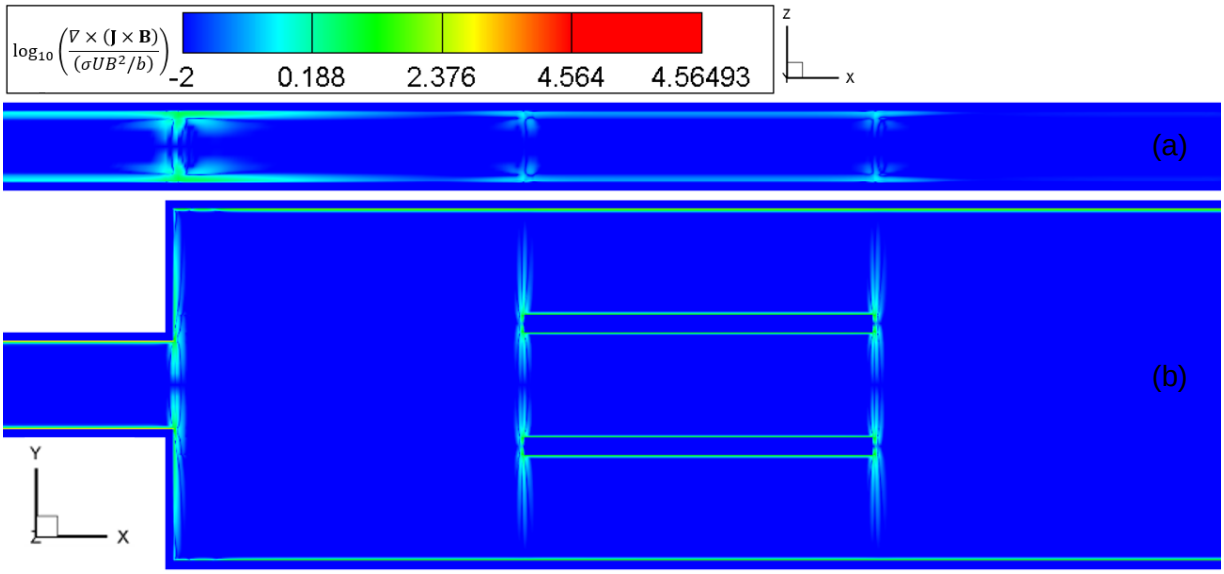

FIG. 10. Contours of the log of the magnitude of $\nabla \times \boldsymbol{J} \times \boldsymbol{B}$ are shown on the y=0 xz-plane (a) and the z=0 xy-plane (b) indicating that most of the manifold flow can be classified as a core flow except for special subdomains at the sudden expansion, entry to and exit from the parallel channels, as well as boundary layers where rotational hydrodynamic forces are important. Here, r_{exp}=4, L_{exp}/b=2, L_{chan}/b=2, s_c=0.3, and n=3 channels for Ha=1465 and Re=50.

Unlike the thin internal and boundary layers highlighted by high magnitudes of $\nabla \times \mathbf{J} \times \mathbf{B}$, the magnitude of $\nabla \times \mathbf{J} \times \mathbf{B}$ is negligibly small in the core flows. When the liquid flows through the manifold, relatively large core flow subdomains are separated by thin internal layers. At such locations where $\nabla \times \mathbf{J} \times \mathbf{B}$ changes along the flow direction, large changes to the velocity field must also occur to generate sufficient hydrodynamic forces [11]. In support of this claim, the formation of M-shaped velocity profiles (Figs. 7c,f,h) are observed near each change in duct cross-section. For example, in the feeding pipe, the flow slowly transitions from a fully developed

Shercliff velocity profile at the inlet (Fig. 7a) to an M-shaped profile (Fig. 7b) as the velocity in the core decreases and the velocity near the sidewalls increases. Then, over a short distance where strong $\nabla \times \mathbf{J} \times \mathbf{B}$ appears in the flow, the velocity profile quickly becomes severely M-shaped and 3D (Fig. 7c). Away from each change in cross-section, the flow transitions towards a fully developed Shercliff velocity profile (Figs. 7a,e,g,i). The formation of M-shaped velocity profiles at expansions was first observed in experiments performed at Riga by Branover and Shcherbinin [55] and was later studied analytically by Walker, Ludford, and Hunt [18] and observed numerically by many authors [19-21, 25, 52, 56-58].

The pressure distribution in the manifold flow is of special interest as typically, high MHD pressure drops in fusion blankets exert critical limitations on any liquid metal blanket design. As shown in Fig. 7 at the bottom, the pressure is distributed non-uniformly along the flow path: local minimums in axial pressure are observed at expansions while contractions experience local maximums. These pressure features arise due to the 3D currents which rotate in opposite directions at expansions compared to contractions. At expansions, Lorentz forces push outwards away from the center of the 3D circulations and so the balancing pressure gradients pinch inwards, creating a local pressure minimum. The reverse situation occurs at contractions. The same explanation accounts for high sidewall pressure (relative to the bulk) at expansions and low sidewall pressure at contractions.

As seen in the axial pressure distribution shown in Fig. 7, the most significant changes in the pressure occur at the sudden expansion at x/*b*=1 because of strong 3D MHD effects associated with the expansion of the flow along the y-direction. The pressure drop which occurs at the sudden expansion is considerably larger than the pressure recovery which follows just downstream. The net effect is referred to as the 3D MHD pressure drop. A sketch explaining the definition of the 3D MHD pressure drop in a flow with a sudden expansion is shown in Fig. 11 as originally proposed by Bühler [21].

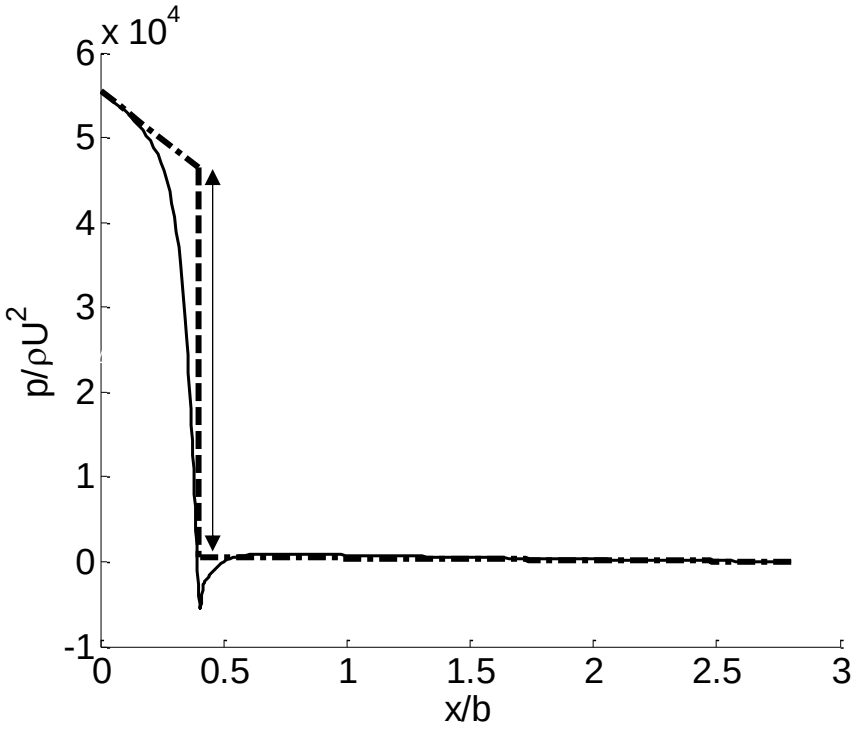

FIG. 11. The length of the vertical dashed line at the sudden expansion is defined as the 3D MHD pressure drop in the hydraulic scale. The two dot-dashed black lines have slopes equal to the local fully developed Shercliff pressure gradient. Here, r_{exp}=10, Ha=5475, and Re=50.

This large axial pressure drop across the sudden expansion has two explanations. Firstly, the current density of 3D circulations (and thus axial Lorentz force) is greater upstream of the expansion because the currents spread out into the expansion region as they close downstream. This is sufficient for explaining the centerline pressure distribution since $\nabla \times \mathbf{J} \times \mathbf{B}$ is zero on the centerline (by symmetry) and so the pressure gradient is nearly entirely balanced by Lorentz force. A more general explanation for the 3D MHD pressure drop is that extra momentum is lost to the walls near the expansion due to 3D flow structures and the formation of near wall jets (e.g. Fig. 7c). The scaling of the 3D MHD pressure drop across sudden expansions was first proposed by Molokov [22] and was later confirmed numerically by Mistrangelo [25] for the IE regime and again numerically in the present work (section 3.4) for both the VE and IE regimes.

3.4 Pressure Analysis

I now go on to discuss my numerical investigation of the 3D MHD pressure drop which is inserted into the flow near the sudden expansion. The 3D MHD pressure drop is numerically determined to scale linearly with $\rho U^2 N^{2/3}$ and $\rho U^2 N Ha^{-1/2}$ for the IE and VE regimes respectively, indicating agreement with the predictions of Molokov [22] who based his conclusions on the scaling arguments made by Hunt and Leibovich [14] in their analysis of the Ludford layer in 2D. The 3D MHD pressure drop is also shown to have a strong dependence on r_{exp}.

Electrically nonconducting manifolds featuring a sudden expansion are simulated to study how the pressure drop changes with flow parameters and geometry. One of my hypotheses is that the influence of the multiple channels can be separated out of the pressure drop provided that the channel walls are not so thick that average velocity inside the channels is much higher than in the expansion region. More succinctly, disturbances caused by the entrances and exits of the multiple channels are expected to be small provided that the product $n \times s_c$ is close to unity, where n is the number of channels. Furthermore, the 2D MHD pressure drops across the channels are also relatively small while L_{chan} is small and $n \times s_c$ is close to unity. To test this hypothesis, I simulate two sets of manifolds with Ha=1000, r_{exp}=4, and Re=50 and 500. One set of manifolds has n=3 channels beginning at L_{exp}/b=1, with s_c=0.3 and L_{chan}/b=2 while the other set of manifolds are simulated without multiple channels (n=1, s_c=1). The resulting pressure distributions are plotted along the centerlines in Fig. 12 below.

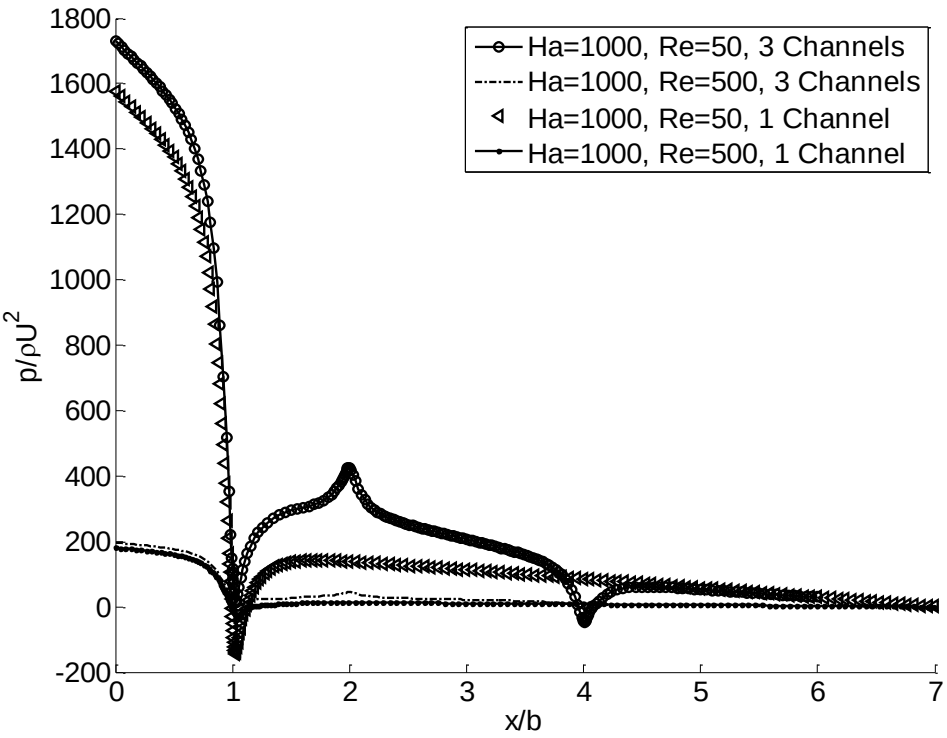

FIG. 12. Centerline pressure of manifold simulations with either 1 or 3 channels, r_{exp}=4. For the cases with 3 channels, L_{exp}/b=1, L_{chan}/b=2, and s_c=0.3. The flow with Re=50 is in the VE regime and the Re=500 flow is in the IE regime. Sudden expansion at x/b=1.

The local minima and maxima seen in Fig. 12 indicate locations where 3D MHD effects are generated. The local minima occur when the pressure gradient steepens and then abruptly switches directions to balance extra Lorentz forces from 3D circulations of electric current. These circulations appear near sudden expansions including the large expansion at x/*b*=1 and the channel exits at x/*b*=4. By contrast, 3D MHD effects at a sudden contraction like the entrance to the multiple channels at x/*b*=2 cause a peak in the pressure distribution. The peaks are caused by 3D electric currents, which circulate in the opposite direction as near sudden expansions. 3D MHD effects at expansions and contractions produce an extra pressure loss called the 3D MHD pressure drop as discussed in section 3.4. This loss is expected to be small when r_{exp} (or $n \times s_c$) is close to 1. Here, $n \times s_c$ is 0.9 so the 3D MHD pressure drops from the channel ends are small and the differences in pressure drop between cases with and without channels are less than 10%.

When r_{exp}~10 as in DCLL manifolds, the 3D MHD pressure drops account for nearly half the pressure drop across the entire liquid metal loop (see section 3.6 for an example). Having demonstrated that the influences of the multiple channels are small provided that $n \times s_c$~1, ducts featuring a sudden expansion without multiple channels are simulated for a range of r_{exp}, Ha, and N in order to study the 3D MHD pressure drop. These simulations' results are discussed below.

Electrically nonconducting ducts featuring a sudden expansion are simulated for a range of r_{exp}=4, 6, 8, 10, and 12, $1000 \leq Ha \leq 6570$, $1918.44 \leq N \leq 863298$ and $50 \leq Re \leq 2500$. The 3D MHD pressure drop for the 96 simulations is determined by subtracting the effective 2D pressure drops (calculated using Shercliff's pressure formula) from the pressure drop of each simulation. This data is then sorted into groups with equal r_{exp}, and curve fitted it to linear functions of either $NHa^{-1/2}$ or $N^{2/3}$. The slopes, k_{ve}, k_{ie}, and offsets, d_{ve}, d_{ie}, of these linear functions are then curve fitted as functions of expansion ratio. The resulting formulas can be used to predict the 3D MHD pressure drop for a wide range of parameters and are shown below.

$$\Delta P_{3D} = \frac{\rho U^2}{2}\left(k_{ve} N Ha^{-1/2} + d_{ve}\right) \text{ for } Ha^{3/2}/N < 3, \tag{7}$$

$$\Delta P_{3D} = \frac{\rho U^2}{2}\left(k_{ie} N^{2/3} + d_{ie}\right) \text{ for } Ha^{3/2}/N > 3. \tag{8}$$

Here, k_{ve}, d_{ve}, k_{ie}, and d_{ie} are functions of the expansion ratio, r_{exp}:

$$k_{ve} = 0.31 r_{exp} + 3.08, \tag{9}$$

$$d_{ve} = 342.92 r_{exp} - 1563.85, \tag{10}$$

$$k_{ie} = 0.33 r_{exp} + 1.19, \tag{11}$$

$$d_{ie} = -11.55 {r_{exp}}^2 + 85.43 r_{exp} - 264.39. \tag{12}$$

Equations (7-12) describe the 3D pressure drop in both the viscous-electromagnetic and inertial-electromagnetic regimes. Fig. 13 shows the pressure model plotted against the computed

results that were used in its making. The RMSD (root-mean-square deviation [not normalized]) and R^2 (coefficient of determination) were also calculated, demonstrating good agreement of the proposed pressure model with the computed pressure drops.

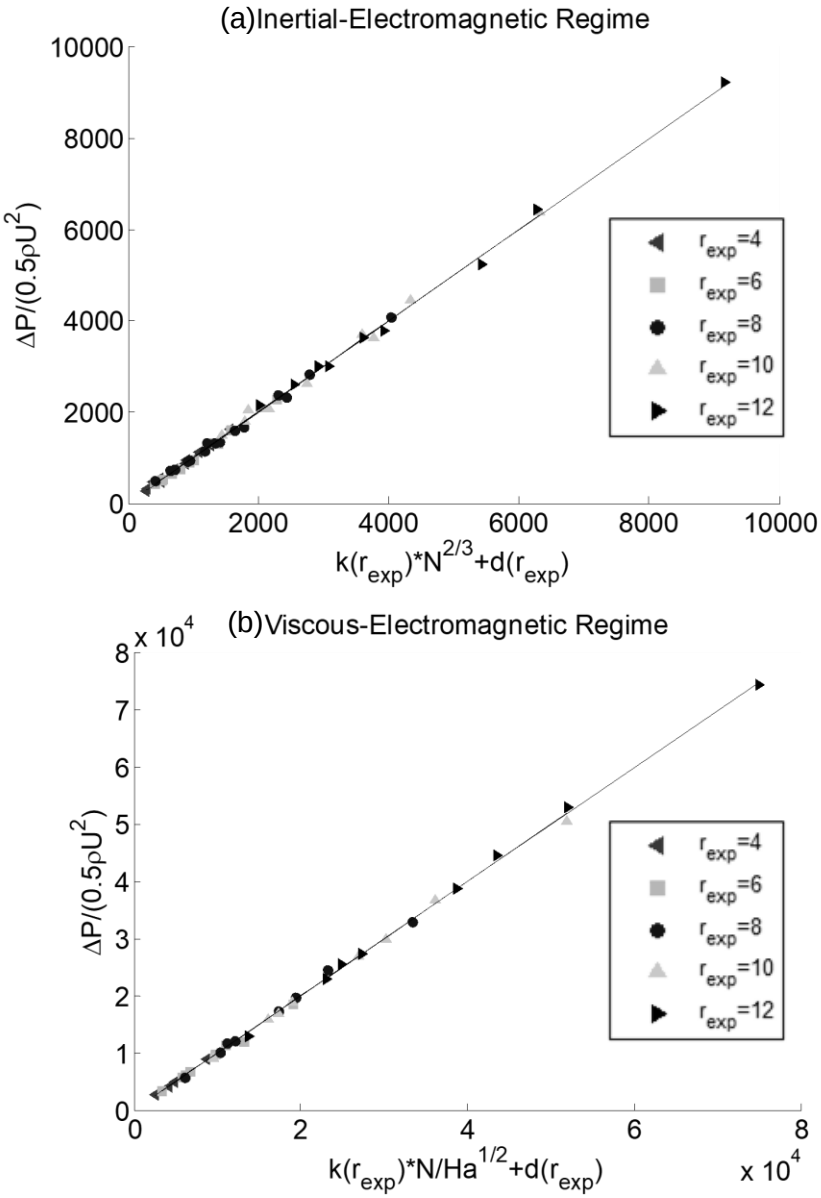

FIG. 13. Proposed pressure model for MHD flows in a nonconducting manifold. (a) For the IE regime ($Ha^{3/2}/N > 3$) the RMSD and R2 is 76.08 and 0.9980 respectively. (b) For the VE regime ($Ha^{3/2}/N < 3$) the RMSD and R2 for the fit is 540.9 and 0.9989 respectively.

3.5 Flow Distribution Analysis

For the purpose of characterizing flow distribution among the parallel channels, it is useful to consider two parameters: one is the length of the expansion region and the second is the length of the parallel channels themselves.

3.5.A Effect of the length of the Expansion Region

Here, the effect of the length of the expansion region on flow distribution is investigated for the case of short, nonconducting channels for various flow parameters (Ha~10^3, Re~10^1-10^3) and expansion ratios (r_{exp}=4-12). According to my observations, if the parallel channels begin before the reattachment length introduced in section 3.3, the flow distribution will be significantly biased towards the center channels. More flow enters central channels because the channel walls interrupt the redistribution of flow which occurs near the sidewalls before the reattachment length. Alternatively, if the expansion length is greater than the reattachment length, the flow distribution will be well balanced. This phenomenon is illustrated below in Fig. 14.

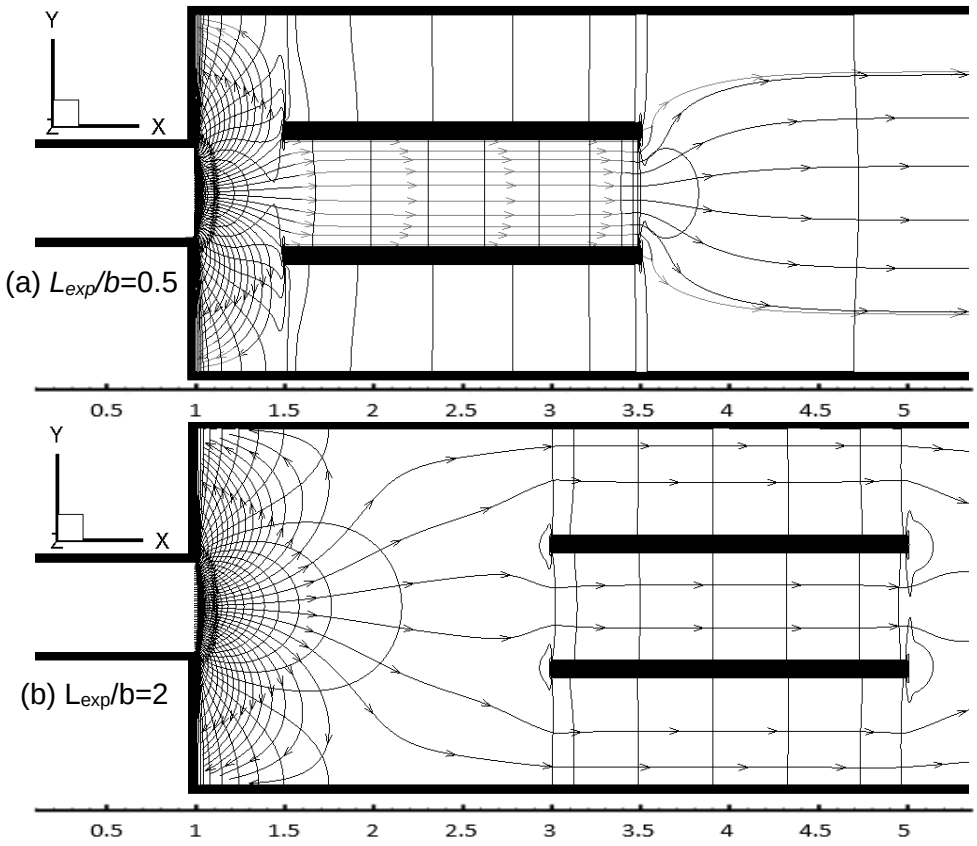

FIG. 14. Velocity streamlines are plotted with pressure contour lines on the sidewall (z/a=0.98) for two manifold geometries. Ha=1465, Re=50, r_{exp}=4, L_{chan}/b=2, s_c=0.3, and L_{exp}/b=0.5 or 2 for (a) and (b) respectively.

Here, the percentage of the flow through the center channel is 41.0% and 33.3% for L_{exp}/b=0.5 and 2 respectively and the reattachment length, non-dimensionalized by b, is approximately 0.8. Note that for three channels, 33.3% is perfectly balanced. The relationship between L_{exp}/b and flow distribution will be quantified later in this section after discussing the relative importance of flow parameters.

Electrically nonconducting manifolds featuring a sudden expansion were simulated to study how the flow distribution produced by a manifold changes with flow parameters and geometry. The percentage of the flow through each channel was then determined by integrating the axial velocity over each channel's cross-section using Simpson's method and then dividing the result by the total flow rate. For the first batch of simulations, manifolds with r_{exp}=4, L_{chan}/b=2 and n=3 channels were considered (as depicted in Fig. 1). These simulations included a range of L_{exp}/b=0.5, 1, 2,

and 3 and *Ha*~1000, 1500, and 2000. Additionally, for each combination of L_{exp} and *Ha*, between 3 and 5 choices of *Re* were included over a range of $50 \leq Re \leq 3750$. The difference in the percentage of flow through each side channel was calculated to be at most on the order 10^{-3}%, thus confirming the symmetry of the flow for the featured parameter space. Fig. 15 shows the percentage of flow through the center channel for each set of parameters.

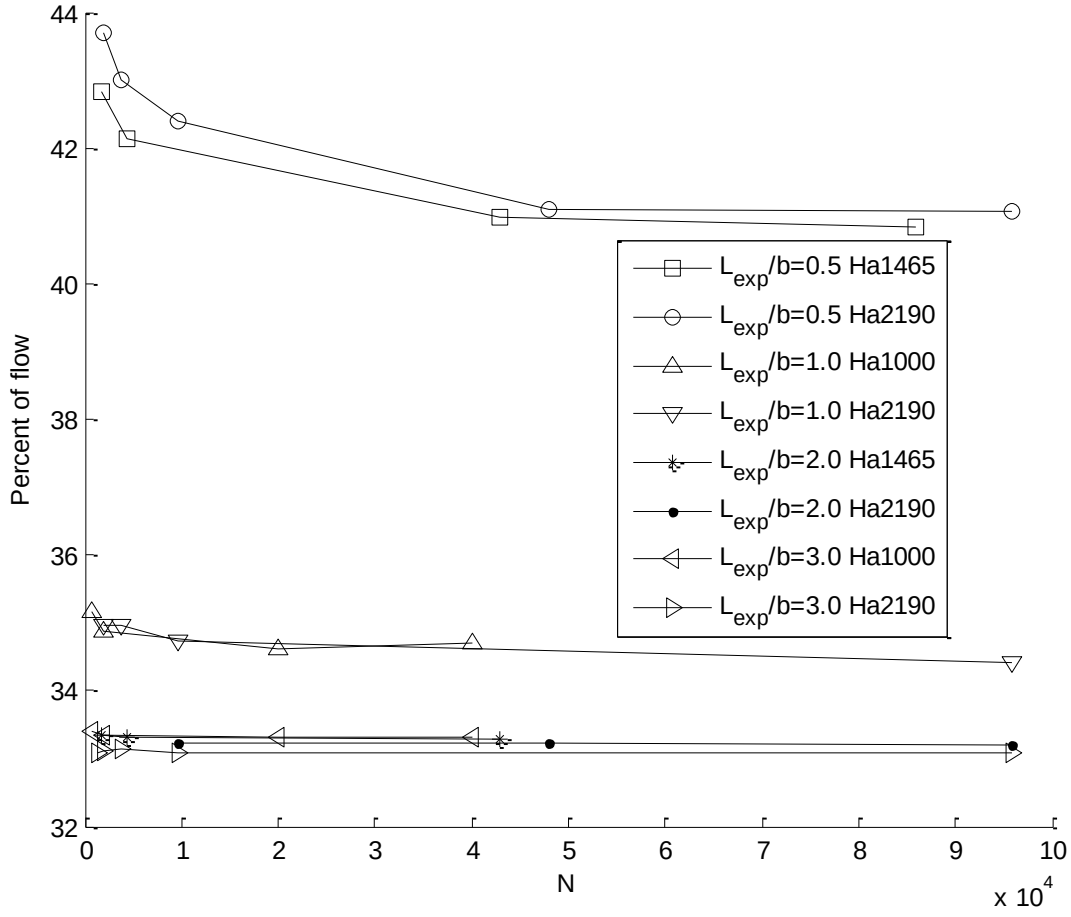

FIG. 15. Percentage of flow through the center channel of manifolds with three channels is plotted for various Ha, N, and L_{exp}. For these simulations, r_{exp}=4, and L_{chan}/b=2.

For the chosen parameter space, the variable that has the biggest impact on flow distribution is L_{exp}. Halving *Ha* or increasing *Re* by a factor of 50 produced O(1%) or smaller differences in flow distribution. As explained in section 3.3, a 3D flow structure attached to the sidewalls is the

primary mechanism for flow redistribution and it penetrates into the expansion region a distance that scales with $N^{-1/3}$ [25] in the IE regime and possibly $Ha^{-1/2}$ in the VE regime based on the arguments in [14]. Thus, for large N and Ha, this distance becomes increasingly insensitive to N and Ha.

One of my hypotheses is that the channels influence flow distribution in part by interrupting the redistribution of flow occurring in the expansion region near the sidewalls. In the present study, the channels are short enough such that the length of the channels almost does not affect the flow balancing and the overall MHD pressure drop. This is done mostly to observe the effects of the flow physics inside the expansion region on the flow balance of the manifold without being masked by the channel length effect. This hypothesis is tested by simulating a manifold without multiple channels and measuring the percentage of flow in the center third of the duct at 4 distances L downstream of the sudden expansion equal to L/b=0.5, 1, 2, and 3 for Ha=2190, Re=500 and r_{exp}=4. These values are then compared with the percentage of flow through the center channel in manifolds with three channels that begin a distance downstream of the sudden expansion equal to L_{exp}/b=0.5, 1, 2, and 3 for the same Ha, Re, and r_{exp}. The results of this comparison are shown in Fig. 16. Note that while calculating the integrals of axial velocity, some values are linearly interpolated because dividing the duct into even thirds split cells for the manifolds without channels.

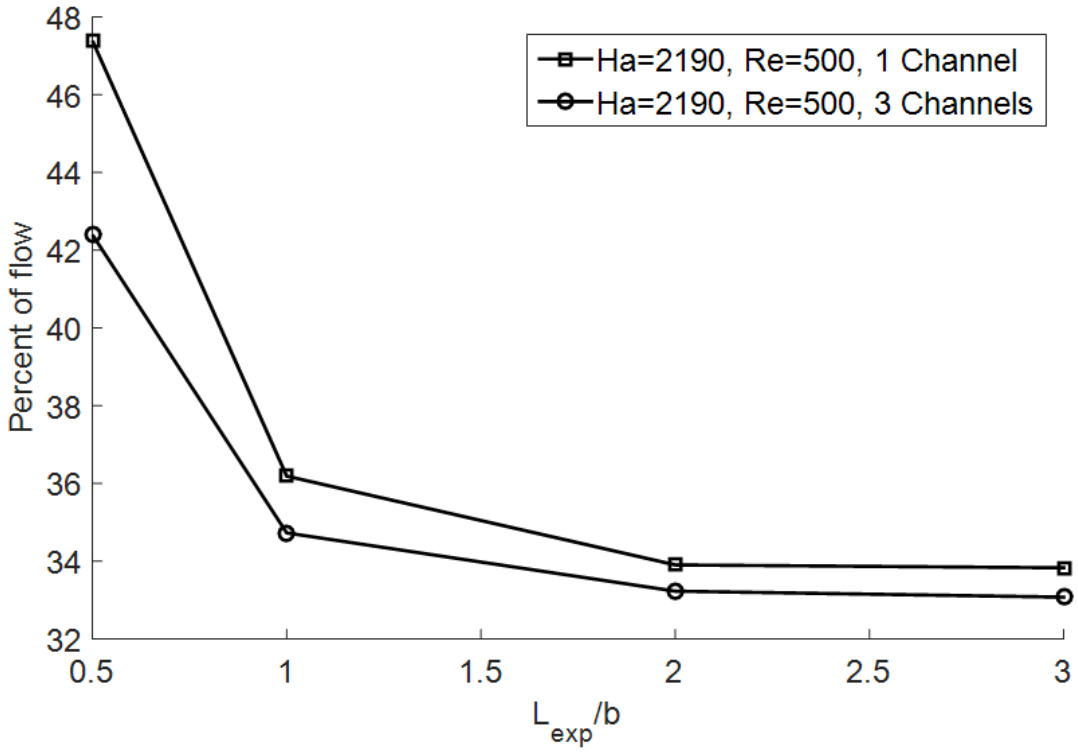

FIG. 16. Percentage of flow through the center channel of manifolds with three channels and manifolds without multiple channels is plotted for various L_{exp} = L. For these simulations, r_{exp}=4 and, for simulations with channels, L_{chan}/b=2.

The differences in percentage of flow for the two cases are within 5% with the manifold having three channels being slightly more balanced. This is the expected result because the channels induce a small balancing effect via 2D MHD pressure drops within the channels that are dependent on the local average velocity. The results shown in Fig. 16 justify using a single simulation of a manifold without channels to predict the flow distributions of manifolds with n>2 short channels which begin after any desired length in the expansion region, L_{exp}. This method makes comparison of multiple manifold designs much less expensive. Electrically nonconducting ducts featuring a sudden expansion without multiple channels were simulated for a range of r_{exp}, *Ha*, and *Re* in order to study flow distribution in manifolds with multiple channels. These simulations' results are discussed below.

Manifold flows with *Re*=1000 and r_{exp}=8 for four choices of *Ha*=2000, 3000, 3400, and 4380 were simulated to study how the flow distribution at various locations downstream of the expansion changes with *Ha*. The results are plotted in Fig. 17 as the percentage of flow through the center third of the duct versus *L/b* where *L* is the axial distance downstream of the sudden expansion where the flow distribution is calculated.

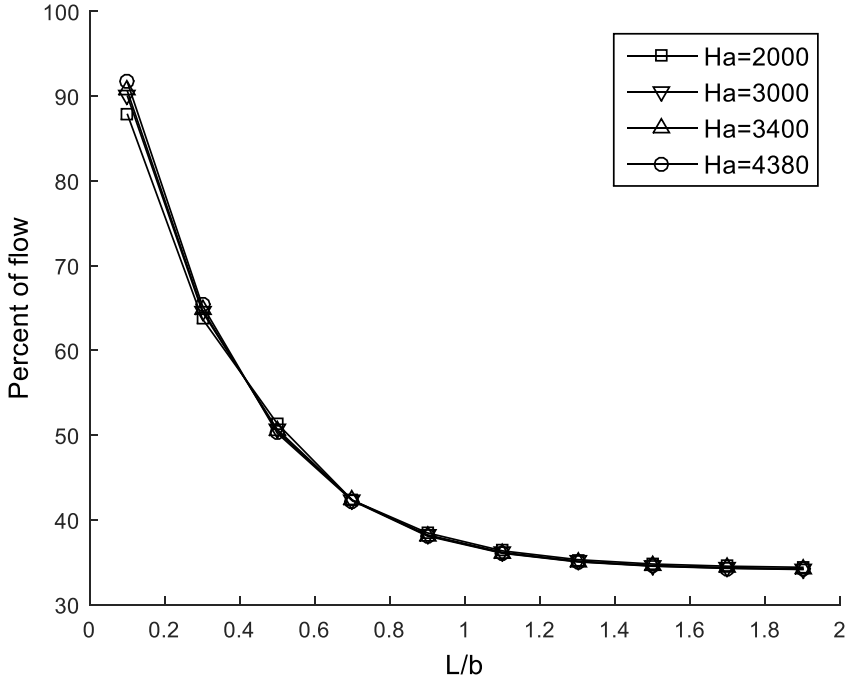

FIG. 17. Percentage of flow through the center virtual channel of manifolds with three virtual channels is plotted for various distances L/b into the expansion region for four choices of Ha. Here, r_{exp}=8 and Re=1000.

In this parameter space, the flow distribution is weakly dependent on *Ha*. As before, the distance downstream is the most important factor for determining flow distribution for this parameter space and now an exponential decay of flow unbalance is apparent along the axial direction.

Manifold flows with *Ha*=5475 and r_{exp}=10 were simulated for six choices of *Re*=50, 100, 500, 1000, 1500, and 2000 to study how the flow distribution at various locations downstream of the expansion changes with *Re*. The results are plotted in Fig. 18 as the percentage of flow through the center third of the duct versus *L/b*.

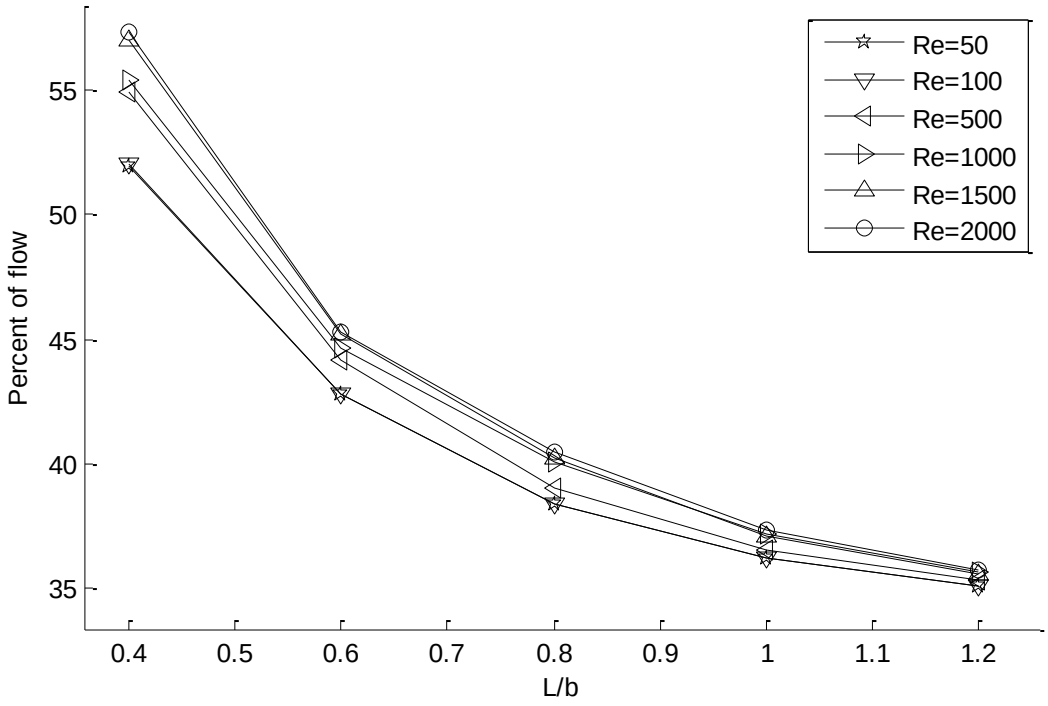

FIG. 18. Percentage of flow through the center virtual channel of manifolds with three virtual channels is plotted for various distances L/b into the expansion region and at multiple Re. Here, r_{exp}=10 and Ha=5475.

The flow becomes less balanced and more flow is in the center third of the duct as *Re* increases. This behavior is also in agreement with the cases with multiple channels shown in Fig. 15.

Electrically nonconducting manifolds with *Re*=2000, *Ha*=547.5r_{exp}, and 4 choices of r_{exp}=6, 8, 10, and 12 were simulated in order to determine the effect of expansion ratio on flow distribution. As with all the simulations in the present work, *d* is fixed so the value *b* changes linearly with r_{exp}. *Ha* also varies with r_{exp} because each simulation in this batch has the same magnetic field and fluid electrical conductivity. For each simulation, the flow distribution is calculated at 8 locations evenly spaced in the axial direction from *L*=0.025m to 0.2m for 3, 10, and 12 virtual channels. The percentage of flow through the center virtual channels are curve fitted to an exponential function of *L* as shown in Eq. 13 below:

$$Percentage\ of\ flow\ in\ center = Ae^{BL} + C, \tag{13}$$

where *A*, *B*, and *C* are dependent on r_{exp} and *n* only. The RMS deviations for the exponential curve fits are found to be smaller than for power law fits (%=DL^E+*F* where *D*, *E*, and *F* are dependent on r_{exp} and *n* only) of the same data. The RMSD of the exponential curve fits are O(0.1%) indicating a good fit. The resulting values for *A*, *B*, and *C* determined for each expansion ratio are shown in Fig. 19.

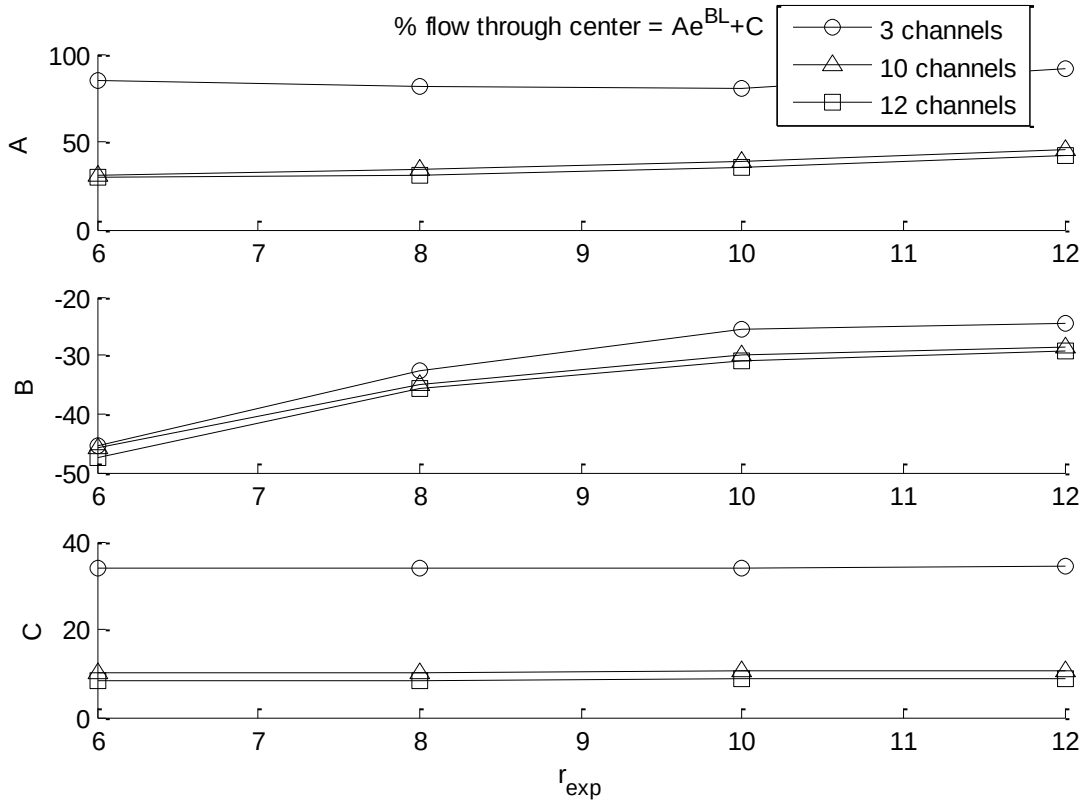

FIG. 19. The parameters A, B, and C plotted versus r_{exp} for the exponential functions describing the percentage of flow through the center virtual channel versus L for manifolds with 3, 10, and 12 virtual channels. Ha=547.5r_{exp} and Re=2000.

The offset *C* showed no dependence on r_{exp} which makes sense because as *L* increases, the flow distribution approaches a balanced state. Here, *C*~34%, 10.3%, and 8.6% for 3, 10, and 12 channels respectively. For perfectly balanced flow, the percentage of flow in each channel would be 33.33%, 10%, and 8.33% respectively. Using the exponential functions determined above, I estimate the balancing length *L*/b,* defined as the non-dimensionalized axial distance downstream of the sudden expansion where the percentage of flow through the center virtual

channel equals *C*+0.1*C*. The estimations for balancing lengths for *Re*=2000, *Ha*=547.5r_{exp}, and r_{exp}=6, 8, 10, and 12 are plotted in Fig. 20.

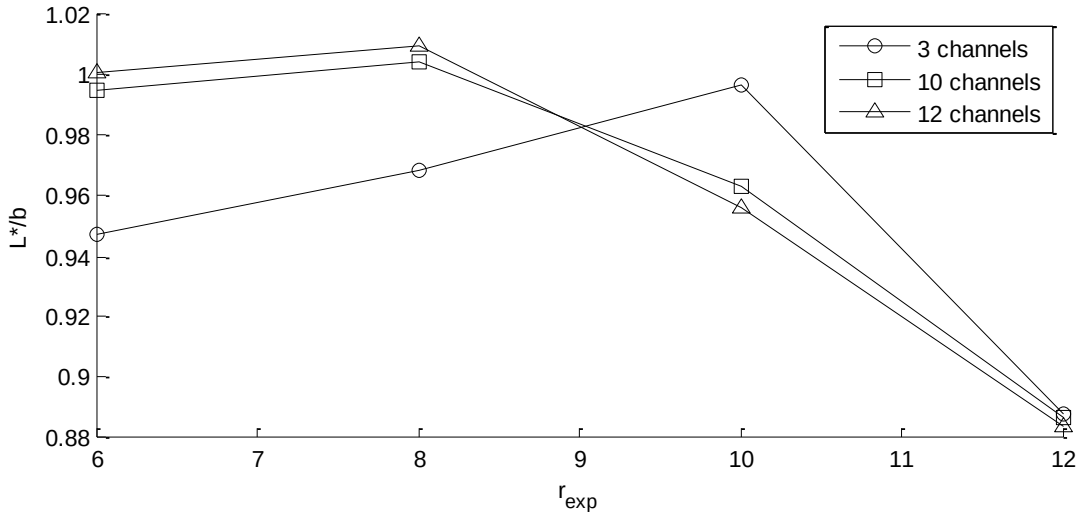

FIG. 20. The balancing length is plotted versus r_{exp} for manifolds with 3, 10, and 12 virtual channels. Ha=547.5r_{exp} and Re=2000.

For r_{exp}=12, manifold flow is estimated to be balanced within *L/b*=0.9 for any number of channels. For all the cases evaluated above, the conclusion $L^*/b \leq 1$ can be drawn.

3.5.B Effect of the Length of the Parallel Channels

To investigate the effect of the length of the parallel channels on flow distribution, electrically nonconducting manifolds featuring a sudden expansion at *Ha*=1465, *Re*=100, r_{exp}=4, L_{exp}/b=0.5, and s_c=0.3 for six choices of L_{chan}/b=2, 10, 20, 30, 40, and 50 were simulated. In Fig. 21, the percentage of the total flowrate carried by each channel is plotted versus L_{chan}.

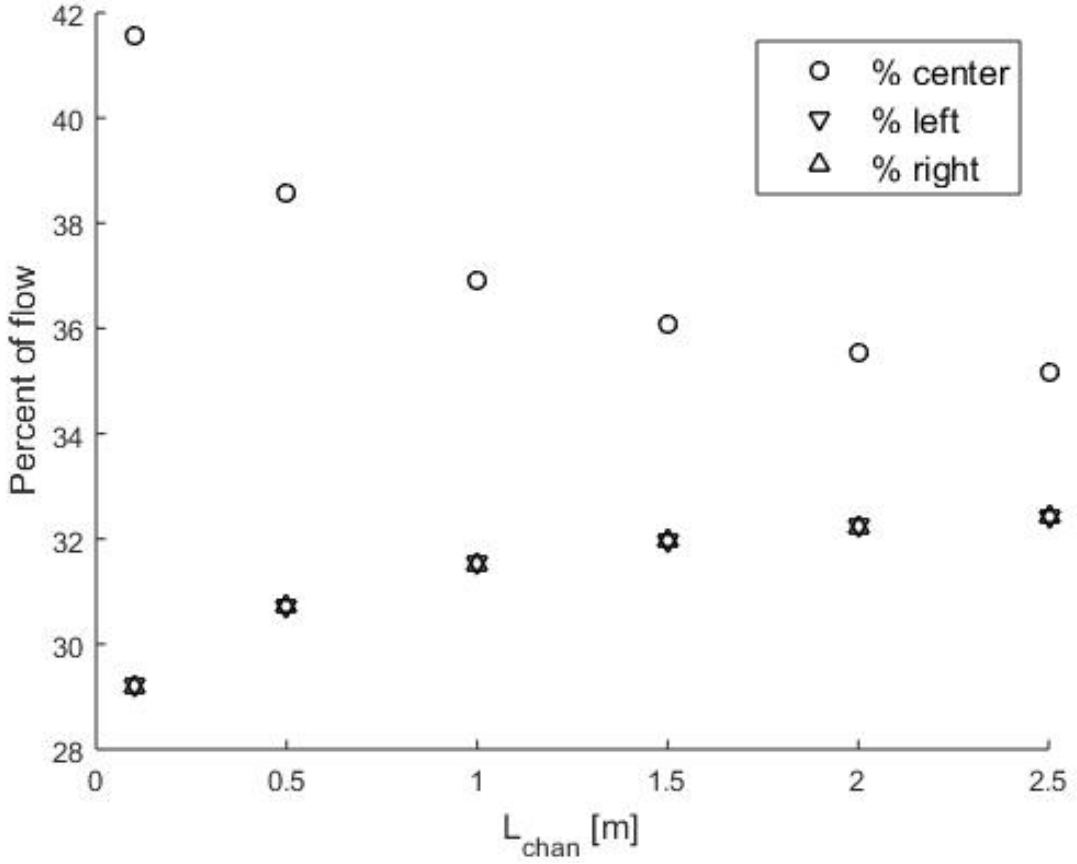

FIG. 21. Percentage of the total flowrate carried by each of the three channels vs length of channels. Ha=1465, Re=100, r_{exp}=4, L_{exp}/b=0.5, and s_c=0.3 for six choices of L_{chan}/b=2, 10, 20, 30, 40, and 50.

The curves for the left and right channels overlap because the flow is symmetrical for the study's parameter space. The manifold flow becomes more balanced as L_{chan} increases, tending towards perfectly balanced flow where each channel carries a third of the total flowrate. The behavior of this effect is best described via analogy to an electrical circuit segment. In this analogy, the manifold geometry is simplified as a Resistor Network Model (RNM) composed of three parallel pairs of resistors as illustrated in Fig. 22.

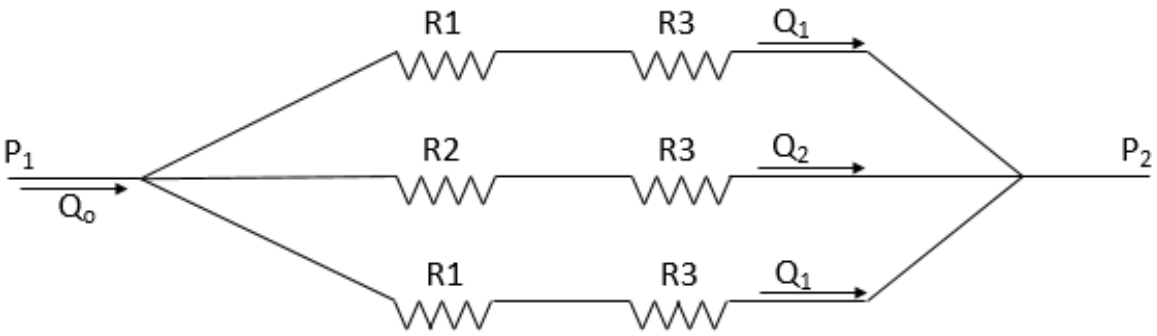

FIG. 22. A Resistor Network Model of the prototypical manifold in Fig.1.

Here, the three parallel channels of the manifold are represented by three identical resistors with variable resistance R3 which increases linearly with L_{chan}. The resistors labeled R1 and R2 have constant resistance and represent the 3D flow in the expansion region which feeds each of the three channels. Since L_{exp} is small ($L_{exp}/b<1$), it is expected that R2<R1. The flow distribution is then governed by the following equations:

$$Q_1(R1 + R3) = P_2 - P_1, \tag{14}$$

$$Q_2(R2 + R3) = P_2 - P_1, \tag{15}$$

$$Q_2 = \frac{(\%center)}{100} Q_o, \tag{16}$$

$$Q_1 = \frac{100-(\%center)}{200} Q_o. \tag{17}$$

Equations (14,15) are analogous to Ohm's law such that electrical current is to flowrate Q as voltage is to pressure P. Eqs. (16,17) relate the total flowrate Q_o and channel flowrates Q_1 and Q_2 to the percentage of the total flowrate carried by the center channel (*%center*).

Assuming that the development length of the flow in the channels is small compared to L_{chan}, R3 may be defined as follows:

$$R3 = L_{chan}S. \tag{18}$$

Here, S is the Shercliff pressure gradient in a fully developed flow [3] per flowrate. Combining Eqs. (14-18) yields

$$(\%center) = 100\frac{L_{chan}S+R1}{3L_{chan}S+2R2+R1}. \quad (19)$$

The resulting Eq. (19) matches the intuition that as L_{chan} approaches infinity, (*%center*) approaches 33.3...%. Values for R1 and R2 cannot be determined analytically due to the complexity of the flow in the expansion region; however, values for R1 and R2 have been determined by curve fitting Eq. (19) to numerical data for (*%center*).

Values of R1 and R2 were selected using a minimization algorithm to minimize the RMSD comparing the 3D numerical results and Eq. (19). Given the pressure gradient per flowrate in a fully developed flow in a channel S=8.800x10^6 Pa·s/m^4, Eq. (19) best fits the data when R1 and R2 equal 6.726x10^6 Pa·s/m^3 and 4.462x10^6 Pa·s/m^3 respectively. The resulting RNM fits the numerical data with an RMSD of 0.0067, indicating an excellent fit. The model is plotted along with the numerical data in Fig. 23. In addition to fitting the numerical data well, the RNM is shown to agree with the expected behavior of the manifold as L_{chan} increases past 2.5m. It is worth noting that in this case, the modelled (*%center*) comes within 1% of the perfectly balanced value (34.33…%) after L_{chan} exceeds 5m.

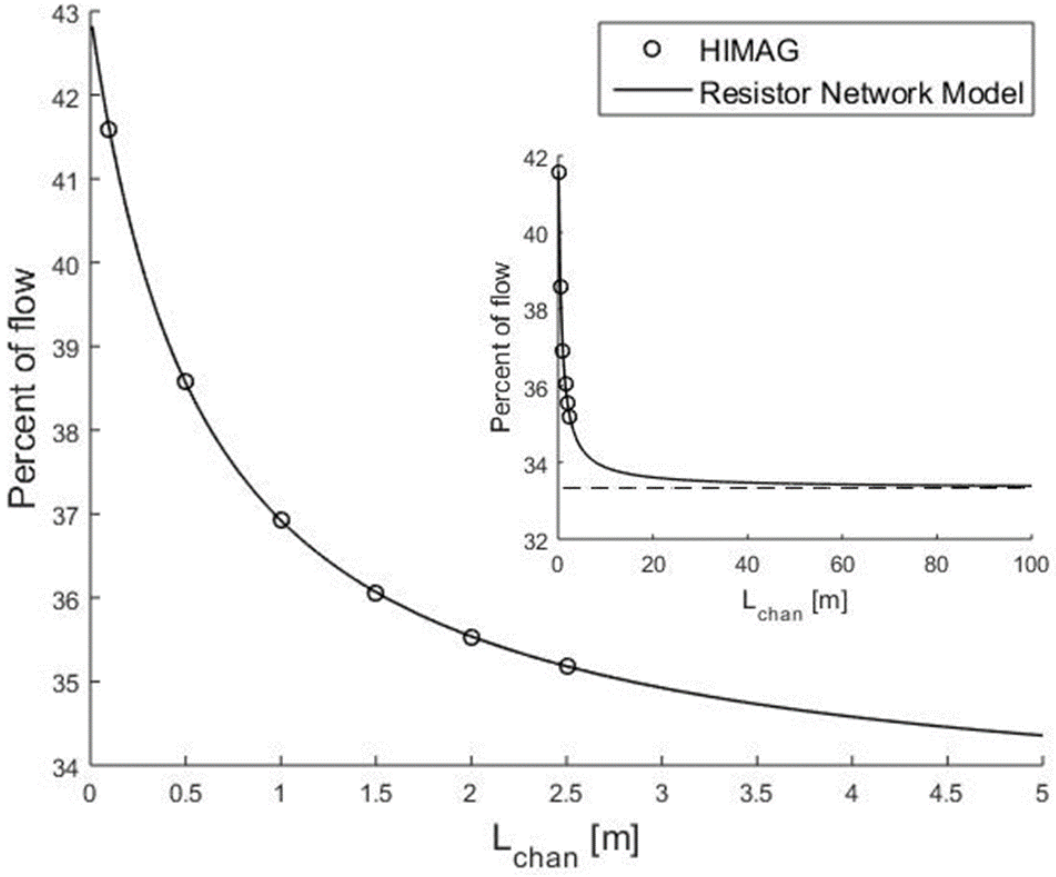

FIG. 23. An RNM is fit to the numerical results for (%center). The smaller plot shows the modelled behavior of the flow distribution for much larger channel length. The flowrate carried by the center channel approaches 1/3 of the total flowrate as L_{chan} increases. The circles are results for Ha=1465, Re=100, r_{exp}=4, L_{exp}/b=0.5, and s_c=0.3 for six choices of L_{chan}/b=2, 10, 20, 30, 40, and 50.

Since there are two unknowns in the RNM, R1 and R2, it is possible to fully define the RNM using only two simulations or experiments. That is, if (*%center*) is known for each of two values of L_{chan} at a particular *Ha* and *Re*, Eq. (19) can be solved for the constants R1 and R2. Below, this is demonstrated by calculating R1 and R2 for each possible pair of the 6 simulations of the present study.

The present study features six simulations with different channel lengths so the number of unique pairs of channel lengths is $15 = \frac{1}{2}\left[\frac{6!}{(6-2)!}\right]$. Thus 15 pairs of resistor values R1 and R2 can be

calculated. The computed resistor values are plotted in Fig. 24 versus the sum of the two channel lengths used for each calculation.

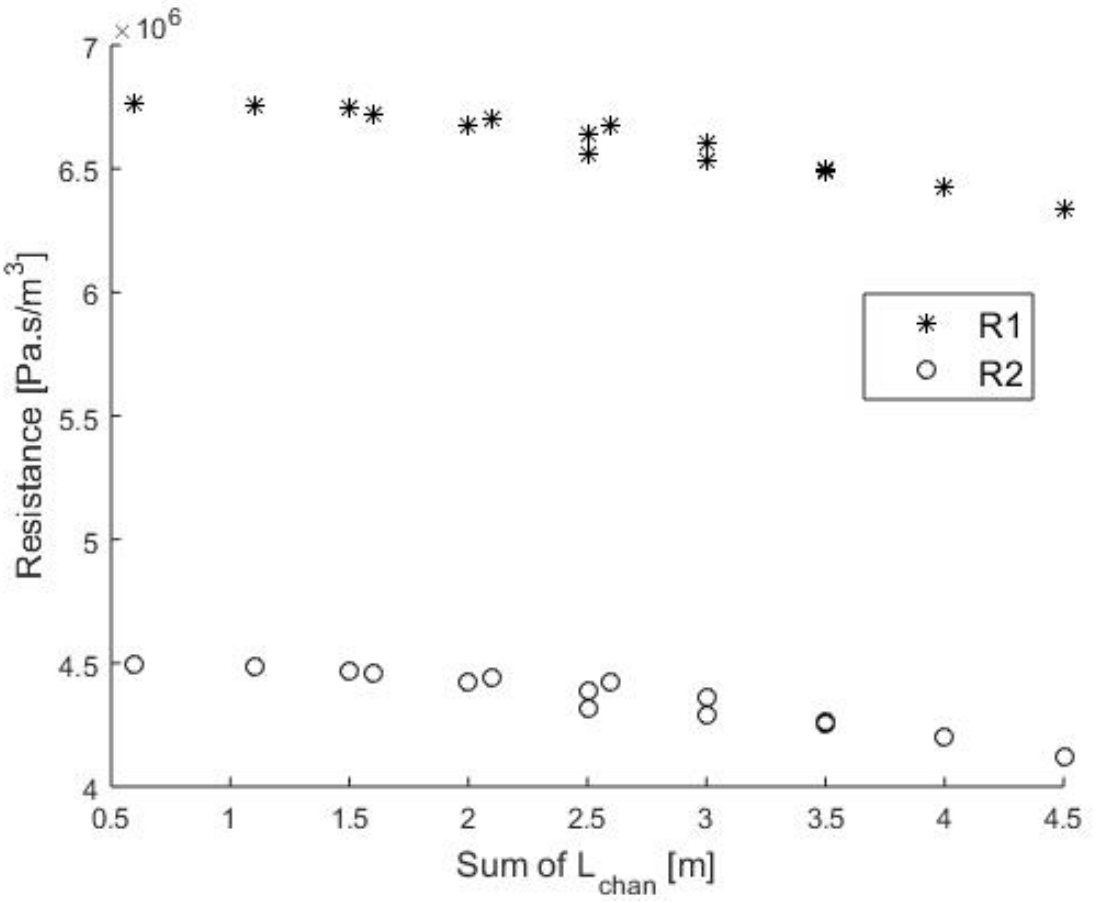

FIG. 24. Resistor values are plotted against the sum of each pair of channel lengths used for the calculations.

A slight decreasing trend is observed even though the model stipulates that R1 and R2 are constants that are not dependent on L_{chan}. Still, the calculated resistances are within 5.7% and 7.7% of the best fit values of R1 and R2 respectively. To get an idea for how these errors affect the model's applicability, the RNMs are compared using the highest and lowest calculated resistor values along with the numerical data in Fig. 25.

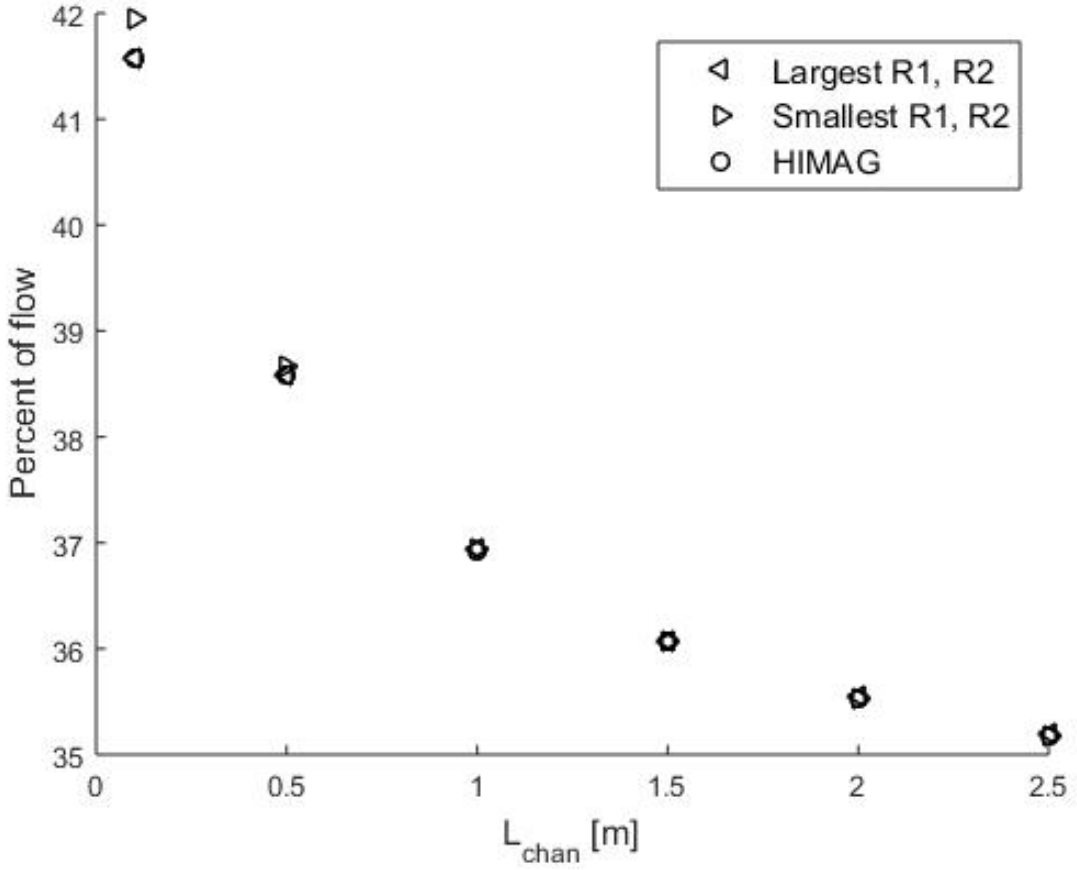

FIG. 25. Two RNMs, each with the highest or lowest values of resistors R1 and R2, are compared to numerical values of the percentage of total flowrate carried by the center channel.

The maximum difference between the two models and the numerical data is 0.36% (at L_{chan}=0.1m) and the error is an order of magnitude smaller for L_{chan}>1m. Thus, all of the calculated resistor pairs are suitable for predicting the flow distribution as a function of L_{chan} with acceptably small error. This is an important result because it indicates that only two simulations or experiments are required for predicting the flow distribution for the full range of L_{chan} so long as the flow behaves according to the RNM analogy. However, it could be that this assumption breaks down at higher *Re,* in the case of electrically conducting walls, or if significant buoyancy effects are present in the multiple channels.

The RNM is not limited to the particular manifold configuration of three parallel channels and can easily be extended to a more complex configuration, though for other configurations the RNM

would require validation. For instance, changing L_{exp} or adding a sudden contraction to the outlet is likely to only affect the values of R1 and R2 in Eq. (19). The model can be generalized to *n* channels, taking the form of *n* parallel pairs of resistors. In that case, *n* data points will be required to fully define the RNM and solve for the *n* unknown resistor values. If the problem is symmetric, as in the present work, the number of unknowns (and required data points) will be reduced to *n*/2 (rounded up).

3.6 Example of Application of the Derived Pressure Model to a Fusion Blanket

Here, the obtained formulas for the 3D MHD pressure drop in a manifold, Eqs. (7-12), are applied to a DCLL blanket design. In the recent fusion nuclear science facility (FNSF) study in the US [59], a DCLL blanket was designed for both inboard and outboard regions (Fig. 26). The entire machine is subdivided into 16 toroidal sectors, such that there are 16 inboard (IB) and 16 outboard (OB) blankets. Each sector with the blankets can be removed via an individual port using a horizontal maintenance scheme. In the IB blanket, the eutectic PbLi alloy flows upwards in the five front ducts facing the plasma, makes a U-turn at the top of the blanket and then flows downwards in the five rear ducts. The flows occur in the presence of a strong plasma-confining magnetic field resulting in a high MHD pressure drop in the flowing liquid breeder. There are two manifolds at the bottom of the blanket to feed the poloidal ducts and to collect the hot PbLi at the exit of the blanket. The OB blanket has a similar structure, but the number of the ducts and blanket dimensions are different to fit into a larger space at the OB. The entire blanket, including the manifolds, has electrically insulating flow channel inserts made of silicon carbide ceramics [60] to reduce the MHD pressure drop, such that the present model that assumes electrically insulating walls is applicable. In this particular example, considerations of the MHD pressure drop are limited to that in the inlet manifold of the IB blanket. More results for manifold flows are presented in [61]. For the reference blanket [61], the magnetic field is 10 T, the poloidal length is 7 m and the toroidal width is 1.69 m. The PbLi velocity in the expansion section of the manifold is 0.076 m/s and the

flow absorbs 0.78 MW/m^2 of heat generated by neutrons. The dimensionless flow parameters and the computed MHD pressure drop are summarized in Table 2.

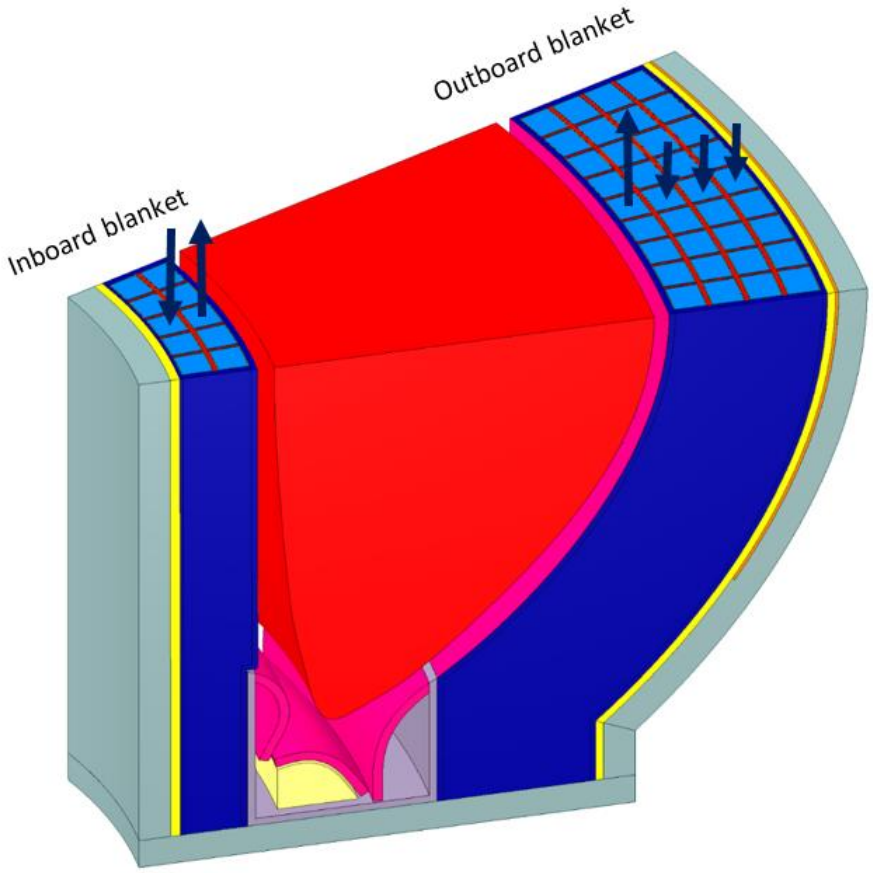

FIG. 26. Crosscut of one of the 16 toroidal sectors in the FNSF with the IB and OB blankets. The arrows show the PbLi flow path in the poloidal ducts.

Table 2. The Dimensionless Blanket Parameters and the Computed 3D MHD Pressure Drop in the Manifold.

Ha	2.13×10^5
Re	5.54×10^5
N	8.21×10^4
r_{exp}	8.45
$Ha^{3/2}/N$	$1.20 \times 10^3 > 3$
ΔP_{3D}	~0.196 MPa

As discussed in section 3.4, the 3D MHD pressure drop (in the MHD scale) was found to scale as $Ha^{-1/2}$ in the VE regime and $N^{-1/3}$ in the IE regime for electrically nonconducting manifolds with sudden expansions. Here, it was found that $Ha^{3/2}/N > 3$. This suggests that the flow in the manifold is in the inertial-electromagnetic regime. The computed MHD pressure drop of 0.196 MPa in the inlet manifold flow is about 20% of the overall PbLi pressure drop in the blanket. Taking into account that the blanket has two manifolds, the associated pressure drop due to 3D effects in the manifold flows approaches nearly half of the blanket pressure drop. This justifies the importance of the obtained pressure drop correlations.

Chapter 4: Conclusions and Future Studies for MHD Flows in Manifolds

As seen from the analyses above, the flow physics in a manifold is dominated by 3D effects. Formation of internal shear layers at the locations where the flow experiences expansions or contractions in the plane parallel to the applied magnetic field is the most important manifestation of the 3D effects as it affects the flow and pressure field and eventually becomes responsible for a high 3D MHD pressure drop. As suggested in this study, an effective way of identifying such internal layers, which is a place of many interesting effects, is to plot the magnitude of the curl of the induced Lorentz force. It also helps to distinguish between the internal shear layers and inviscid, irrotational core flows, where the electromagnetic force is fully balanced by the pressure gradients and the curl of the Lorentz force is correspondingly small. Applying this technique to the flow in the manifold suggests that the internal shear layers are formed at the sudden expansion and at the entry to and exit from the parallel channels. Of them, the internal shear layer at the sudden expansion is the main source of 3D MHD effects.

In designing manifolds for fusion applications, the 3D MHD effects which influence the pressure and the flow distribution cannot be ignored. These effects are caused by 3D electric currents which form near expansions and contractions parallel to the applied magnetic field. The Lorentz force field is rotational at these locations, and since pressure gradients are not rotational, hydrodynamic forces must develop to balance the electromagnetic force. Ultimately, 3D flow structures form and this results in extra pressure losses.

A 3D MHD pressure drop resulting from 3D MHD effects is inserted into the pressure distribution which accounts for a significant portion of the pressure drop across the liquid metal loop. In section 3.4, pressure correlations informed by scaling analysis were introduced and it was shown that the 3D MHD pressure drop scales linearly with r_{exp} and, depending on the size of N relative to $Ha^{3/2}$, with either $\rho U^2 N^{2/3}$ in the IE regime or $\rho U^2 N Ha^{-1/2}$ in the VE regime. A similar pressure drop is expected for an outlet manifold featuring a sudden contraction. While this claim is likely to be true for the VE regime, the pressure drop may change significantly for the IE regime because while Lorentz and viscous forces are reversible, inertial forces are not. Future studies are therefore necessary as fusion blankets will operate firmly inside the IE regime.

3D MHD effects at sudden expansions are also responsible for the occurrence of a complex flow structure which quickly redistributes flow along the transverse direction downstream of the sudden expansion. In section 3.5.A, it was discussed that the flow distribution among short parallel channels is mostly controlled by the length of the expansion region for Ha and $N \gg 1$, particularly when the expansion region ends before the flow becomes fully developed. Results for $r_{exp}=12$, $Ha=6570$, and $N=21582$ indicate that MHD manifold flows at even higher Ha and N will feature a balanced flow distribution so long as the channels begin after a length $L_{exp}/b=1$ downstream of the expansion. However, if the walls are electrically conducting, multi-channel effects such as the Madarame effect and electromagnetic coupling can impact the flow distribution and the MHD pressure drop [2, 57, 58]. These effects account for phenomena associated with electric currents

that connect through two or more parallel channels when the channels are stacked perpendicular or parallel to the magnetic field respectively. When the walls are nonconducting, as in the present work, multi-channel effects can obviously be neglected.

Increasing L_{chan} causes flow to become more evenly distributed among the parallel channels [62]. Furthermore, a Resistor Network Model was introduced to model the flow distribution as a function of L_{chan}. The RNM was shown to fit the flow distribution data as well as the expected behavior of the flow distribution as L_{chan} becomes very large. In the analysis, it was shown that prohibitively long channels would be required to achieve a balanced flow distribution (L_{chan}~5m for 34.33% of flow passing through the center channel). However, this problem may be mitigated by increasing the length (L_{exp}) between the sudden expansion and the inlets of the parallel channels [63] or by electrically coupling the channels [64]. As a design tool, the proposed RNM is useful because only two simulations or experiments are required to determine a channel length which produces a desired flow distribution given a set of flow parameters and manifold geometry. By contrast, other methods for optimizing channel length will require more than two iterations. Thus, using an RNM may save blanket designers months or years of computational time and may prevent the need for many expensive experiments for optimizing blanket designs. However, the analysis in this study was based on *Ha* and *Re* values much lower compared to real LM blankets and the flow considered here was isothermal. And while the present case does have *Ha* and $N>>1$ which indicates strong MHD effects, it is not clear how applicable the main conclusions of the proposed RNM analysis will be in designing a blanket, which will certainly have nonlinear buoyant effects and perhaps significant inertial effects as well. Thus, further assessment of the RNM at fusion blanket conditions is required.

It should be mentioned that the manifold model in Fig. 1 has a simpler geometry compared to a “real” blanket manifold where the flow may turn from the radial to poloidal direction right after the expansion region. This feature is not included here as the change in the flow direction from radial

to poloidal in the real blanket occurs in the plane perpendicular to the applied magnetic field such that associated changes in the MHD pressure drop are known to be small [22]. The outlet region at the exit of the manifold is another special feature of the proposed model. It was added to the model mostly because of the computational reasons to minimize the downstream effect of the outlet boundary condition on the flow inside the manifold. Also, in a real manifold design, the height of the expansion region can be different from the size of the feeding duct. A real manifold may also need rounded corners in the expansion region to provide smooth transition from the flow in the inlet pipe to that in the expansion region. This will result in a lower MHD pressure drop in the manifold by reducing 3D effects [29]. In spite of these simplifications, the proposed model preserves the most important features of a real manifold flow. Future design studies might need to account for such details, but this will hardly change the main conclusions of the present study about the fundamental flow physics associated with the 3D MHD effects.

The analysis done in this study covers a range of flow parameters significantly lower compared to real blanket flows. In this range, the flow was found to be laminar while the blanket flows are expected to demonstrate quasi-2D (Q2D) turbulence [65]. In Q2D turbulent flows, turbulent vortices are big (comparable in size with the duct dimension) coherent structures stretched along magnetic field lines between the two Hartmann layers at the flow confining walls. Such vortices are known to have low Joule and negligible viscous dissipation due to their orientation with respect to the magnetic field [66]. Therefore, the contribution of the Q2D vortices in the MHD pressure drop seems to be much smaller compared to other pressure-affecting factors, first of all the internal shear layer at the expansion as studied here. Though Eqs. (7-12) were determined for steady laminar MHD flows, these formulae will likely need only small corrections to account for turbulence effects.

Part II: MHD Duct Flows with Buoyancy Effects

In Part II, I perform 3D numerical analysis of MHD flows in a vertical, straight, square duct subject to applied one-sided heating and a fringing, transverse magnetic field (Fig. 27).

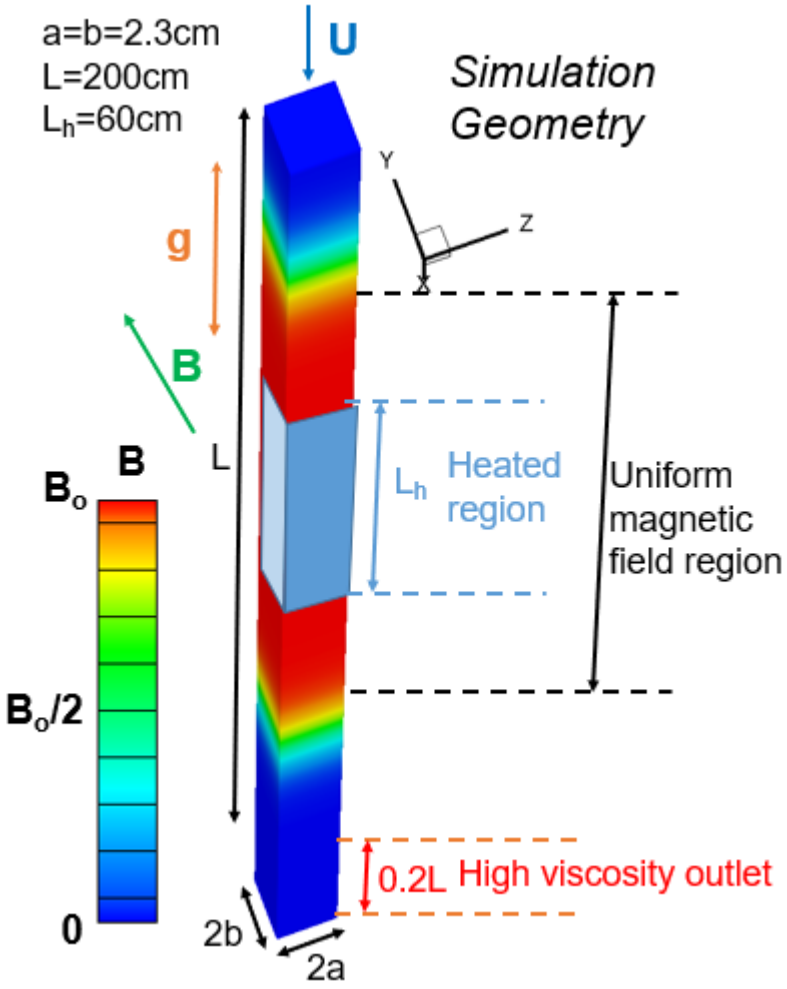

FIG. 27. A test blanket submodule geometry for numerical simulation. The origin for the coordinate system is at the center of the duct's cross-section in the center of the heated region. Uniform flow enters the duct in a zero-magnetic field region. The flow continues into a region with a fringing, y-direction magnetic field which is uniform for 80cm along the duct. Inside the uniform magnetic field region, the flow encounters a 60cm region where heating is applied either as volumetric heating in the fluid or as surface heating on the z=-a-t_w sidewall. The flow exits the duct, fully developed, through a region of zero-magnetic field. The final 40cm of the duct has artificially high viscosity for numerical reasons.

Part II of this dissertation is organized as follows: Chapter 5 contains a description of the problem formulation and numerical methods used; Chapter 6 contains a mesh refinement study, a

discussion of the physics and phenomena of MHD mixed convection flows, a parametric study of magneto-buoyant effects, a discussion of axial forces, an analysis of non-uniformity along the magnetic field direction, a comparison of volumetric heating cases, which approximate nuclear heating, to surface heating cases, and selected results for comparison with experiments and other codes with a brief discussion of velocimetry theory; Chapter 7 contains a summary of conclusions and suggestions for future work.

Chapter 5: Physical and Mathematical Model of MHD Duct Flows with Buoyancy Effects

To study MHD mixed convection flow behavior sketched in Fig. 27, HIMAG (see Part 1, Chapter 2) was used to simulate the flow of liquid metal of kinematic viscosity v, electrical conductivity σ, density ρ, specific heat capacity C_p, thermal conductivity k, and coefficient of thermal expansion β, through a vertical straight square duct with thickness t_w = 0.002 m, and material properties denoted by a subscript w, subjected to heating, a strong transverse magnetic field B, and gravity g = 9.81 m/s^2. Such a flow is characterized by the following key dimensionless parameters: the Hartmann number, which when squared, represents the strength of electromagnetic forces relative to viscous forces, $Ha = bB_o\sqrt{\sigma/\nu\rho}$; the Reynolds number, which represents the strength of inertial forces relative to viscous forces, $Re = \frac{aU}{\nu}$; the Grashof number, which represents the strength of buoyant force relative to viscous force, $Gr = \frac{g\beta\Delta T a^3}{\nu^2}$; the wall conductance ratio, $c_w = \frac{\sigma_w t_w}{\sigma b}$; and the Prandtl number, which is the ratio of viscous diffusion to thermal diffusion, $Pr = \frac{\rho\nu Cp}{k}$. The dimensionless parameters combined with the flow orientation with respect to gravity (upward or downward flow) and the distribution of the applied surface or volumetric heating define the flow completely. In the definition of Gr, ΔT is a characteristic temperature difference calculated using the following formula:

$$\Delta T = \frac{a}{k}\int_{-a}^{+a} q'''(z)dz \quad \text{for volumetric heating,} \tag{20a}$$

$$\Delta T = \frac{a}{k} q_o'' \text{ for surface heating.} \tag{20b}$$

In Eq. (20a), $q'''(z)$ is the distribution of applied heating per unit volume inside the fluid domain. In Eq. (20b), q_o'' is the prescribed heating per unit area in the special case that the heating mode is purely surface heating applied to the outside surface of the sidewall. The axial length of the heated region, L_h, in all cases is 0.6096 m centered at x=0 m. In the volumetric heating cases, the heating spans the fluid domain uniformly from y=-*b* to y=*b* and is largest at the z=-*a* sidewall and decreases exponentially or otherwise follows the trend of nuclear heating data towards the z=*a* sidewall. In surface heating cases, the heating is uniform at z=-*a*-t_w, spanning from y=-*b*-t_w to y=*b*+t_w.

In addition to *Re*, *Ha*, and *Gr*, the interaction parameter, $N = \frac{Ha^2}{Re}$, which represents the ratio of electromagnetic to inertia forces, and the Richardson number $Ri = \frac{Gr}{Re^2}$ which represents the ratio of buoyant to inertial forces, are also important parameters. The total axial length is 2.4 m with the first 2 m representing the test blanket submodule (TBSM) of the MaPLE-U experiment, which is also close to the poloidal blanket length in some design studies [2]. The final 0.4 m are included for numerical reasons discussed later in this section. The half width of the duct in the magnetic field direction, *b,* is the length scale in the definition of *Ha* and c_w while the half width perpendicular to the plane of maximum heating, *a,* is the length scale in the definition of *Gr* and *Re*. The prescribed average velocity *U* is the velocity scale. Physical properties of the LM were chosen to equal those of eutectic lead-lithium alloy (PbLi) at 300ºC (*Pr*=0.033) using HIMAG's built-in material properties while the physical properties of the wall were chosen to be those of stainless steel at 300ºC (c_w=0.12) or those of an insulating wall (c_w=1.2x10^{-9}) (Table 3). The applied magnetic field's maximum strength B_o was varied to control *Ha, U* was varied to control *Re*, and

the magnitude and shape of the applied heating was varied to control *Gr*. All of the simulations feature square ducts such that $\frac{a}{b} = 1$ for every simulation.

Table 3: Material Properties

LM PbLi Properties at 300°C		Wall Properties	
σ	7.89205x10^5 S/m	σ_w	1.09x10^6 S/m or 1.09x10^{-2} S/m
ρ	9486.0 kg/m^3	ρ_w	7800 kg/m^3
C_p	200.22 J/K	C_{pw}	500 J/(kg*K)
k	13.123 W/(m*K)	k_w	19.0 W/(m*K)
v	2.15269x10^{-3} Pa*s		
β	1.77362x10^{-4} K^{-1}		

The simulated magnetic field fringes to imitate the field of an electromagnet which produces a region of uniform field with an axial length of 0.8 m centered at x=0 m. The shape of the field is defined in the following way. Firstly, the domain is divided into three types of regions: 1) a downstream region where the magnetic field is zero, 2) a uniform region, and 3) two fringing regions which boarder the uniform region:

1) If $x \geq x_o + 2*(x_c - x_o)$ then B=*0*. (21a)
2) Else if $x_1 < x < x_2$ then B=B_0 (21b)
3) Else if $x_1 > x$ or $x > x_2$ then $\mathrm{B} = \frac{1}{2} B_0 * \left(1 - 0.1 * \tanh\left(\frac{|x - x_c|}{c_1} - c_2\right)\right)$ (21c)

Here, $x_c = \frac{x_2 + x_1}{2}$ and x_1 and x_2 are the boundaries of the uniform field region. x_o is the location of the duct entrance. In the present cases, x_1=-0.4 m and x_2=0.4 m and so x_c=0 m. B_0 is the uniform magnetic field strength (e.g. 0.5T). c_1 is set to 0.01 m in the simulations such that the argument inside the tanh function reads $\left(\frac{|x|}{0.01m} - c_2\right)$ and here, x ranges from -1 m to 1.4 m. c_2 is a constant

equal to 73.15. The magnetic field distribution is uniform in y and z and its magnitude along the axial direction is plotted in Fig. 28.

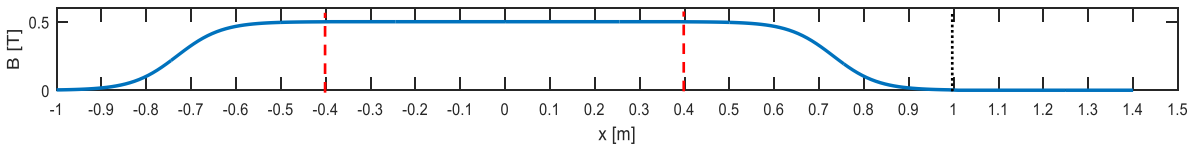

FIG. 28. An example magnetic field plotted using Eq. (21) with B_o=0.5 T. The vertical dashed lines mark the bounds of the uniform magnetic field region. The vertical dotted line marks where the magnetic field strength goes to zero.

The HIMAG code solves the MHD equations coupled with the thermal energy equation, shown below as Eqs. (22-26), in 3D using an electric potential formulation with the assumption that the induced magnetic field is small enough to be neglected compared to the applied one. Furthermore, the fluid is assumed Newtonian and incompressible, and Joule heating and heating from viscous dissipation are assumed to be negligibly small compared to the applied heating. Additionally, the Boussinesq approximation (BA) is applied such that all material properties are assumed constant except for inside the buoyant force term of Eq. (23), where it is as though density decreases linearly with increasing temperature.

The BA is a powerful and convenient approach to making nonisothermal problems tractable for numerical investigation; however, the errors associated with using BA are difficult to quantify. Currently, no studies have analyzed the applicability of the BA in MHD flows despite the fact that use of BA is widespread for such problems (e.g. [32, 33, 40-47]). And though the only sure way to evaluate error related to BA in a particular flow is to compare results of methods which do not employ BA, a preliminary justification for using BA can be made using some criteria developed for hydrodynamic flows.

Many criteria for the applicability of BA in hydrodynamic flows have been published [67-70], the simplest of these, put forth by Crapper and Bains (1977) [67], stipulates that the density should change by no more than 5% by thermal expansion for BA to be applicable. To achieve a 5%

decrease in the density of PbLi, the temperature would need to exceed 713°C [71], approximately 160°C greater than the maximum temperature of the present simulations. Additional criteria, such as $\frac{\nu}{(gb)^{\cdot 5}b} \ll 1$ (presently ~2x10^{-5}), $\frac{U}{(gb)^{\cdot 5}} \ll 1$ (~6x10^{-2}), and others which ensure incompressibility of the fluid and negligible heating from viscous dissipation [70], are also satisfied in the present simulations.

Therefore, my approach is to use the BA in the present work and to suggest that future efforts be made to rigorously qualify the use of BA via comparison with methods which do not rely on this approximation.

Equations (22-26) include the continuity equation, momentum equation with the Lorenz force term and the buoyant force term on the right-hand-side, Ohm's law to compute the induced electric current, the electric potential equation, and the thermal energy equation respectively:

$$\nabla \cdot \mathbf{u} = 0, \tag{22}$$

$$\frac{\partial \mathbf{u}}{\partial t} + \mathbf{u} \cdot \nabla \mathbf{u} = -\frac{1}{\rho}\nabla \mathrm{p} + \nabla \cdot \nu \nabla \mathbf{u} + \frac{1}{\rho}\mathbf{J} \times \mathbf{B} - \boldsymbol{g}\beta(\mathrm{T} - T_o), \tag{23}$$

$$\mathbf{J} = \sigma(-\nabla \phi + \mathbf{u} \times \mathbf{B}), \tag{24}$$

$$\nabla \cdot (\sigma \nabla \phi) = \nabla \cdot (\sigma \mathbf{u} \times \mathbf{B}), \tag{25}$$

$$\rho c_p \left(\frac{\partial \mathrm{T}}{\partial \mathrm{t}} + \mathbf{u} \cdot \nabla \mathrm{T}\right) = \nabla \cdot k \nabla \mathrm{T} + q'''. \tag{26}$$

Here, **u**, **J**, and **B,** and ***g*** are the velocity, electric current density, magnetic field, and gravity vectors respectively and p, ϕ, and T are the pressure, electric potential, and temperature scalars. T_o is the inlet temperature which is set to 300°C for all present cases. A term equal to ***g*** is omitted from the right-hand-side of Eq. (23) as this term would be easily absorbed by the pressure gradient and simply omitting it precludes the need to subtract the static pressure distribution from the results. Eq. (25) is obtained by taking the divergence of Eq. (24) while stipulating that electric

current is continuous ($\nabla \cdot \mathbf{J} = 0$). To consider both the liquid and the surrounding solid wall, which may have different electrical conductivity, the electrical conductivity σ is put inside the derivatives in Eq. (25). Similarly for the thermal conductivity in Eq. (26) and the viscosity in Eq. (23).

Equations (22-26) were solved numerically on non-uniform rectangular meshes (Fig. 29). There are at least 8 nodes inside all Hartmann layers on the walls perpendicular to the magnetic field and 10 nodes inside each side layer on the wall parallel to the magnetic field. Lower mesh resolution is used throughout the central region of the duct as it is expected that the magnetic field damps out flow features with small length scales in the bulk of the flow. Where the magnetic field is small or zero, the mesh is still not refined as the small-scale flow behavior in those regions are not a topic of interest in this work. A mesh sensitivity study was performed, and the results are presented in section 6.1.

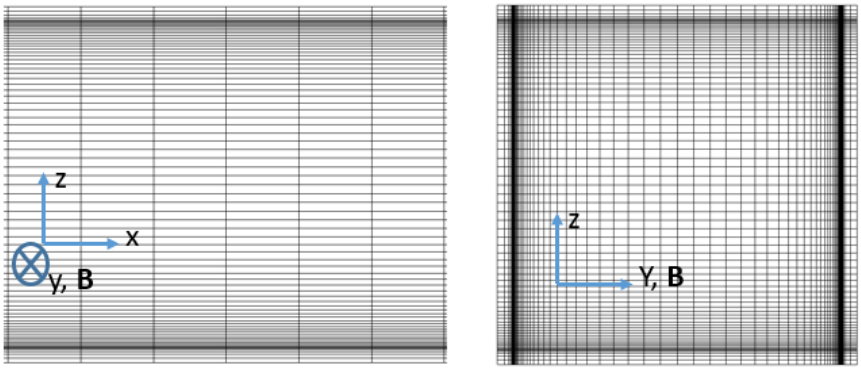

FIG. 29. An example computational mesh with 1510400 cells. Due to the large aspect ratio of x:z, only a small segment of the x-axis is included.

The inlet velocity boundary condition specifies uniform flow with velocity *U* at x=-1 m while a fully developed flow outlet boundary condition in the form $\frac{\partial \boldsymbol{u}}{\partial \mathrm{x}} = 0$ is used at the outlet at x=1.4 m. The no slip and no flow-through conditions are enforced at fluid-wall interfaces ($\mathbf{u_{wall}} = \mathbf{0}$). The pressure is set to zero at the outlet. The fluid-wall boundaries and the inlet have Neumann pressure conditions $\left(\frac{\partial p}{\partial n} = 0\right)$. Normal components of electric current density are set to zero at

the outer domain boundary $\left(\frac{\partial \phi}{\partial n} = (\mathbf{u} \times \mathbf{B}) \cdot \hat{\boldsymbol{n}}\right)$. Adiabatic conditions $\left(\frac{\partial \mathrm{T}}{\partial n} = 0\right)$ are set for all outer domain boundaries except for the inlet, where the temperature is prescribed as T=T_o=300°C, and, when the applied heating mode is surface heating, the outer boundary of the wall at $\mathrm{z} = -a - t_w, -b - t_w \leq \mathrm{y} \leq b + t_w, \ -\frac{L_h}{2} \leq \mathrm{x} \leq \frac{L_h}{2}$, has $\frac{\partial \mathrm{T}}{\partial z} = -q_o''/k$.

For numerical stability reasons the viscosity of the LM is linearly ramped up artificially from 1 to 1000 times the inlet value over the last 0.4 m of the duct in what is referred to here as the high viscosity outlet region but is otherwise known as a viscous sponge layer [72]. The purpose of this is to quickly develop the flow and to damp out vortices which may otherwise make their way to the outlet. Without a high viscosity outlet region, vortices have been observed to approach and ultimately straddle the outlet, and the simulation eventually diverges. Including the high viscosity outlet region fixes this and ensures that the outlet boundary conditions behave properly without the need of an extremely long and prohibitively expensive outlet region.

Simulations were started with initially uniform flow and uniform temperature conditions with initial velocity *U* and temperature T_o. A time step size of $\Delta t=10^{-4}$ s was used for all cases. To reduce risk of divergence in the early development of the flow, partial up-winding (λ_u=0.7) was used for the first 200,000 timesteps in each case, after which the up-winding factor was set to λ_u=1.0 (central differencing/no up-winding) to restore the 2nd-order accuracy of the solver for the remainder of the simulation. Each simulation was run in parallel on 1024 cores on either the EDISON or CORI super computers which are owned and operated by the National Energy Research Scientific Computing Center (NERSC). Using 1024 cores, the computations proceeded at a rate of ~1 million timesteps per 24 hours such that the shortest simulations were finished in ~3 days. MHD mixed convection flows at high *Gr* numbers are inherently unsteady so the stopping criteria of the simulations is one based on statistical steadiness. Simulations must run long enough to converge

(~1.5 million steps), but must also continue running to confirm statistical steadiness (~1.5 million steps) meaning that the time rate of change of time-averaged flow variables goes to zero.

In total, for Part II, I computed 16 cases as listed in the simulation matrix of Table 4. Unless specified, the results of simulations presented in this work are the outputs of the simulations at their final timesteps listed in Table 4. Some of the presented data; however, is specified as time-averaged meaning the flow variables are averaged over all the timesteps between step number 1 million and the final timestep number listed in Table 4.

Table 4. Simulation Matrix

#	**Flow Direction**	**Wall Conductivity**	**Heating Mode**	**Ha**	**Re**	**Gr**	**c_w**	**Final Timestep**
1	Down	Conducting	Surface	220	2027	$1.44x10^8$	0.12	$3.4x10^6$
2	Down	Insulating	Surface	220	2027	$1.44x10^8$	$1x10^{-9}$	$3.5x10^6$
3	Up	Conducting	Surface	220	2027	$1.44x10^8$	0.12	$3.5x10^6$
4	Up	Insulating	Surface	220	2027	$1.44x10^8$	$1x10^{-9}$	$3.15x10^6$
5	Down	Conducting	Exponential	220	2027	$1.57x10^8$	0.12	$8.1x10^6$
6	Down	Insulating	Exponential	220	2027	$1.57x10^8$	$1x10^{-9}$	$4.65x10^6$
7	Up	Conducting	Exponential	220	2027	$1.57x10^8$	0.12	$3.235x10^6$
8	Up	Insulating	Exponential	220	2027	$1.57x10^8$	$1x10^{-9}$	$2.95x10^6$
9*	Down	Conducting	Surface	220	5068	$5.04x10^7$	0.12	$3.65x10^6$
10*	Down	Conducting	Surface	220	5068	$5.04x10^7$	0.12	$4x10^6$
11*	Down	Conducting	Surface	220	5068	$5.04x10^7$	0.12	$2.65x10^6$
12	Up	Conducting	Nuclear	220	2027	$1.57x10^8$	0.12	$2.7x10^6$
13	Up	Insulating	Nuclear	220	2027	$1.57x10^8$	$1x10^{-9}$	$2.75x10^6$
14	Down	Conducting	Nuclear	220	2027	$1.57x10^8$	0.12	$4.25x10^6$
15	Down	Insulating	Nuclear	220	2027	$1.57x10^8$	$1x10^{-9}$	$2.9x10^6$
16	Down	Conducting	Surface	220	3041	$2.88x10^7$	0.12	$4.9x10^6$

**cases 9-11 are part of a mesh refinement study. They feature the same parameters but three different meshes.*

Chapter 6: Results of MHD Duct Flow Simulations with Buoyancy Effects and Discussion

6.1 Mesh Refinement Study

Prior to the main computations, a mesh sensitivity study was performed using a downward flow of PbLi in an electrically conducting duct with surface heating q_o''=0.07 MW/m^2, B_o=0.5 T, U=0.05 m/s, and ΔT=122.7^{o}C (Ha=220, Re=5068, Gr=5.04x10^7, c_w=0.12) for which more complex flow features (that might require higher mesh resolution) are expected compared to upward flows. In order to quantify the discretization error, the sensitivity study featured three computational meshes with approximately 10^6 cells each including “coarse”, “medium” and “fine” meshes. Each consecutive mesh featured approximately twice as many cells as the previous mesh. The number of cells in each mesh is shown in Table 5.

Table 5. Mesh Refinement Details.

Mesh	# of cells along x	# of cells along y	# of cells along z	Total # of cells
Coarse	188	64	65	782080
Medium	236	80	80	1510400
Fine	297	100	100	2970000

The simulation results were recorded once the simulations reached a statistically steady state at 2.65 million timesteps. The time-averaged mean temperature distributions (Fig. 30a) were calculated by averaging the time-averaged temperature at each cross-section along the axis of the duct in each of the three simulations.

The mean outlet temperatures are 309.9^{o}C, 310.1^{o}C, and 310.6^{o}C for the sparse, medium, and fine meshes respectively with a maximum difference of 0.2% between the sparse and fine cases. Similarly, the mean pressure distributions at t=265s were calculated and plotted in Fig. 30b. The pressure drops across the duct are found to be 1685.1 Pa, 1673.6 Pa, and 1683.7 Pa for the

sparse, medium, and fine meshes respectively with a maximum difference of 0.6% between the medium and fine cases.

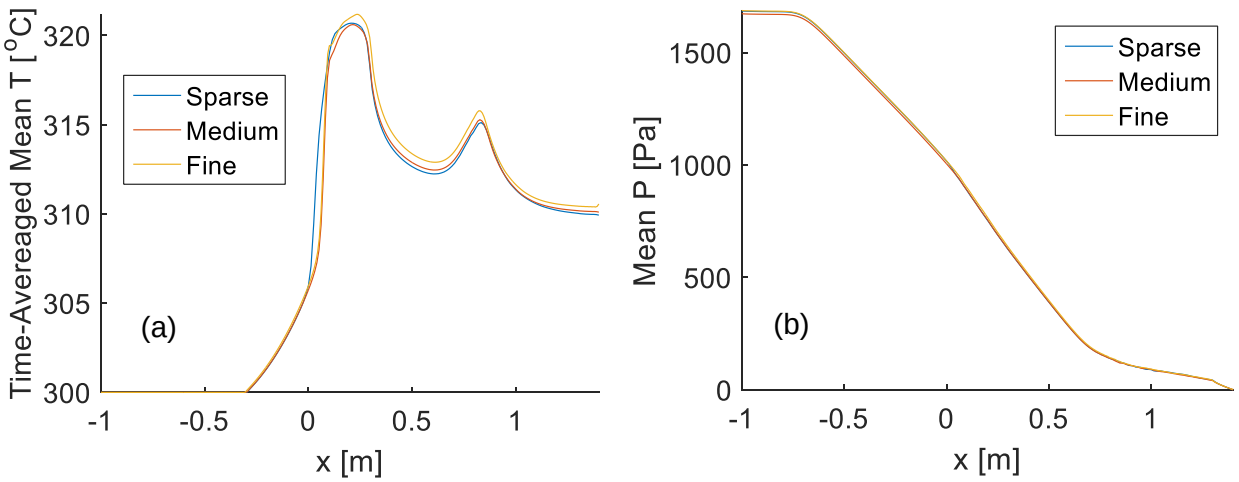

FIG. 30. (a) Time-averaged mean temperature of fluid cross-sections along x are plotted for each computational mesh. (b) The instantaneous mean pressure of fluid cross-sections along x are plotted for each computational mesh.

As a consequence of discretizing the advective terms in the governing equations, dispersion errors [73] appear in the solution, particularly near the beginning of the heated region where flow reversal causes the axial temperature gradient to be quite large (Fig. 31). These errors, which manifest as spurious the natural oscillations caused by flow instability.

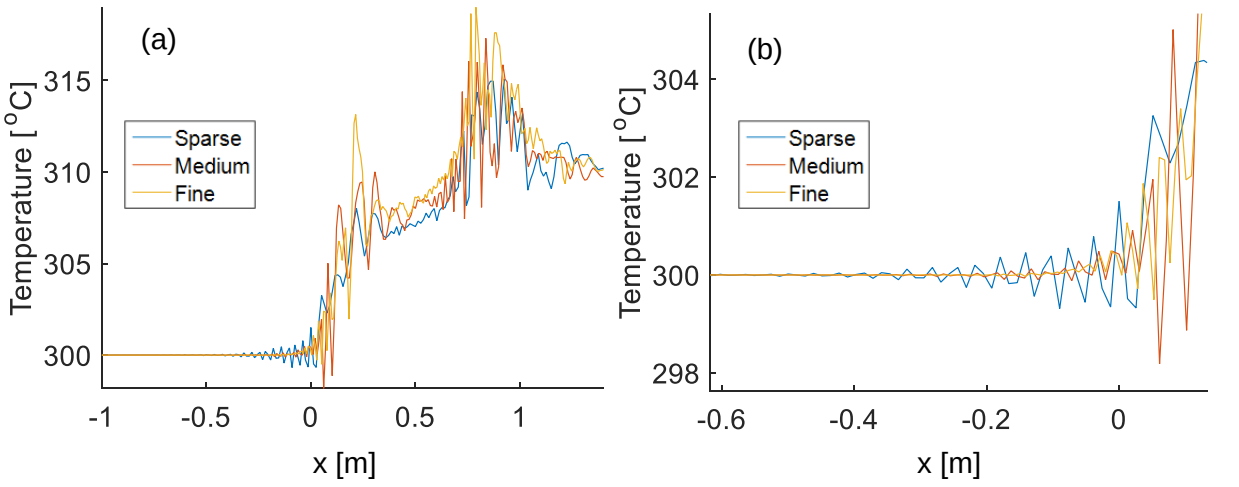

FIG. 31. (a) The instantaneous centerline temperature is plotted for each of the computational meshes. (b) Instantaneous centerline temperature, zoomed in on x= [-0.6 m, 0.1 m].

For all other computations in the present work, meshes similar to the medium mesh are used.

6.2 Characteristic Features of MHD Mixed Convection Flows in a Vertical Duct

An overview of the behavior of MHD flow through vertical ducts with applied surface heating and transverse magnetic field is presented in this section to provide context for more detailed parametric and comparison studies in the following sections. Both upward flowing and downward flowing cases are presented for ducts with either electrically conducting or nonconducting walls, totaling to four flow scenarios. The simulations feature surface heating q_o''=0.20 MW/m^2, B_o=0.5 T, U=0.02 m/s, and ΔT=350.5^{o}C (Ha=220, Re=2027, Gr=1.44x10^8) for all four scenarios presented in this section with two having c_w=0.12 and the other two having c_w=1x10^{-9}. The velocity fields on the y=0 m center-plane are provided in Fig. 32. Even though the flow was computed in 3D, the flow structure within the magnetic field region is mostly quasi-two-dimensional (Q2D) with an almost uniform core and thin Hartmann boundary layers at the duct walls perpendicular to the magnetic field. Such a Q2D flow structure is typical to many MHD duct flows in a strong magnetic field, such that plotting the data at the mid-plane is a good way to represent the entire flow. Some deviations of the computed flows from the idealized Q2D flow are discussed in section 6.5.

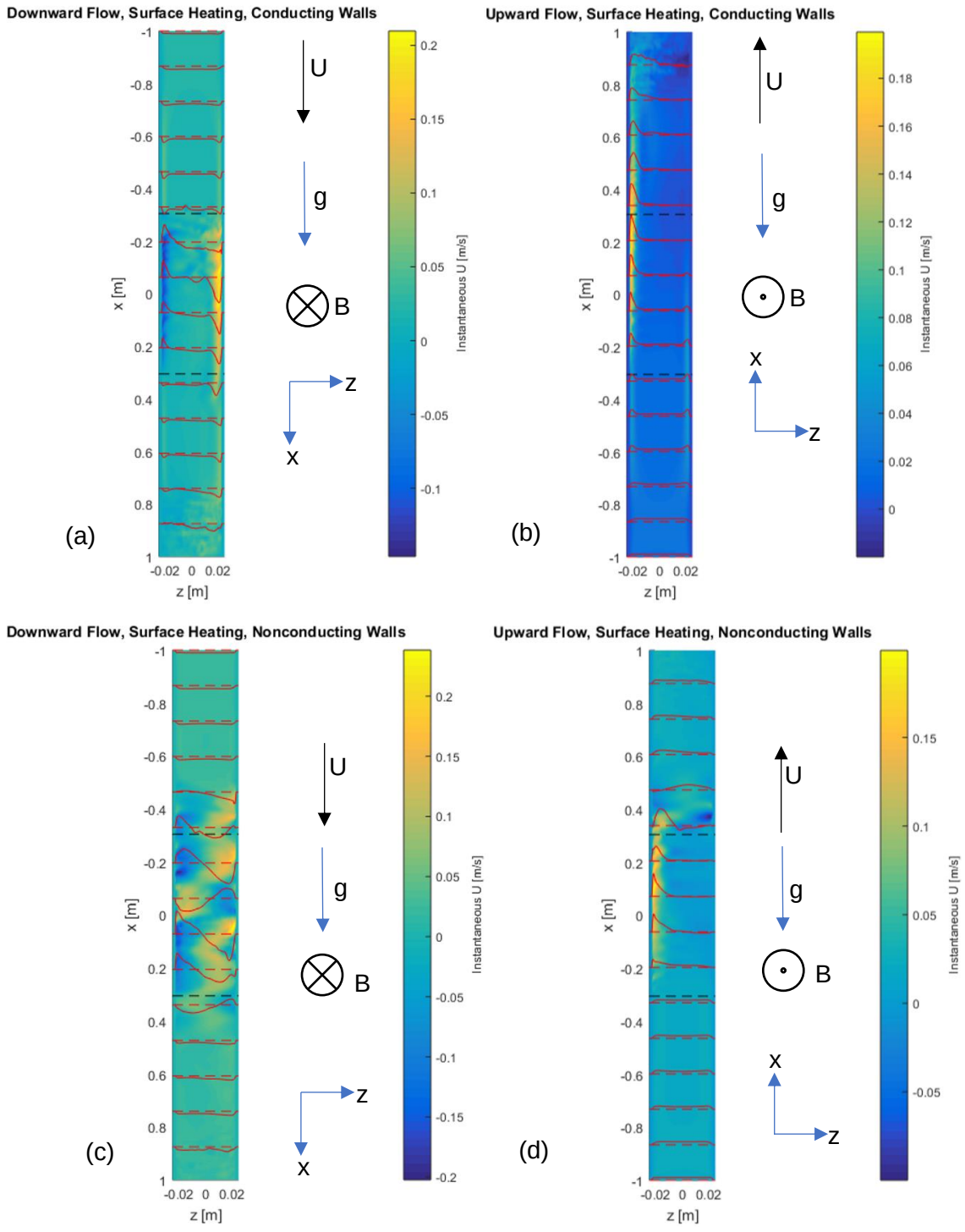

FIG. 32. Instantaneous axial velocity contours and profiles on the y=0 center-plane. Surface heating q_o''=0.20 MW/m^2, B_o=0.5 T, U=0.02 m/s, and ΔT=350.5^{o}C (Ha=220, Re=2027, Gr=1.44x10^8). (a, b) c_w=0.12, (c, d) c_w~0. (a, c) Downward flow, (b, d) upward flow. The z-axis is stretched compared to the x-axis by a factor of 5 to more easily view the entire flow field. The dashed red lines space every 13.3 cm are the zero lines for the profiles which are solid red lines. The black dashed lines ark the bounds of the heated region.

The flow enters as isothermal, uniform flow from either the top or the bottom end of the vertical duct. One consequence of the flow entering the duct isothermally is that buoyant force is zero near the inlet such that the orientation of the flow relative to gravity is irrelevant until the flow encounters heat.

As the flow proceeds downstream, the flow develops hydrodynamically and a viscous boundary layer begins to grow near the walls, smoothening out the sharp discontinuity of the velocity profile there. With enough space, the flow would eventually become hydrodynamically fully developed once the boundary layer grows to span the entire thickness of the duct; however, the hydrodynamic development is interrupted by the growth of the transverse magnetic field which ramps up quickly downstream.

The effect of a fringing magnetic field (i.e. a magnetic field which is uniform in some region but decays to zero or “fringes” on the periphery of the region) on liquid metal flows has been thoroughly studied in the past (e.g. [12, 74, 75]). A 3D electromagnetic disturbance occurs in the vicinity of the fringe. This disturbance is characterized by 3D electric currents which close along the axial direction. Additionally, a 3D MHD pressure drop is inserted into the flow and the velocity profile becomes M-shaped. This effect is prominent in electrically nonconducting ducts but is somewhat less important in ducts with conducting walls where the 3D effects are overshadowed by the larger 2D circulations of electrical current which close in the conducting walls rather than inside the fluid.

As the flow moves deeper into the region of uniform transverse magnetic field, the 3D disturbance caused by the fringe fades and the flow quickly develops towards classical Shercliff [3] or Hunt flow [6] for the case of electrically nonconducting and conducting ducts respectively. Both fully developed flows feature nearly uniform velocity in the “bulk” – a central region which includes the vast majority of the duct’s cross-section. The flow in the bulk is characterized by a dominance of electromagnetic Lorentz force (=$\mathbf{J}\times\mathbf{B}$) which is balanced by the pressure gradient. The bulk is

framed by special layers attached to the walls inside which viscous forces are significant. Layers attached to walls perpendicular to the transverse magnetic field are “Hartmann layers” and have thickness which scales inversely with the Hartmann number. Layers attached to walls parallel to the magnetic field are “side layers” and have thickness which scales with the inverse of the square-root of Hartmann number.

As the flow is exposed to heat from the hot wall, or when the heat is transported upstream of the heated region once the flow near the hot wall reverses in the case of buoyancy-opposed flows, the incoming flow becomes non-isothermal. The instantaneous temperature distribution is shown for each of the four scenarios in Fig. 33. Buoyant force acts on warm fluid in the direction opposite gravity, thus the orientation of the flow with respect to gravity becomes important in and around the heated region. In the upward flow cases, the flow remains isothermal until entering the heated region at x=0.3 m since the heat is advected downstream much faster than it can conduct upstream; however, in the downward flow cases, buoyant flow structures advect heat upstream of the heated region, most notably in the case of nonconducting walls where elevated temperatures are observed as far as ~20 cm upstream of the entrance to the heated region.

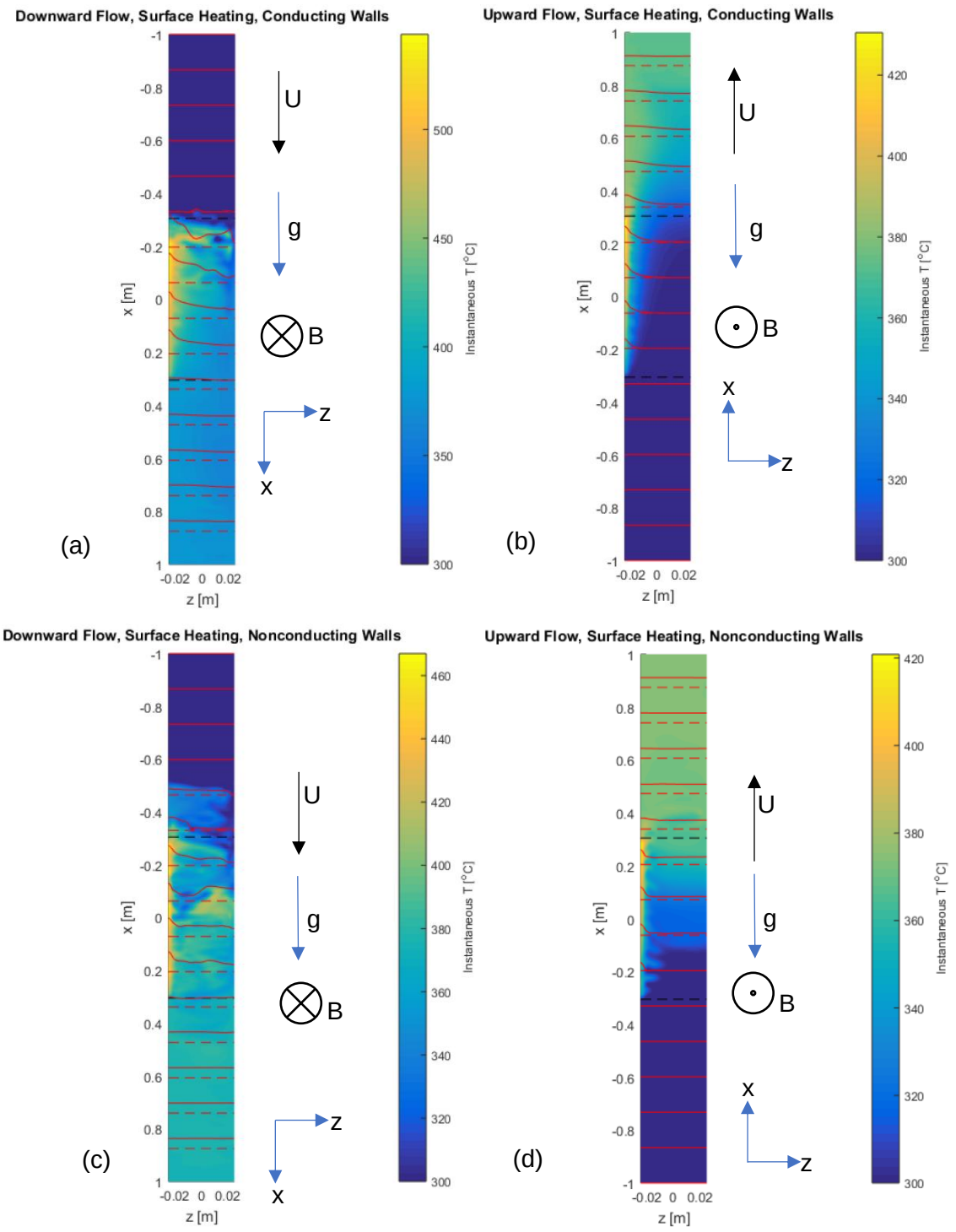

FIG. 33. Instantaneous temperature contours and profiles on the y=0 center-plane. Surface heating q_o''=0.20 MW/m^2, B_o=0.5 T, U=0.02 m/s, and ΔT=350.5°C (Ha=220, Re=2027, Gr=1.44x10^8). (a, b) c_w=0.12, (c, d) c_w~0. (a, c) Downward flow, (b, d) upward flow. The z-axis is stretched compared to the x-axis by a factor of 5 to more easily view the entire flow field. The dashed, red lines spaced every 13.3 cm are the zero lines for the profiles which are solid red lines. The dashed, black lines mark the bounds of the heated region.

In the case of downward flow, the buoyant force opposes the forced flow while the buoyant force assists the forced flow in the case of upward flow. In all four of the reference scenarios, buoyant force causes significant changes to the velocity field. Wherever the buoyant force field has nonzero curl, pressure is not able to balance it and so the velocity field is forced to adapt to give rise to rotational electromagnetic and/or hydrodynamic forces. As such, the flow tends to demonstrate patterns typical to rotational flows, such as inflection points in the velocity profile, formation of high-velocity jets and associated internal shear layers. Furthermore, buoyant effects tend to destabilize the flow. As shown in Figs. 32 and 33, velocity and temperature fluctuations are present where the flow cross-sections are non-isothermal. These fluctuations are partially suppressed by toggling the wall conductivity from nonconducting to conducting due to the conducting wall cases having stronger Joule dissipation which tends to stabilize flow by dissipating kinetic energy as heat due to strong induced currents closing through the walls.

Strongly **buoyancy opposed flows** are characterized by the detachment of the side layer from the heated sidewall, followed by a region of reverse flow that spans the length of the heated region near the hot sidewall. By time-averaging the velocity field (Fig. 34), it can be seen that generally, the flow recirculates inside the heated region, moving up on the hot side and down on the cold side, with maximum speeds several times larger than the forced flow mean speed.

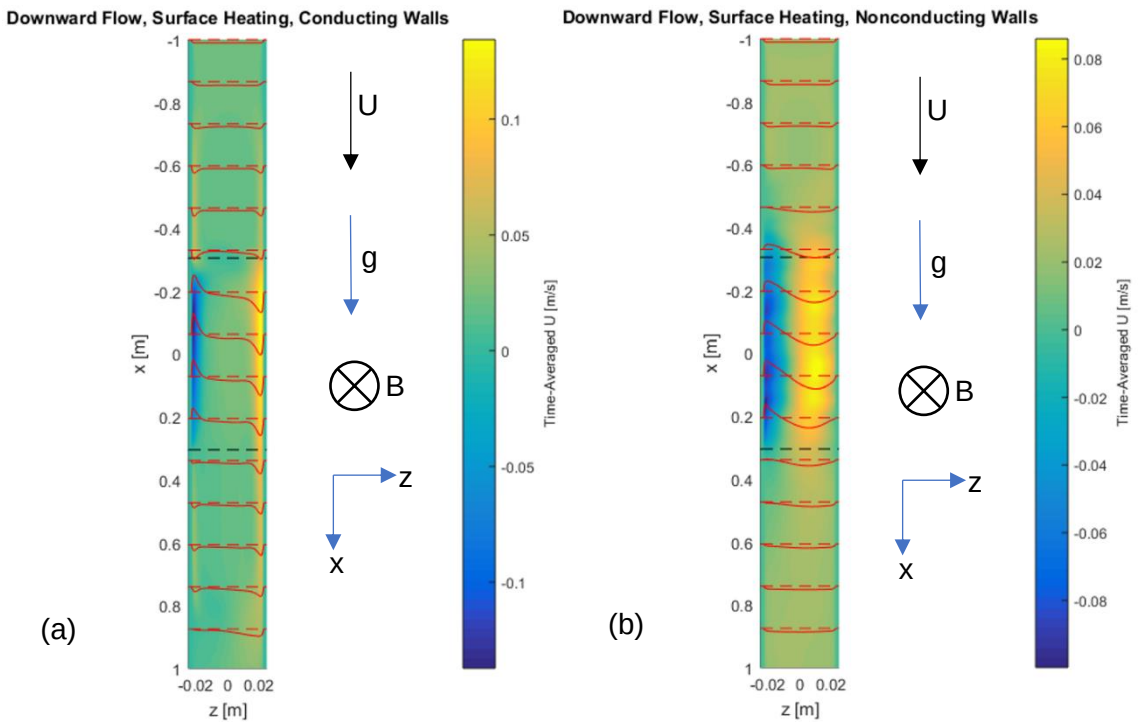

FIG. 34. Instantaneous time-averaged axial velocity contours and profiles on the y=0 m center-plane. Downward flow with surface heating q_o''=0.20 MW/m^2, B_o=0.5 T, U=0.02 m/s, and ΔT=350.5^{o}C (Ha=220, Re=2027, Gr=1.44x10^8). (a) c_w=0.12, (b) c_w~0. The z-axis is stretched compared to the x-axis by a factor of 5 to more easily view the entire flow field. The dashed, red lines spaced every 13.3 cm are the zero lines for the profiles which are solid red lines. The dashed, black lines mark the bounds of the heated region.

Strongly **buoyancy assisted flows** are characterized by the development of a buoyant jet attached to the heated wall. As the flow moves further into the heated region and the temperature of the hot wall increases, the portion of the flow carried by the buoyant jet increases to ~100% of the total flowrate while the flow stagnates or recirculates weakly away from the hot sidewall. Significant velocity fluctuations in the jet are observed in the case of electrically nonconducting walls as a wavelike instability grows along the axial direction, culminating in large vortices which span the entire thickness of the duct. The instability mechanism is possibly Kelvin-Helmholtz instability as it often happens in MHD flows with an inflection point in the velocity profile [76]. This instability is fully suppressed or reduced in the case of conducting walls, likely due to increased Joule dissipation. It should be mentioned that unlike the downward flow scenario, the separation of the boundary layer within the heated region does not occur, obviously because of the accelerating effect of the buoyancy force near the hot wall.

Downstream of the heated region, the flow slowly tends to redevelop towards Shercliff and Hunt flows. This development is limited by the rate of heat transfer inside the fluid. Large scale flow structures born in the heated region, driven by buoyant force, die down quickly as heat is redistributed by advection - as the buoyant force becomes increasingly more uniform, the pressure gradient is increasingly able to absorb its influence and so the flow behavior becomes dominated by electromagnetic force which damps out velocity fluctuations. Thus, soon after the heated region ends, the heat is mostly transferred by conduction alone. This results in a large development length required for the flow to become isothermal and fully developed and so the velocity field remains asymmetrical.

Near the outlet of the duct, the magnetic field ramps down, causing a 3D disturbance similar to the one near the entrance to the magnetic field region.

As the magnetic field disappears, the flow transitions to turbulence. Or rather, it would be turbulent, but the mesh is not fine enough to properly capture the fluctuations which occur over very small length scales (e.g. the Kolmogorov scale). Still, strongly 3D fluctuations are present in this region. As a result of these fluctuations, the flow rapidly becomes isothermal. The unphysical nature of this region does not affect the upstream flow. Lastly, inside the high viscosity outlet, flow undergoes rapid laminarization and subsequent development before exiting the duct as fully developed hydrodynamic flow.

6.3 Parametric Study of MHD Mixed Convection Flows in a Conducting Duct

To test the effect of Hartmann (*Ha*=110-880), Reynolds (*Re*=2027-20270), and Grashof (*Gr*=1.44x10^8, 3.6x10^8) numbers on the behavior of MHD mixed convection flows in vertical ducts (Fig. 27), G. Pulugundla simulated the 17 cases shown in Table 6 below using the same methods described in Chapter 5.

Table 6. Simulation Matrix for Parametric Survey

#	Flow Direction	Wall Conductivity	Ha	Re	Gr	B [T]	U [m/s]	q_o'' [MW/m^2]	c_w
1	Down	Conducting	220	2027	$1.44x10^8$	0.50	0.02	0.20	0.12
2	Up	Conducting	220	2027	$1.44x10^8$	0.50	0.02	0.20	0.12
3	Down	Conducting	220	5068	$1.44x10^8$	0.50	0.05	0.20	0.12
4	Down	Conducting	220	10135	$1.44x10^8$	0.50	0.10	0.20	0.12
5	Down	Conducting	220	15203	$1.44x10^8$	0.50	0.15	0.20	0.12
6	Down	Conducting	220	20270	$1.44x10^8$	0.50	0.20	0.20	0.12
7	Down	Conducting	110	2027	$1.44x10^8$	0.25	0.02	0.20	0.12
8	Down	Conducting	440	2027	$1.44x10^8$	1.00	0.02	0.20	0.12
9	Down	Conducting	880	2027	$1.44x10^8$	2.00	0.02	0.20	0.12
10	Down	Conducting	220	2027	$3.6x10^8$	0.50	0.02	0.50	0.12
11	Up	Conducting	220	5068	$1.44x10^8$	0.50	0.05	0.20	0.12
12	Up	Conducting	220	10135	$1.44x10^8$	0.50	0.10	0.20	0.12
13	Up	Conducting	220	15201	$1.44x10^8$	0.50	0.15	0.20	0.12
14	Up	Conducting	220	20270	$1.44x10^8$	0.50	0.20	0.20	0.12
15	Up	Conducting	110	2027	$1.44x10^8$	0.25	0.02	0.20	0.12
16	Up	Conducting	880	2027	$1.44x10^8$	2.00	0.02	0.20	0.12
17	Up	Conducting	220	2027	$3.6x10^8$	0.50	0.02	0.50	0.12

I describe the effect of changing *Ha, Re,* and *Gr* in the present analysis. To support the findings of the parametric study, the dimensionless governing equations and associated dimensionless numbers are first discussed. A dimensionless version of the governing equations (22-26) for the

particular case of constant thermophysical properties is shown below as Eqs. (27-31), using the MHD scale for pressure ([p]=[σUB^{2}L]):

$$\nabla^* \cdot \mathbf{u}^* = 0, \tag{27}$$

$$Re\left(\frac{\partial \mathbf{u}^*}{\partial\, t^*} + \mathbf{u}^* \cdot \nabla^* \mathbf{u}^*\right) = -Ha^2 \nabla^* \mathrm{p}^* + \nabla^2 \mathbf{u} + Ha^2 \mathbf{J}^* \times \mathbf{B}^* - Gr\hat{\boldsymbol{g}}\theta, \tag{28}$$

$$\mathbf{J}^* = (-\nabla^* \phi^* + \mathbf{u}^* \times \mathbf{B}^*), \tag{29}$$

$$\nabla^2 \phi = \nabla \cdot (\mathbf{u} \times \mathbf{B}), \tag{30}$$

$$\left(\frac{\partial \mathrm{T}^*}{\partial \mathrm{t}^*} + \mathbf{u}^* \cdot \nabla^* \theta\right) = \frac{1}{PrRe} \nabla^2 \theta + q'''^*. \tag{31}$$

Here, $\theta = (\mathrm{T} - T_o)/\Delta T$. In the previous section, it was discussed that buoyant effects cause changes in the velocity field which must arise due to the inability of the pressure field to balance rotational forces. In purely MHD flows, the most important rotational force is the electromagnetic Lorentz force. The imbalance between the irrotational pressure forces and the electromagnetic forces in the purely MHD flows lead to the well-known M-shaped velocity profiles and associated shear layers. In mixed convection MHD flows at high *Gr* numbers, even more complex flow behavior can be observed because the buoyancy forces, which can also be rotational, are comparable to or even larger than the electromagnetic forces. The parametric study presented below is aimed at the identification and characterization of several flow regimes and associated flow/temperature field patterns whose manifestation strongly depends on the rotational forces, which in turn are fully controlled by the dimensionless parameters *Ha, Re* and *Gr*.

The dimensionless flow variable distributions are controlled by the nondimensional parameters such that if, for example, *Re* is increased, comparatively smaller changes to the velocity field are required to generate sufficient inertial force to balance the buoyant force. In a similar way, Ha^2 controls the strength of the Lorentz force relative to other terms and *Gr* controls the strength of buoyant force as indicated by Eq. (28). It is also worth noting that in Eq. (31), for a given *Pr*, Re^{-1}

controls the strength of heat diffusion compared to heat advection. This makes sense in that fast-moving fluid will move heat faster by advection than by conduction. The consequence is that higher *Re* flows are likely to have thinner thermal boundary layers as the heat is swept quickly downstream before it can diffuse into the bulk. These are not new ideas, but they provide important context to the following analysis. The results reported below have been made dimensionless by dividing the flow variables by characteristic values (i.e. *U* for velocity and *b* for lengths). Temperatures are reported as dimensionless temperature increase $\theta = (\mathrm{T} - T_o)/\Delta T$.

6.3.A Downward Flows

6.3.A.i Effect of Reynolds number in downward flows

Five downward flow simulations were performed with *Ha*=220, *Gr*=1.44x10^8 and various Reynolds numbers ranging from 2027 to 20270. Some selected results are included in Figs. 35-37 to illustrate the effect of increasing *Re*. It can be seen that as *Re* increases, the flow regime shifts into purely forced convection MHD regime where the effect of the buoyant forces are negligible and the velocity profiles are symmetrical (Figs. 35, 37a). Obviously, at high enough *Re* there would be no differences between the upward and downward flows. While the lower *Re* flows feature prominent flow reversal in the heated region, the reverse flow is severely diminished at *Re*=10135 and nonexistent in the higher *Re* flows. At low Re, the hot wall temperature becomes very large (θ~0.6) compared to high Re cases (θ~.15) because the flow reversal present in the low *Re* cases recirculates hot fluid near the hot wall as a buffer between the wall and the incoming cold fluid. With the disappearance of the buoyant flow reversal, the temperature of the wall and the LM is significantly decreased as shown in Fig. 36 and Fig. 37b. However, further increase in *Re* decreases the temperature more slowly as also shown in the figures. Lastly, the flow is shown to be more stable as the *Re* increases and the buoyant effects become less influential.

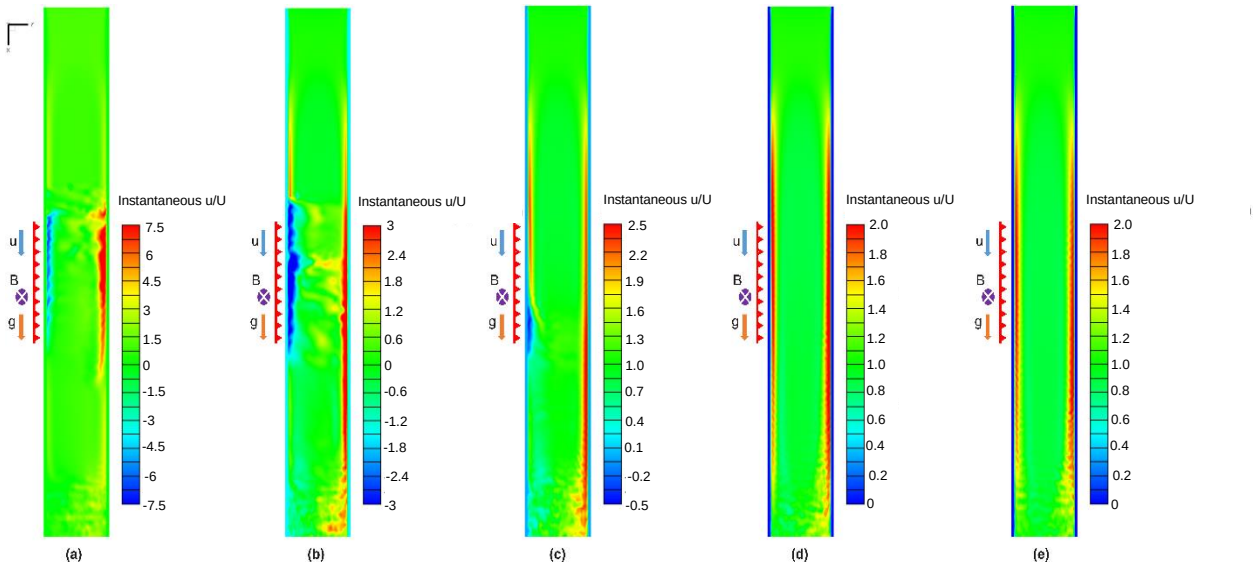

FIG. 35. Contours of instantaneous axial velocity on the y=0 center-plane for the case of downward flow at Ha = 220, Gr = 1.44x10^8 and c_w=0.12. (a) Re = 2027, (b) Re = 5067, (c) Re = 10135, (d) Re = 15201, and (e) Re = 20270. The z-axis is stretched relative to the x-axis by a factor of 5 to more easily show the entire flow domain.

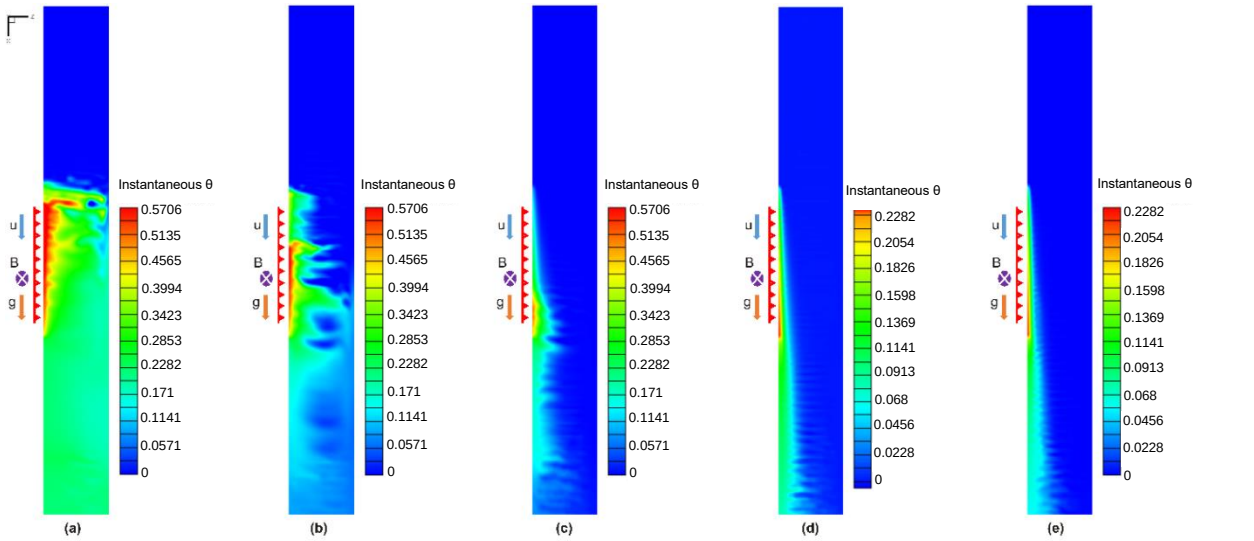

FIG. 36. Contours of instantaneous temperature on the y=0 center-plane for the case of downward flow at Ha = 220, Gr = 1.44x10^8 and c_w=0.12. (a) Re = 2027, (b) Re = 5067, (c) Re = 10135, (d) Re = 15201, and (e) Re = 20270. The z-axis is stretched relative to the x-axis by a factor of 5 to more easily show the entire flow domain.

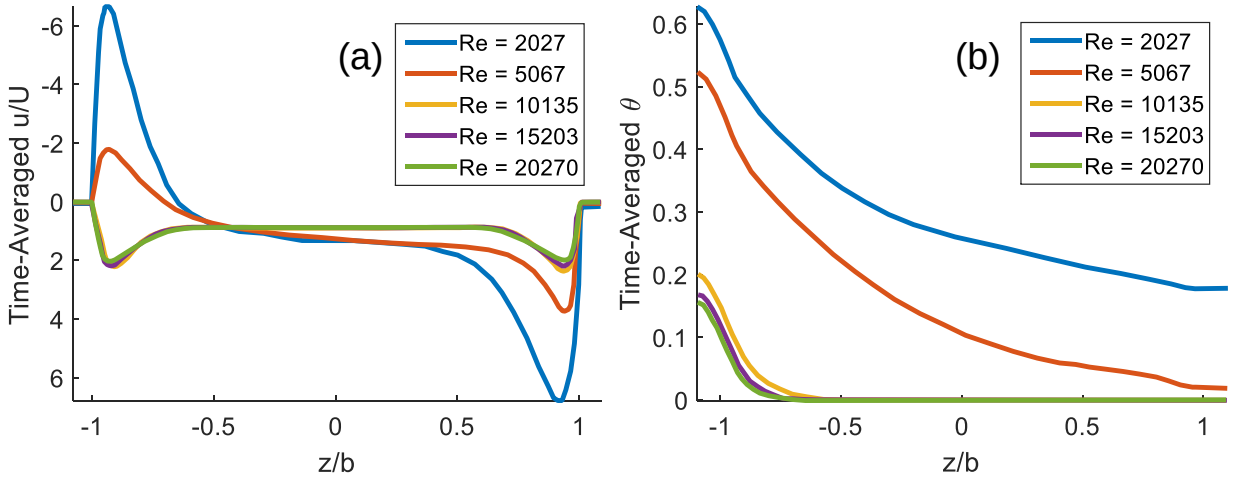

FIG. 37. Profiles of (a) time-averaged axial velocity, and (b) time-averaged temperature along the z-direction at x/b = -4.35 and y/b = 0 for Ha = 220, Gr = 1.44x10^8, c_w = 0.12, Re=2027 ,5067, 10135, 15203, and 20270, and downward flow.

6.3.A.ii Effect of Hartmann number in downward flows

Four downward flow simulations were performed with *Re*=2027, *Gr*=1.44x10^8 and various Hartmann numbers ranging from 110 to 880. Some selected results are included in Figs. 38-40 to illustrate the effect of increasing *Ha*. It can be seen that as *Ha* increases, the strength of the reverse flow decreases slightly, despite the growing strength of buoyant forces. The temperature difference between the cold and hot walls also increases with *Ha*. This effect is a consequence of the improved stability of the flow afforded by stronger electromagnetic effects. Vortices which would transport heat away from the hot wall are damped by the increased Joule dissipation. More simply, there are two competing mechanisms related to the effect of *Ha* on the temperature field in the liquid near the heated wall: one is reduction of the peak velocity in the reverse flow near the hot wall as *Ha* is increased (this is supposed to reduce the temperature), the other one is reduction of the transverse heat transport associated with Q2D turbulence (this is supposed to increase the temperature), which also happens at higher *Ha*. It appears that that the latter is stronger so that higher wall temperatures occur at higher *Ha* as seen in Fig. 40b. It can be observed that the jets attached to the sidewalls become thinner as electromagnetic force steadily becomes more influential compared to viscous and buoyant forces in shaping the velocity profile.

At *Ha*=110, the velocity profile does not feature thin jets attached to the wall because the MHD effects are overshadowed by comparatively larger natural convection effects.

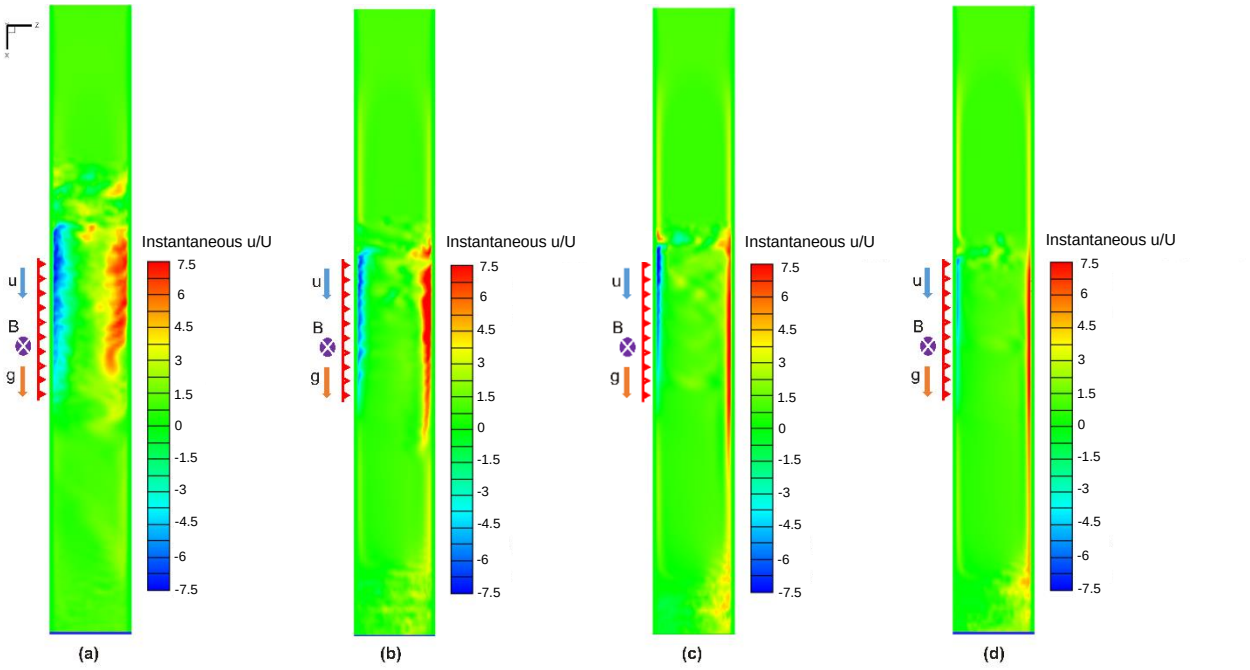

FIG. 38. Contours of instantaneous axial velocity on the y=0 center-plane for the case of downward flow at Re = 2027, Gr = 1.44x10^8 and c_w = 0.12. (a) Ha = 110, (b) Ha = 220, (c) Ha = 440, (d) Ha = 880. The z-axis is stretched relative to the x-axis by a factor of 5 to more easily show the entire flow domain.

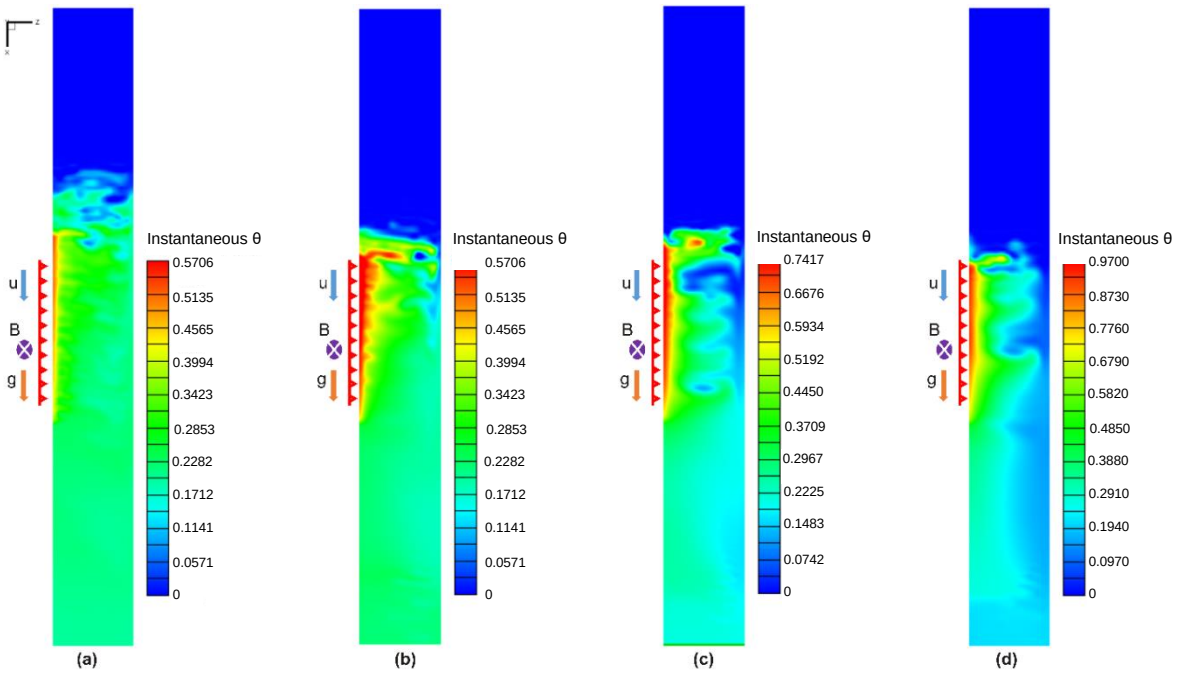

FIG. 39. Contours of instantaneous temperature on the y=0 center-plane for the case of downward flow at Re = 2027, Gr = 1.44x10^8 and c_w = 0.12. (a) Ha = 110, (b) Ha = 220, (c) Ha = 440, (d) Ha = 880. The z-axis is stretched relative to the x-axis by a factor of 5 to more easily show the entire flow domain.

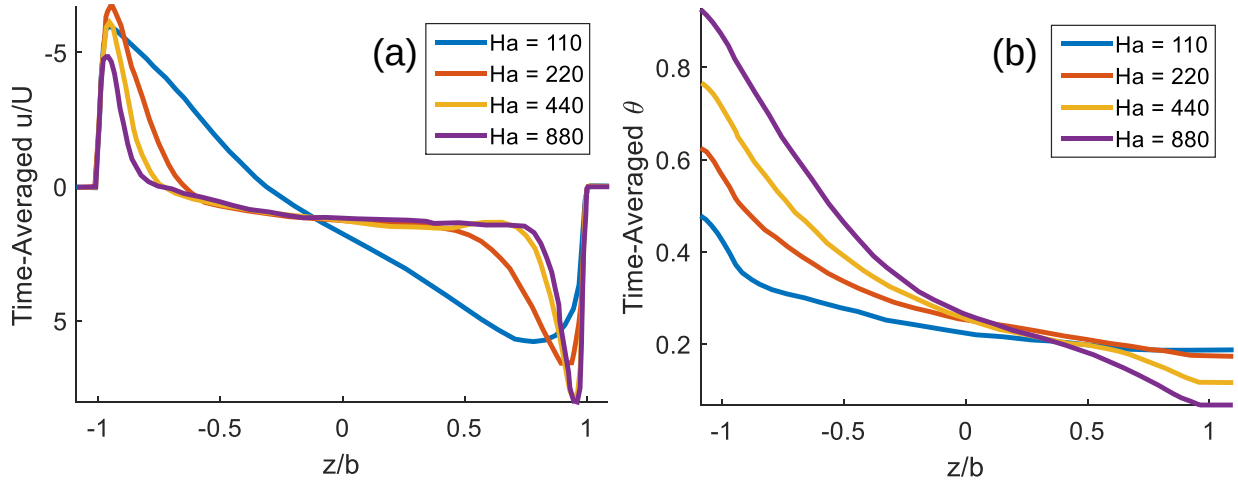

FIG. 40. Profiles of (a) time-averaged axial velocity, and (b) time-averaged temperature along the z-direction at x/b = -4.35 and y/b = 0 for Re = 2027, Gr = 1.44x10^8 and c_w = 0.12. Ha = 110, 220, 440, and 880.

6.3.A.iii Effect of Grashof number in downward flows

Two downward flow simulations were performed with *Ha*=220, *Re*=2027, and two Grashof numbers, 1.44x10^8 and 3.6x10^8. Some selected results are included in Figs. 41-42 to illustrate the effect of increasing *Gr*. As *Gr* increases, the buoyant effects grow. In the case of *Gr*=3.6x10^8,

the reverse flow is comparatively larger than in the case of Gr=1.4x10^8 and buoyant pockets of warm fluid even travel upstream of the heated region. By increasing Gr by a factor of 2.5, the dimensionless temperature increase θ of the hot wall measured at x/b=-4.35 (Fig. 42b) decreases by 0.14. This decrease can be explained by the decreased stability at higher Gr. As heat is advected away from the hot wall by vortices more strongly, the dimensionless temperature near the wall decreases despite having stronger flow reversal.

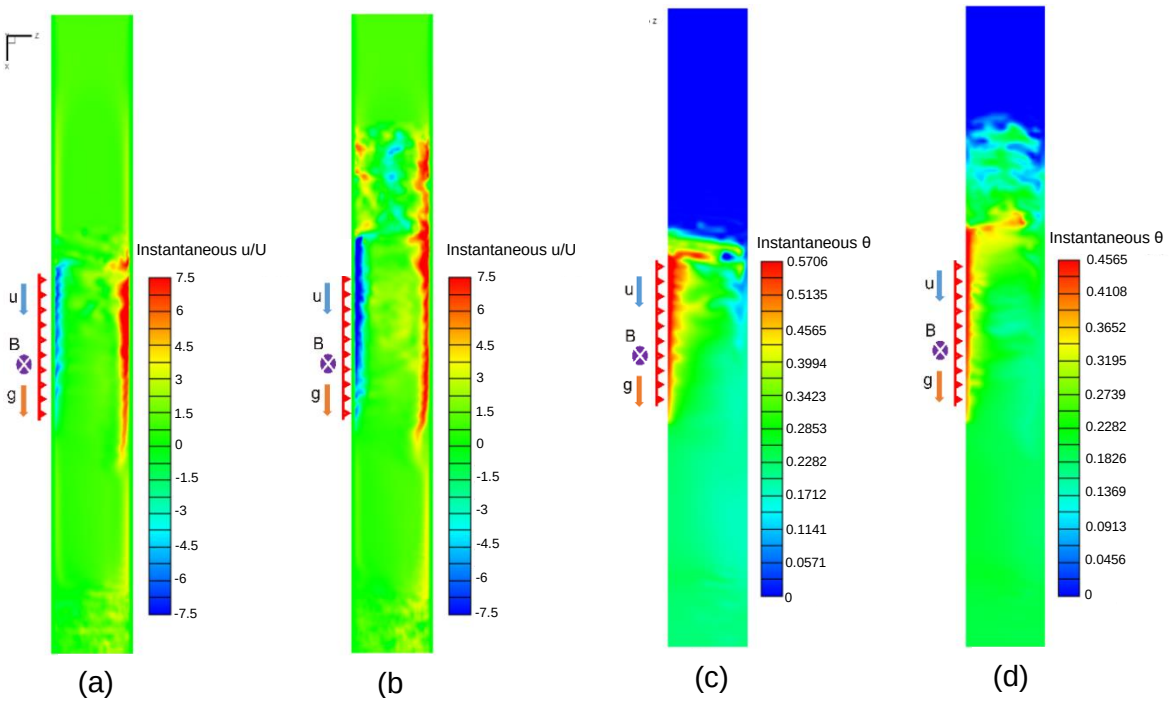

FIG. 41. Results of the numerical simulations performed at Ha = 220, Re = 2027, and c_w = 0.12 for downward flow. (a, c) Gr = 1.44x10^8, (b, d) Gr = 3.6x10^8. Contours on the y=0 center-plane are plotted for (a, b) instantaneous streamwise velocity, and (c, d) instantaneous temperature. The z-axis is stretched relative to the x-axis by a factor of 5 to more easily show the entire flow domain.

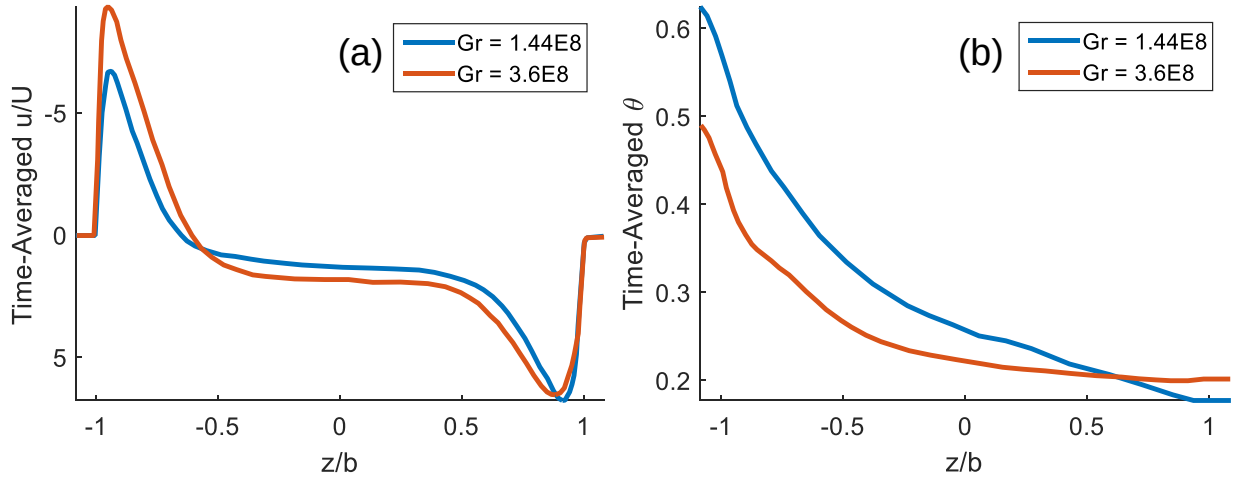

FIG. 42. Profiles of (a) time-averaged axial velocity, and (b) time-averaged temperature along the z-direction at x/b = -4.35 and y/b = 0 for Ha = 220, Re = 2027, and c_w = 0.12 for downward flow. Gr = 1.44x10^8, 3.6x10^8.

6.3.B Upward Flows

6.3.B.i Effect of Reynolds number in upward flows

Five upward flow simulations were performed with *Ha* = 220, *Gr* = 1.44x10^8 and various Reynolds numbers ranging from 2027 to 20270. Some selected results are included in Figs. 43-45 to illustrate the effect of increasing *Re*. The conclusions which can be drawn from these results are the same as in the downward flow case except that the non-existence of flow reversal makes the effect of increasing *Re* clearer and simpler. The most prominent effect of buoyancy here is the asymmetry of the velocity profiles: the hot wall features forward flow jets which are faster than the jets on the cold wall. As *Re* grows, this asymmetry fades until the jets have the same velocity and the regime is MHD forced flow rather than MHD mixed convection flow. Fig. 45b confirms that increasing *Re* decreases both the thermal boundary layer thickness and the maximum temperature by consequence of increased advection. Additionally, higher *Re* means inertial force can balance buoyant forces with smaller adjustments to the dimensionless velocity field and the combined result of these effects is a rapid departure from the MHD mixed convection regime.

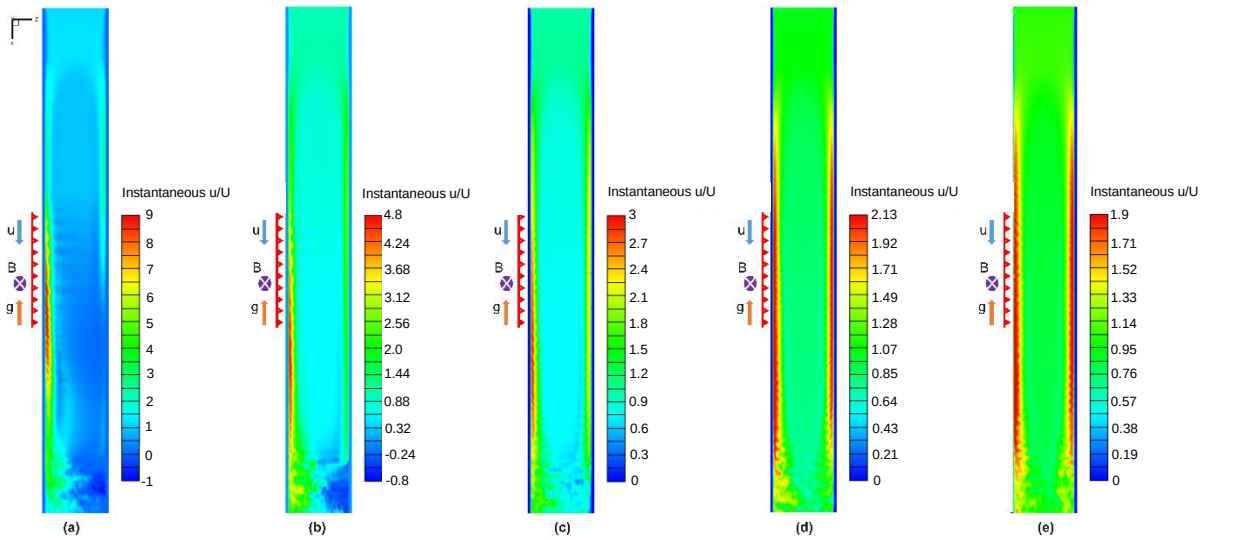

FIG. 43. Contours of instantaneous axial velocity along the y=0 center-plane for the case of upward flow at Ha = 220, Gr = 1.44x10^8 and c_w = 0.12. (a) Re = 2027, (b) Re = 5067, (c) Re = 10135, (d) Re = 15201, and (e) Re = 20270. The z-axis is stretched relative to the x-axis by a factor of 5 to more easily show the entire flow domain.

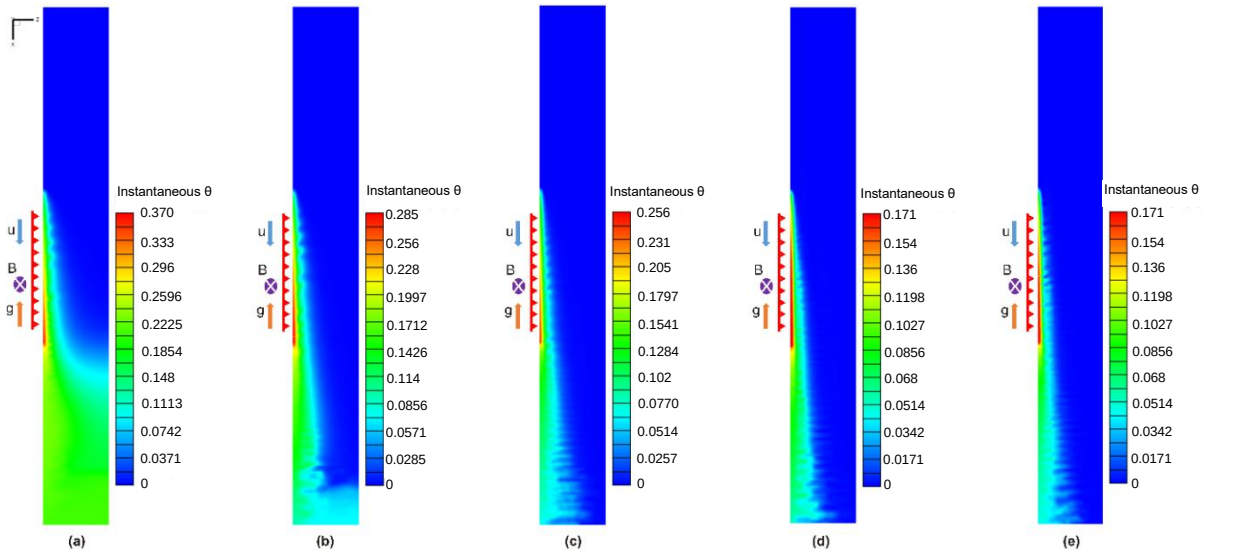

FIG. 44. Contours of instantaneous temperature on the y=0 center-plane for the case of upward flow at Ha = 220, Gr = 1.44x10^8 and c_w = 0.12. (a) Re = 2027, (b) Re = 5067, (c) Re = 10135, (d) Re = 15201, and (e) Re = 20270. The z-axis is stretched relative to the x-axis by a factor of 5 to more easily show the entire flow domain.

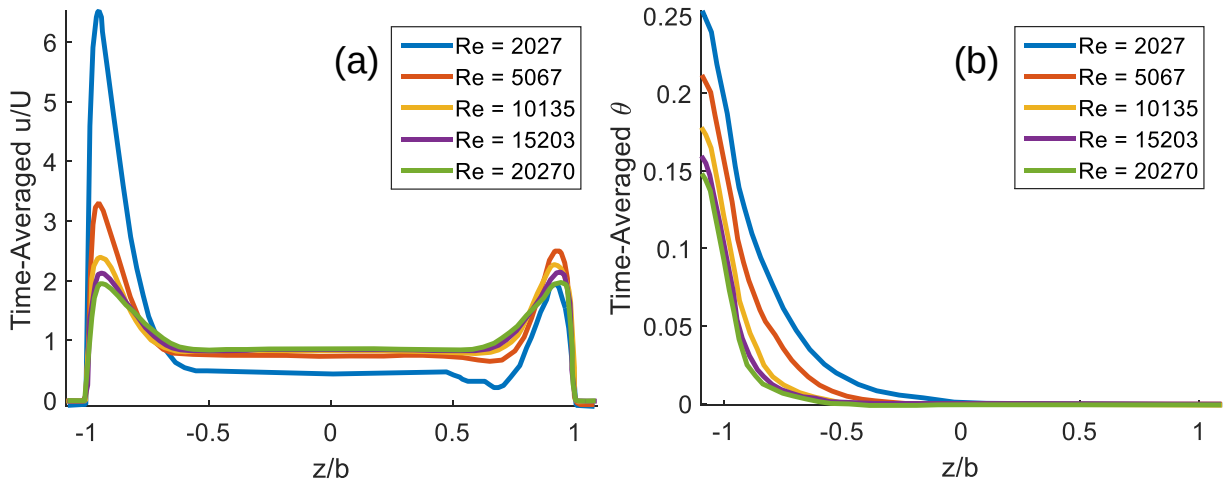

FIG. 45. Profiles of (a) time-averaged axial velocity, and (b) time-averaged temperature along the z-direction at x/b = -4.35 and y/b = 0. Ha = 220, Gr = 1.44x10^8 and c_w = 0.12. Re=2027, 5067, 10135, 15203, and 20270.

6.3.B.ii Effect of Hartmann number in upward flows

Three upward flow simulations were performed with *Re*=2027, *Gr*=1.44x10^8 and various Hartmann numbers ranging from 110 to 880. Some selected results are included in Figs. 46-48 to illustrate the effect of increasing *Ha.* As in the downward flows, the effect of increasing *Ha* is mainly to improve the stability of the flow. The consequence of this is larger maximum temperatures at the hot wall. Additionally, as *Ha* increases, the jets attached to the sidewalls become thinner and the bulk flow becomes more uniform due to increased MHD effect.

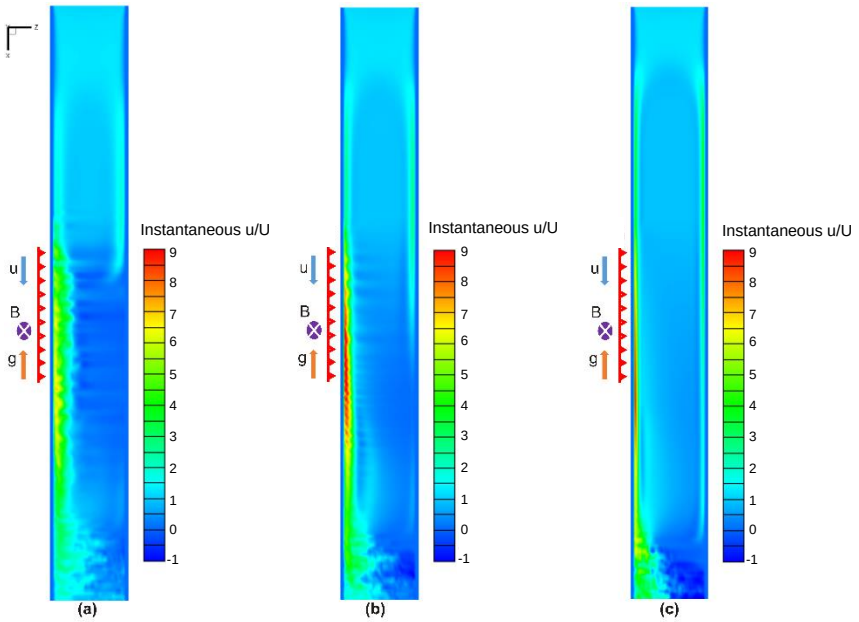

FIG. 46. Contours of instantaneous axial velocity on the y=0 center-plane for the case of upward flow at Re = 2027, Gr = 1.44x10^8 and c_w = 0.12. (a) Ha = 110, (b) Ha = 220, (c) Ha = 880. The z-axis is stretched relative to the x-axis by a factor of 5 to more easily show the entire flow domain.

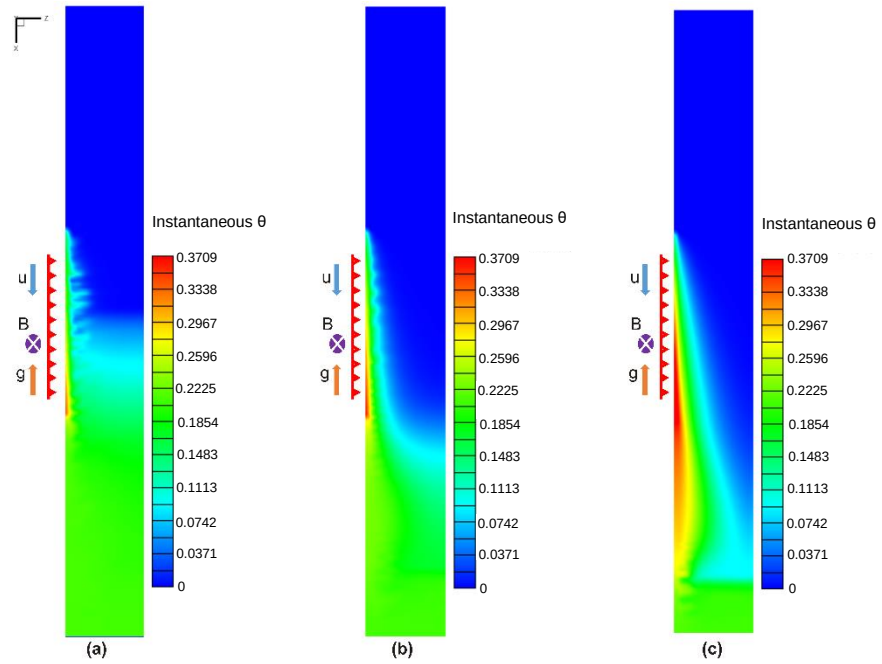

FIG. 47. Contours of instantaneous temperature on the y=0 center-plane for the case of upward flow at Re = 2027, Gr = 1.44x10^8 and c_w = 0.12. (a) Ha = 110, (b) Ha = 220, (c) Ha = 880. The z-axis is stretched relative to the x-axis by a factor of 5 to more easily show the entire flow domain.

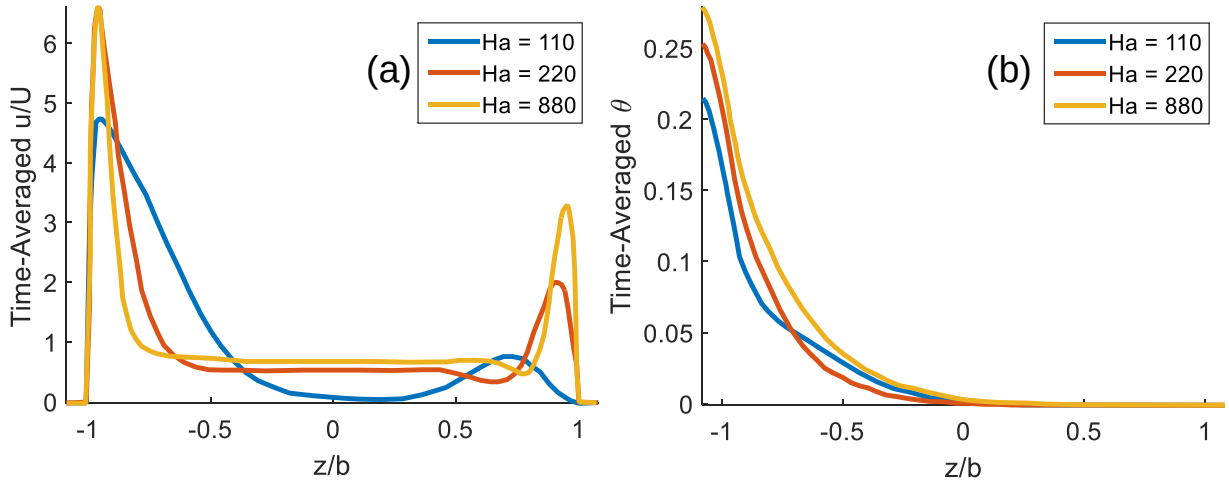

FIG. 48. Profiles of (a) time-averaged axial velocity, and (b) time-averaged temperature along the z-direction at x/b = -4.35 and y/b = 0 for Ha = 220, Re = 2027, and c_w = 0.12 for upward flow. Ha = 110, 220, and 880.

6.3.B.iii Effect of Grashof number in upward flows

Two upward flow simulations were performed with *Ha*=220, *Re*=2027, and two Grashof numbers, 1.44×10^8 and 3.6×10^8. Some selected results are included in Figs. 49-50 to illustrate the effect of increasing *Gr*. The increased buoyant effects from increasing *Gr* are similar to the effects seen in downward flows, though they are simpler. In the case of $Gr=3.6 \times 10^8$, flow instabilities grow more quickly than in the case of $Gr=1.44 \times 10^8$ as demonstrated by the faster growth of the thermal boundary layer which, due to advection by large vortices which recirculate flow in the bulk, is smeared across the thickness of the duct all at once. As in the downward cases, increasing *Gr* causes the dimensionless temperature to decrease at the hot wall.

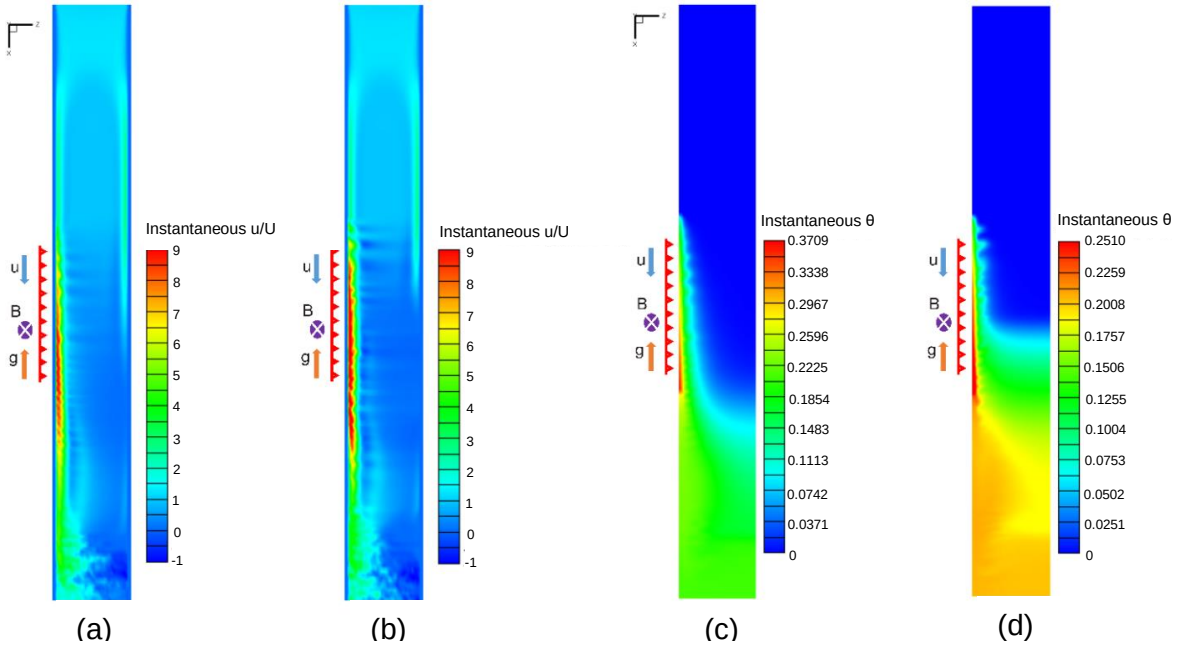

FIG. 49. Results of the numerical simulations performed at Ha = 220, Re = 2027, and c_w = 0.12 for downward flow. (a, c) Gr = 1.44x10^8, (b, d) Gr = 3.6x10^8. Contours on the y=0 center-plane are plotted for (a, b) instantaneous streamwise velocity, and (c, d) instantaneous temperature. The z-axis is stretched relative to the x-axis by a factor of 5 to more easily show the entire flow domain.

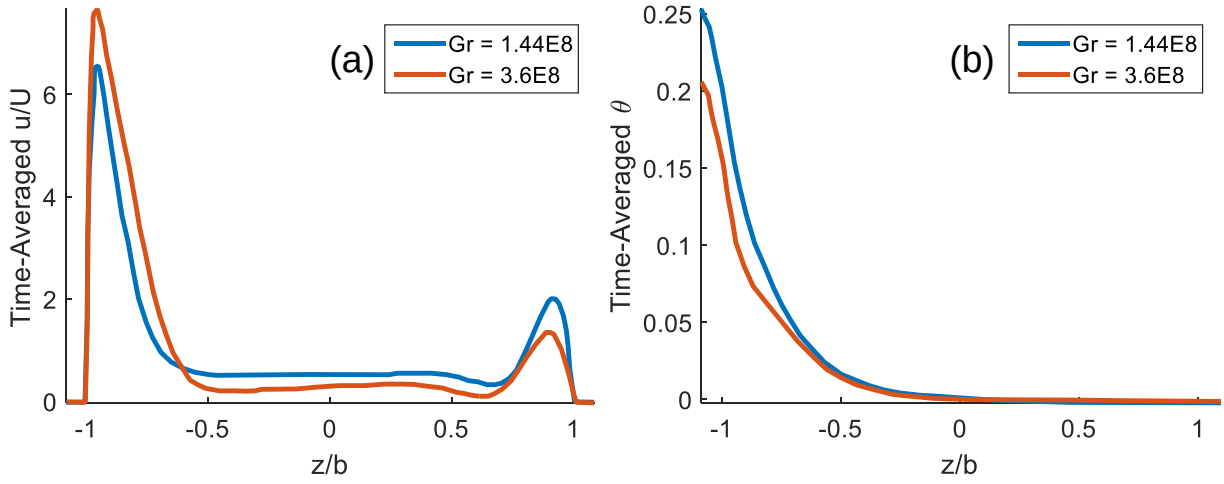

FIG. 50. Profiles of (a) time-averaged axial velocity, and (b) time-averaged temperature along the z-direction at x/b = -4.35 and y/b = 0 for Ha = 220, Re = 2027, and c_w = 0.12 for upward flow. Gr = 1.44x10^8, 3.6x10^8.

6.4 Balance of X-direction Forces

To provide a deeper understanding of the physics and phenomena of MHD mixed convection flows, the results of four simulations with surface heating q_o''=0.20 MW/m^2, B_o=0.5 T, U=0.02 m/s, and ΔT=350.5^{o}C (Ha=220, Re=2027, Gr=1.44x10^8), both electrically conducting (c_w=0.12) and nonconducting walls (c_w~0), and both upwards and downwards flow orientations are presented and discussed. The discussion focuses primarily on the pressure distribution and the x-direction forces which shape it, including electromagnetic (EM) Lorentz force, buoyant force, and hydrodynamic forces which include viscosity and inertia. At every point and time in the simulations, the pressure gradients in each direction are perfectly balanced with the sum of all the forces listed here. Often, the sum of forces is dominated by one force which is much larger than the others. For instance, in fully developed MHD flows with N, Ha>>1, EM force alone balances the axial pressure gradient in the bulk region while hydrodynamic forces are negligible everywhere except for special layers attached to the walls. It will be shown that no such simplifications are applicable in the present cases due to the unsteady nature of mixed convection flows, despite the MHD effects.

This discussion begins with the pressure distribution. The pressure distributions for the four cases are plotted together in Fig. 51. For each case, the pressure is plotted along the axis of the duct, x, on the y=0 center-plane for 5 values of z to span the thickness of the flow domain.

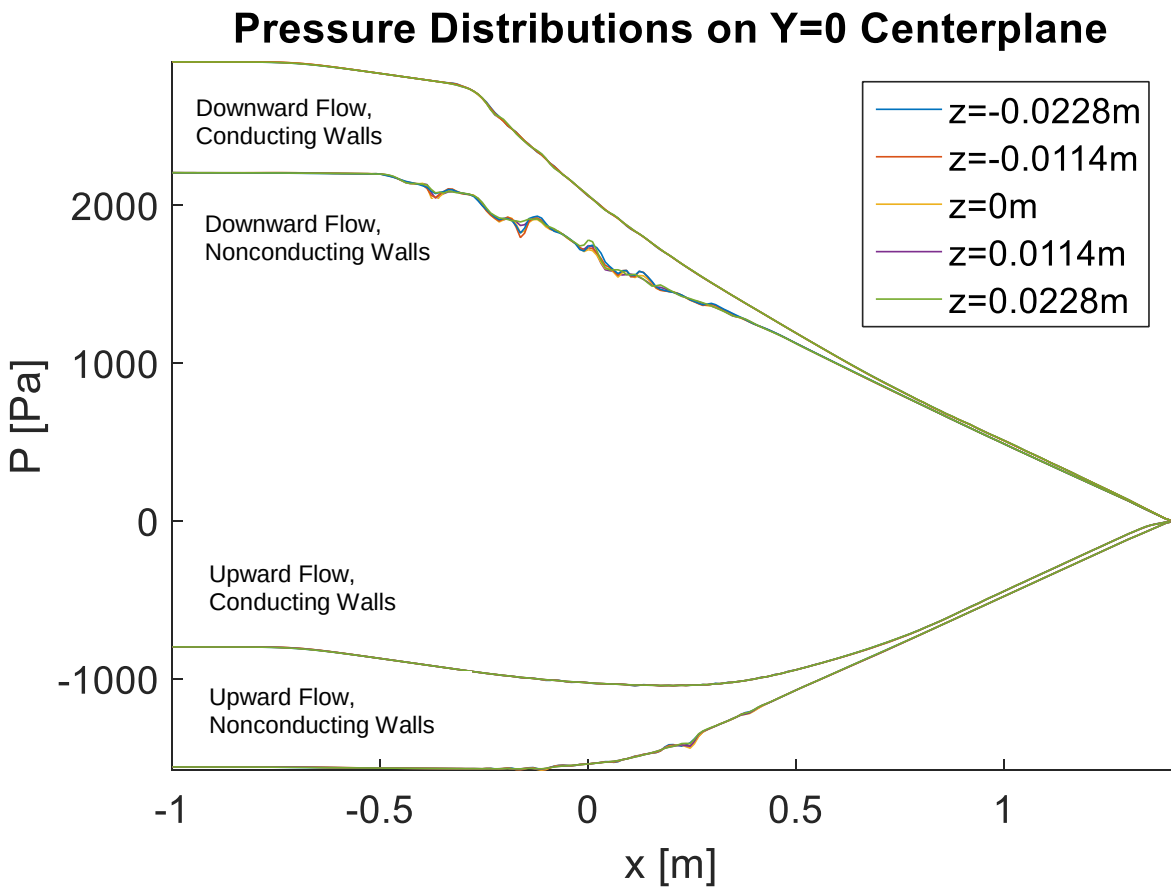

FIG. 51. Instantaneous pressure at y=0 for 5 values of z is plotted along the x-axis for each of 4 cases with surface heating and variable flow orientation (upwards or downwards) and wall conductivity (c_w=0.12 or ~0). q_o''=0.20 MW/m^2, B_o=0.5 T, U=0.02 m/s, and ΔT=350.5^{o}C (Ha=220, Re=2027, Gr=1.44x10^8).

With the exception of the downward flow case with nonconducting walls, the variation of pressure along the z-direction are so small compared to the variations along x that the five spatially distributed curves seem to be one. The differences between cases, by contrast, are large enough that the four collections of curves are quite distinct from one another, though the outlet boundary condition specifies that they all end with p=0. There are only small deviations from the mean pressure distribution so the pressure field essentially balances the mean distribution of the sum of other axial forces. In the following analysis, the axial forces which shape the pressure distribution are investigated.

To begin, the mean axial buoyant force is integrated along the axis of the duct and compared to the pressure distribution (Fig. 52). For the present simulations, the majority of the pressure drop is shown to come from buoyancy, though there is still a significant portion of pressure loss which is unaccounted for in cases with conducting walls. For cases with nonconducting walls, the integrated buoyant force is shown to account for all but a tiny fraction of the pressure drop which is easily accounted for by viscous drag.

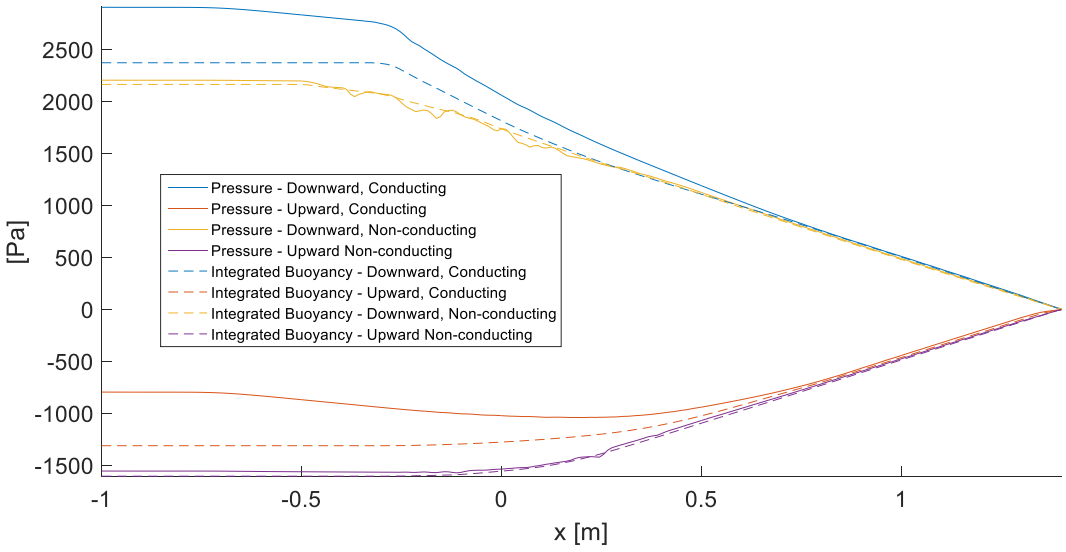

FIG. 52. The instantaneous mean pressure of each fluid cross-section is plotted along x for each of 4 cases with surface heating and variable flow orientation (upwards or downwards) and wall conductivity (c_w=0.12 or ~0). q_o''=0.20 MW/m^2, B_o=0.5 T, U=0.02 m/s, and ΔT=350.5^{o}C (Ha=220, Re=2027, Gr=1.44x10^8). The integraded buoyant force is also plotted for each case. Here, "integrated buoyancy" refers to the integral from 1.4m to x of the instantaneous bouyancy force, $-\rho g\beta(T-T_o)$, averaged on fluid cross-section. g>0 for downward flows and g<0 for upward flows.

In Fig. 53, the remaining pressure losses (excluding some small viscous drag) in the cases with conducting walls are accounted for by adding the integral of the mean EM force to the integral of mean buoyant force. EM force is expected to account for the losses because, in conducting wall cases, electric currents reconnect through the walls such that the current in the fluid nets EM force which opposes the flow. By contrast, the net EM force is zero in cases with nonconducting walls because the currents must close entirely in the fluid, leading to an equal quantity of EM forces which aid and oppose the flow.

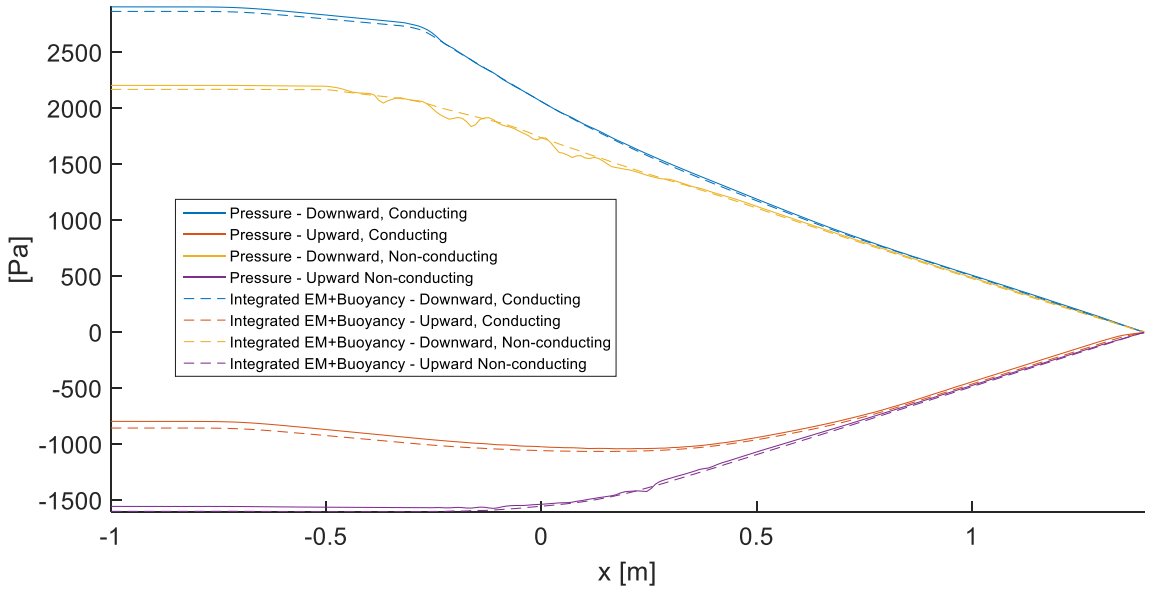

FIG. 53. The instantaneous mean pressure of each fluid cross-section is plotted along x for each of 4 cases with surface heating and variable flow orientation (upwards or downwards) and wall conductivity (c_w=0.12 or ~0). q_o''=0.20 MW/m^2, B_o=0.5 T, U=0.02 m/s, and ΔT=350.5^{o}C (Ha=220, Re=2027, Gr=1.44x10^8). The integraded EM+buoyancy is also plotted for each case. Here, "integrated EM+Buoyancy" refers to the integral from 1.4m to x of the sum of the instantaneous bouyancy force and axial Lorentz force, $-\rho g\beta(T-T_o)-J_zB$, averaged on fluid cross-sections. g>0 for downward flows and g<0 for upward flows.

Interestingly, there are regions where strong mean inertial force causes temporary deviations between the curves in Fig. 53, most notably in the case of downward flow with nonconducting walls between x=-0.5 m and 0.2 m. It is also clear that viscous drag accounts for only a very small portion of the total pressure drop compared to buoyancy (and EM forces in the case of conducting walls). By subtracting the two sets of curves from one another (mean pressure and the sum of mean buoyant and EM forces), the portion of the mean pressure distribution which balances viscous and inertial forces is revealed more clearly (Fig. 54). Interestingly, the temporary pressure drops of the downward cases coincide with the separation of the boundary layer and the pressure recovers when the boundary layer reattaches to the sidewall.

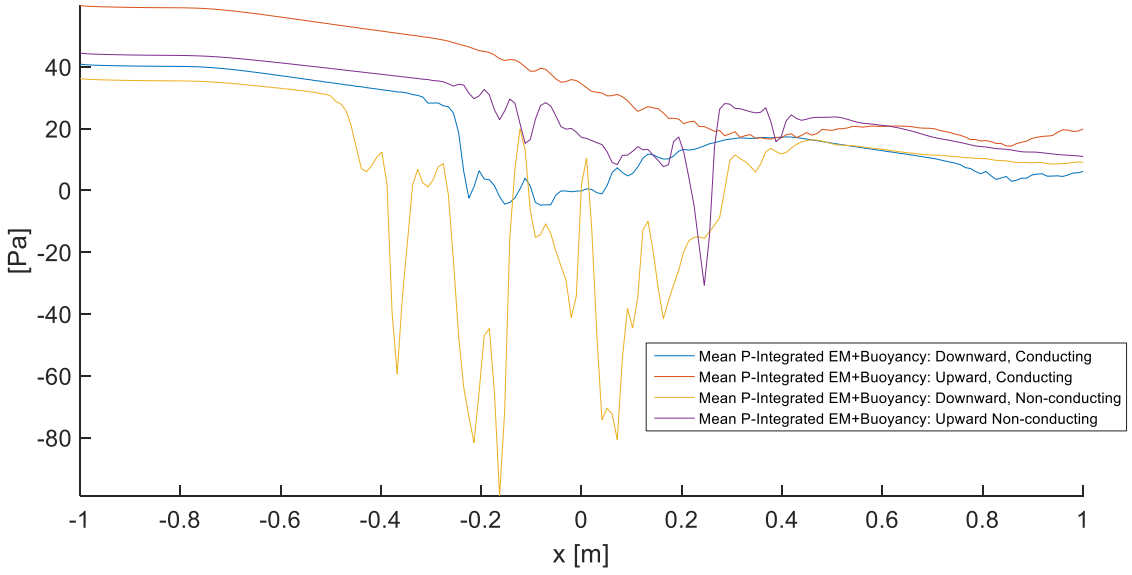

FIG. 54. The contribution of hydrodynamic forces to the mean pressure distribution is plotted for each of 4 cases with surface heating and variable flow orientation (upwards or downwards) and wall conductivity (c_w=0.12 or ~0). q_o"=0.20 MW/m^2, B_o=0.5 T, U=0.02 m/s, and ΔT=350.5^{o}C (Ha=220, Re=2027, Gr=1.44x10^8). This contribution is the difference between the instantaneous mean pressure of each fluid cross-section and the sum of integrated EM+Buoyancy forces. Here, "integrated EM+Buoyancy" refers to the integral from 1.4m to x of the sum of the instantaneous bouyancy force and axial Lorentz force, $-\rho g\beta(T-T_o)-J_zB$, averaged on fluid cross-sections. g>0 for downward flows and g<0 for upward flows.

The mean pressure accounted for by hydrodynamic forces steadily decreases along the axial direction due to viscous losses to the walls. The larger temporary pressure losses are inertial – the pressure drops sharply as the kinetic energy of the fluid increases, and the pressure recovers when the kinetic energy decreases as the fluid stabilizes. While these temporary drops are small compared to the total pressure drop across the duct, it cannot be said that inertial forces are unimportant to the behavior of the flow as these forces are dominant in small regions and account for the largest pressure gradients in the flow. This point is illustrated in Figs. 55-58 where the mean pressure gradients are plotted along with mean buoyant force, mean EM force, and mean hydrodynamic forces. Below, the mean force distributions along the axis of the duct are discussed case by case.

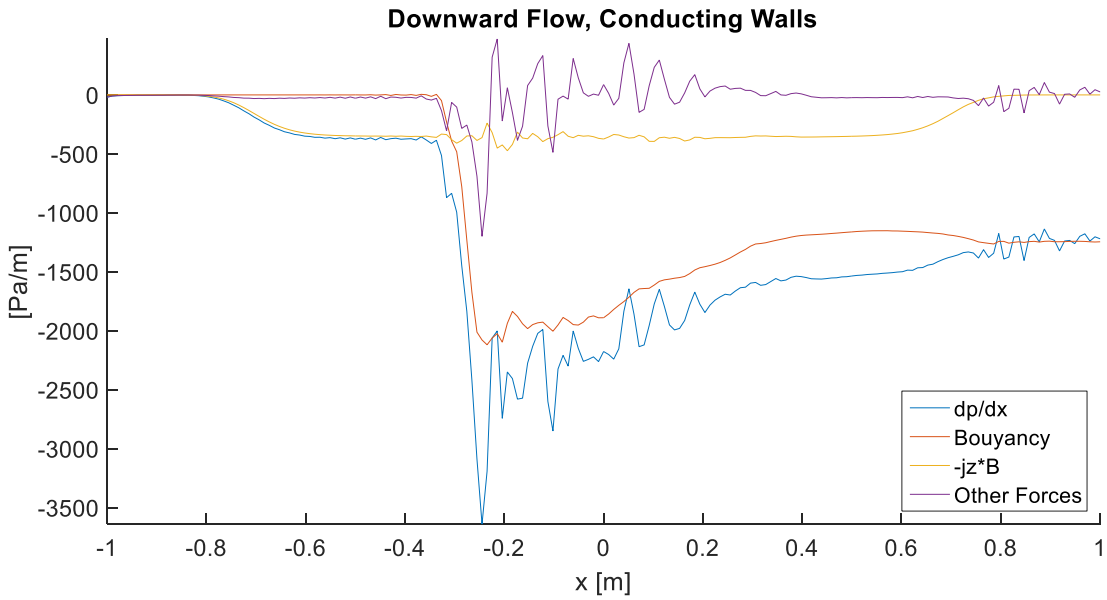

FIG. 55. The instantaneous mean pressure gradient of each fluid cross-section is plotted along with the instantaneous mean values of buoyant force, axial Lorentz force, and the sum of axial hydrodynamic forces on each fluid cross-section. q_o"=0.20 MW/m^2, B_o=0.5 T, U=0.02 m/s, and ΔT=350.5^{o}C (Ha=220, Re=2027, Gr=1.44x10^8). c_w=0.12, downward flow with surface heating.

In the case of downward flow with conducting walls, hydrodynamic forces are on average the weakest of the forces except for a few places where they briefly exceed the net electromagnetic force, most notably where the boundary layer separates near the beginning of the heated region. Buoyant force is by far the strongest force inside the heated region. This case has the highest mean temperature as it features a reverse flow bubble attached to the hot sidewall and it is more stable than the nonconducting downward flow.

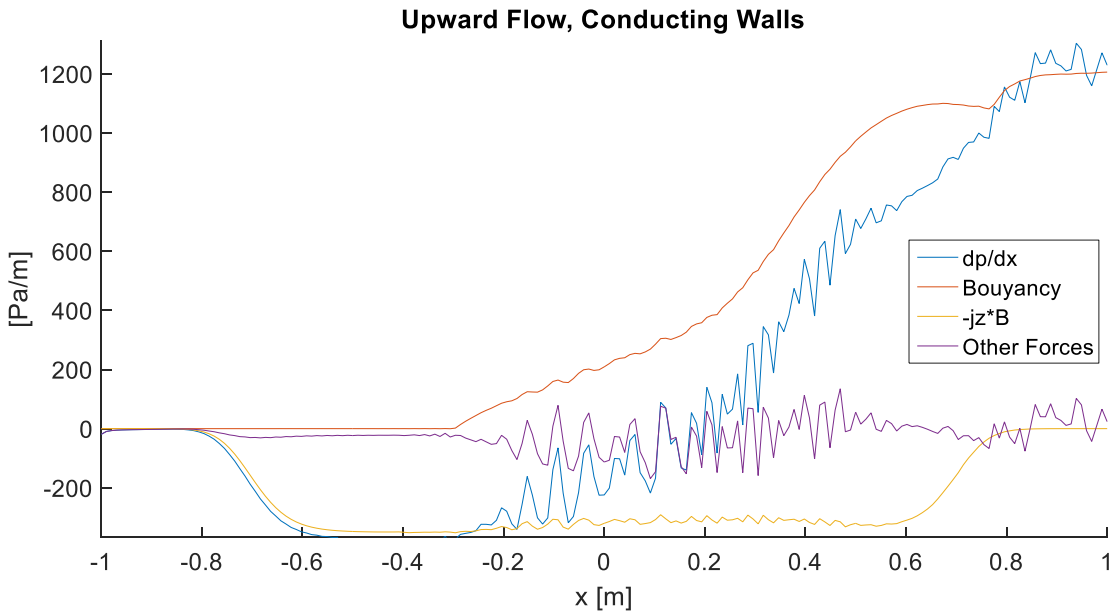

FIG. 56. The instantaneous mean pressure gradient of each fluid cross-section is plotted along with the instantaneous mean values of buoyant force, axial Lorentz force, and the sum of axial hydrodynamic forces on each fluid cross-section. q_o"=0.20 MW/m^2, B_o=0.5 T, U=0.02 m/s, and ΔT=350.5^{o}C (Ha=220, Re=2027, Gr=1.44x10^8). c_w=0.12, upward flow with surface heating.

Since the upward flow case with conducting walls is the most stable case, the mean hydrodynamic forces are smallest. The mean electromagnetic force dominates the mean force balance until near the end of the heated region where buoyancy becomes the largest contributor to the pressure drop.

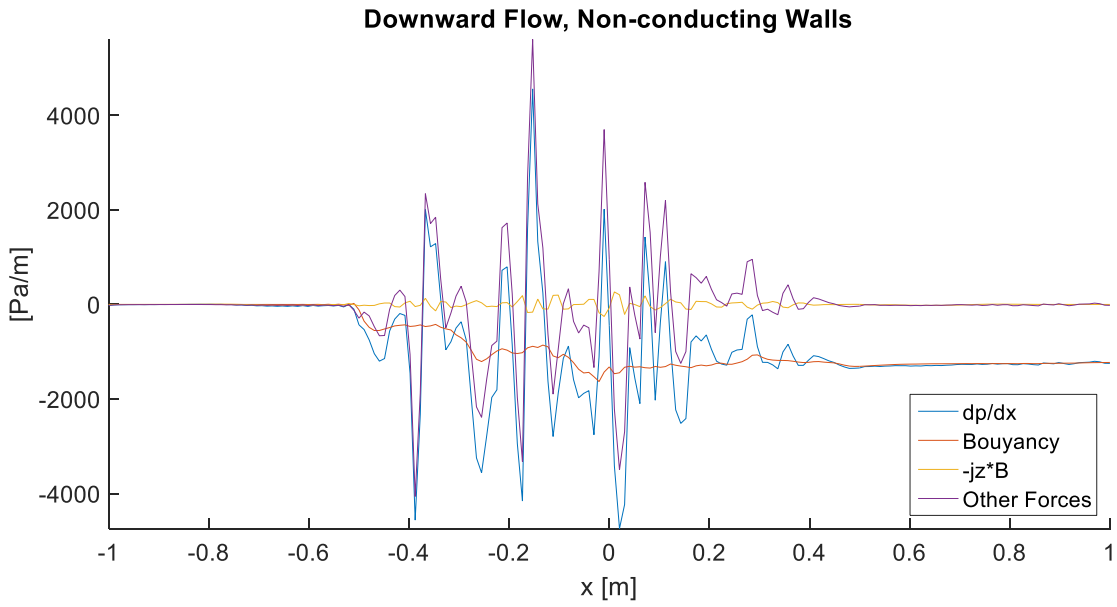

FIG. 57. The instantaneous mean pressure gradient of each fluid cross-section is plotted along with the instantaneous mean values of buoyant force, axial Lorentz force, and the sum of axial hydrodynamic forces on each fluid cross-section. q_o"=0.20 MW/m^2, B_o=0.5 T, U=0.02 m/s, and ΔT=350.5^{o}C (Ha=220, Re=2027, Gr=1.44x10^8). c_w~0, downward flow with surface heating.

The downward case with nonconducting walls is the most unstable case as it has less Joule dissipation than the conducting wall case to stabilize the flow and because the buoyancy opposing the flow tends to destabilize it similarly to adverse pressure gradients in other flows. This highly unsteady flow has the largest hydrodynamic forces of the four cases and the mean hydrodynamic forces are shown to have the largest magnitude of the mean forces. The mean EM force is interesting here because it oscillates about zero, indicating that axial currents exist. After all, if the current were strictly 2D, then the mean EM force in this case would be zero throughout the axis of the duct. Interestingly, local minima in mean EM force often correspond to local maxima in mean buoyancy and *vise versa* (e.g. at x=0 m). This implies that mean buoyancy is partially balanced by mean EM force by virtue of axial currents which redistribute the EM force. This effect is somewhat masked by the even larger hydrodynamic forces in this case.

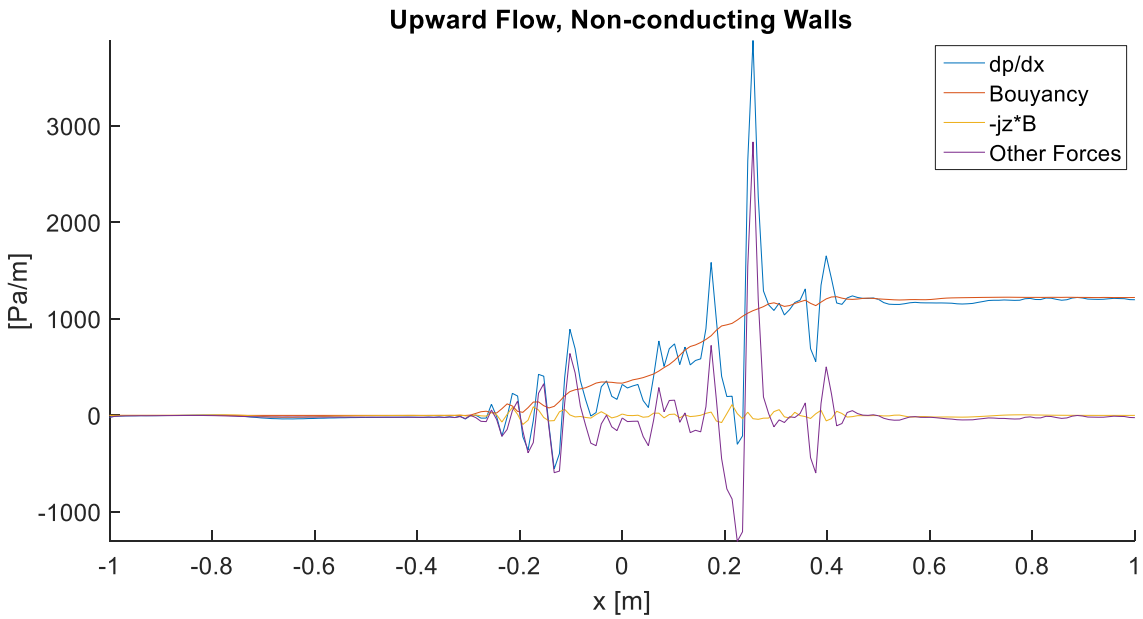

FIG. 58. The instantaneous mean pressure gradient of each fluid cross-section is plotted along with the instantaneous mean values of buoyant force, axial Lorentz force, and the sum of axial hydrodynamic forces on each fluid cross-section. q_o"=0.20 MW/m^2, B_o=0.5 T, U=0.02 m/s, and ΔT=350.5^{o}C (Ha=220, Re=2027, Gr=1.44x10^8). c_w~0, downward flow with surface heating.

In the case of upward flow with nonconducting walls, an interesting instability occurs at the beginning of the heated region which causes the mean x-direction forces to oscillate. As the instability grows, the mean hydrodynamic forces grow to dominate the force balance, reaching a maximum magnitude around x=-0.1 m before the mean hydrodynamic forces abruptly diminish and mean buoyancy becomes the largest force. This instability is very interesting as it is shaped by the combined effect of EM, buoyant, and hydrodynamic forces. A large vortex situated near the end of the heated region (x~0.25 m) brings with it a temporary dominance of mean hydrodynamic forces. A smaller vortex can be seen downstream (x~0.38 m) to provide the same effect but much diminished. As in the other case with nonconducting walls, the oscillations of mean EM force are indicative of axial electric currents.

So far, the force balance has been discussed with respect to the mean values to show the relationship between the mean forces and the pressure distribution. However, the wealth of phenomenon these cases offer stems mostly from how anisotropic the flows are, particularly along

the z-direction due to steep z-direction temperature gradients and the tendency for EM forces to damp velocity gradients along the y-direction. The axial pressure gradients are not able to balance the entire buoyant force distribution because the buoyancy has nonzero curl and pressure gradients are curl-free by definition. So, while the mean buoyant force can be absorbed by the pressure, other forces must arise to balance the deviations from the mean.

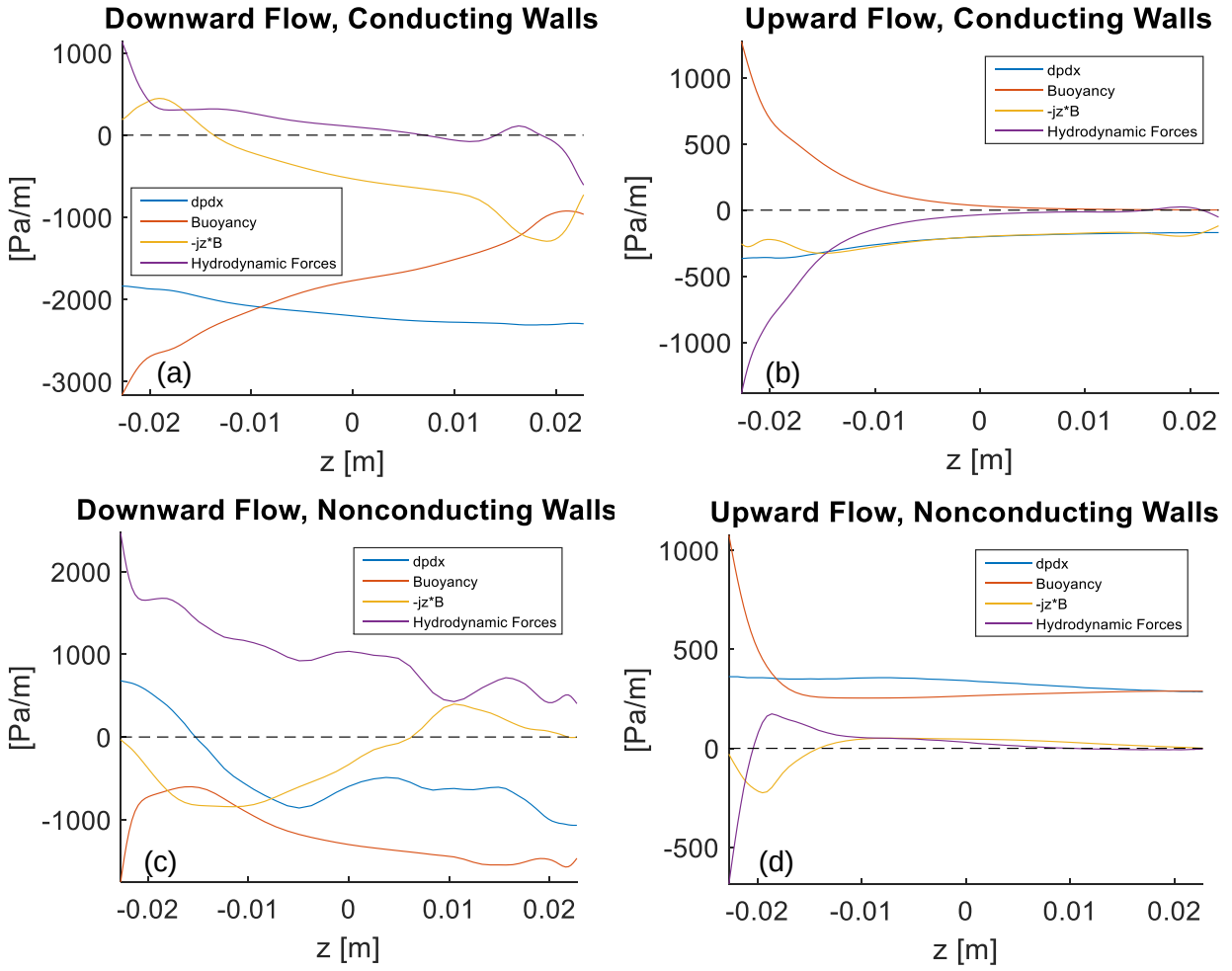

FIG. 59. The instantaneous pressure gradient is plotted along with instantaneous values of buoyant force, axial Lorentz force, and the sum of axial hydrodynamic forces at y=0m, x=0m. q_o"=0.20 MW/m^2, B_o=0.5 T, U=0.02 m/s, and ΔT=350.5^{o}C (Ha=220, Re=2027, Gr=1.44x10^8), surface heating only, (a, c) downward flow, (b, d) upward flow, (a, b) c_w=0.12, (c, d) c_w~0.

The x-direction forces are plotted at x=0 m, y=0 m, for each of the cases in Fig. 59a-d to show how the buoyant force is not entirely balanced by the pressure gradient. From the figures, it is clear that generally, hydrodynamic forces cannot be neglected outside of boundary layers as is

commonly assumed in MHD flows with *Ha*, *N*>>1 (here *Ha*=220 and *N*~20). It is also worth pointing out that while the hydrodynamic forces are not confined to thin layers attached to the walls, they do tend to be larger near the walls where viscous boundary layers form.

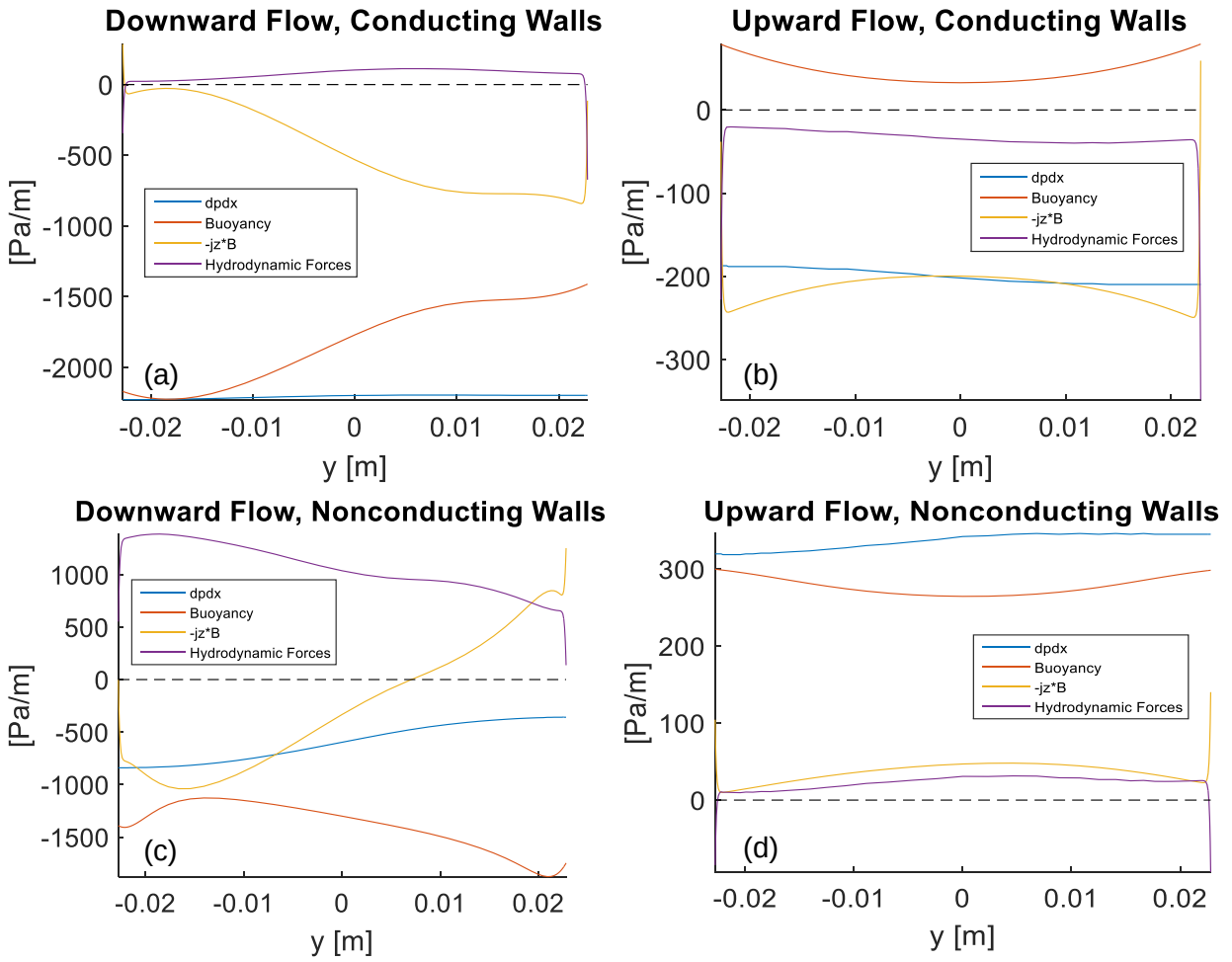

FIG. 60. The instantaneous pressure gradient is plotted along with instantaneous values of buoyant force, axial Lorentz force, and the sum of axial hydrodynamic forces at z=0 m, x=0 m. q_o''=0.20 MW/m^2, B_o=0.5 T, U=0.02 m/s, and ΔT=350.5^{o}C (Ha=220, Re=2027, Gr=1.44x10^8), surface heating only, (a, c) downward flow, (b, d) upward flow, (a, b) c_w=0.12, (c, d) c_w~0.

The x-direction forces are plotted at x=0 m, z=0 m in Figs. 60a-d to show how forces vary along the y-axis. The traditional assumption that for large N, the flow becomes quasi-two-dimensional (Q2D) is perhaps not justifiable in the downward cases which feature large variations in forces along the y-axis. This topic of evaluating whether or not these flows are Q2D is discussed in section 6.5. Lastly, it is worth noting that the EM force varies sharply very near the Hartmann walls

and the hydrodynamic forces react accordingly. This is evidence that Hartmann layers are intact in the present flows.

6.5 3D Flow Features

In sufficiently strong transverse magnetic fields, turbulence in conducting fluids appears in a special form such that turbulent eddies are elongated parallel to the magnetic field and grow to length scales comparable to the duct dimension in the transverse plane. The turbulence is said to be quasi-two-dimensional (Q2D) when, outside of the Hartmann layers, the flow is two-dimensional with negligible velocity nonuniformity along the magnetic field direction due to Joule dissipation [77]. However, the influence of buoyant effects may diminish the Q2D quality of the flow as indicated by the plots (Fig. 60) of axial force along the y-direction in section 6.4. To investigate these effects, the results of four cases (#1-4 in Table 4) consisting of upwards and downwards flows in both conducting and nonconducting ducts with surface heating in the setup described in Chapter 5 (Fig. 27) are examined for *Ha*=220, *Re*=2027, *Gr*=1.44x10^8. In the following analysis, the means by which the buoyant forces diminish the Q2D quality of the flow is explored; however, one should note that the turbulence is still not isotropic due to the effects of Joule dissipation.

The following metric is proposed for evaluating how nonuniform along the y-direction a flow's velocity distribution is. The y-nonuniformity metric, s_y, is evaluated at each cross-section along the axis as in Eq. 32:

$$s_y(x) = \frac{\sum_i \Delta z_i \sum_j \Delta y_j \left| u_{ij}(x) - \overline{U_{y_i}}(x) \right|}{A\overline{U}} \tag{32}$$

Here, $\overline{U_{y_i}} = \frac{\int_{-b}^{b} u\,dy}{\int_{-b}^{b} dy}$ is the velocity averaged across y at each z location denoted by the subscript, i. The subscript j corresponds to grid locations along the y direction. Δz_i and Δy_j are grid cell widths, $\overline{U}$ is the mean velocity, and *A* is the area.

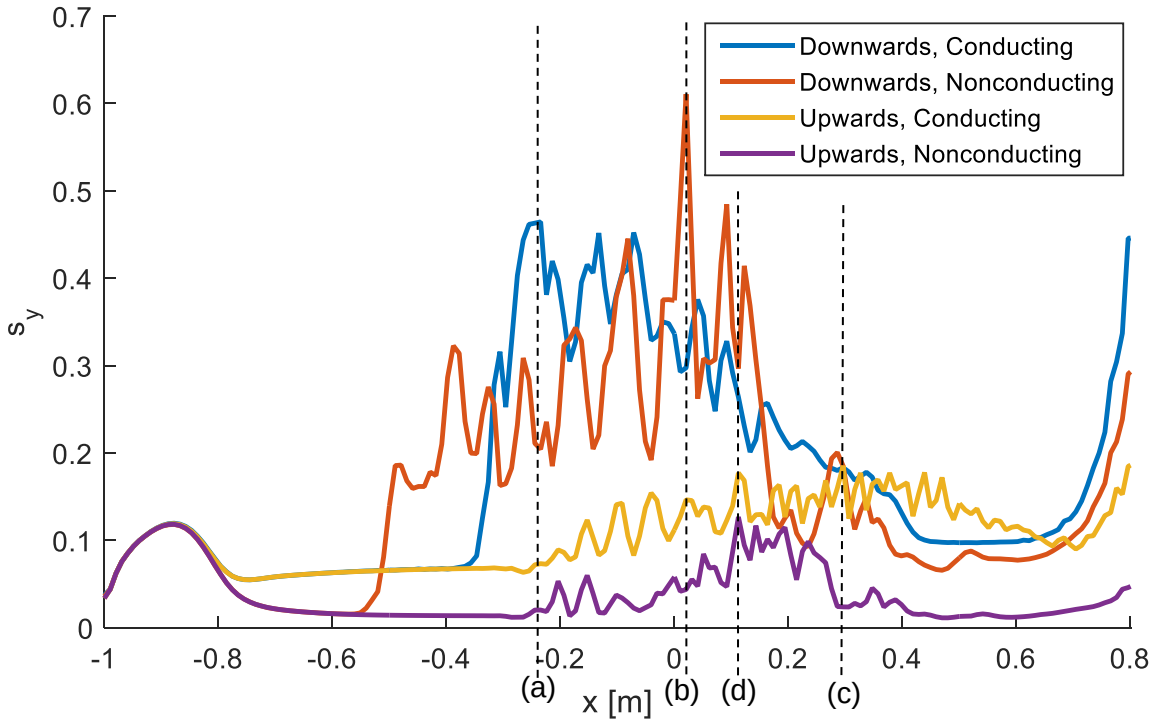

FIG. 61. y-nonuniformity of the instantaneous axial velocity field on fluid cross-sections for each of 4 cases with surface heating and variable flow orientation (upwards or downwards) and wall conductivity (c_w=0.12 or ~0). q_o''=0.20 MW/m^2, B_o=0.5 T, U=0.02 m/s, and ΔT=350.5^{o}C (Ha=220, Re=2027, Gr=1.44x10^8). The locations where y-nonuniformity is maximum are marked by black dotted lines (a)-(d) for (a) downward flow in a conducting duct, (b) downward flow in a nonconducting duct, (c) upward flow in a conducting duct, and (d) upward flow in a nonconducting duct.

s_y is plotted for upwards and downwards flows with both conducting and nonconducting walls in Fig. 61. From the inlet, s_y increases as the initially uniform flow hydrodynamically develops viscous boundary layers. This is interrupted by the magnetic field ramping up which causes the flow to redistribute evenly along the magnetic field direction outside of very thin MHD boundary layers. The Shercliff and Hunt velocity profiles downstream of x=-0.8 m feature s_y= 0.01 and 0.07 respectively with the latter having a higher value due to the parabolic shape of the side-layer jets. The value of s_y increases in the heated region, especially in the downward flow cases. The increase in s_y can be explained by a combination of 3 proposed effects: (1) buoyancy may shape the velocity field to promote flow instability and inertial transfers of momentum, a competing mechanism to Joule dissipation that acts to restore isotropic turbulence [77]; (2) the temperature profile may be asymmetrical along the magnetic field direction, resulting in asymmetrical velocity

profiles necessary to balance the buoyant force; and (3) buoyancy may increase the flow rate inside the side layers where, in electrically conducting ducts, the velocity profile is significantly rounded by viscous forces. These effects will be addressed in the context of the base flow before examining the full unsteady flow.

The so-called "time-averaged s_y" is calculated from replacing the flow variables in Eq. 32 with the time-averaged flow variables. The time-averaged s_y is plotted in Fig. 62.

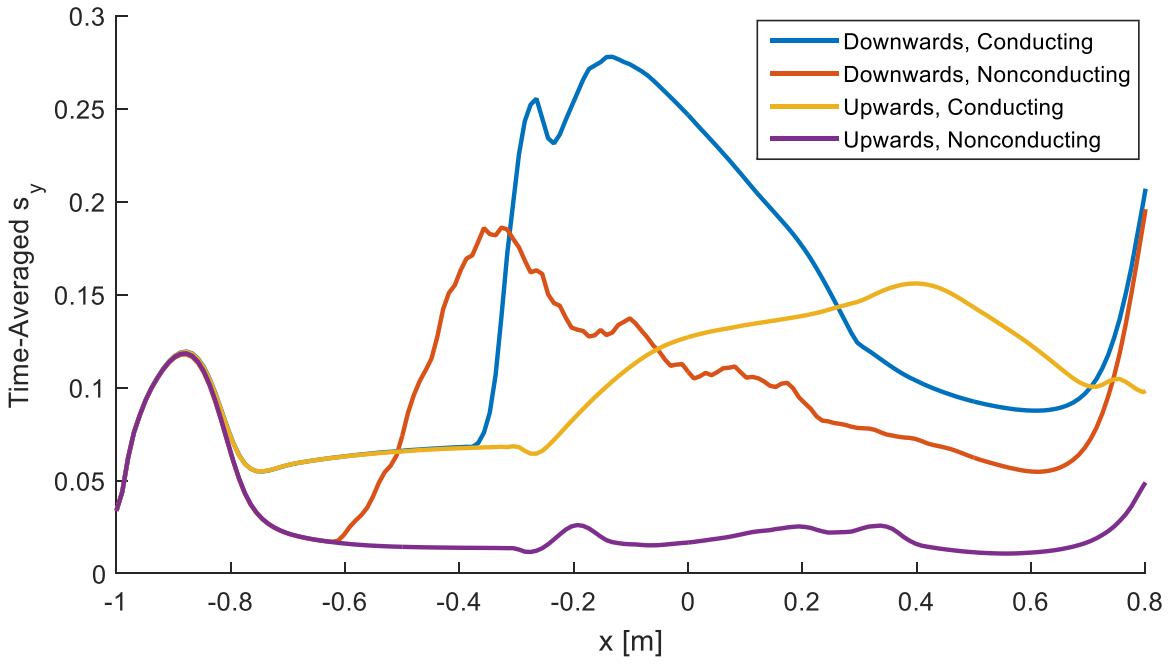

FIG. 62. y-nonuniformity of the time-averaged axial velocity field on fluid cross-sections for each of 4 cases with surface heating and variable flow orientation (upwards or downwards) and wall conductivity (c_w=0.12 or ~0). q_o''=0.20 MW/m^2, B_o=0.5 T, U=0.02 m/s, and ΔT=350.5^{o}C (Ha=220, Re=2027, Gr=1.44x10^8).

Except for the upwards conducting case, the time-averaged s_y is generally less than the instantaneous s_y which indicates that the base flow is generally more uniform along the y-direction than any instant of the full unsteady flow. As shown in Figs. 61 and 62, inside the heated region, the buoyancy opposed flows have higher s_y than their upward flow counterparts, and the conducting duct flows have higher s_y than electrically nonconducting ducts with the same

orientation. The time-averaged flow behavior inside the heated region of each duct is illustrated in Figs. 63-70.

Time-Averaged u

Downward, conducting

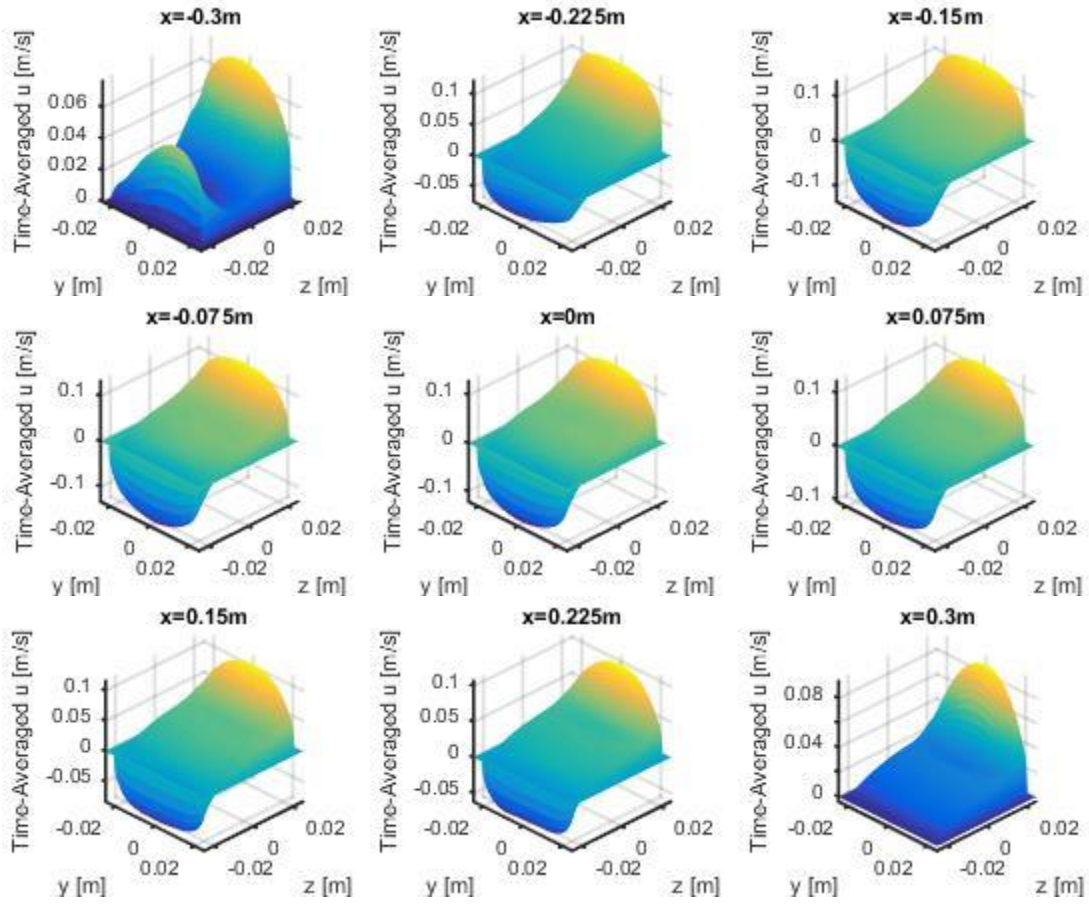

FIG. 63. 2D profiles of the time-averaged axial velocity field on duct cross-sections at x= -0.3m, -0.225m, -0.15m, -0.075m, 0m, 0.075m, 0.15m, 0.225m, 0.3m for downward flow with surface heating, q_o"=0.20 MW/m^2, B_o=0.5 T, U=0.02 m/s, and ΔT=350.5^{o}C (Ha=220, Re=2027, Gr=1.44x10^8). c_w=0.12.

Downward, nonconducting

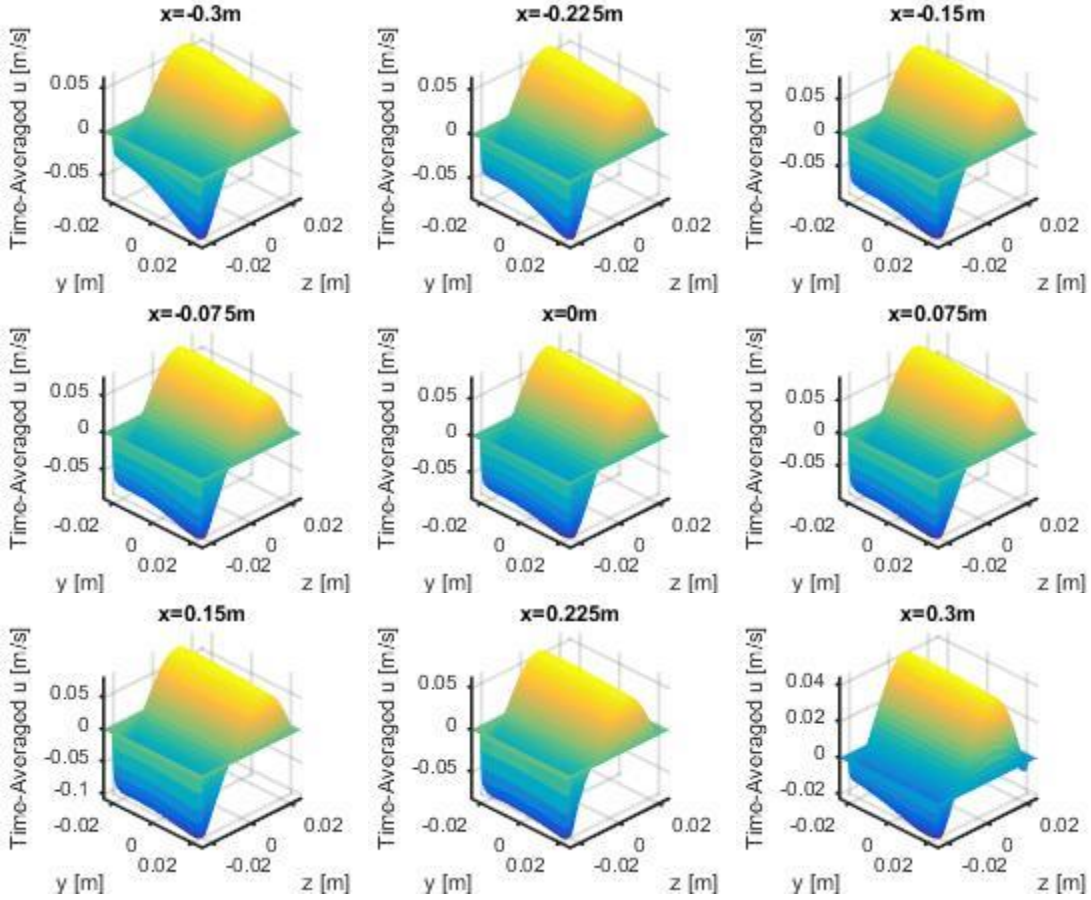

FIG. 64. 2D profiles of the time-averaged axial velocity field on duct cross-sections at x= -0.3m, -0.225m, -0.15m, -0.075m, 0m, 0.075m, 0.15m, 0.225m, 0.3m for downward flow with surface heating, q_o"=0.20 MW/m^2, B_o=0.5 T, U=0.02 m/s, and ΔT=350.5^{o}C (Ha=220, Re=2027, Gr=1.44x10^8). c_w~0.

Upward, conducting

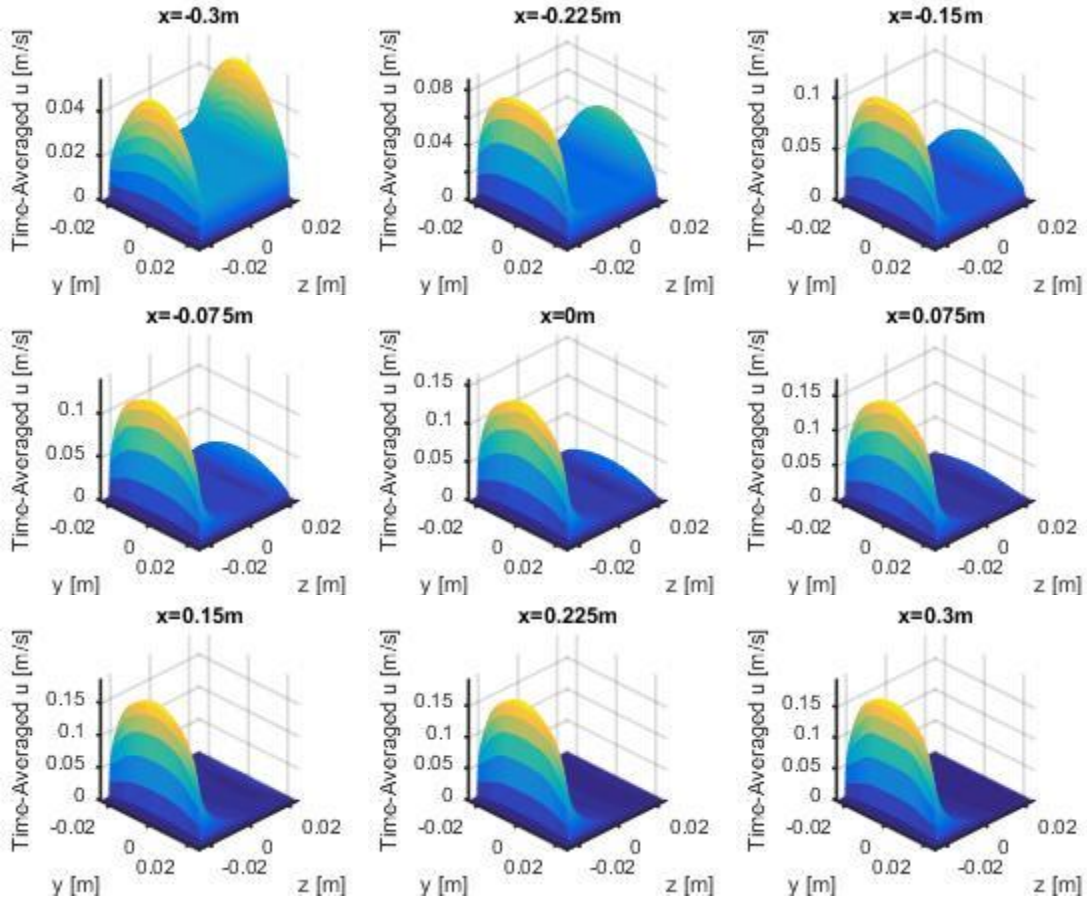

FIG. 65. 2D profiles of the time-averaged axial velocity field on duct cross-sections at x= -0.3m, -0.225m, -0.15m, -0.075m, 0m, 0.075m, 0.15m, 0.225m, 0.3m for upward flow with surface heating, q_o"=0.20 MW/m^2, B_o=0.5 T, U=0.02 m/s, and ΔT=350.5^{o}C (Ha=220, Re=2027, Gr=1.44x10^8). c_w=0.12.

Upward, nonconducting

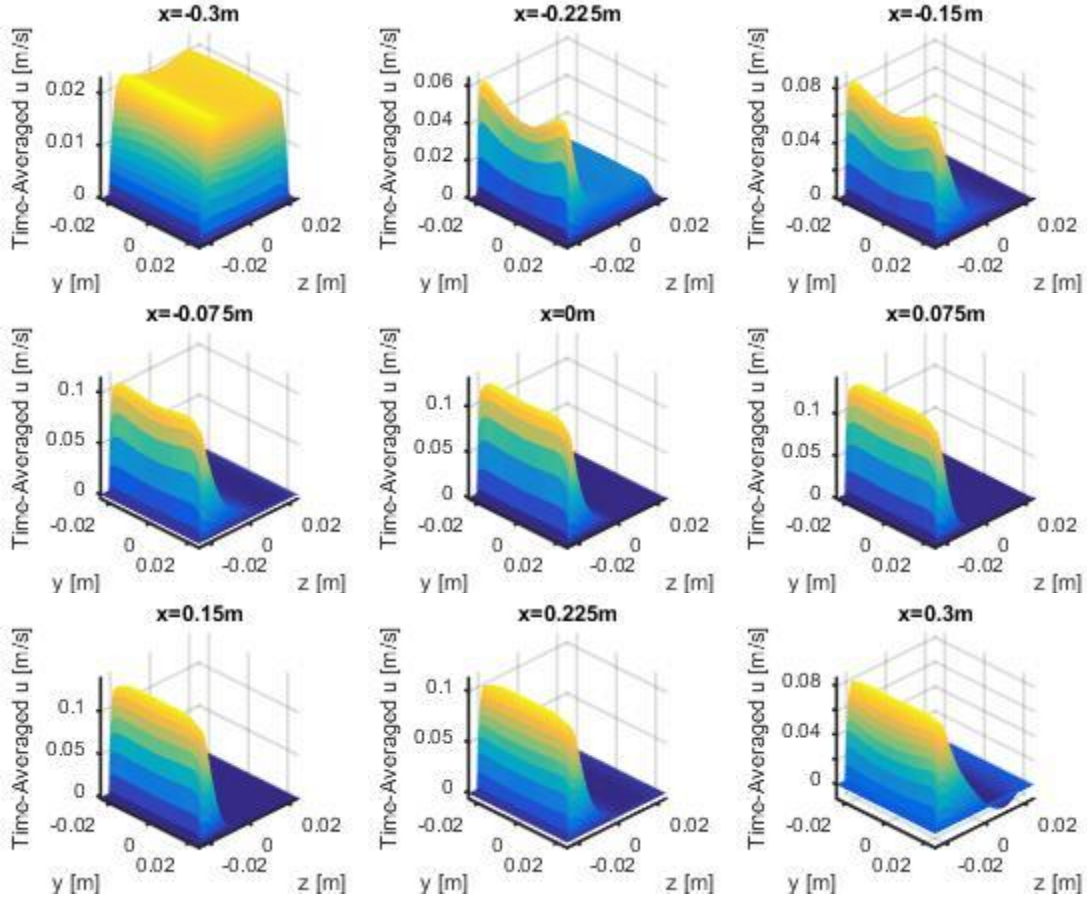

FIG. 66. 2D profiles of the time-averaged axial velocity field on duct cross-sections at x= -0.3m, -0.225m, -0.15m, -0.075m, 0m, 0.075m, 0.15m, 0.225m, 0.3m for upward flow with surface heating, q_o''=0.20 MW/m^2, B_o=0.5 T, U=0.02 m/s, and ΔT=350.5^{o}C (Ha=220, Re=2027, Gr=1.44x10^8). c_w~0.

Time-Averaged T

Downward, conducting

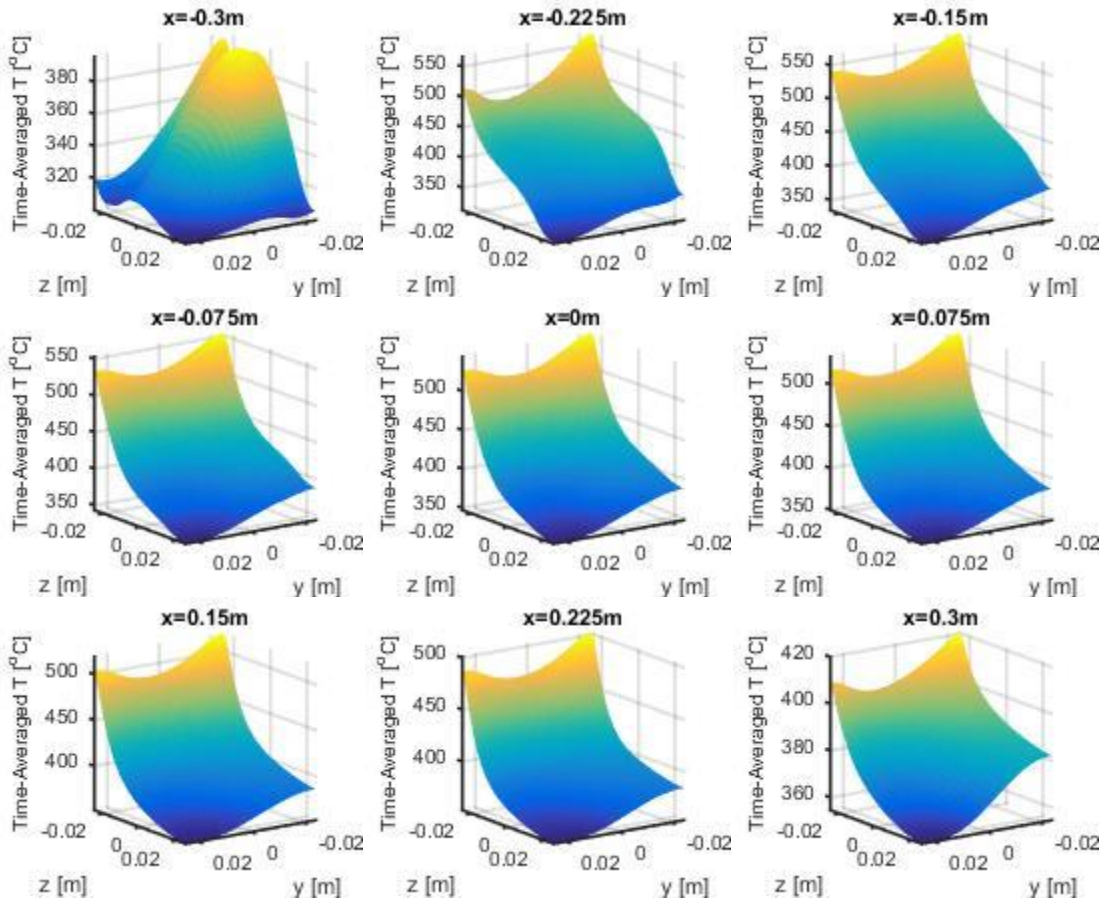

FIG. 67. 2D profiles of the time-averaged temperature field on duct cross-sections at x= -0.3m, -0.225m, -0.15m, -0.075m, 0m, 0.075m, 0.15m, 0.225m, 0.3m for downward flow with surface heating, q_o"=0.20 MW/m^2, B_o=0.5 T, U=0.02 m/s, and ΔT=350.5^{o}C (Ha=220, Re=2027, Gr=1.44x10^8). c_w=0.12.

Downward, nonconducting

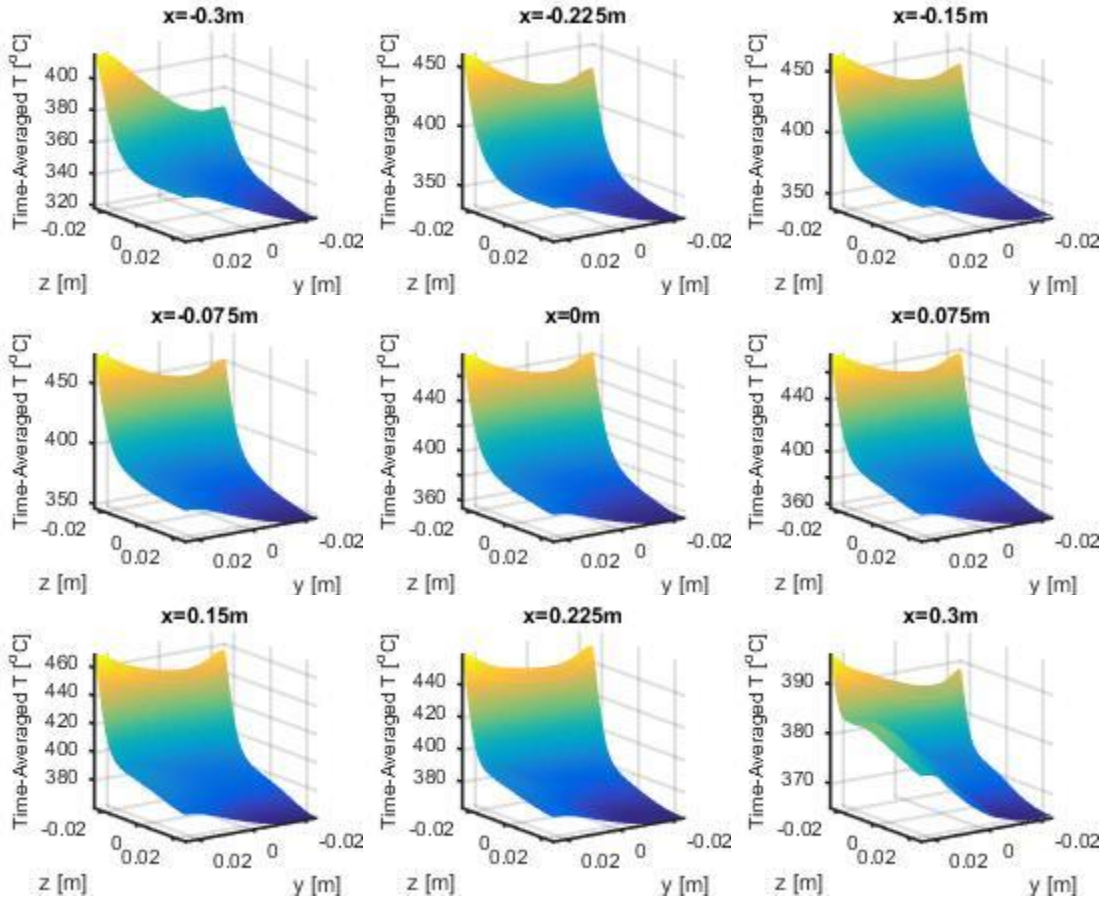

FIG. 68. 2D profiles of the time-averaged temperature field on duct cross-sections at x= -0.3m, -0.225m, -0.15m, -0.075m, 0m, 0.075m, 0.15m, 0.225m, 0.3m for downward flow with surface heating, q_o"=0.20 MW/m^2, B_o=0.5 T, U=0.02 m/s, and ΔT=350.5°C (Ha=220, Re=2027, Gr=1.44x10^8). c_w~0.

Upward, conducting

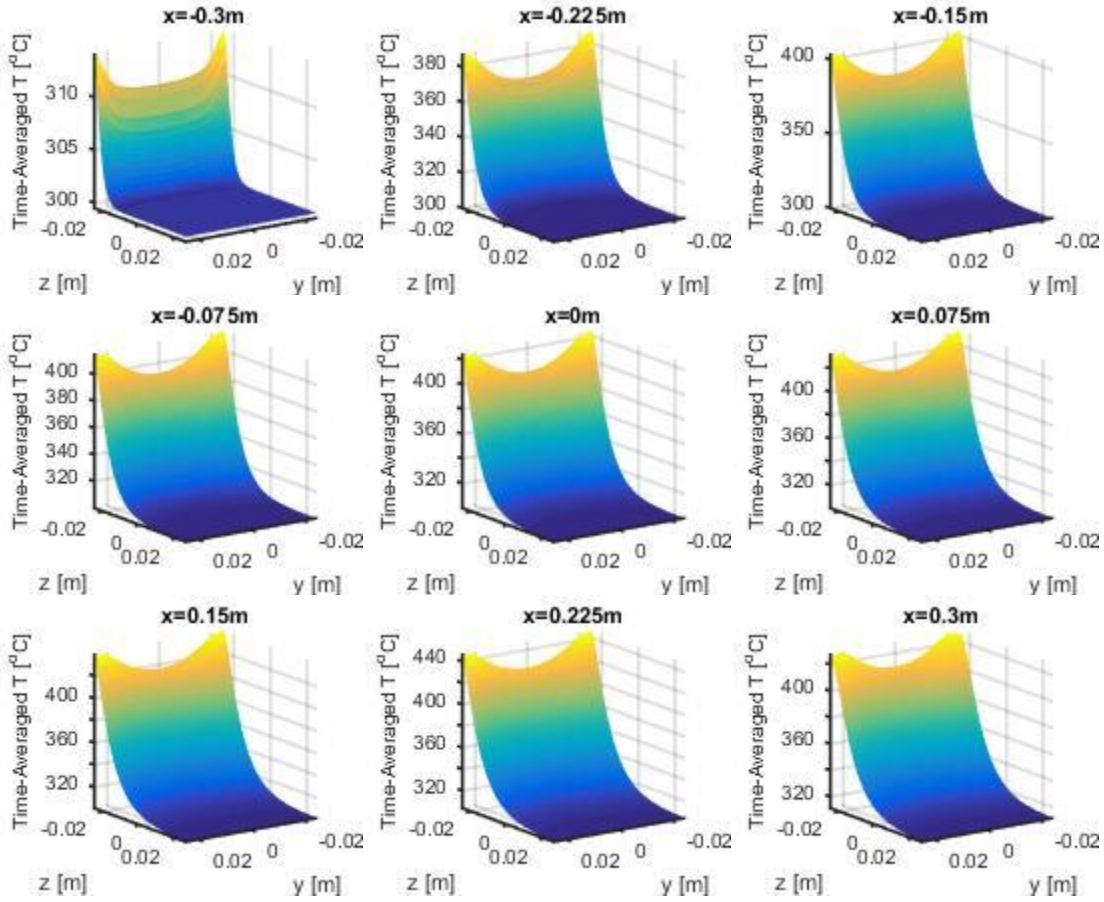

FIG. 69. 2D profiles of the time-averaged temperature field on duct cross-sections at x= -0.3m, -0.225m, -0.15m, -0.075m, 0m, 0.075m, 0.15m, 0.225m, 0.3m for upward flow with surface heating, q_o''=0.20 MW/m^2, B_o=0.5 T, U=0.02 m/s, and ΔT=350.5°C (Ha=220, Re=2027, Gr=1.44x10^8). c_w=0.12.

Upward, nonconducting

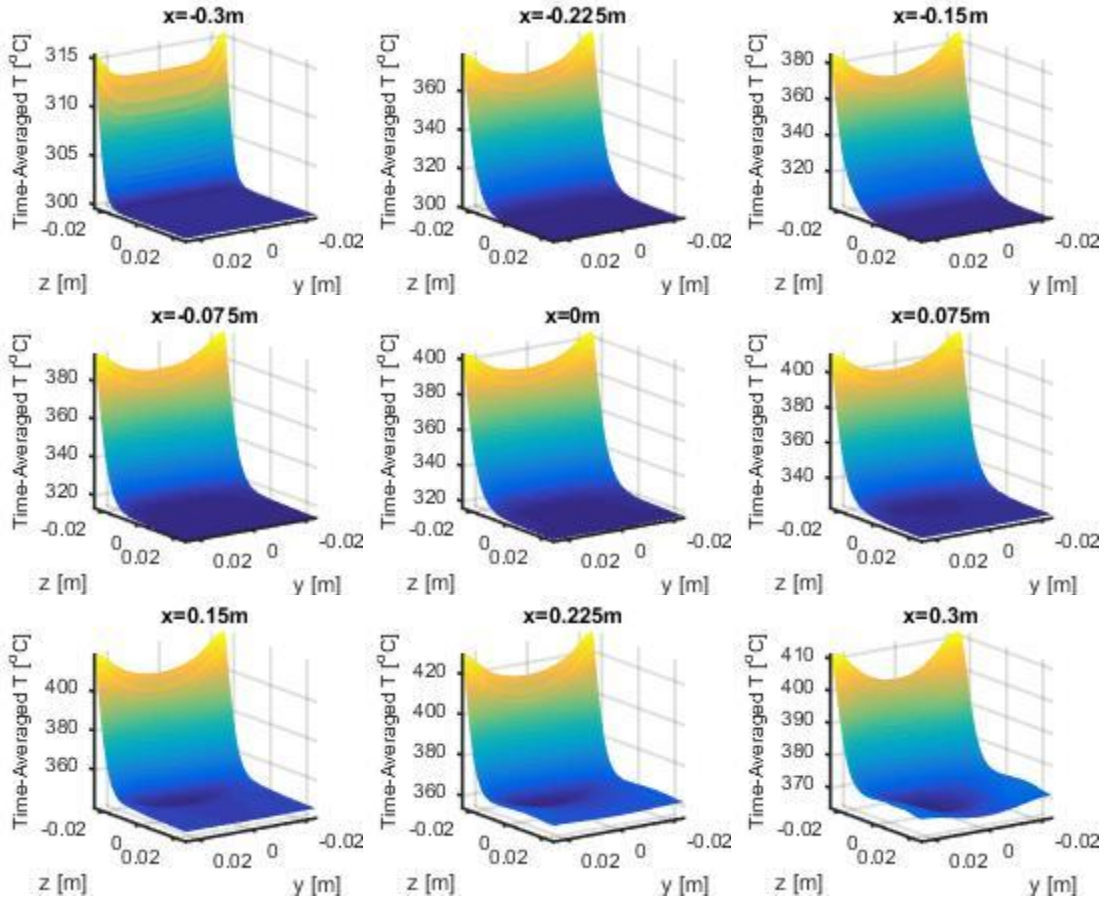

FIG. 70. 2D profiles of the time-averaged temperature field on duct cross-sections at x= -0.3m, -0.225m, -0.15m, -0.075m, 0m, 0.075m, 0.15m, 0.225m, 0.3m for upward flow with surface heating, q_o''=0.20 MW/m^2, B_o=0.5 T, U=0.02 m/s, and ΔT=350.5^{o}C (Ha=220, Re=2027, Gr=1.44x10^8). c_w~0.

Interestingly, the downward cases feature lasting temperature difference between the Hartmann walls which has caused the base velocity profiles to slope along the y-direction. Such stable asymmetry is only possible in the downward scenarios because a feedback relationship exists between velocity and temperature which behaves oppositely in upward scenarios. In (upward) buoyancy assisted flows, the velocity of slightly warmer fluid increases which cools the hot spot and restores temperature uniformity. However, in buoyancy opposed flows, the velocity of relatively warmer fluid decreases which causes the temperature to increase until an asymmetric temperature statistical equilibrium is reached. This asymmetry is observed in the time-averaged

temperature profiles shown below in Fig. 71 which correspond to the location of maximum instantaneous s_y in Fig. 61.

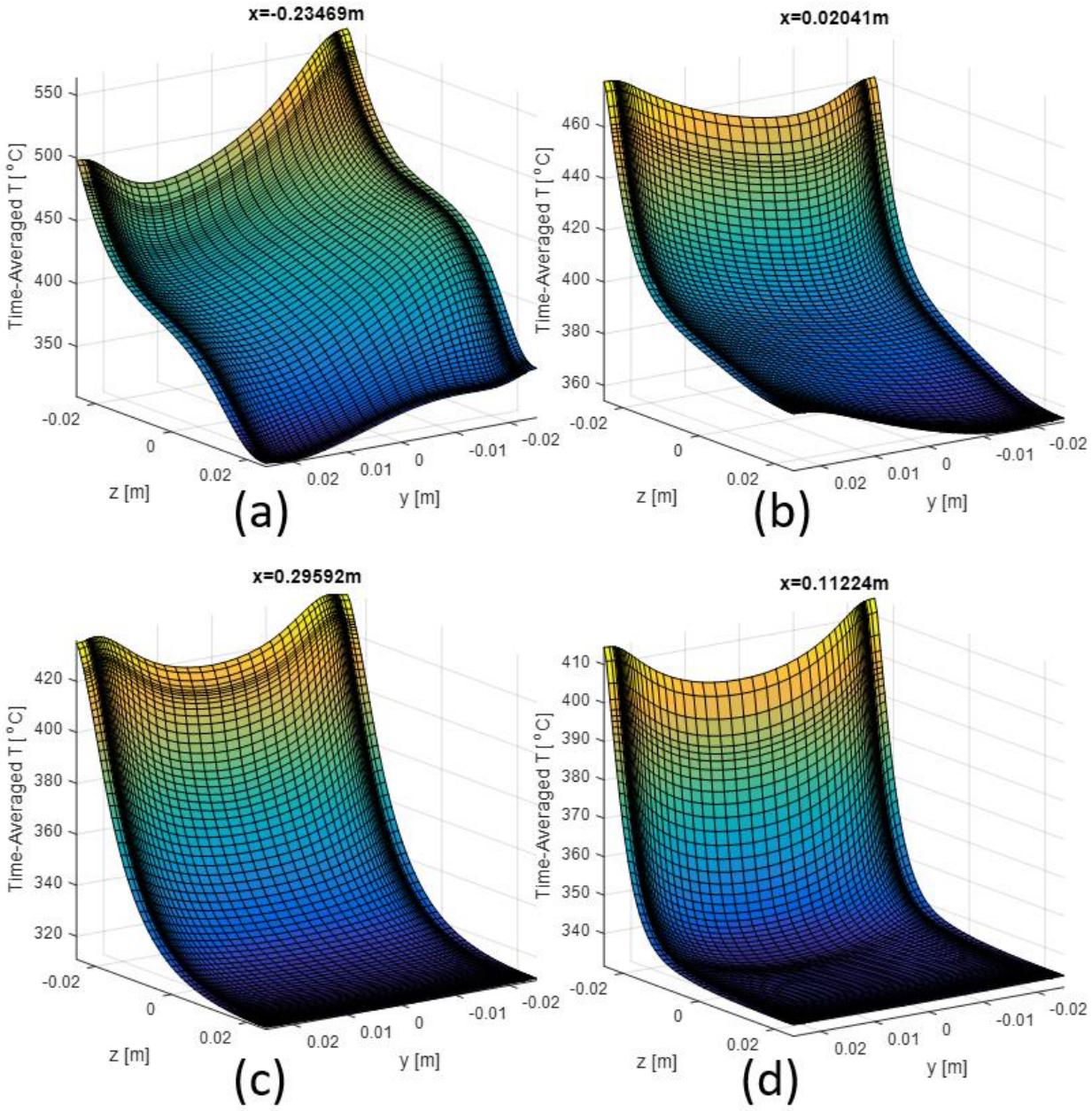

FIG. 71. 2D profiles of the time-averaged temperature field on duct cross-sections where the y-nonuniformity is maximum for q_o"=0.20 MW/m^2, B_o=0.5 T, U=0.02 m/s, and ΔT=350.5°C (Ha=220, Re=2027, Gr=1.44x10^8), surface heating, (a, c) c_w=0.12, (b, d) c_w~0, and (a, b) downward flow, (c, d) upward flow.

The time-averaged temperature profiles reveal ~63°C and ~15°C temperature differences between Hartmann walls for conducting and nonconducting walls respectively for downward flows

despite the symmetry of the problem setup. There is no significant asymmetry in upward scenarios. The time-averaged velocity profiles corresponding to the same locations are plotted below in Fig. 72.

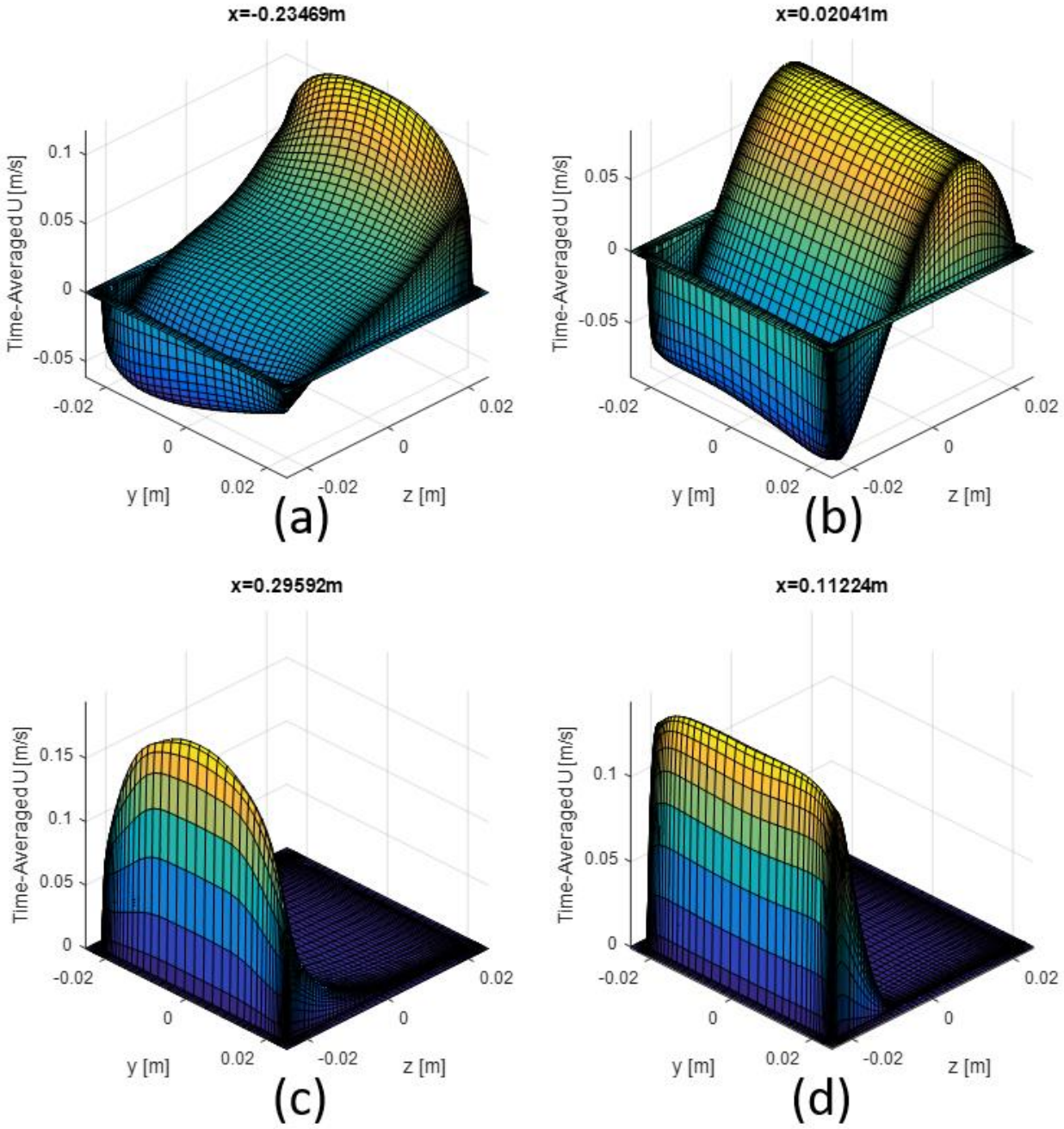

FIG. 72. 2D profiles of the time-averaged velocity field on duct cross-sections where the y-nonuniformity is maximum for q_o''=0.20 MW/m^2, B_o=0.5 T, U=0.02 m/s, and ΔT=350.5^{o}C (Ha=220, Re=2027, Gr=1.44x10^8), surface heating, (a, c) c_w=0.12, (b, d) c_w~0, and (a, b) downward flow, (c, d) upward flow.

The velocity asymmetry due to temperature asymmetry is observed above for the downward cases. Thus, the fact that downward base flows have generally higher flow nonuniformity than upwards base flows can be attributed to this proposed feedback mechanism that promotes asymmetric temperature profiles. Fig. 72 also shows how the base flows in electrically conducting ducts have rounded velocity profiles near the sidewalls while the flows in nonconducting ducts do not. In locations where buoyant forces are strongest, the jets are largest which accounts for the increased y-nonuniformity in the heated region of electrically conducting ducts.

The nonuniformity along the magnetic field direction is contributed to by unsteady flow features as observed in the oscillations of s_y in the heated region (Fig. 61). The oscillations of s_y have amplitudes of ~0.1 for downward flows and ~0.05 for upward flows indicating stronger y-nonuniformity associated with turbulence in buoyancy opposed flow. The axial velocity profiles are provided in Fig. 73 for locations where s_y is largest inside the uniform magnetic field region at the instants shown.

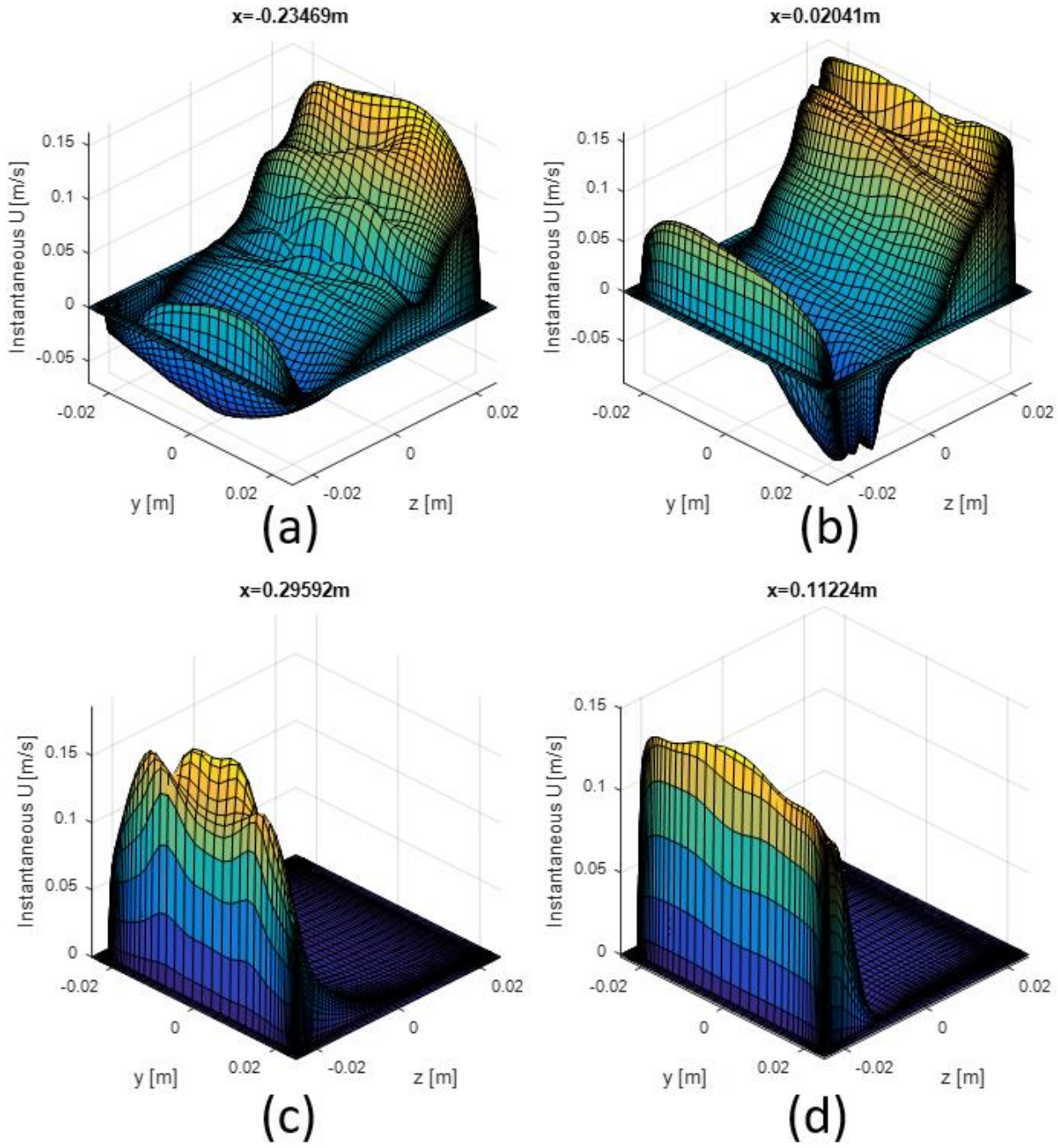

FIG. 73. 2D profiles of the instantaneous velocity field on duct cross-sections where the y-nonuniformity is maximum for q_o''=0.20 MW/m^2, B_o=0.5 T, U=0.02 m/s, and ΔT=350.5^{o}C (Ha=220, Re=2027, Gr=1.44x10^8), surface heating, (a, c) c_w=0.12, (b, d) c_w~0, and (a, b) downward flow, (c, d) upward flow.

The four axial velocity profiles in Fig. 73 show that the sources of y-nonuniformity go beyond the mechanisms which were introduced in the base flow analysis. As shown in the corresponding temperature profiles below (Fig. 74), the y-nonuniformity in temperature is even stronger than in

the base temperature field with ~145^{o}C difference between Hartmann walls in the conducting downward case. While the unsteady temperature asymmetry certainly contributes to y-nonuniformity, there are y-nonuniformities in the above velocity profiles which appear independent of the temperature asymmetry. These fluctuations can be explained by the presence of flow instabilities in which inertial forces transfer momentum in all three dimensions.

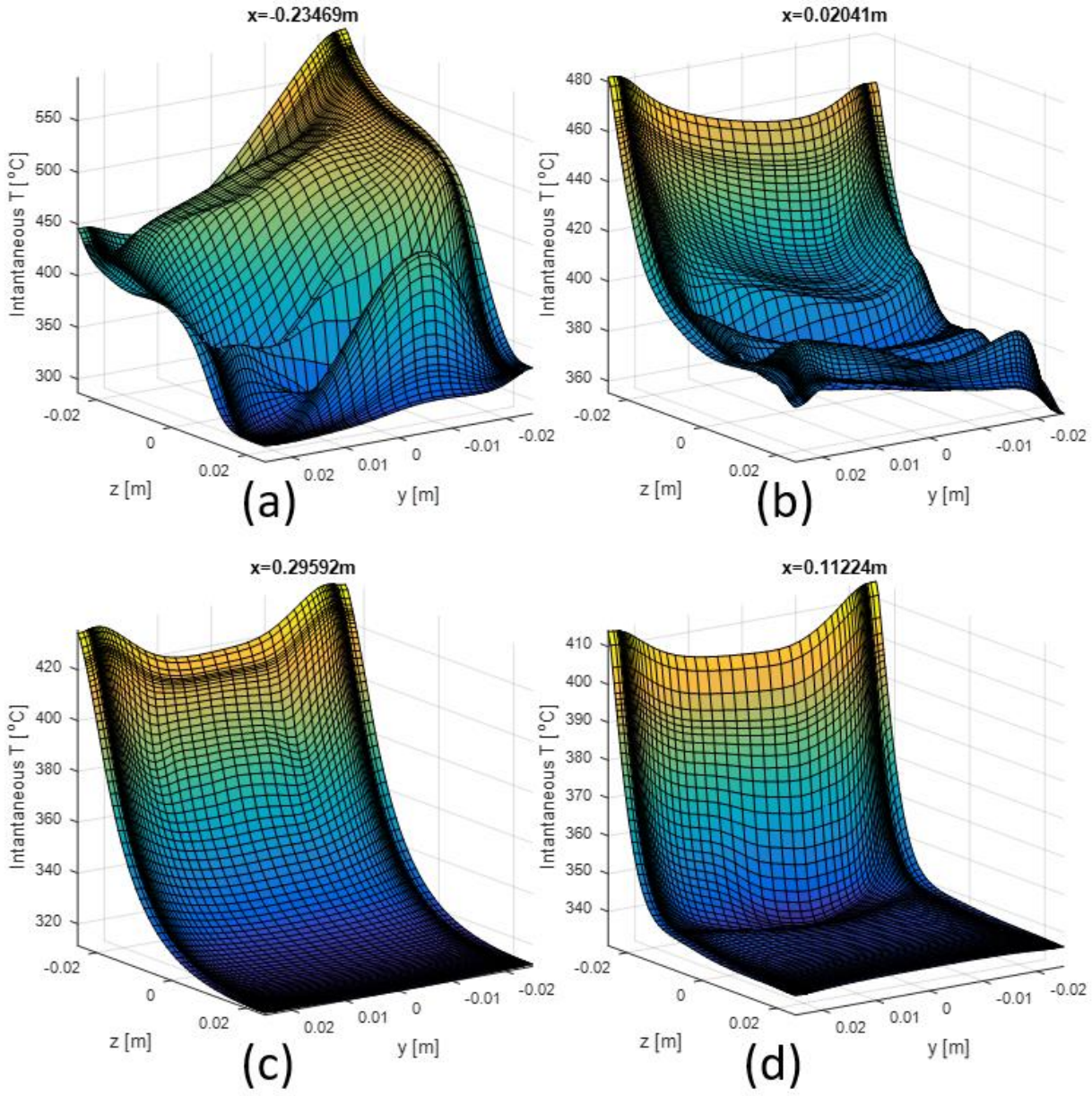

FIG. 74. 2D profiles of the instantaneous temperature field on duct cross-sections where the y-nonuniformity is maximum for q_o''=0.20 MW/m^2, B_o=0.5 T, U=0.02 m/s, and ΔT=350.5°C (Ha=220, Re=2027, Gr=1.44x10^8), surface heating, (a, c) c_w=0.12, (b, d) c_w~0, and (a, b) downward flow, (c, d) upward flow.

In downward flows where s_y is largest due to strong fluctuations, there are two modes of instability to consider: (1) shear instability which requires an inflection point in the velocity profile and (2) buoyant instability which requires that the temperature increase in the direction of gravity. In the conducting wall reference case, the shear instability is prevalent throughout the heated region while the buoyant instability mode dominates the nonconducting duct flow.

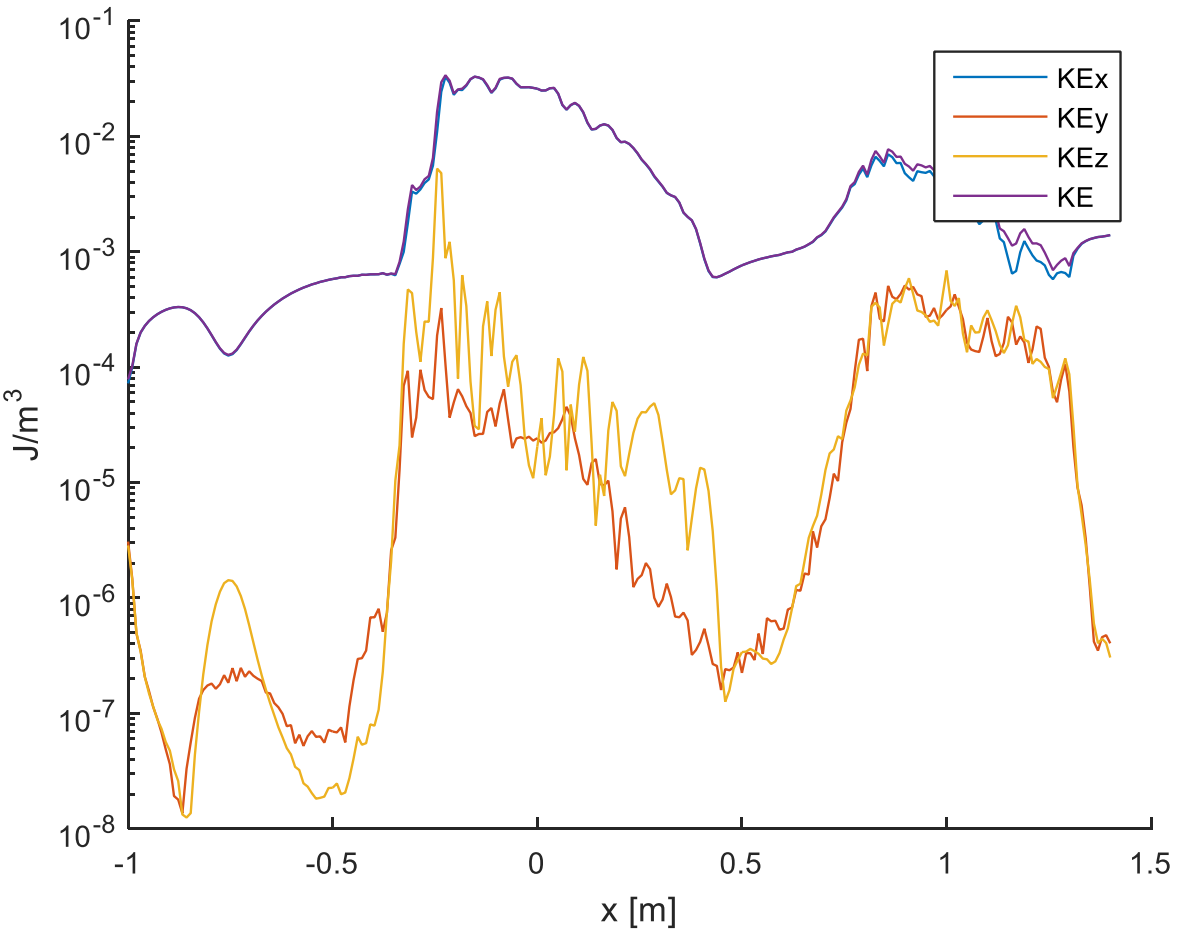

FIG. 75. Total kinetic energy and components of kinetic energy are calculated for fluid cross-sections along the x-direction for downward flow with surface heating, q_o"=0.20 MW/m^2, B_o=0.5 T, U=0.02 m/s, and ΔT=350.5^{o}C (Ha=220, Re=2027, Gr=1.44x10^8), and c_w=0.12. The kinetic energy calculations do not include the mean axial flowrate.

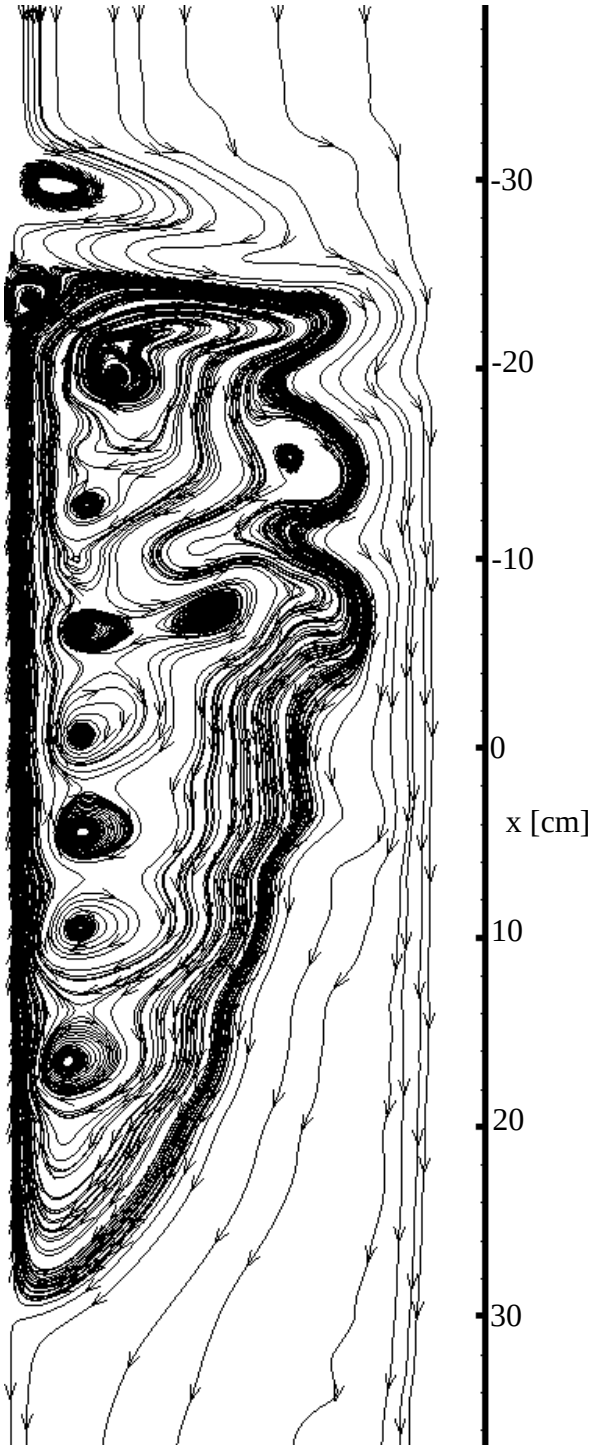

FIG. 76. Velocity streamlines on the y=0 center-plane for downward flow with surface heating, q_o"=0.20 MW/m^2, B_o=0.5 T, U=0.02 m/s, and ΔT=350.5^{o}C (Ha=220, Re=2027, Gr=1.44x10^8). c_w=0.12.

In the electrically conducting downward flow case, the influence of buoyant effects causes flow reversal and recirculation inside the heated region as shown in Fig. 76. In transitioning between

the forced flow velocity profile to the MHD mixed convection profile with flow reversal, the boundary layer separates from the heated surface and the oncoming flow migrates to the cold sidewall. The transition region beginning at the boundary layer separation is ~10 cm long and includes a smaller region of ~3 cm where a distinct spike in z-direction kinetic energy and steep increase in x-direction kinetic energy (Fig. 75) occurs as the flow migrates to the cold sidewall. Actually, in the instant depicted, the boundary layer separates in two locations but quickly reattaches downstream of the first location. The disturbance caused by the second (and lasting) separation is shown to coincide with the location of maximum y-direction kinetic energy which, unsurprisingly, is the precise location where s_y is largest (x=-0.2347 m). In section 6.4 it was shown that fluctuations in downwards flows are associated with significant inertial forces and it is likely that these fluctuating inertial forces contribute to y-nonuniformity. Inertial transfers of momentum are a competing mechanism to Joule dissipation as the inertial transfers tend to promote isotropic turbulence while Joule dissipation tends to promote Q2D turbulence [77].

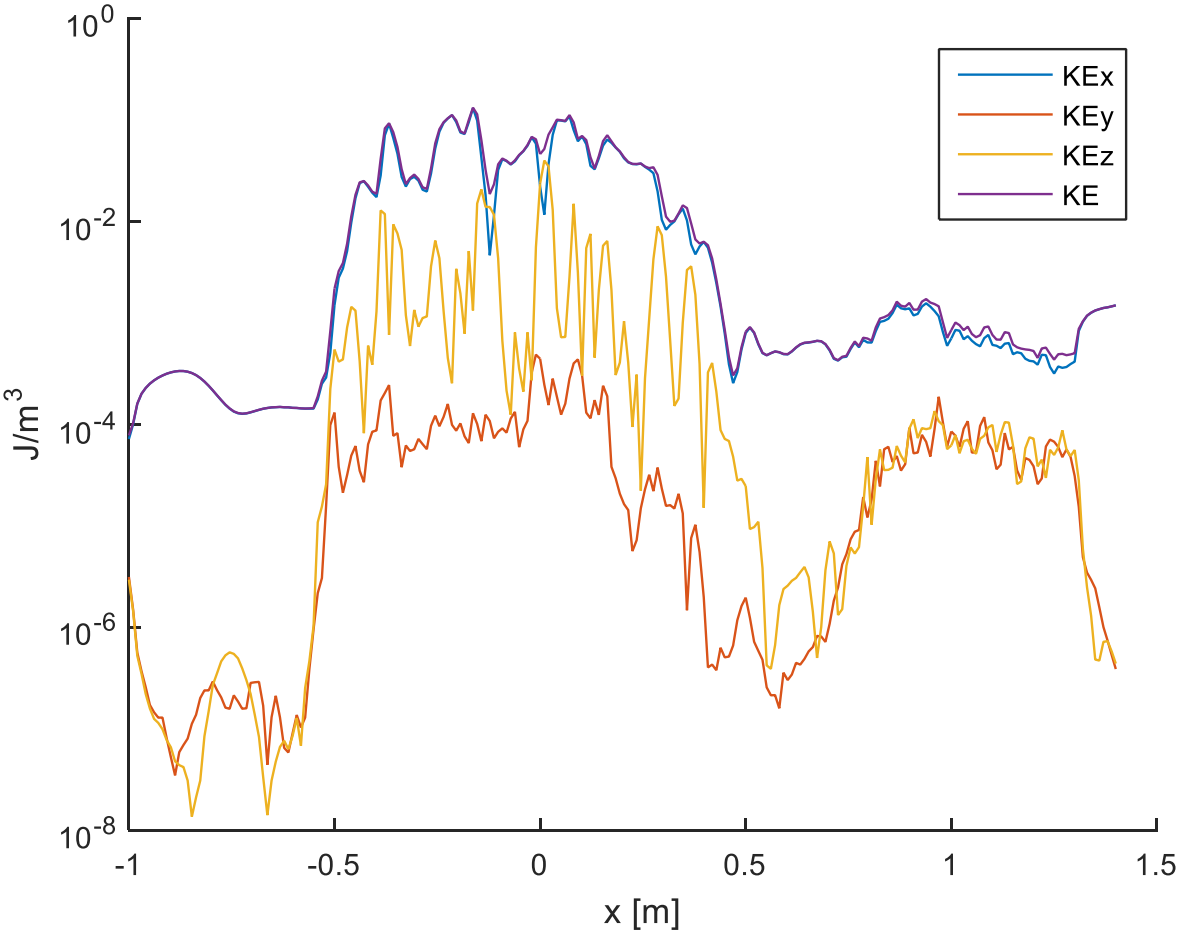

FIG. 77. Total kinetic energy and components of kinetic energy are calculated for fluid cross-sections along the x-direction for downward flow with surface heating, q_o"=0.20 MW/m^2, B_o=0.5 T, U=0.02 m/s, and ΔT=350.5^{o}C (Ha=220, Re=2027, Gr=1.44x10^8), and c_w~0. The kinetic energy calculations do not include the mean axial flowrate.

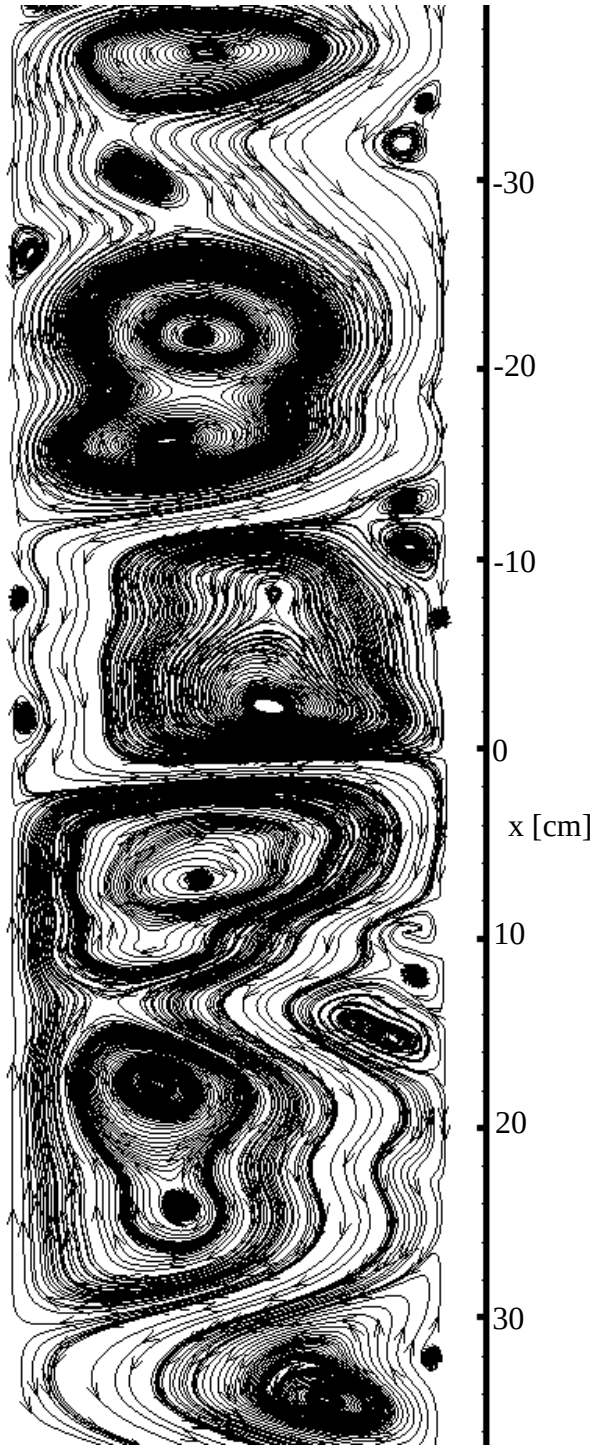

FIG. 78. Velocity streamlines on the y=0 center-plane for downward flow with surface heating, q_o"=0.20 MW/m^2, B_o=0.5 T, U=0.02 m/s, and ΔT=350.5^{o}C (Ha=220, Re=2027, Gr=1.44x10^8). c_w~0.

In the electrically insulated downward flow case, the buoyant effects cause flow reversal which is most often near the hot wall but which also appears near the cold wall due to the large-scale

mixing which is generated by buoyant instability. With less Joule dissipation than the electrically conducting case, the flow is more unstable and large vortices span the width of the duct for the entire heated region and even ~20cm upstream and downstream of the heated region. These large bulk vortices, hallmarks of MHD turbulence, dominate the flow. Because they alternate between clockwise and counterclockwise, the boundary layer tends to separate frequently and flow migrates to the opposite sidewall to avoid flowing counter to the circulation of the vortices. As in the electrically conducting scenario, the boundary layer separations coincide with spikes in s_y, and y and z-direction kinetic energy, the largest of these occurring at x=0.0204 m in the instant shown. Though boundary layer separation coincides with the strongest fluctuations of kinetic energy and nonuniformity, fluctuations of these quantities exist throughout the turbulent heated region.

In both electrically conducting and nonconducting buoyancy opposed flows, spikes in y-direction kinetic energy and y-direction nonuniformity were shown to coincide with boundary layer separation. Smaller fluctuations were shown to coincide with vortices that did not cause boundary layer separation. It is important to note that in both scenarios, the kinetic energy associated with z-direction motions is everywhere larger than kinetic energy associated with y-direction motions and x-direction motions have larger energy still, reinforcing the notion that Joule dissipation modifies turbulence in MHD flows to dampen fluctuations not perpendicular to the magnetic field. To get a better understanding of the extent to which the flow is Q2D, observe the velocity profiles in the heated region shown in Figs. 79-86 below. Then note how the temperature profiles are not directly influenced by the magnetic field to be uniform along the y-direction and are extremely asymmetric in downward flow cases while being symmetric in upward flows due to the feedback mechanism proposed in this section.

Instantaneous u

Downward, conducting

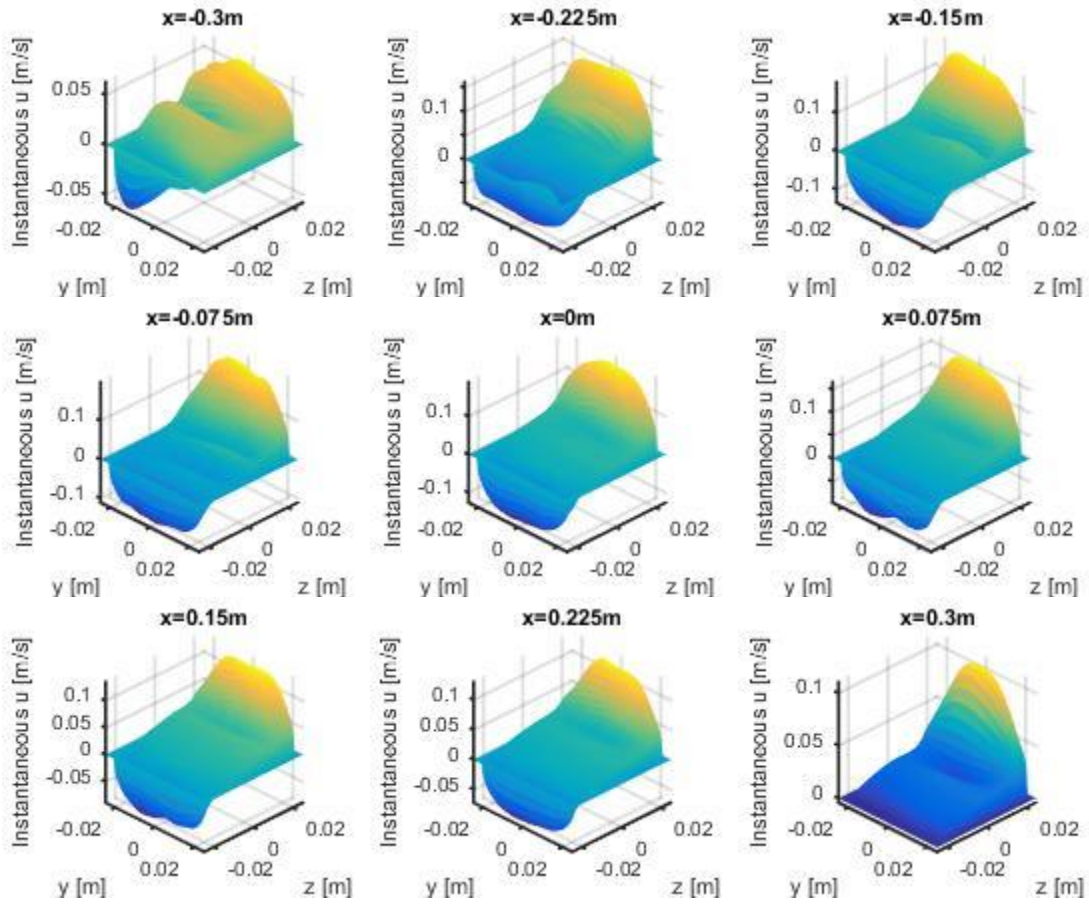

FIG. 79. 2D profiles of the instantaneous velocity field on duct cross-sections at x= -0.3m, -0.225m, -0.15m, -0.075m, 0m, 0.075m, 0.15m, 0.225m, 0.3m for downward flow with surface heating, q_o''=0.20 MW/m^2, B_o=0.5 T, U=0.02 m/s, and ΔT=350.5^{o}C (Ha=220, Re=2027, Gr=1.44x10^8). c_w=0.12.

Downward, nonconducting

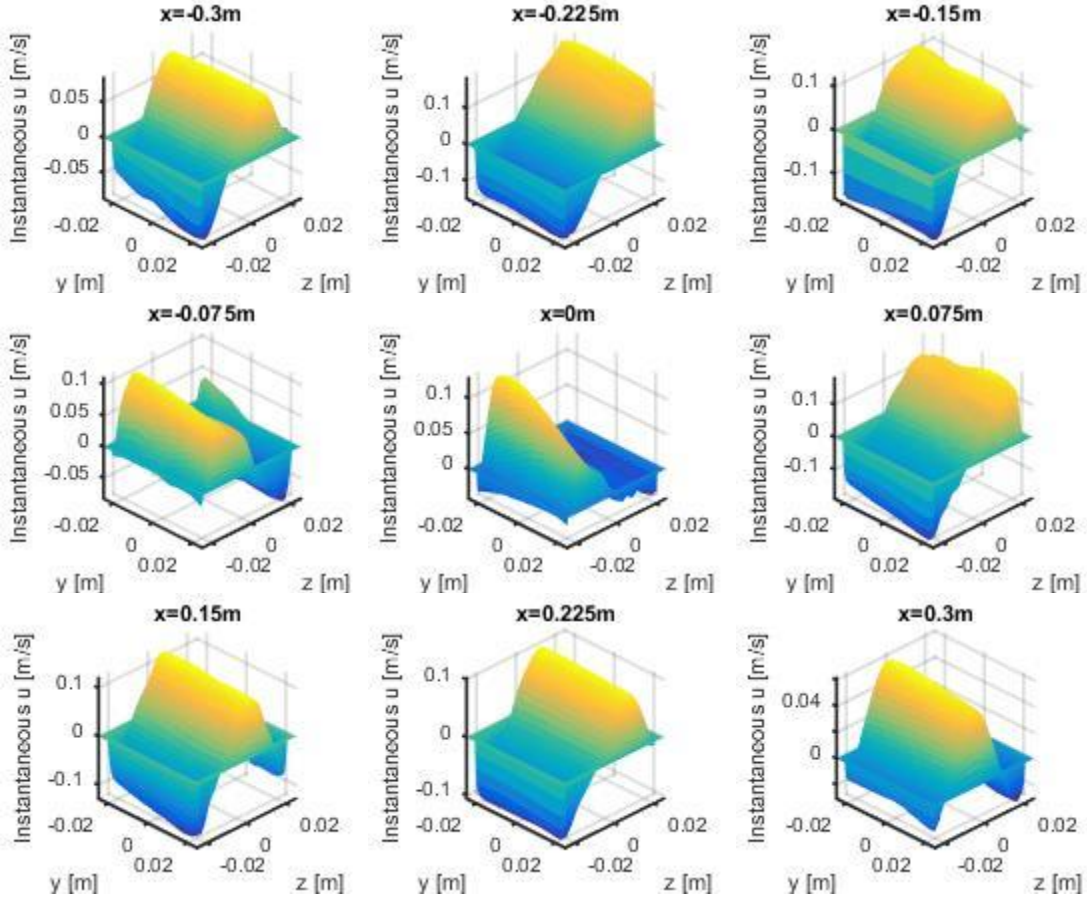

FIG. 80. 2D profiles of the instantaneous velocity field on duct cross-sections at x= -0.3m, -0.225m, -0.15m, -0.075m, 0m, 0.075m, 0.15m, 0.225m, 0.3m for downward flow with surface heating, q_o"=0.20 MW/m^2, B_o=0.5 T, U=0.02 m/s, and ΔT=350.5^{o}C (Ha=220, Re=2027, Gr=1.44x10^8). c_w~0.

Upward, conducting

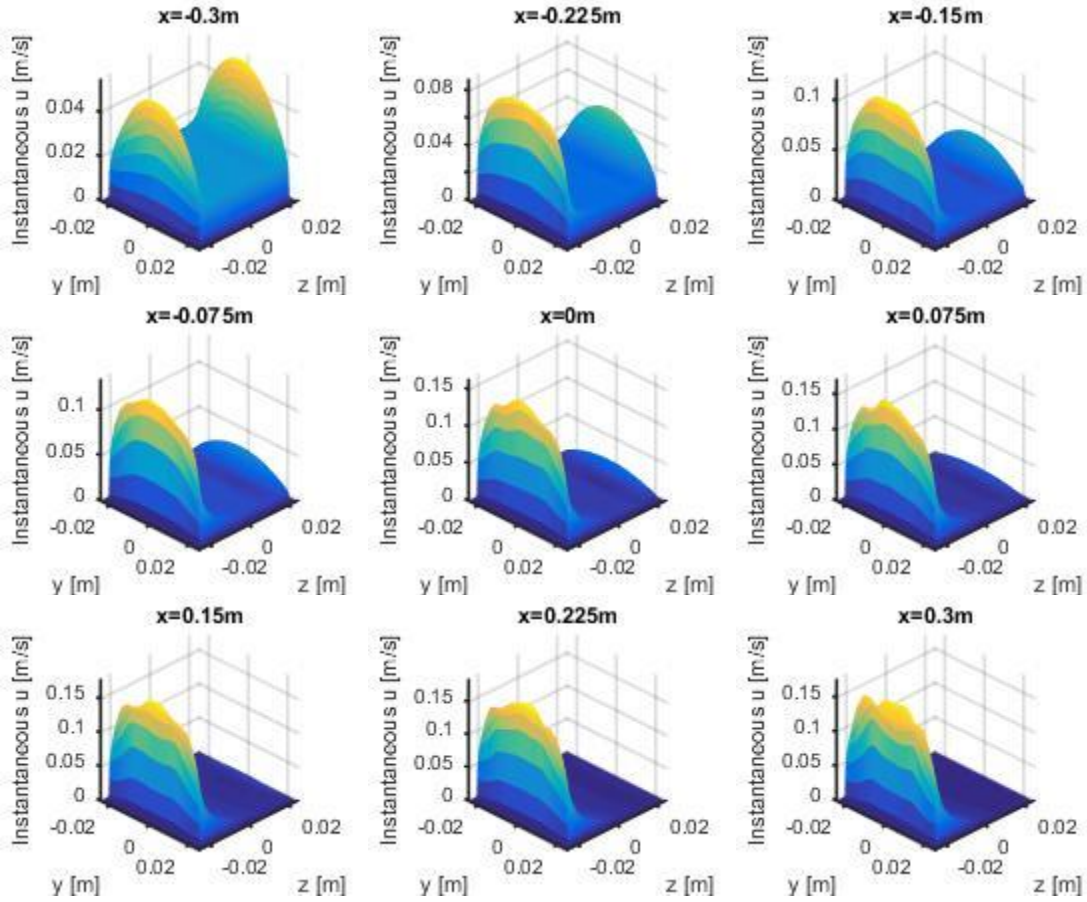

FIG. 81. 2D profiles of the instantaneous velocity field on duct cross-sections at x= -0.3m, -0.225m, -0.15m, -0.075m, 0m, 0.075m, 0.15m, 0.225m, 0.3m for upward flow with surface heating, q_o"=0.20 MW/m^2, B_o=0.5 T, U=0.02 m/s, and ΔT=350.5^{o}C (Ha=220, Re=2027, Gr=1.44x10^8). c_w=0.12.

Upward, nonconducting

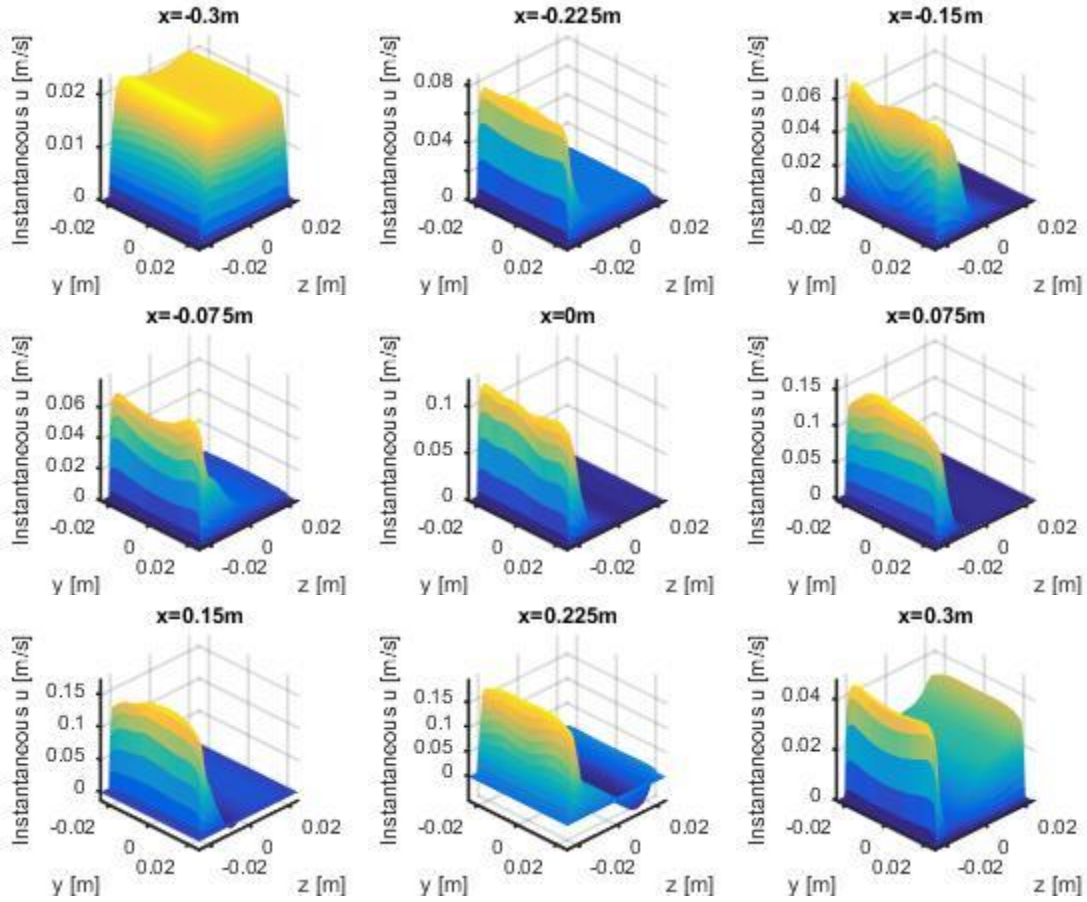

FIG. 82. 2D profiles of the instantaneous velocity field on duct cross-sections at x= -0.3m, -0.225m, -0.15m, -0.075m, 0m, 0.075m, 0.15m, 0.225m, 0.3m for upward flow with surface heating, q_o"=0.20 MW/m^2, B_o=0.5 T, U=0.02 m/s, and ΔT=350.5^{o}C (Ha=220, Re=2027, Gr=1.44x10^8). c_w~0.

Instantaneous T

Downward, conducting

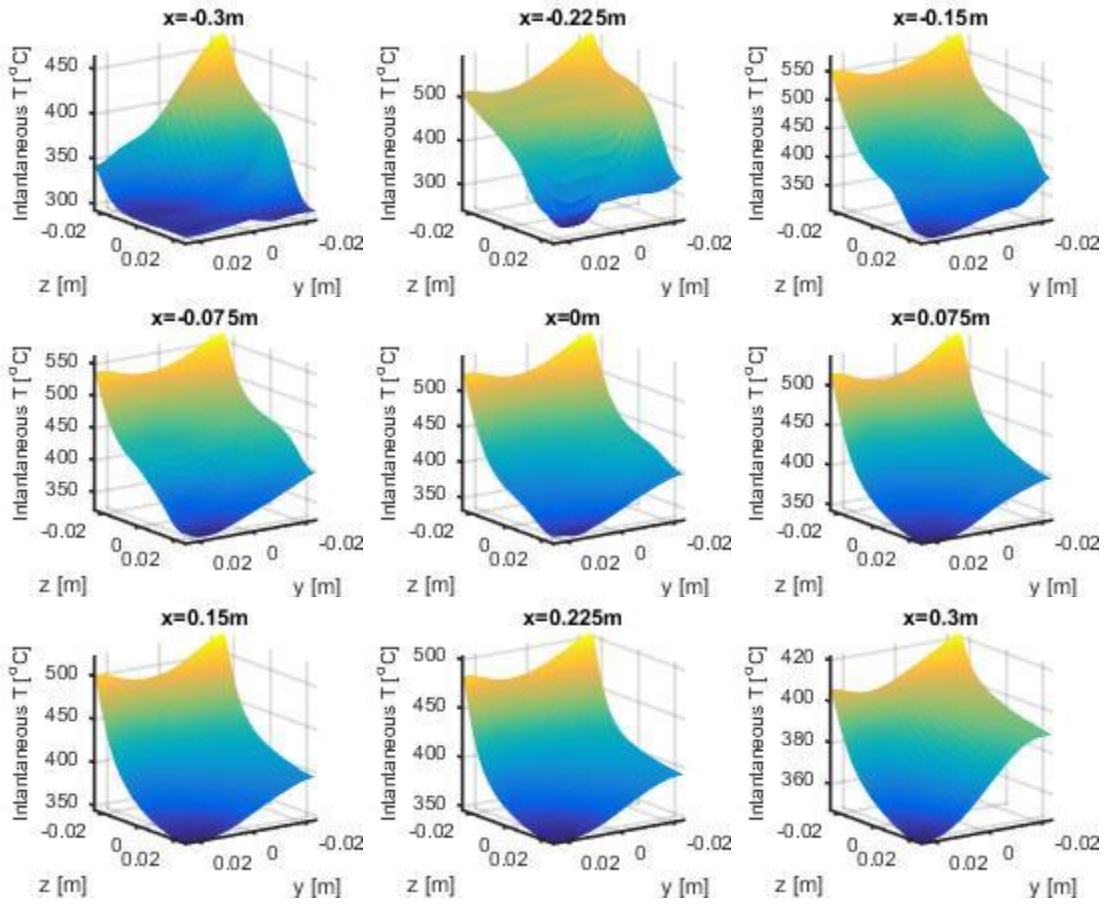

FIG. 83. 2D profiles of the instantaneous temperature field on duct cross-sections at x= -0.3m, -0.225m, -0.15m, -0.075m, 0m, 0.075m, 0.15m, 0.225m, 0.3m for downward flow with surface heating, q_o"=0.20 MW/m^2, B_o=0.5 T, U=0.02 m/s, and ΔT=350.5^{o}C (Ha=220, Re=2027, Gr=1.44x10^8). c_w=0.12.

Downward, nonconducting

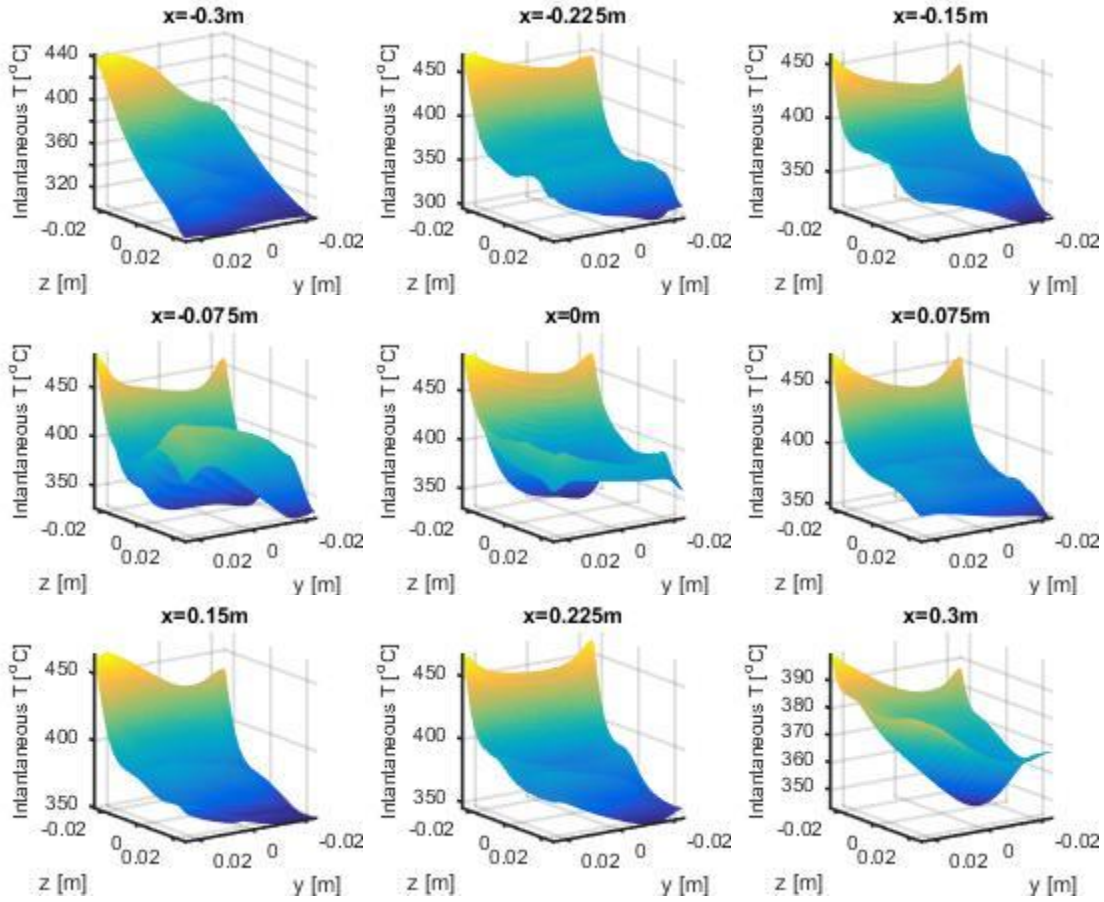

FIG. 84. 2D profiles of the instantaneous temperature field on duct cross-sections at x= -0.3m, -0.225m, -0.15m, -0.075m, 0m, 0.075m, 0.15m, 0.225m, 0.3m for downward flow with surface heating, q_o"=0.20 MW/m^2, B_o=0.5 T, U=0.02 m/s, and ΔT=350.5°C (Ha=220, Re=2027, Gr=1.44x10^8). c_w~0.

Upward, conducting

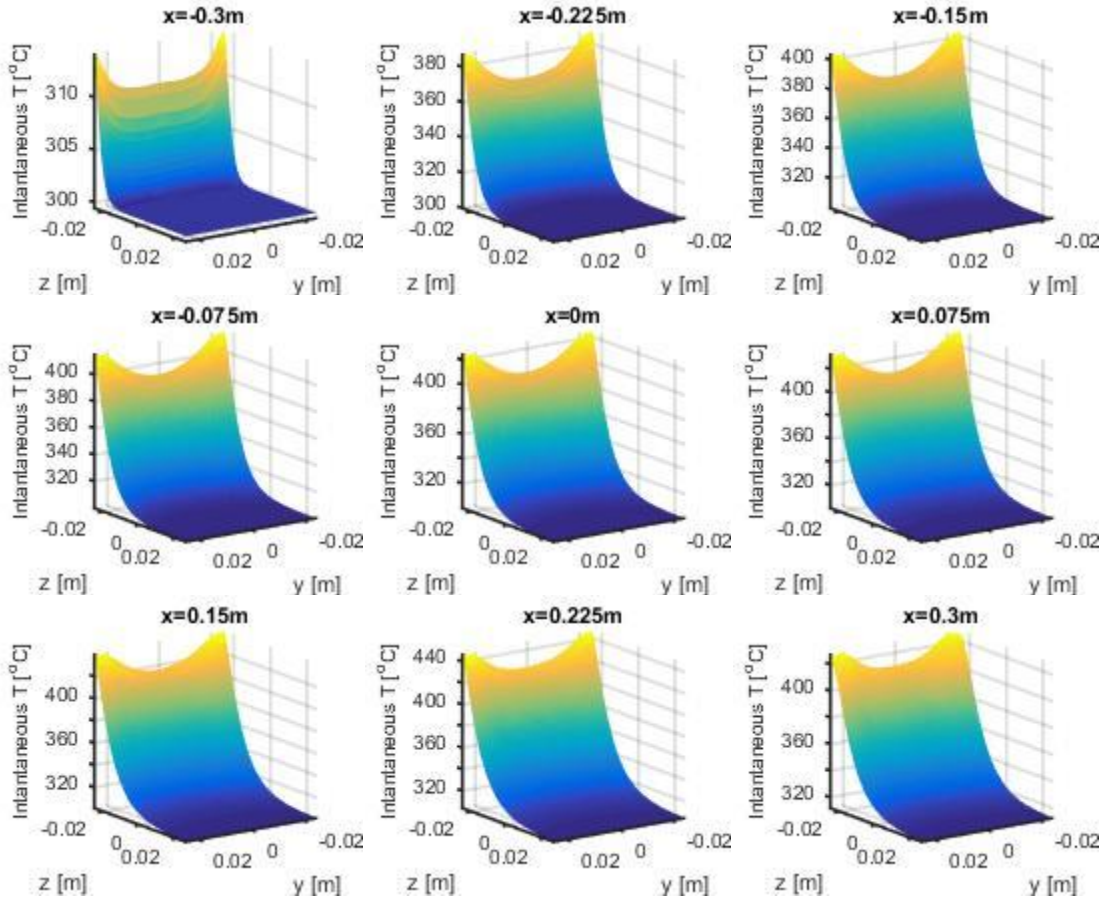

FIG. 85. 2D profiles of the instantaneous temperature field on duct cross-sections at x= -0.3m, -0.225m, -0.15m, -0.075m, 0m, 0.075m, 0.15m, 0.225m, 0.3m for upward flow with surface heating, q_o''=0.20 MW/m^2, B_o=0.5 T, U=0.02 m/s, and ΔT=350.5°C (Ha=220, Re=2027, Gr=1.44x10^8). c_w=0.12.

Upward, nonconducting

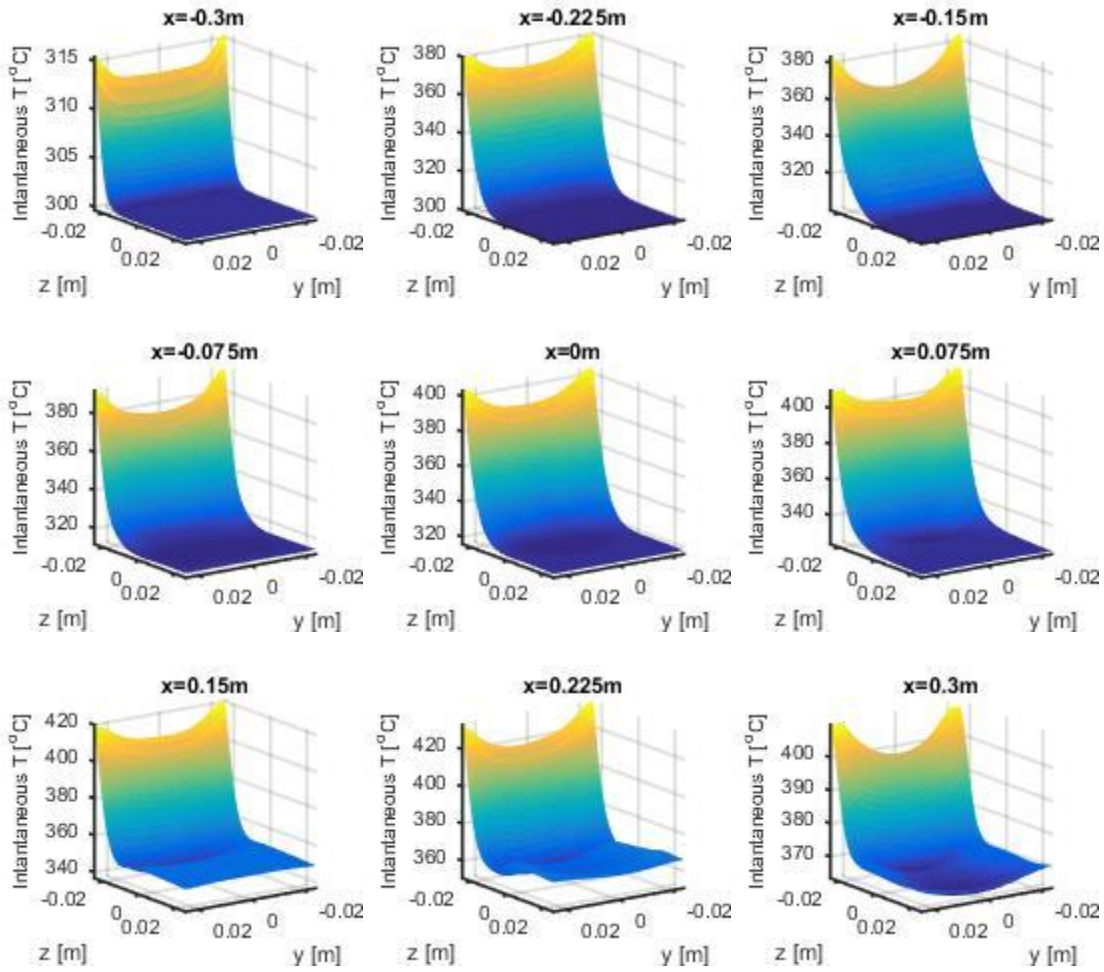

FIG. 86. 2D profiles of the instantaneous temperature field on duct cross-sections at x= -0.3m, -0.225m, -0.15m, -0.075m, 0m, 0.075m, 0.15m, 0.225m, 0.3m for upward flow with surface heating, q_o''=0.20 MW/m^2, B_o=0.5 T, U=0.02 m/s, and ΔT=350.5^{o}C (Ha=220, Re=2027, Gr=1.44x10^8). c_w~0.

6.6 Volumetric Heating

Eight simulations were performed to study the effect of volumetric heating on MHD flows in vertical ducts as compared to surface heating. Both upwards and downwards flows inside conducting and nonconducting duct walls were considered. The magnetic field B_o=0.5 T, mean velocity U=0.02 m/s and total heating per axial length Q'=0.01 MW/m (ΔT=381^{o}C) are the same for all 8 cases (Ha=220, Re=2027, Gr=1.57x10^8). In the first 4 cases, a volumetric heating profile similar to the results of a neutronics simulation performed by M. Riva was used. In the second set of 4 cases, an exponential heating profile was used that is much steeper than the nuclear heating profile such

that nearly all of the heating occurs very near to the sidewall at z=-*a*. In all 8 cases, the volumetric heating occurs inside the fluid domain only. Lastly, the volumetric heating cases are compared with surface heating cases with the same *Q'* to qualify the use of surface heating in studying MHD flows with steep volumetric heating profiles.

In fusion reactor designs, compressed and heated plasma in the reactor core fuses, producing neutrons which then permeate the device. As the neutrons interact with matter in the blankets surrounding the core, volumetric heating is generated within the material. In PbLi, neutrons interact with lead and gammas are emitted, causing the heating to drop off quickly with much of the energy being deposited near the first wall. The high photon production in lead is typical of heavy elements because of high inelastic and capture resonance cross-sections at neutron energy of the order of MeV. As the gammas have a very short mean free path, the energy is ultimately absorbed to become heat near the first wall. The resulting heating curve is much steeper than if the neutrons impinged on pure Li, for instance, which does not have high Z material to quickly attenuate neutrons and produce photons. In the Li, the neutrons have to bounce off of many Li atoms, depositing much of their energy as heat, until the neutron energy is low enough for the nuclear reaction n+Li6->T+He4 + 4.78 MeV (exothermic), to be likely. Furthermore, high energy neutrons are likely to interact with Li7 through the endothermic reaction n+Li7->T+n'+He4-2.5 MeV, thus affecting the shape of the heating curve. As the neutrons behave differently depending on the materials, the volumetric heating curve depends not only on the breeder material but also on the structure and cooling scheme of the blankets. Indeed, the geometry of the reactor and even the shape of the plasma can influence the heating curve in the breeding material. For the present analysis, a heating curve is constructed to resemble the heating produced in PbLi in a wedge piece of a 3D torus which represents a piece of tokamak simulated by M. Riva using MCNP6 1.0 neutron transport code with ENDFB/VII.0. The PbLi is situated behind a thin (5mm) first wall composed of ferritic steel which bounds the plasma region

in the center of the wedge. Though not including the volumetric heating inside the walls or the surface heating on the first wall by bremsstrahlung radiation, this configuration most closely corresponds to the heating inside a self-cooled blanket. The results show that heating is generally higher in the inboard where the magnetic field is also higher compared to the outboard blanket. However, the normalized heating curves for the inboard and outboard blankets were shown to match closely in shape. More information regarding neutronics simulation can be found elsewhere [78]. In Fig. 87 below, the heating profile used in the present analysis is compared with the first 5 cm of the heating curve produced in MCNP for an outboard LM blanket with PbLi at the equator of a tokamak.

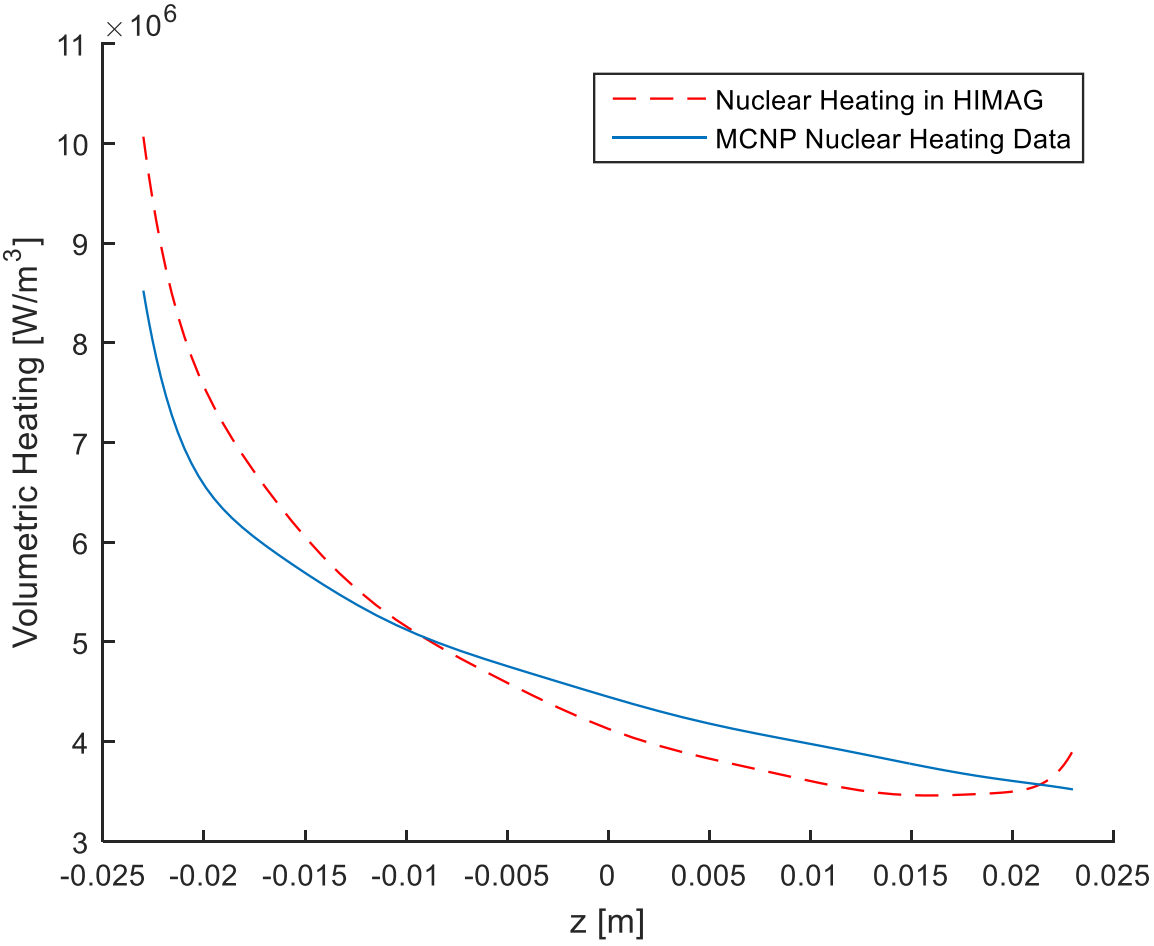

FIG. 87. Volumetric heating profiles. Both heating distributions have the same total heating per axial length Q'=0.01 MW/m when integrated over the fluid cross-section. The heating is uniform along the y-direction.

Here, the curves have been scaled such that their total heating per unit length is the same (*Q'*=0.01 MW/m), assuming that the heating is uniform along the y-direction inside the fluid. In Fig. 87, the dashed red curve is given by the following polynomial and parameters as implemented in HIMAG:

$$q'''(z) = p1 * \left(\frac{z}{a}+1\right)^{10} + p2 * \left(\frac{z}{a}+1\right)^{9} + p3 * \left(\frac{z}{a}+1\right)^{8} + p4 * \left(\frac{z}{a}+1\right)^{7} \ldots \quad (33)$$
$$+p5 * \left(\frac{z}{a}+1\right)^{6} + p6 * \left(\frac{z}{a}+1\right)^{5} + p7 * \left(\frac{z}{a}+1\right)^{4} + p8 * \left(\frac{z}{a}+1\right)^{3} \ldots$$
$$+p9 * \left(\frac{z}{a}+1\right)^{2} + p10 * \left(\frac{z}{a}+1\right) + p11,$$

a=2.3x10^{-2} m,

C=1.012055394224199x10^{7} W/m^{3},

*p*1=1.7569865669577**C*,

*p*2=-1.81685787408323x10^{1}**C*,

*p*3=8.08211328842193x10^{1}**C*,

*p*4=-2.023006874524559x10^{2}**C*,

*p*5=3.130259698018951x10^{2}**C*,

*p*6=-3.100016305296208x10^{2}**C*,

*p*7=1.971743300940257x10^{2}**C*,

*p*8=-7.92480180180538x10^{1}**C*,

*p*9=1.98526103983034x10^{1}**C*,

*p*10=-3.4988089715951**C*,

*p*11=9.946374499912x10^{-1}**C*.

Here, *C* is the maximum heating, *a* is the duct half width, z= [-0.023 m, 0.023 m], and *q'''* is given in W/m^{3}.

In the present analysis, the buoyant effects produced by the nuclear heating distribution given by Eq. 33 are compared with the buoyant effects produced by a much steeper heating profile that is constructed using an exponential formulation. Then, the effect of increasing the heating gradient

can be explored for the same total applied heating. The present analysis' exponential heating curve is plotted along with the nuclear heating curves in Fig. 88 below.

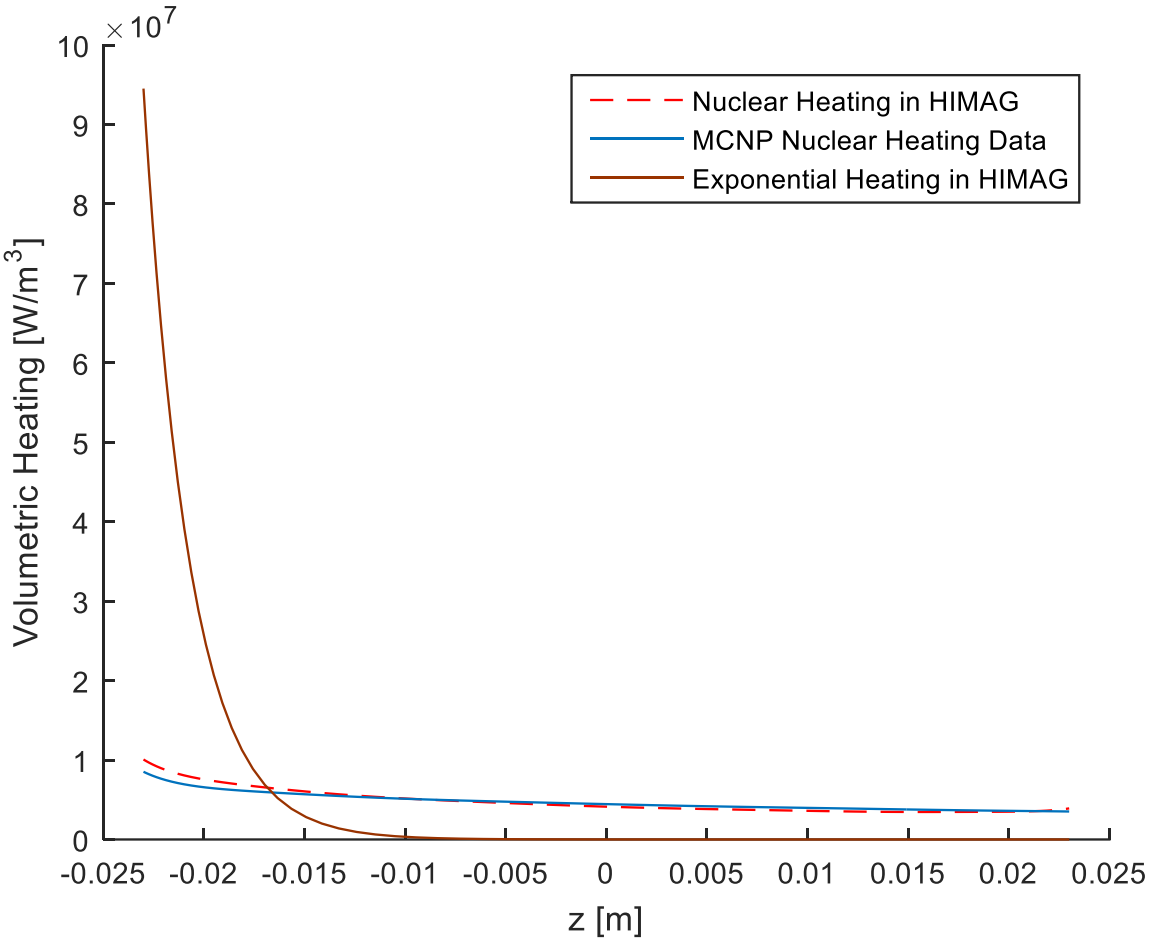

FIG. 88. Volumetric heating profiles. All three heating distributions have the same total heating per axial length Q'=0.01 MW/m when integrated over the fluid cross-section. The heating is uniform along the y-direction.

The curves shown in Fig. 88 all have the same total heating per unit length (*Q'*=0.01 MW/m), assuming that the heating is uniform along the y-direction inside the fluid. The exponential heating curve above is given by:

$$q'''(z) = C * exp(-M * (z/a + 1)), \quad (34)$$

M=10,

C=9.451795860691433x10^7 W/m^3,

a=2.3x10^{-2} m.

Here, C is the maximum heating, a is the duct half width, z= [-0.023 m, 0.023 m], q''' is given in W/m^3, and M is the shape parameter which determines the steepness of the exponential curve. A shape parameter of M=1 would more closely approximate the nuclear heating curves while the high value of M=10 will yield buoyant effects similar to surface heating at the same Q' as will be shown near the end of this analysis. Indeed, one of the motivations for using such a steep exponential heating was to see if such approximation could be used to mimic surface heating.

The volumetric heating in the present simulations is applied uniformly along the y-direction in the fluid domain only.

6.6.A Results of Volumetric Heating Comparison

Both time-averaged and instantaneous results of simulations performed in HIMAG using either an exponential heating or a nuclear heating distribution are shown below including velocity and temperature fields on the y=0 midplane.

6.6.A.i Downward flow with conducting walls:

Exponential

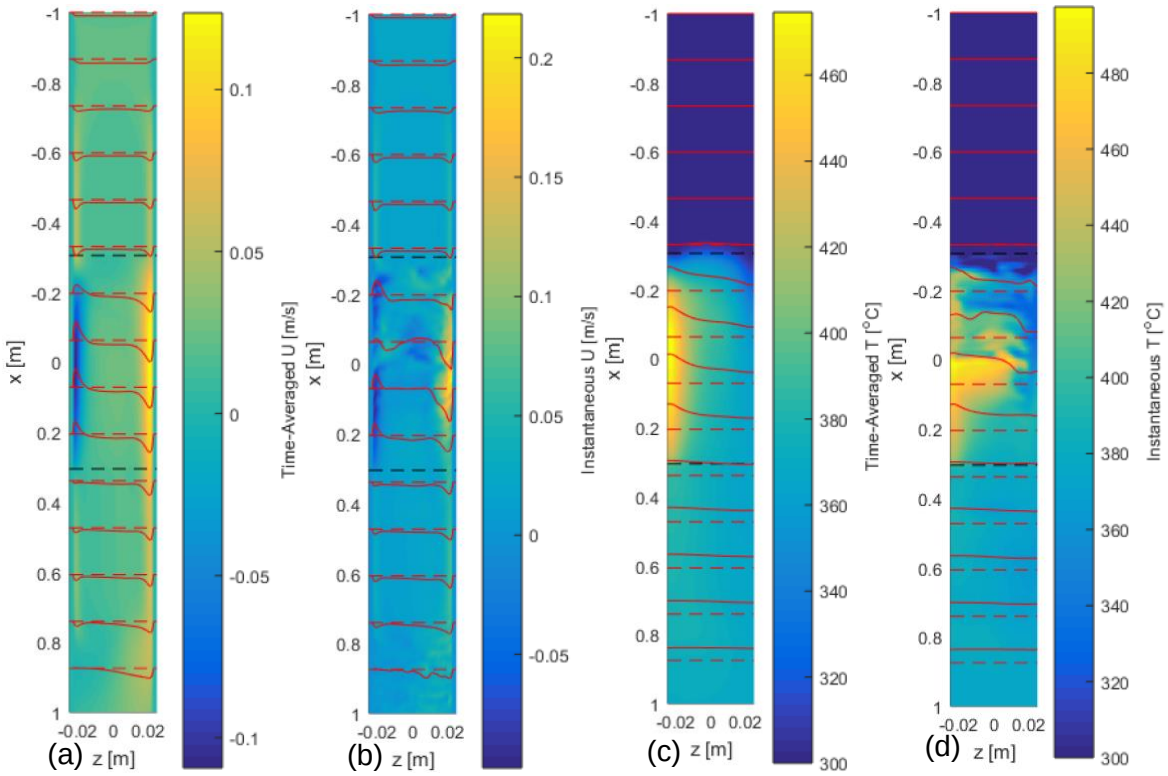

FIG. 89. (a) Time-averaged axial velocity, (b) instantaneous axial velocity, (c) time-averaged temperature, and (d) instantaneous temperature contours and profiles on the y=0 center-plane. B_o=0.5 T, U=0.02 m/s, and ΔT=381°C (Ha=220, Re=2027, Gr=1.57x10^8). c_w=0.12, downward flow with exponential heating. The flow enters from the top in the direction of gravity. The z-axis is stretched compared to the x-axis by a factor of 5 to more easily view the entire flow field. The dashed, red lines spaced every 13.3cm are the zero lines for the profiles which are solid red lines. The dashed, black lines mark the bounds of the heated region.

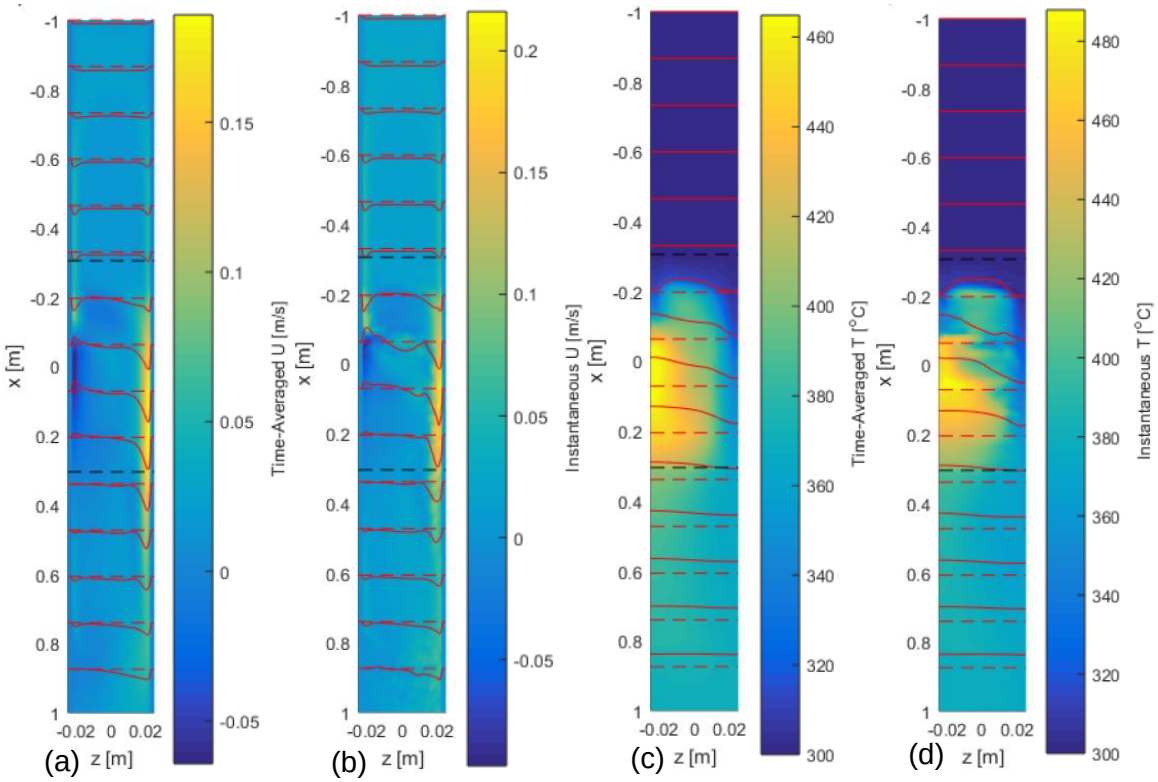

FIG. 90. (a) Time-averaged axial velocity, (b) instantaneous axial velocity, (c) time-averaged temperature, and (d) instantaneous temperature contours and profiles on the y=0 center-plane. B_0=0.5 T, U=0.02 m/s, and ΔT=381°C (Ha=220, Re=2027, Gr=1.57x10^8). c_w=0.12, downward flow with nuclear heating. The flow enters from the top in the direction of gravity. The z-axis is stretched compared to the x-axis by a factor of 5 to more easily view the entire flow field. The dashed, red lines spaced every 13.3cm are the zero lines for the profiles which are solid red lines. The dashed, black lines mark the bounds of the heated region.

For downward flow in electrically conducting ducts, the exponential heating case (Fig. 89), on average, features a longer, thinner reverse flow bubble in the base flow compared to the nuclear heating case (Fig. 90), with the initial boundary layer separation occurring further upstream (x~-0.2 m vs. x~-0.1 m) and the final boundary layer reattachment occurring further downstream (x~0.3 m vs. x~0.2 m). Additionally, the base flow of the exponential heating case features faster reverse flow on the hot sidewall, but also slower forward flow near the cold sidewall and, in general, caries a higher flowrate in the bulk compared to the nuclear heating base flow. Due to the higher concentration of heating near the hot sidewall in the exponential heating case, the time-averaged temperature distribution includes generally steeper gradients and higher

temperatures near the hot wall compared to the nuclear heating case but also has a flatter time-averaged z-direction temperature gradient near the cold wall and is generally colder in the bulk. Interestingly, due to the faster forward flow at the cold wall in the nuclear heating case, the temperature is colder there compared to the exponential case as the competition between advection and diffusion terms becomes more important than the volumetric heating term near the cold wall. The nuclear heating case features a unique behavior near the entrance to the heated region where the temperature maximum is in the center of the duct instead of near the hot wall for ~20 cm until the location of boundary layer separation. In this region, the side layer jets from the M-shaped profile upstream are still strong enough to advect the heat downstream while the balance between conduction and the applied heating term dominates the temperature solution in the slower bulk flow. The applied heating is too concentrated in the exponential heating case and its flow is too unstable to support such a region. As instabilities in buoyancy opposed MHD mixed convection flows are related to both steep axial and steep transverse temperature gradients, the exponential heating case is more unstable than the nuclear heating case, featuring multiple boundary layer separations in the instant shown. And, as the convection terms associated with large-scale flow instability tends to dominate, there is higher temperature contrast in the exponential case than the nuclear case, though both cases have hotspots and coldspots advected into the bulk. This high contrast is also due to the absence of small-scale turbulence that would blend the flow and smooth out the steepest gradients.

6.6.A.ii Upward flow with conducting walls:

Exponential

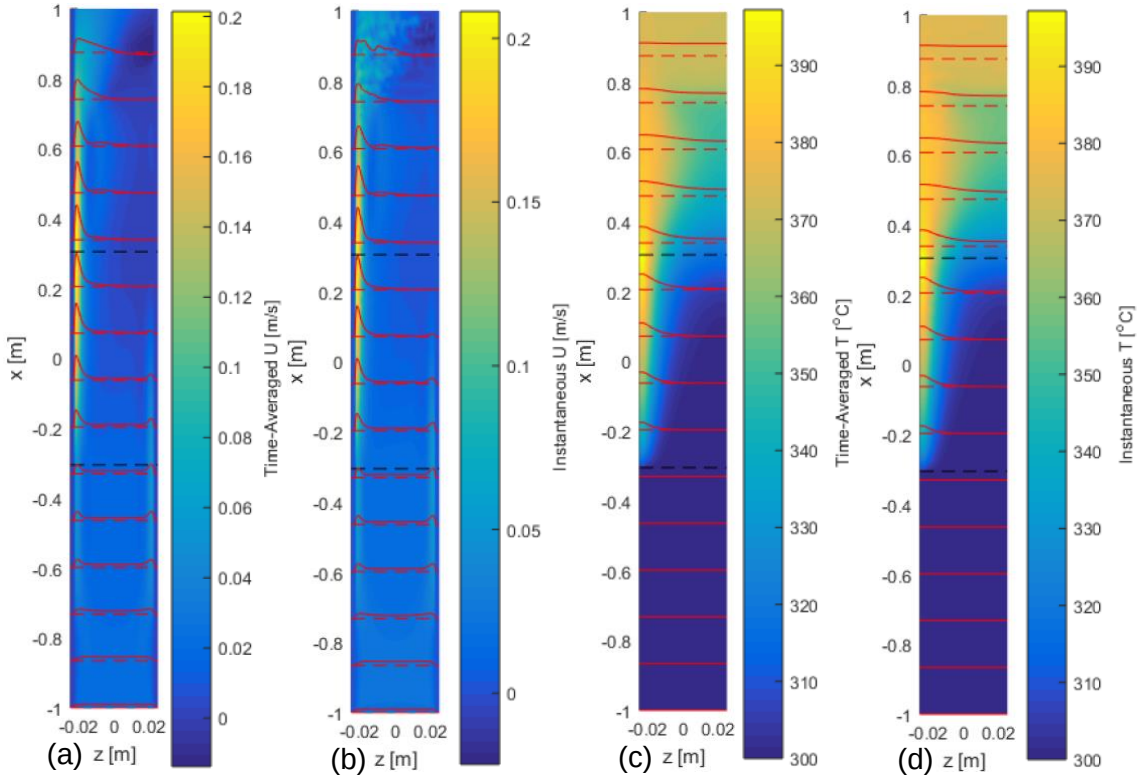

FIG. 91. (a) Time-averaged axial velocity, (b) instantaneous axial velocity, (c) time-averaged temperature, and (d) instantaneous temperature contours and profiles on the y=0 center-plane. B_o=0.5 T, U=0.02 m/s, and ΔT=381°C (Ha=220, Re=2027, Gr=1.57x10^8). c_w=0.12, upward flow with exponential heating. The flow enters from the bottom opposite the direction of gravity. The z-axis is stretched compared to the x-axis by a factor of 5 to more easily view the entire flow field. The dashed, red lines spaced every 13.3cm are the zero lines for the profiles which are solid red lines. The dashed, black lines mark the bounds of the heated region.

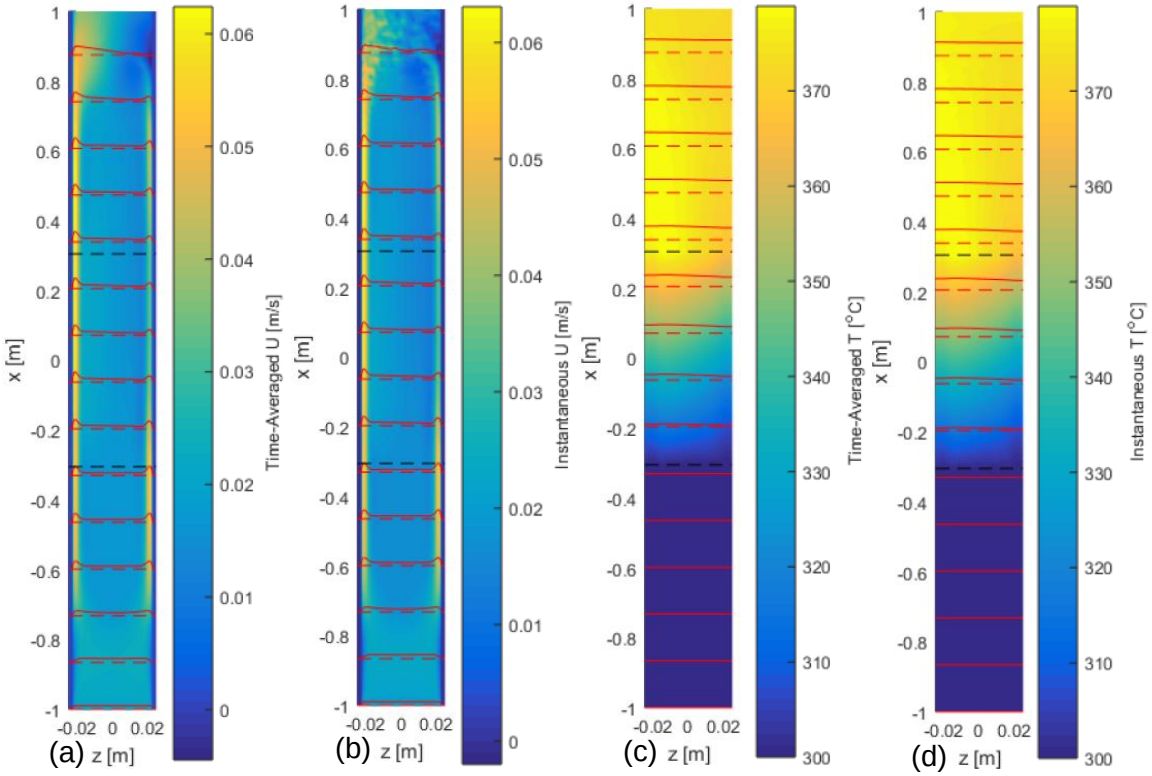

FIG. 92. (a) Time-averaged axial velocity, (b) instantaneous axial velocity, (c) time-averaged temperature, and (d) instantaneous temperature contours and profiles on the y=0 center-plane. B_o=0.5 T, U=0.02 m/s, and ΔT=381°C (Ha=220, Re=2027, Gr=1.57x10^8). c_w=0.12, upward flow with nuclear heating. The flow enters from the bottom opposite the direction of gravity. The z-axis is stretched compared to the x-axis by a factor of 5 to more easily view the entire flow field. The dashed, red lines spaced every 13.3cm are the zero lines for the profiles which are solid red lines. The dashed, black lines mark the bounds of the heated region.

For upward flow in electrically conducting ducts, it is clear from the flow behavior that the buoyant effects are much stronger in the exponential heating case (Fig. 91) than in the nuclear heating case (Fig. 92). Firstly, there is significant flow asymmetry in the heated region of the exponential case with a large buoyant jet forming on the hot sidewall while the side layer jet on the cold wall shrinks to nothing near x=0.2 m. In the nuclear heating case however, the flow remains M-shaped with much smaller velocity asymmetry in the z-direction and more flow carried in the bulk and in the cold side layer than the exponential heating flow. Both flows are stable with only small differences between the base flow and the flow at the instants shown. The temperature profiles show higher temperatures in the exponential case due to the heat being concentrated at the hot

wall where advection associated with the large buoyant jet balances the volumetric heating term. As such, a thin thermal boundary layer exists in the heated region and the cold wall remains at the inlet temperature until the end of the heated region. The opposite is true in the nuclear heating case which features much flatter temperature and velocity profiles as the solution is dominated by the balance of conduction and the more evenly distributed volumetric heating term. Consequently, the temperature maximum is in the bulk rather than near the sidewall and there is only slight temperature asymmetry along the z-direction.

6.6.A.iii Downward flow with nonconducting walls:

Exponential

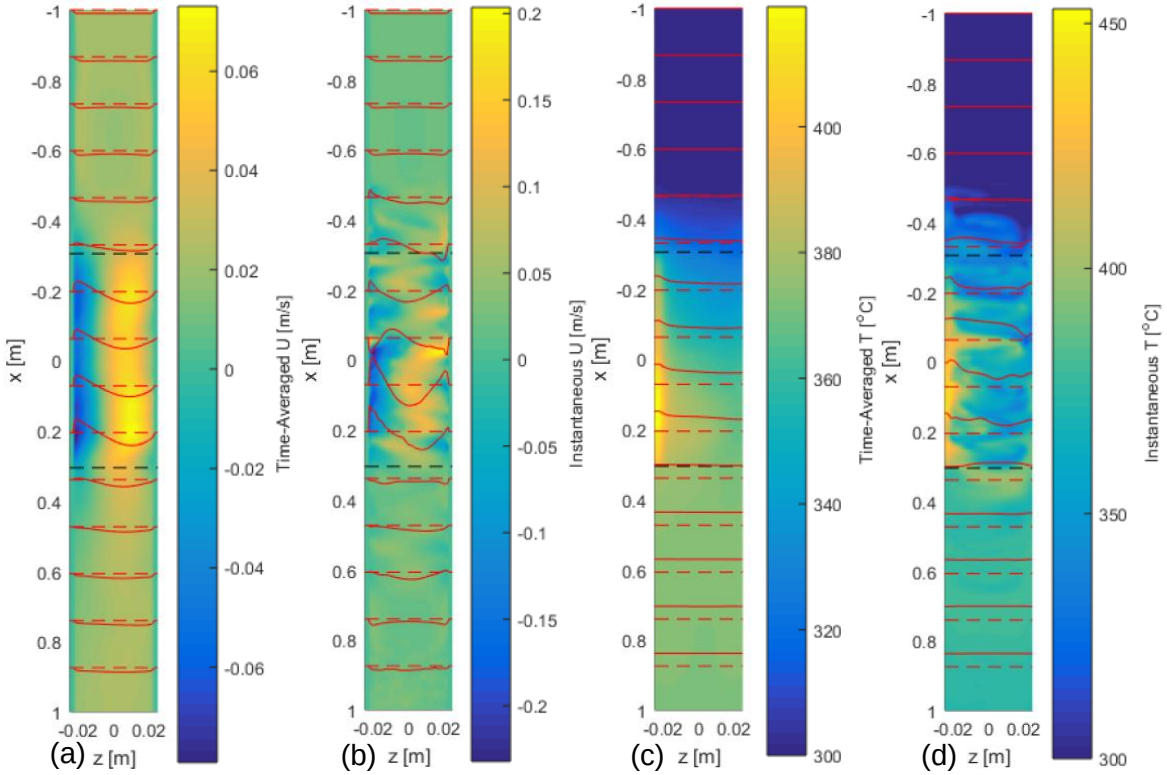

FIG. 93. (a) Time-averaged axial velocity, (b) instantaneous axial velocity, (c) time-averaged temperature, and (d) instantaneous temperature contours and profiles on the y=0 center-plane. B_o=0.5 T, U=0.02 m/s, and ΔT=381°C (Ha=220, Re=2027, Gr=1.57x10^8). c_w~0, downward flow with exponential heating. The flow enters from the top in the direction of gravity. The z-axis is stretched compared to the x-axis by a factor of 5 to more easily view the entire flow field. The dashed, red lines spaced every 13.3cm are the zero lines for the profiles which are solid red lines. The dashed, black lines mark the bounds of the heated region.

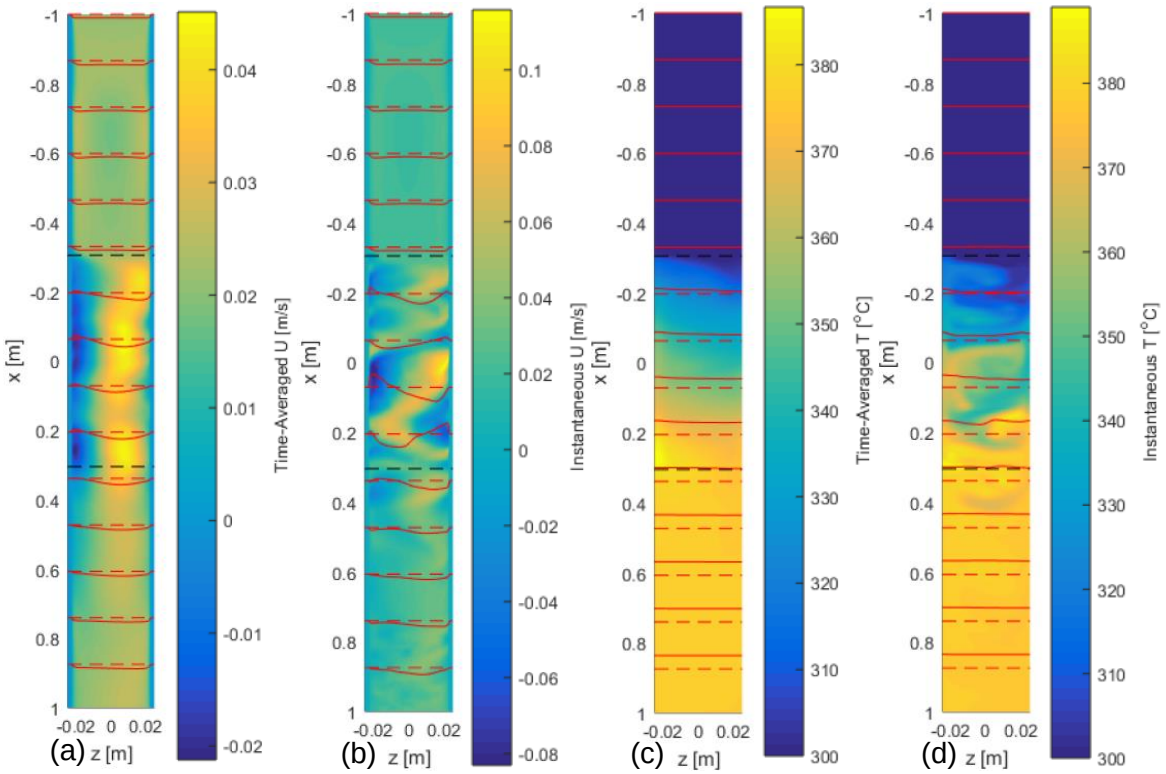

FIG. 94. (a) Time-averaged axial velocity, (b) instantaneous axial velocity, (c) time-averaged temperature, and (d) instantaneous temperature contours and profiles on the y=0 center-plane. B_o=0.5 T, U=0.02 m/s, and ΔT=381°C (Ha=220, Re=2027, Gr=1.57x10^8). c_w~0, downward flow with nuclear heating. The flow enters from the top in the direction of gravity. The z-axis is stretched compared to the x-axis by a factor of 5 to more easily view the entire flow field. The dashed, red lines spaced every 13.3cm are the zero lines for the profiles which are solid red lines. The dashed, black lines mark the bounds of the heated region.

For downward flow in electrically nonconducting ducts, both the exponential heating case (Fig. 93) and the nuclear heating case (Fig. 94) feature large scale flow instability in the heated region which is caused by buoyant effects via the axial temperature gradient as in Rayleigh-Taylor instability. In the time-averaged sense, the exponential case has higher time-averaged temperatures and temperature gradients than the nuclear case near the hot wall. As the buoyant effects are therefore stronger, the exponential case features a longer and thicker reverse flow region attached to the hot wall with buoyant flow propagating upstream of the heated region by ~.13 m while in the nuclear heating case, the reverse flow begins only after the beginning of the heated region. This is because the higher concentration of heating in the exponential case is

sufficient for driving buoyant convection of hot pockets of fluid that propagate upstream until they are cooled enough by conduction to be swept downstream by the oncoming MHD flow. In the nuclear case, the buoyant recirculation of flow is limited to the heated region because the buoyant effects are weaker due to the heating being more spread out. Moreover, in the exponential heating case, the reverse flow and the forward flow demonstrate higher speed and the fluctuations of the velocity field are higher magnitude. Notably, both cases have maximum temperatures near the hot wall on average.

6.6.A.iv Upward flow with nonconducting walls:

Exponential

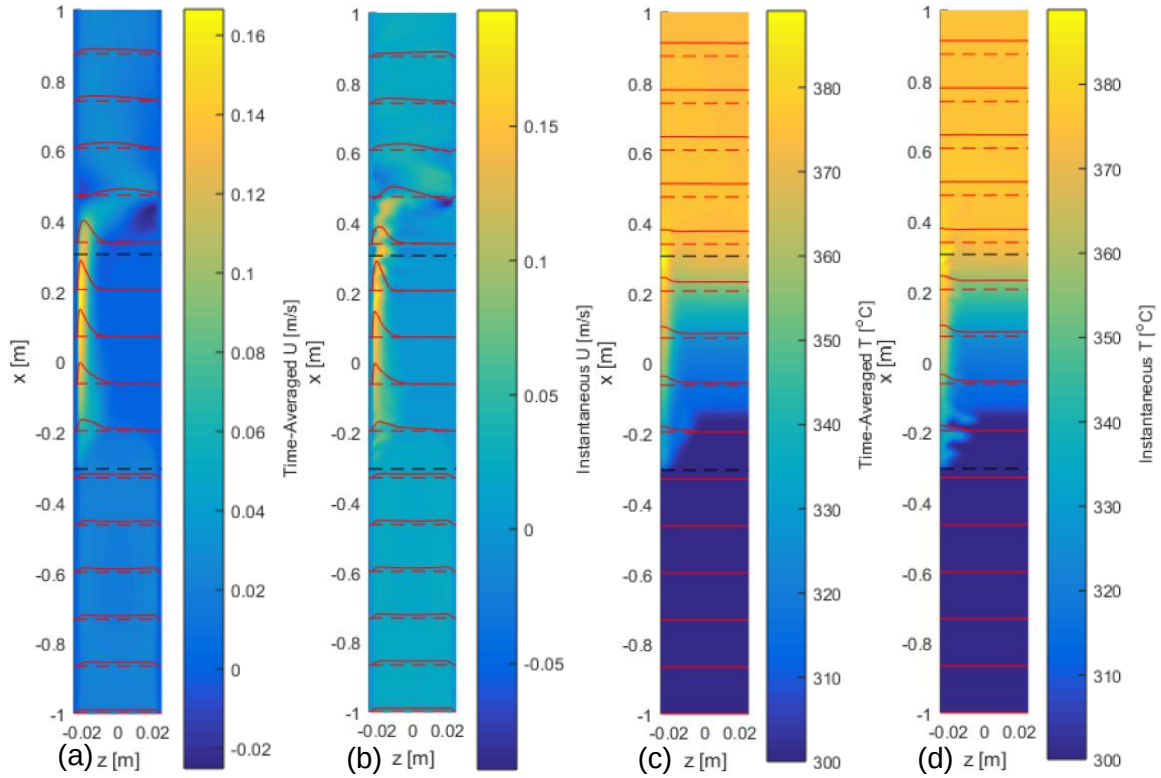

FIG. 95. (a) Time-averaged axial velocity, (b) instantaneous axial velocity, (c) time-averaged temperature, and (d) instantaneous temperature contours and profiles on the y=0 center-plane. B_o=0.5 T, U=0.02 m/s, and ΔT=381°C (Ha=220, Re=2027, Gr=1.57x10^8). c_w~0, upward flow with exponential heating. The flow enters from the bottom opposite the direction of gravity. The z-axis is stretched compared to the x-axis by a factor of 5 to more easily view the entire flow field. The dashed, red lines spaced every 13.3cm are the zero lines for the profiles which are solid red lines. The dashed, black lines mark the bounds of the heated region.

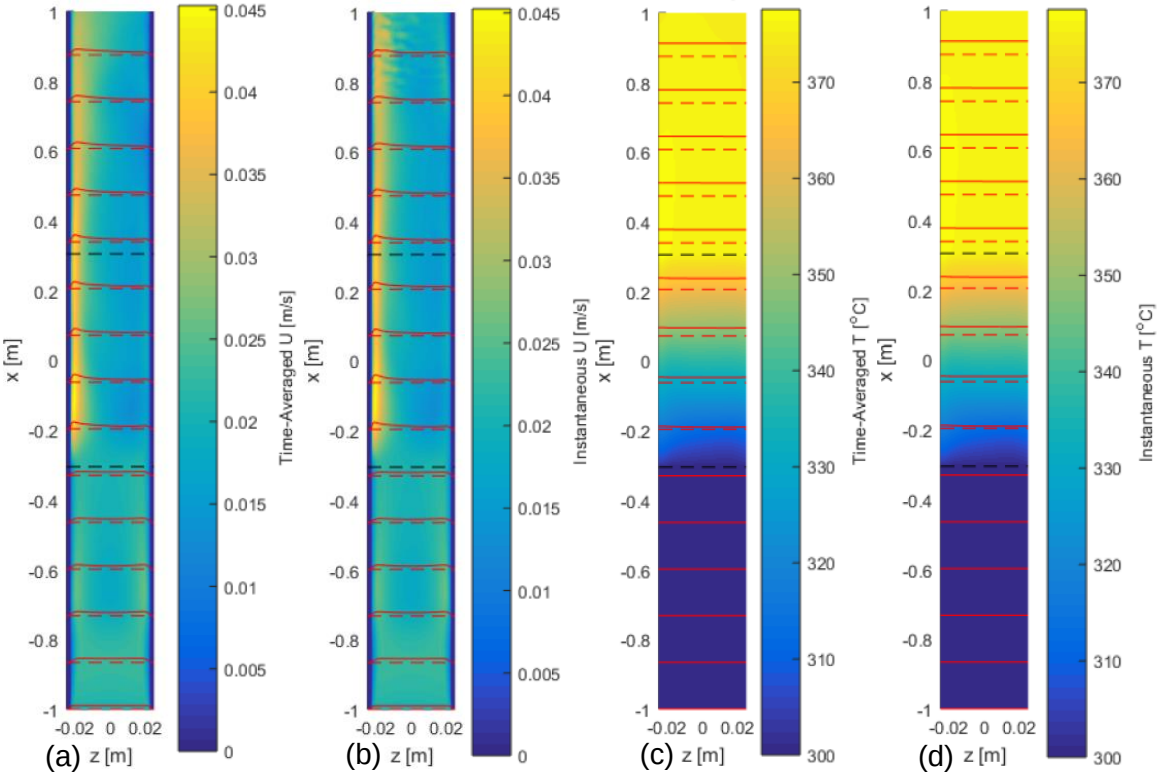

FIG. 96. (a) Time-averaged axial velocity, (b) instantaneous axial velocity, (c) time-averaged temperature, and (d) instantaneous temperature contours and profiles on the y=0 center-plane. B_o=0.5 T, U=0.02 m/s, and ΔT=381°C (Ha=220, Re=2027, Gr=1.57x10^8). c_w~0, upward flow with exponential heating. The flow enters from the bottom opposite the direction of gravity. The z-axis is stretched compared to the x-axis by a factor of 5 to more easily view the entire flow field. The dashed, red lines spaced every 13.3cm are the zero lines for the profiles which are solid red lines. The dashed, black lines mark the bounds of the heated region.

For upward flow in electrically nonconducting ducts, the exponential heating flow (Fig. 95) is unstable whereas the nuclear heating flow (Fig. 96) is stable. The instability advects heat away from the hot wall, smearing out the thermal boundary layer. The nuclear heating flow has no thermal boundary layer and the temperature profile is nearly uniform though it is slightly asymmetric, accounting for the velocity asymmetry along the z-direction. As before, the lack of thermal boundary layer can be explained in part by the fact that the nuclear heating is more spread out than the exponential heating. Consequences of the high concentration of heating in the exponential case include higher temperature and temperature gradient near the hot wall, and lower temperature away from the hot wall where the transverse temperature gradient is very flat.

Furthermore, nearly 100% of the flow rate is carried by the buoyant jet near the hot wall in the exponential heating case while the flow stagnates or recirculates weakly elsewhere. Meanwhile, some of the nuclear heating flow is still carried inside the bulk and the cold side layer.

6.6.B Comparison to Surface Heating Scenarios

Now I go further to compare the results of the exponential heating and nuclear heating cases with the surface heating cases described in section 6.2 for the same magnetic field B_o=0.5 T, mean velocity U=0.02 m/s, and total heating per axial length Q'=0.01 MW/m (Ha=220, Re=2027) and including all four configurations of upward/downward and conducting/nonconducting ducts. ΔT=381°C and Gr=1.57x10^8 for cases with volumetric heating and ΔT=350.5°C and Gr=1.44x10^8 for cases with surface heating. The differences in ΔT are due to the surface heating being applied over y=-b-t_w to b+t_w while the volumetric heating is applied from y=-b to y=b. This results in $q''_{surface}$ being 8% smaller than q''_{volume}. However, both cases are directly comparable since the total heating applied to the system is the same. Time-averaged velocity and temperature profiles at x=0 m, y=0 m are plotted in Figs. 97-100.

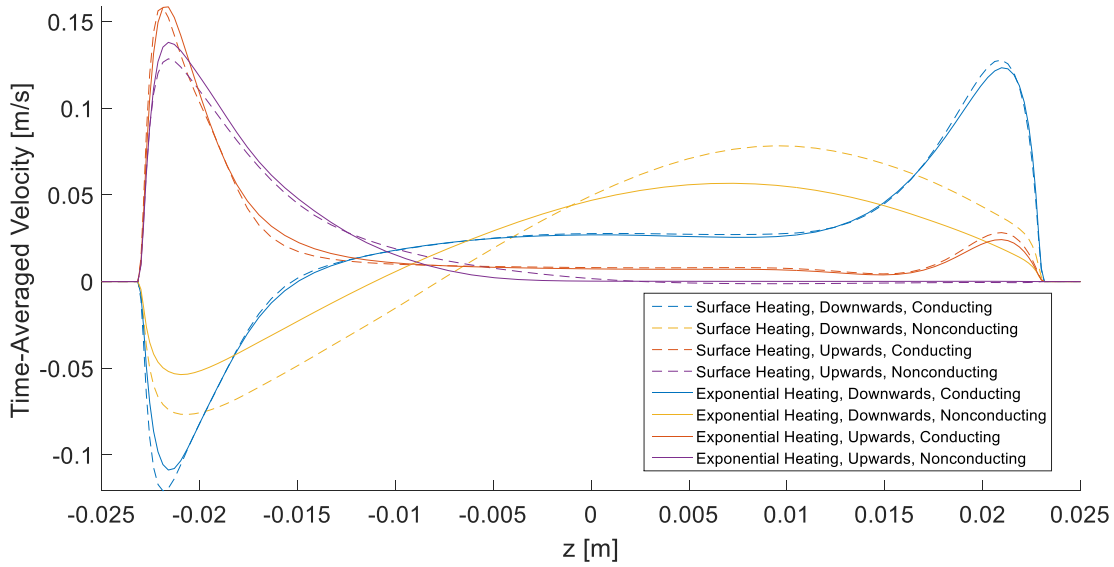

FIG. 97. A comparison of time-averaged velocity profiles at x=y=0m for flows with exponential volumetric heating in the fluid domain or surface heating applied to the outside surface of the duct wall at z=-t_w-a. In all cases, the total heating

is the same. B_o=0.5 T, U=0.02 m/s (Re=2027, Ha=220). c_w=0.12 or ~0, Gr=1.57x10^8 for volumetric heating scenarios and Gr=1.44x10^8 for surface heating scenarios.

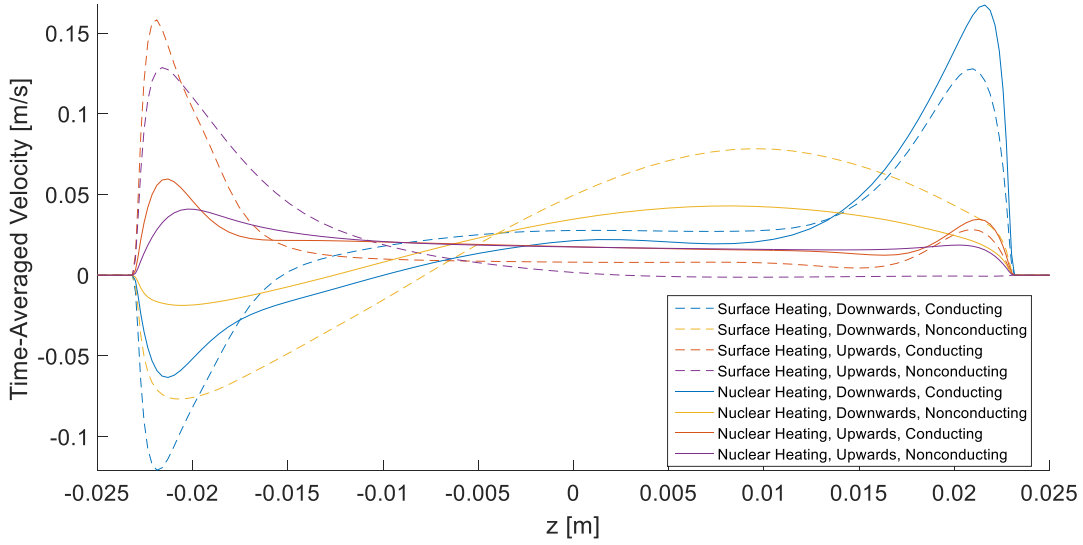

FIG. 98. A comparison of time-averaged velocity profiles at x=y=0m for flows with nuclear volumetric heating in the fluid domain or surface heating applied to the outside surface of the duct wall at z=-t_w-a. In all cases, the total heating is the same. B_o=0.5 T, U=0.02 m/s (Re=2027, Ha=220). c_w=0.12 or ~0, Gr=1.57x10^8 for volumetric heating scenarios and Gr=1.44x10^8 for surface heating scenarios.

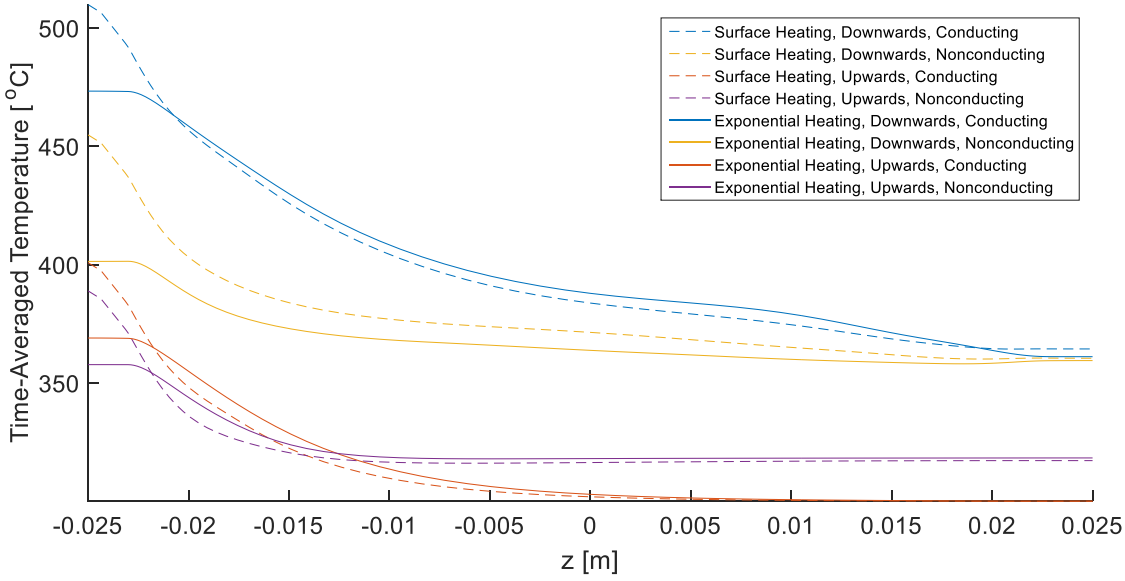

FIG. 99. A comparison of time-averaged temperature profiles at x=y=0m for flows with exponential volumetric heating in the fluid domain or surface heating applied to the outside surface of the duct wall at z=-t_w-a. In all cases, the total heating is the same. B_o=0.5 T, U=0.02 m/s (Re=2027, Ha=220). c_w=0.12 or ~0, Gr=1.57x10^8 for volumetric heating scenarios and Gr=1.44x10^8 for surface heating scenarios.

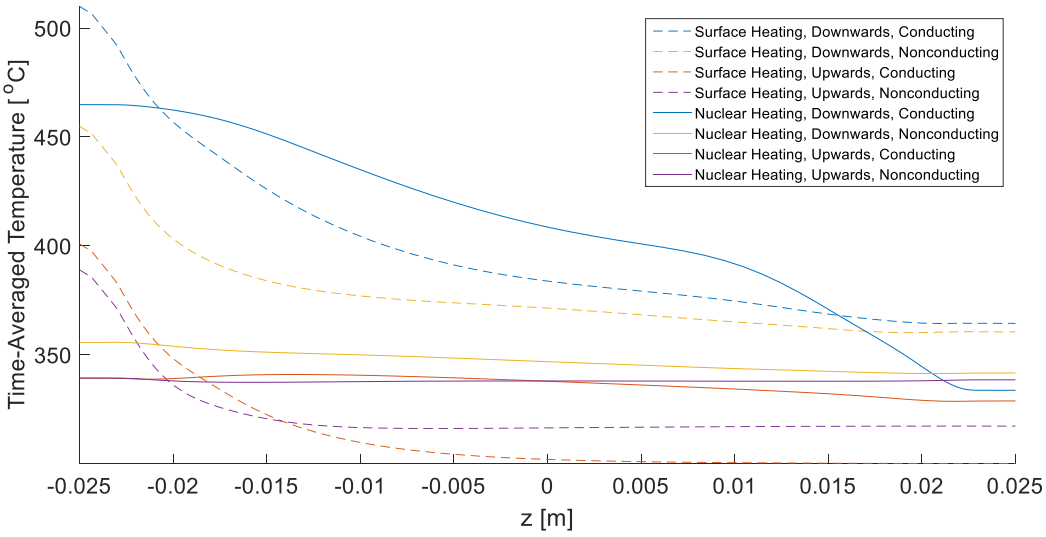

FIG. 100. A comparison of time-averaged velocity profiles at x=y=0m for flows with nuclear volumetric heating in the fluid domain or surface heating applied to the outside surface of the duct wall at z=-t_w-a. In all cases, the total heating is the same. B_o=0.5 T, U=0.02 m/s (Re=2027, Ha=220). c_w=0.12 or ~0, Gr=1.57x10^8 for volumetric heating scenarios and Gr=1.44x10^8 for surface heating scenarios.

As demonstrated in the figures above, the results of the exponential heating case are in close agreement with the surface heating case except for the downward nonconducting case which exhibits somewhat stronger buoyant effects in the surface heating case. The results of the nuclear heating cases then differ from the surface heating cases' results as they did from the exponential heating results in the above analysis. This follows from the concept that as the heating distribution becomes more concentrated near the hot wall, volumetric heating eventually becomes indistinguishable from surface heating. Inside the hot wall, the surface heating cases show much higher temperatures. This is merely a consequence of the boundary conditions and has not been shown to have a significant effect on the flow.

Despite significant differences between results, many of the same phenomena occur for both nuclear heating and the steeper exponential heating cases. For instance, reverse flow occurs in all the downward flows studied here, though the values and magnitude of the velocity and temperature fluctuations were found to depend on the heating distribution. Additionally, velocity

asymmetry occurs in all the upward cases, though again, the magnitude of this effect at constant *Q'* is also dependent on the heating distribution.

Though surface heating is more attainable in laboratory settings, future numerical efforts should consider using nuclear heating distributions at higher *Gr* to more closely model fusion reactor conditions. Since the nuclear heating case exhibits weaker buoyant effects than the surface heating case with the same *Q'*, perhaps the flow behavior of surface heating cases better approximates nuclear heating cases with much higher *Q'*. Consider that increasing *Q'* by scaling up the magnitude of the nuclear heating will also increase the gradient of the heating by a proportional amount. Thus, it follows that the temperature gradients will be steeper and the buoyant effects will be stronger.

The differences between upward and downward flows or differences between conducting and nonconducting ducts are associated with significant differences in the types of phenomena observed while the differences caused by varying the heating profiles were more a matter of magnitude such that surface heating has been proven to serve as a reasonable approximation for the volumetric heating profile in experimental settings; however, it can be expected that surface heating cases will have somewhat stronger buoyant effects than volumetric heating cases with the same *Q'*. Surface heating cases can be simulated using either purely surface heating (i.e. through the boundary conditions) or exponential volumetric heating at high *M* (i.e. through the source term on the right-hand-side of the energy equation). These conclusions were made by comparing instantaneous and time-averaged temperature and velocity fields.

6.7 Results for Comparison

Results for an MHD mixed convection flow simulation (#16 in Table 4) is presented in this section for the purpose of comparison to experimental and numerical results. A comparison to Y. Yan's

COMSOL Multiphysics numerical results is also provided. Additionally, techniques for measuring velocity via electric potential measurements in an experimental setting are discussed.

Case 16 is a benchmark case with simulation parameters that correspond with an experiment in the MaPLE-U facility at UCLA. The flow behavior of Case 16 is interesting in that the velocity decreases moving into the heated region and then reverses direction near the hot wall. This makes Case 16 a good case for comparison because the temperature distribution is strongly affected by the flow reversal so both temperature and velocity measurements can be used to identify this phenomenon. The simulation parameters are listed in Table 7 below. The fluid properties are that of PbLi at 300°C. See Chapter 5 for more simulation details including the geometry, magnetic field, initial and boundary conditions, and more. Some of the presented data is time-averaged, meaning the flow variables are averaged over all the timesteps between step number 1 million and the final timestep number listed in Table 7.

Table 7. Simulation Parameters for Case 16

Flow Direction	Down
c_w	0.12
Heating Mode	Surface
U	3 cm/s
B	0.5 T
q_o''	0.04 MW/m^2
ΔT	70.11°C
Ha	220
Re	3041
Gr	2.88x10^7
Final Timestep	4.9x10^6

6.7.A Calculating Velocity Via Electric Potential Measurements

Measuring electric potential is a convenient way to measure the velocity in MHD flow experiments, particularly due to the challenges posed by the opacity of the LM and the temperature gradients and non-hydrodynamic forces present in the fluid. The y=0 centerline velocity profile at an axial location $x=x_i$, can be estimated via data from a line of multiple electric potential probes on the Hartmann walls at x_i. However, the error associated with this measurement can theoretically be reduced by measuring the electric potential inside the fluid with a Levi probe on the y=0 centerline instead. The theory is as follows, beginning with Ohm's law shown in Eq. 34:

$$\frac{\mathbf{J}}{\sigma} = -\nabla\phi + \mathbf{U} \times \mathbf{B} \tag{34}$$

An assumption is made that since σ is large, the left-hand-side of Eq. 34 can be neglected, and with $\mathbf{B} = \mathrm{B}\hat{\boldsymbol{y}}$ Ohm's law reduces to Eq. 35.

$$\begin{bmatrix} -\mathrm{w} \\ 0 \\ \mathrm{u} \end{bmatrix} = \frac{1}{\mathrm{B}} \begin{bmatrix} \partial_{\mathrm{x}}\phi \\ \partial_{\mathrm{y}}\phi \\ \partial_{\mathrm{z}}\phi \end{bmatrix} \tag{35}$$

From the z-component of Eq. 35, the axial velocity can be calculated by taking the derivative of φ along the z-direction. Additionally, the y-component of Eq. 35 shows that the electric potential is uniform along the magnetic field direction since $\partial_y\phi = 0$. Thus $\partial_{\mathrm{z}}\,\partial_{\mathrm{y}}\phi = 0$, and so, it can be concluded that the velocity profile is uniform along the magnetic field direction. However, this conclusion is not valid where our assumption that $\mathbf{J}/\sigma$ is negligible breaks down (i.e. inside MHD boundary layers and the solid walls). Fig. 101 shows axial velocity profiles at x=-0.3 m and x=0 m for Case 16. Note how the velocity is not uniform along the magnetic field direction inside the side layers (z~+/-0.02 m) and the Hartmann layers (y~+/-0.02 m) but is uniform in y inside the bulk.

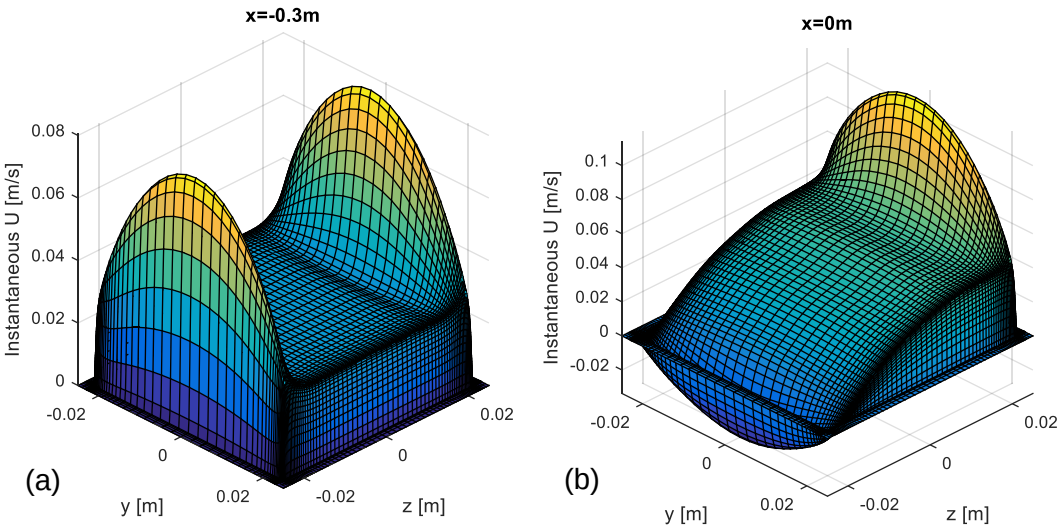

FIG. 101. Instantaneous axial velocity profiles at (a) x=-0.3 m and (b) x=0 m. Downward flow with surface heating. B_o=0.5 T, U=0.03 m/s, q_o"=0.04 MW/m^2 (Ha=220, Re=3041, Gr=2.88x10^7). c_w=0.12.

However, the bulk velocity can be calculated accurately by measuring φ at the outside of the Hartmann walls since the conclusion that $\partial_y \phi = 0$ still holds as J_y is generally close to zero outside of the side layers and sidewalls. Still, since J_y is nonzero in the side layers, wall measurements of φ will be insufficient for calculating the velocity in the side layers. Fig. 102 shows electric potential distribution at x=-0.3 m and x=0 m for Case 16. Note the regions where $\partial_y \phi = 0$ as indicated by flat horizontal isolines of φ.

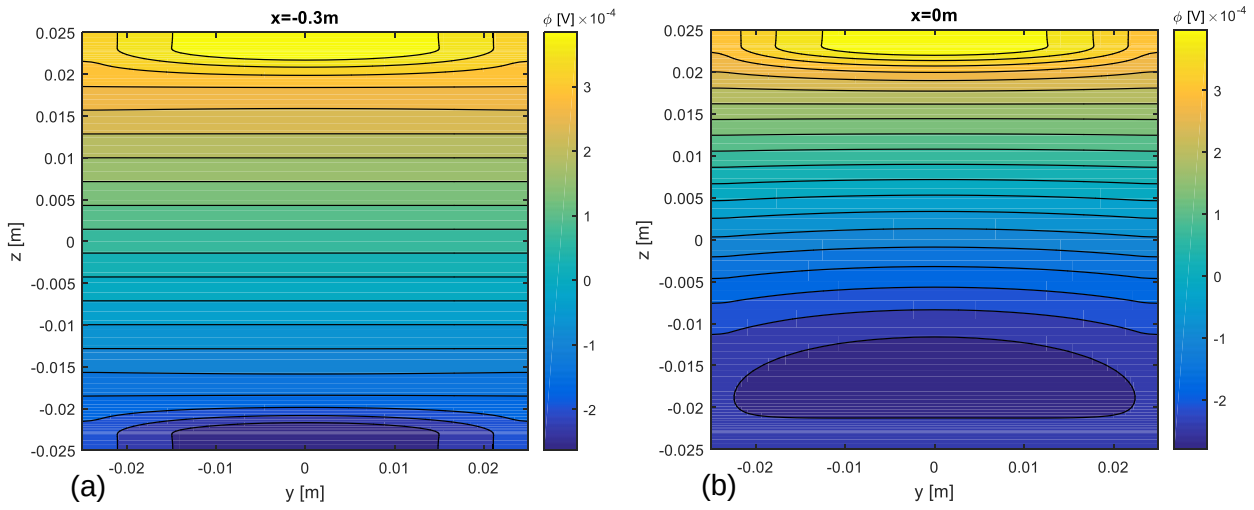

FIG. 102. Contours of instantaneous electric potential on duct cross-sections at (a) x=-0.3 m and (b) x=0 m. Downward flow with surface heating. B_o=0.5 T, U=0.03 m/s, q_o"=0.04 MW/m^2 (Ha=220, Re=3041, Gr=2.88x10^7). c_w=0.12.

By using a Levi probe to measure $\partial_z\phi$ along the y=0 centerline in order to measure the y=0 centerline velocity profile with low error, the need to rely on $\partial_y\phi$ being equal to zero is eliminated. The remaining source of error is the small amount of z-direction current which will generally cause the velocity predictions to be slightly smaller than the actual velocity.

To illustrate the method of using electric potential probes to measure the velocity, example calculations are performed using the results from Case 16 at x=0 m and x=-0.3 m. To imitate both surface electric potential probes and Levi probes which penetrate the fluid domain at y=0, electric potential data are taken from the outsides of each Hartmann wall as well as from the y=0 centerline. The results of these calculations, along with the computed velocity profiles, are shown in Fig. 103.

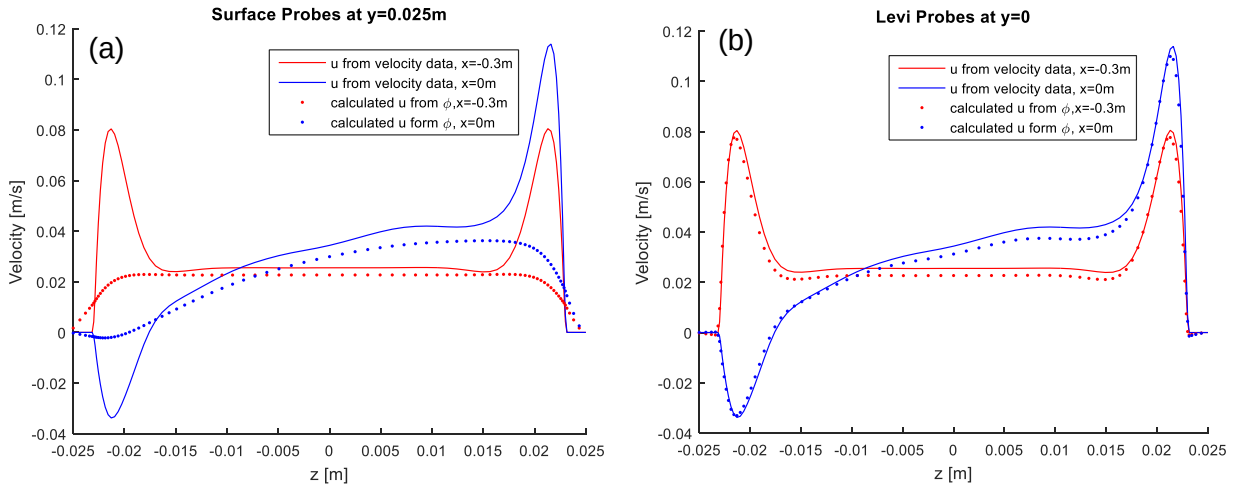

FIG. 103. Instantaneous axial velocity profiles at y=0m, x=-0.3m, 0m. Using Eq. 35, velocity profiles are constructed with electric potential data from (a) y=0.025m and (b) y=0m. Downward flow with surface heating. B_o=0.5 T, U=0.03 m/s, q_o''=0.04 MW/m^2 (Ha=220, Re=3041, Gr=2.88x10^7). c_w=0.12.

As predicted, the measured velocity features large errors in the side layers when using the surface electric potential due to y-direction electric currents. Such currents also exist near the velocity zero near z~-0.17 though they are smaller. These errors disappear when probing the electric potential at y=0 since the calculation does not rely on $J_y = -\partial_y \phi = 0$. The remaining error in both cases is attributed to z-direction current which approaches zero near the sidewalls.

6.7.B Simulation Results for Direct Comparison

The results of Case 16 are presented below in Figs. 104-117 for the purposes of code-to-code and code-to-experiment comparison.

The bulk temperature, which represents the average temperature of the fluid, is calculated using Eq. 36 below.

$$Bulk\ Temperature = \frac{\iint UTdydz}{\iint Udydz} \tag{36}$$

In a steady flow, the difference between the value of the bulk temperature at the end of the duct and the inlet temperature corresponds to a temperature difference, ΔT_b, in the following statement of energy conservation in the duct:

$$A\rho UC_p\Delta T_b = \iint q''dydx \tag{37}$$

Solving for ΔT_b with Case 16's parameters (A=0.02116m^2, L_h=0.6096m, ρ=9486kg/m^3, U=0.03m/s, C_p=200.22 J/kg K, q_o"=0.04MW/m^2), the result is ΔT_b=10.11K. The bulk temperature of Case 16 at the final timestep is plotted in Fig. 104 and shows a temperature difference of 9.9K (a difference of 2.08% compared to the ΔT_b computed from Eq. 37). The difference could be accounted for by the unsteadiness of the flow.

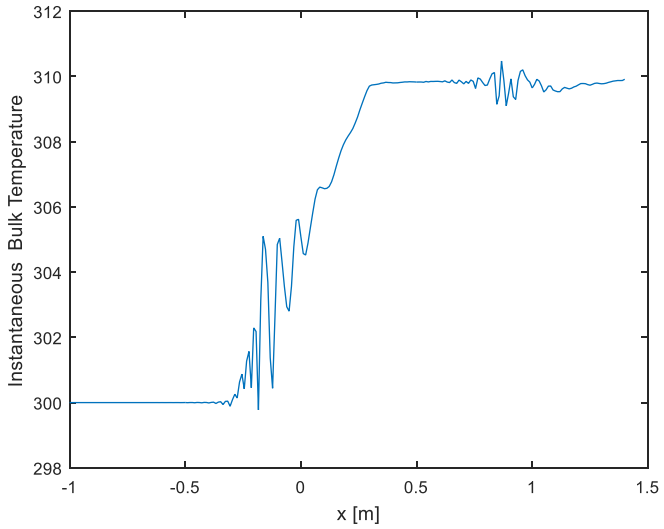

FIG. 104. The instantaneous bulk temperature for downward flow and surface heating for B_o=0.5 T, U=0.03 m/s, q_o"=0.04 MW/m^2 (Ha=220, Re=3041, Gr=2.88x10^7). c_w=0.12.

The time-averaged axial velocity profiles at six axial locations x=-0.25 m, -0.15 m, -0.05 m, 0.05 m, 0.15 m, and 0.25 m are shown in Figs. 105 and 106 below for y=0 and z=0 respectively.

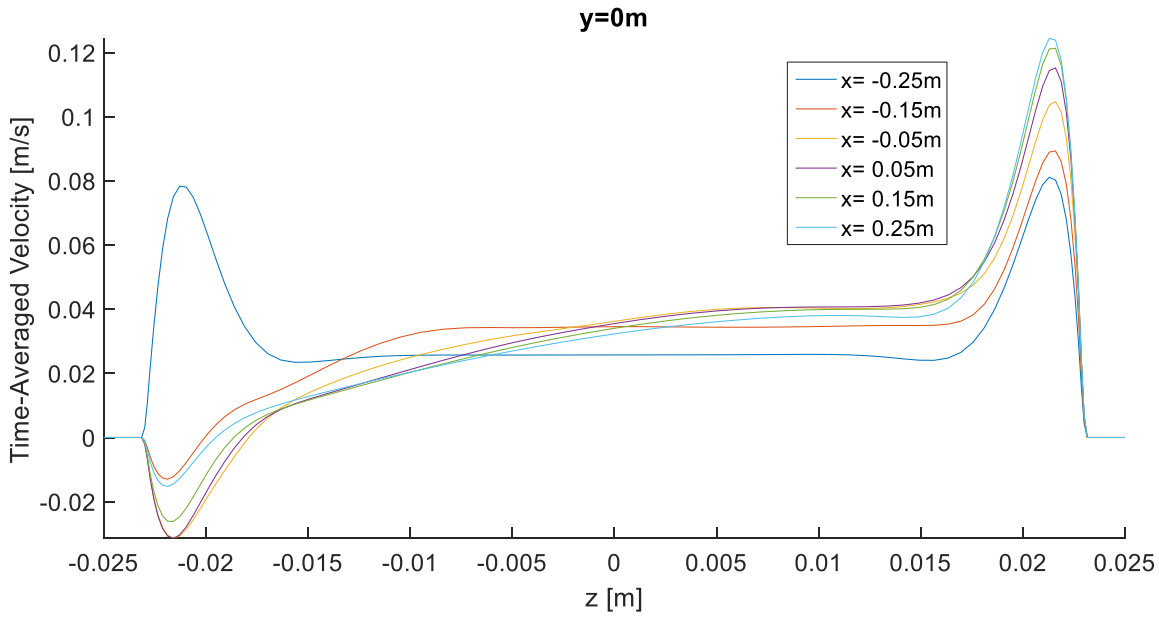

FIG. 105. Time-averaged velocity at y=0m, x= -0.25 m, -0.15 m, -0.05 m, 0.05 m, 0.15 m, and 0.25 m. Downward flow with surface heating. B_o=0.5 T, U=0.03 m/s, q_o''=0.04 MW/m^2 (Ha=220, Re=3041, Gr=2.88x10^7). c_w=0.12.

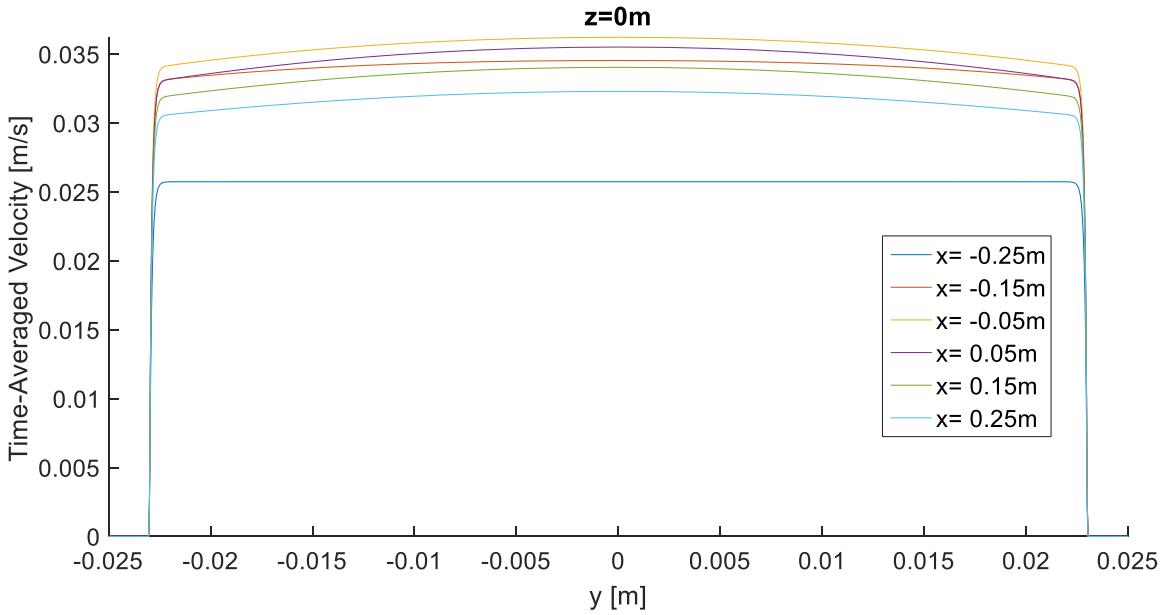

FIG. 106. Time-averaged velocity at z=0m, x= -0.25 m, -0.15 m, -0.05 m, 0.05 m, 0.15 m, and 0.25 m. Downward flow with surface heating. B_o=0.5 T, U=0.03 m/s, q_o''=0.04 MW/m^2 (Ha=220, Re=3041, Gr=2.88x10^7). c_w=0.12.

The time averaged temperature profiles at six axial locations x=-0.25 m, -0.15 m, -0.05 m, 0.05 m, 0.15 m, and 0.25 m are shown in Figs. 107 and 108 below for y=0 and z=0 respectively.

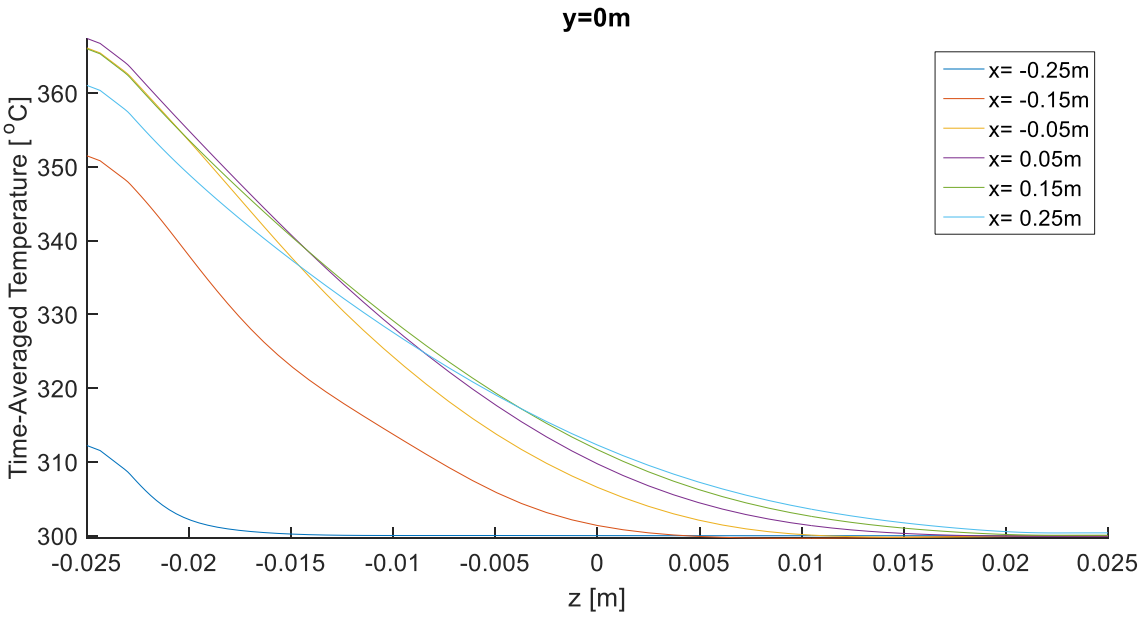

FIG. 107. Time-averaged temperature at y=0 m, x= -0.25 m, -0.15 m, -0.05 m, 0.05 m, 0.15 m, and 0.25 m. Downward flow with surface heating. B_o=0.5 T, U=0.03 m/s, q_o"=0.04 MW/m^2 (Ha=220, Re=3041, Gr=2.88x10^7). c_w=0.12.

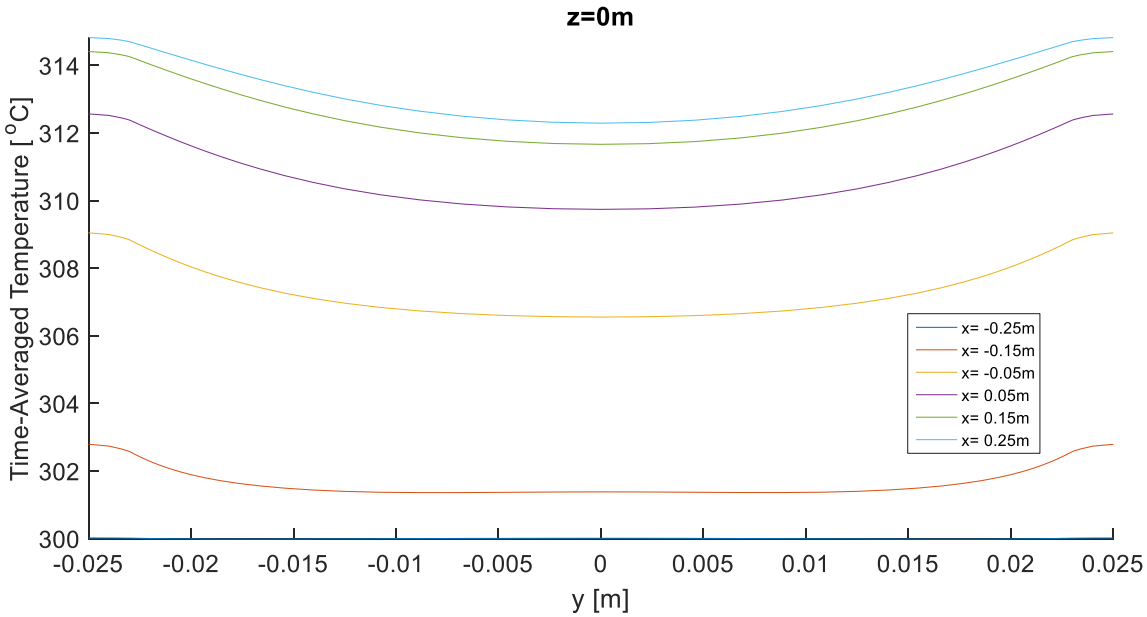

FIG. 108. Time-averaged temperature at z=0 m, x= -0.25 m, -0.15 m, -0.05 m, 0.05 m, 0.15 m, and 0.25 m. Downward flow with surface heating. B_o=0.5 T, U=0.03 m/s, q_o"=0.04 MW/m^2 (Ha=220, Re=3041, Gr=2.88x10^7). c_w=0.12.

The time-averaged temperature at 7 axial locations x=-0.3 m, -0.2 m, -0.1 m, 0 m, 0.1 m, 0.2 m, and 0.3 m on the outside surfaces of each of the four walls are shown in Figs. 109-112.

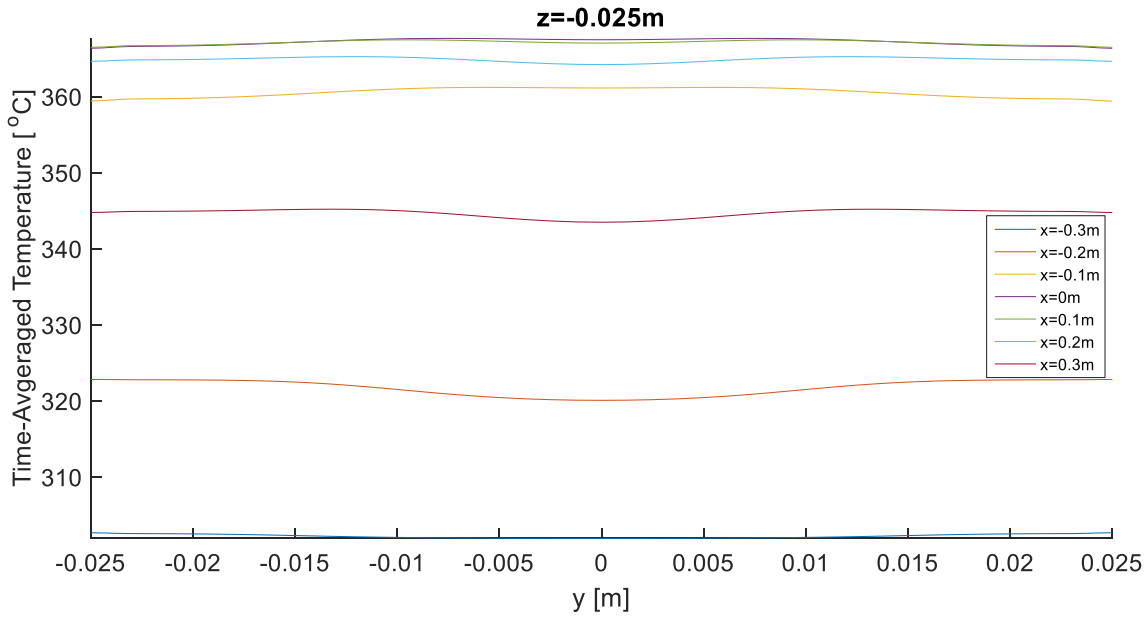

FIG. 109. Time-averaged temperature on the outer surface of the wall at z=-0.025 m, x=-0.3 m, -0.2 m, -0.1 m, 0 m, 0.1 m, 0.2 m, and 0.3 m. Downward flow with surface heating. B_o=0.5 T, U=0.03 m/s, q_o"=0.04 MW/m^2 (Ha=220, Re=3041, Gr=2.88x10^7). c_w=0.12.

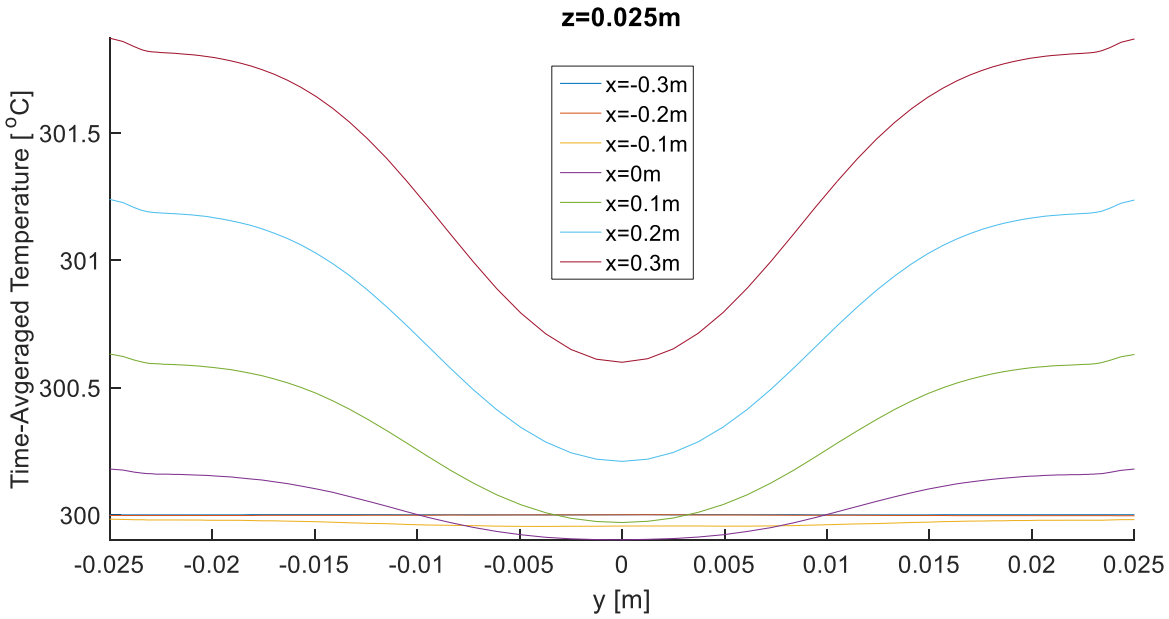

FIG. 110. Time-averaged temperature on the outer surface of the wall at z=0.025 m, x=-0.3 m, -0.2 m, -0.1 m, 0 m, 0.1 m, 0.2 m, and 0.3 m. Downward flow with surface heating. B_o=0.5 T, U=0.03 m/s, q_o"=0.04 MW/m^2 (Ha=220, Re=3041, Gr=2.88x10^7). c_w=0.12.

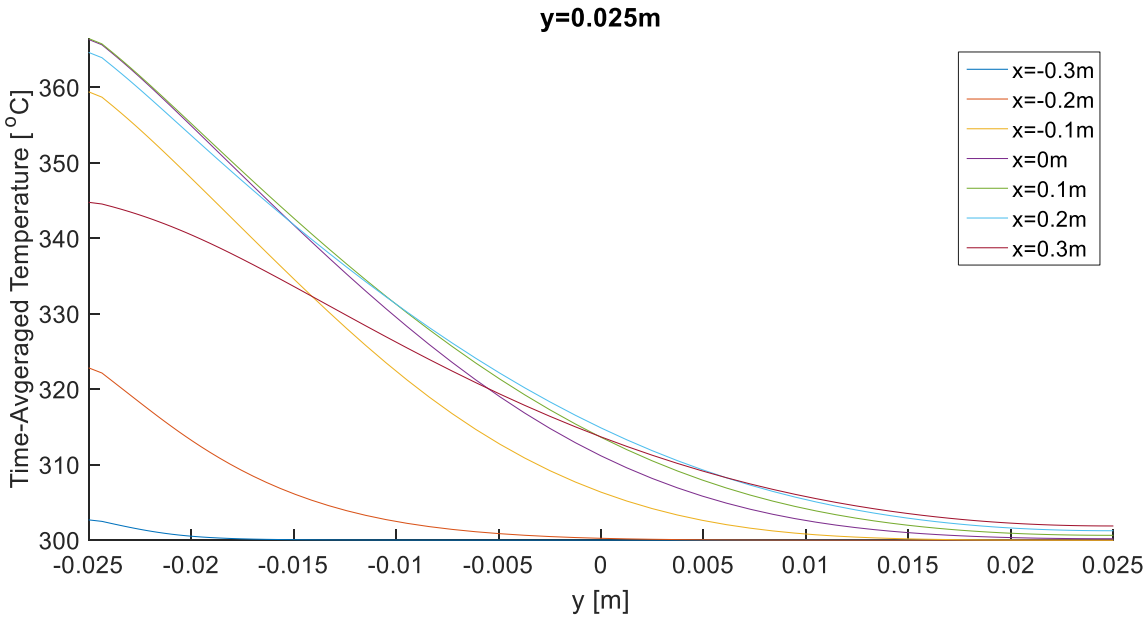

FIG. 111. Time-averaged temperature on the outer surface of the wall at y=0.025 m, x=-0.3 m, -0.2 m, -0.1 m, 0 m, 0.1 m, 0.2 m, and 0.3 m. Downward flow with surface heating. B_o=0.5 T, U=0.03 m/s, q_o"=0.04 MW/m^2 (Ha=220, Re=3041, Gr=2.88x10^7). c_w=0.12.

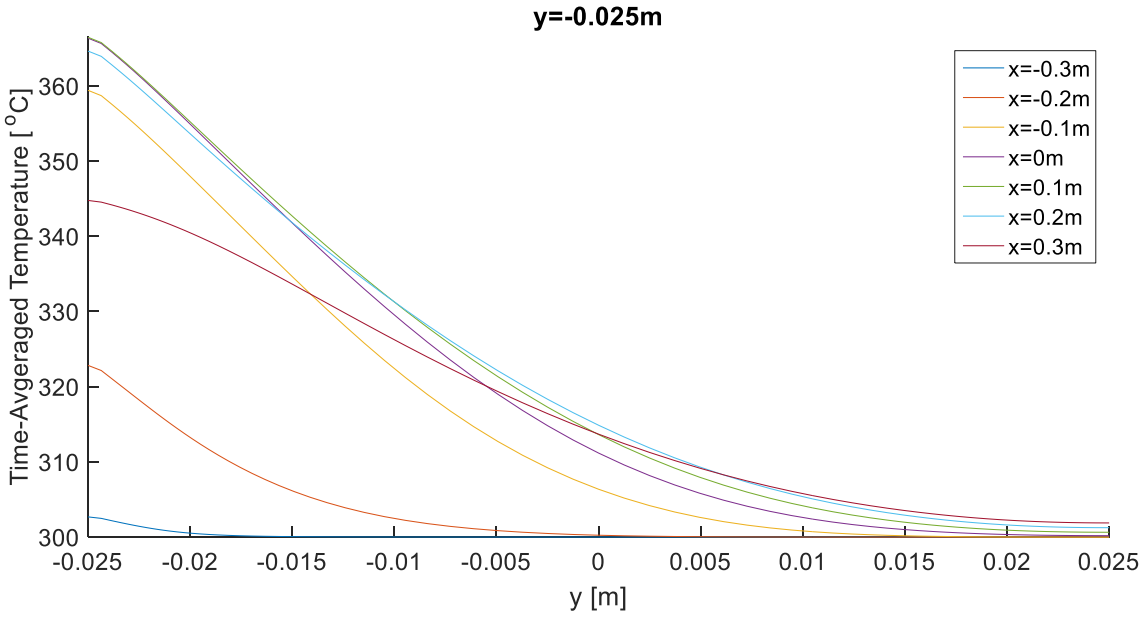

FIG. 112. Time-averaged temperature on the outer surface of the wall at y=-0.025 m, x=-0.3 m, -0.2 m, -0.1 m, 0 m, 0.1 m, 0.2 m, and 0.3 m. Downward flow with surface heating. B_o=0.5 T, U=0.03 m/s, q_o"=0.04 MW/m^2 (Ha=220, Re=3041, Gr=2.88x10^7). c_w=0.12.

The electric potential recorded at the final timestep is plotted at 7 axial locations x=-0.3 m, -0.2 m, -0.1 m, 0 m, 0.1 m, 0.2 m, and 0.3 m. on the outside surfaces of each of the four walls as shown in Figs. 113-116.

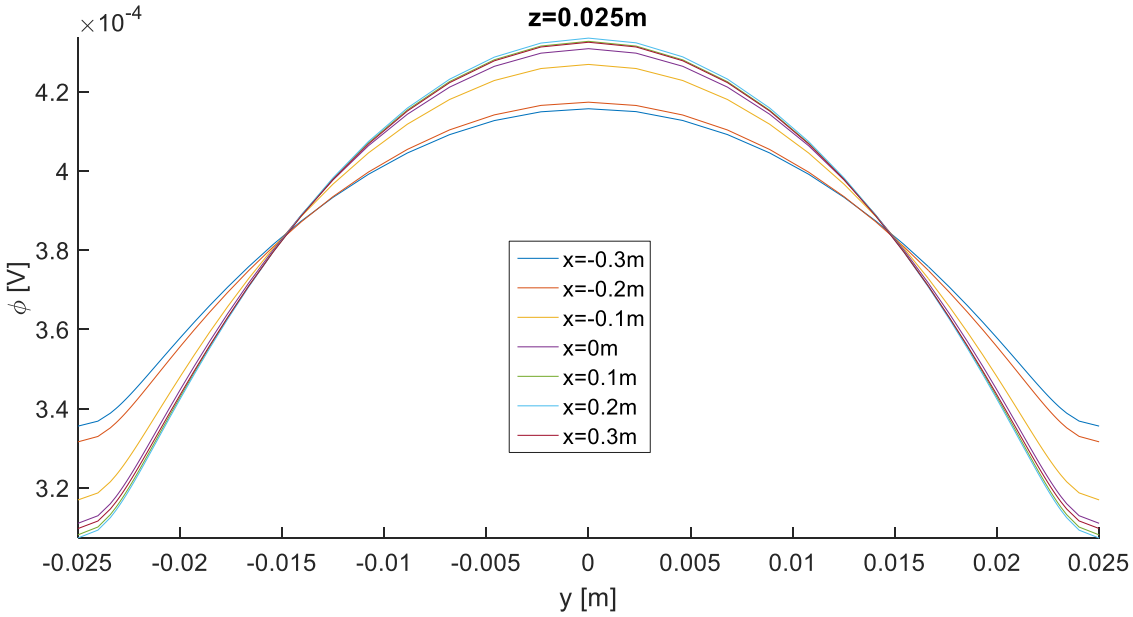

FIG. 113. Instantaneous electric potential on the outer surface of the wall at z=0.025 m, x=-0.3 m, -0.2 m, -0.1 m, 0 m, 0.1 m, 0.2 m, and 0.3 m. Downward flow with surface heating. B_o=0.5 T, U=0.03 m/s, q_o"=0.04 MW/m^2 (Ha=220, Re=3041, Gr=2.88x10^7). c_w=0.12.

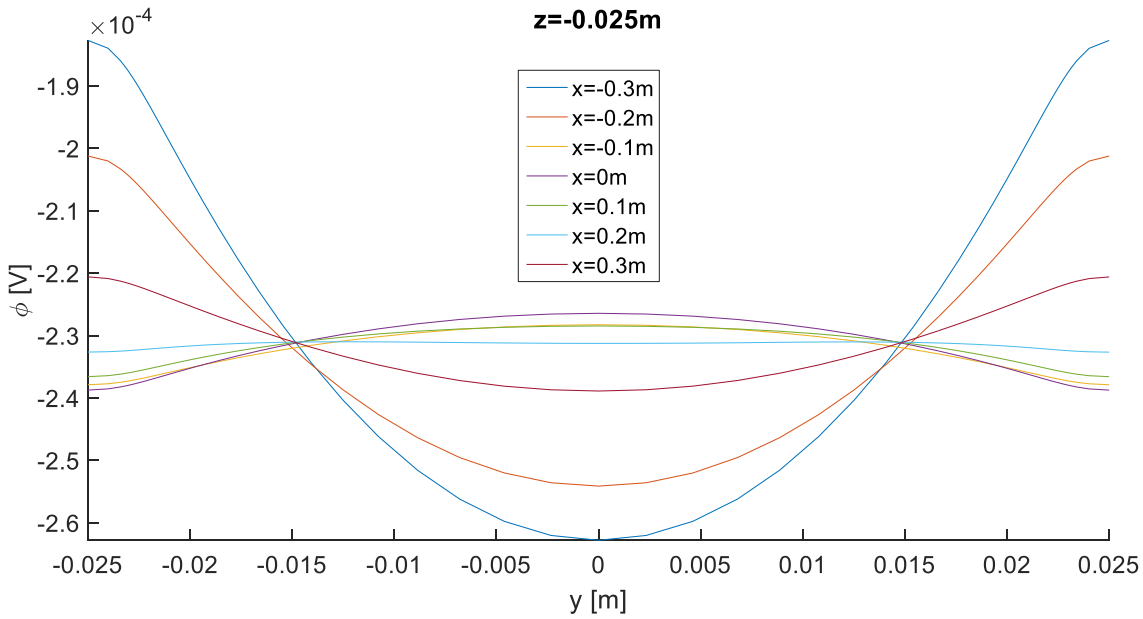

FIG. 114. Instantaneous electric potential on the outer surface of the wall at z=-0.025 m, x=-0.3 m, -0.2 m, -0.1 m, 0 m, 0.1 m, 0.2 m, and 0.3 m. Downward flow with surface heating. B_o=0.5 T, U=0.03 m/s, q_o"=0.04 MW/m^2 (Ha=220, Re=3041, Gr=2.88x10^7). c_w=0.12.

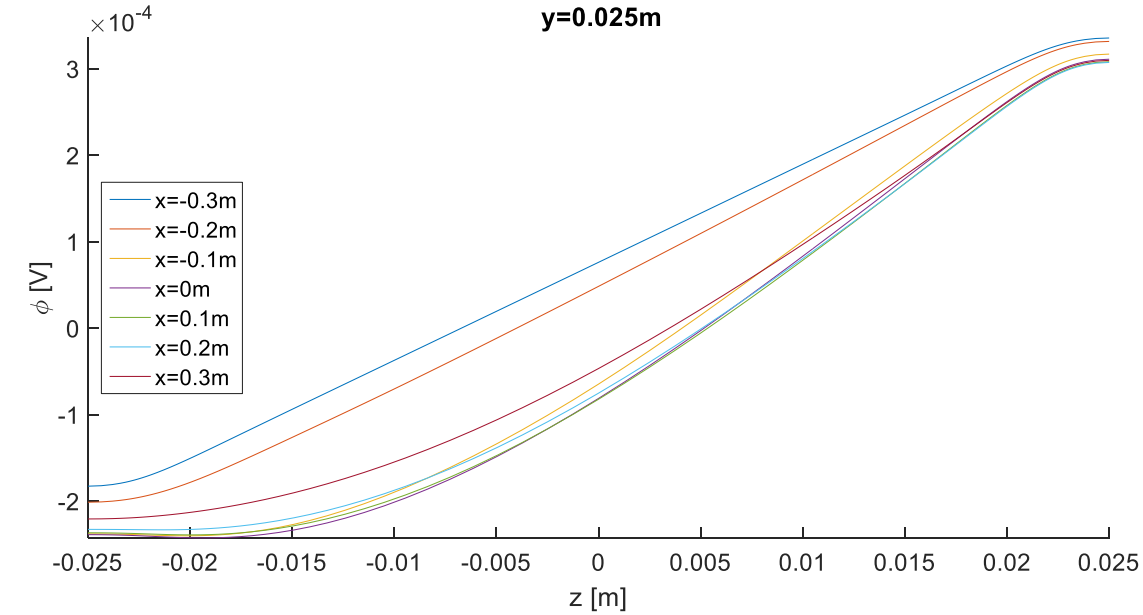

FIG. 115. Instantaneous electric potential on the outer surface of the wall at y=0.025 m, x=-0.3 m, -0.2 m, -0.1 m, 0 m, 0.1 m, 0.2 m, and 0.3 m. Downward flow with surface heating. B_o=0.5 T, U=0.03 m/s, q_o"=0.04 MW/m^2 (Ha=220, Re=3041, Gr=2.88x10^7). c_w=0.12.

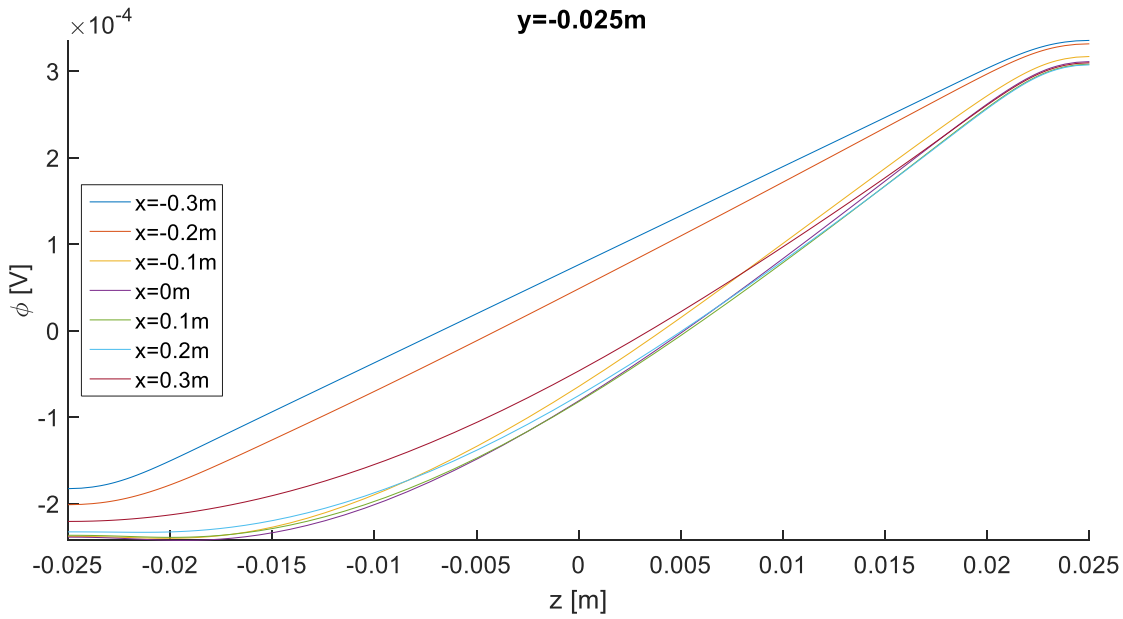

FIG. 116. Instantaneous electric potential on the outer surface of the wall at y=-0.025 m, x=-0.3 m, -0.2 m, -0.1 m, 0 m, 0.1 m, 0.2 m, and 0.3 m. Downward flow with surface heating. B_o=0.5 T, U=0.03 m/s, q_o''=0.04 MW/m^2 (Ha=220, Re=3041, Gr=2.88x10^7). c_w=0.12.

Lastly, to aid in the interpretation of the above data, 2D cross-sections at y=0 of time-averaged velocity and temperature are included below in Fig. 117 a and b respectively. The aspect ratio of the plots is scaled x:z::1:5. 1D profiles are included every 0.1 m for ease of understanding.

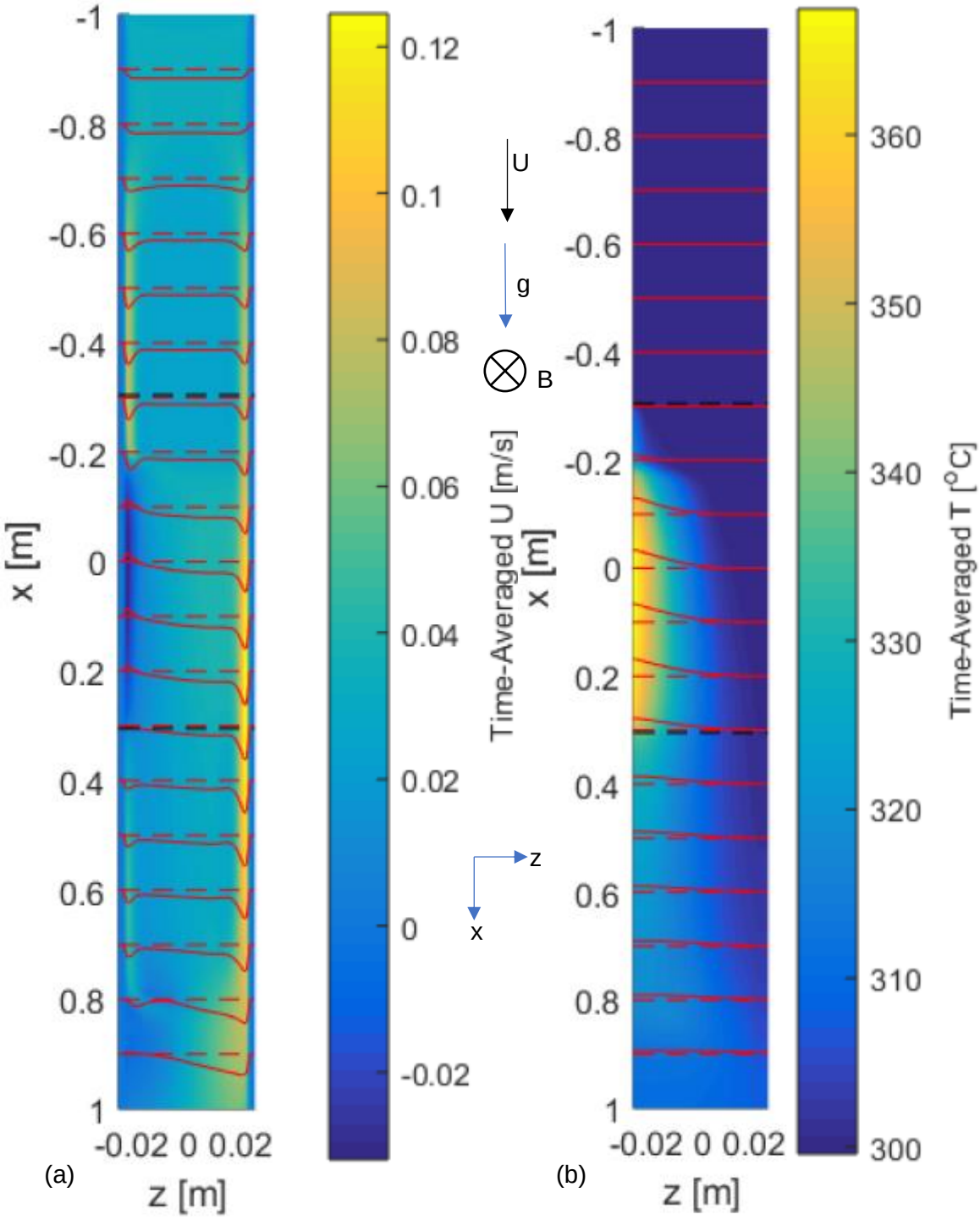

FIG. 117. (a) Time-averaged velocity contours and profiles on the y=0 center-plane. (b) Time-averaged temperature contours and profiles on the y=0 center-plane. Downward flow with surface heating. B_0=0.5 T, U=0.03 m/s, q_0''=0.04 MW/m^2 (Ha=220, Re=3041, Gr=2.88x10^7). c_w=0.12. The z-axis is stretched compared to the x-axis by a factor of 5 to more easily view the entire flow field. The dashed, red lines spaced every 0.1 m are the zero lines for the profiles which are solid red lines. The dashed, black lines mark the bounds of the heated region.

6.7.C Direct Comparison with Results From COMSOL

Yi Yan provided results [79] for comparison by using a different numerical solver to simulate the same problem as outlined in section 6.7. Yan's COMSOL Multiphysics based solver uses a finite element method to solve the 3D MHD equations coupled with the energy equation. His dimensionless parameters, geometry, heating, magnetic field, and boundary conditions are those of Case 16 in the present work though his approach does not require the use of a viscous sponge layer at the outlet. All of Yan's results are time-averaged over the times between 244s and 414s. 2D cross-sections at y=0 of time-averaged velocity and temperature are included below in Fig. 118 a and b respectively. The aspect ratio of the plots is scaled x:z::1:5. 1D profiles are included for ease of understanding every 0.1 m. Based on a qualitative comparison between Figs. 117 and 118, the results are shown to have decent agreement. One noteworthy exception is that the boundary layer separation occurs slightly further upstream in the results from HIMAG compared to the results from COMSOL. The location of the boundary separation was determined for both sets of results by finding where the wall shear stress is zero. This is done by averaging the axial velocity field along the y-direction and then evaluating the z-direction derivative of the result along the hot wall at z=-*a*. The location of the boundary layer separation is where this derivative is equal to zero. The location of boundary layer separation was determined to be x=-0.163 m for the HIMAG results and x=-0.128 m for the COMSOL results.

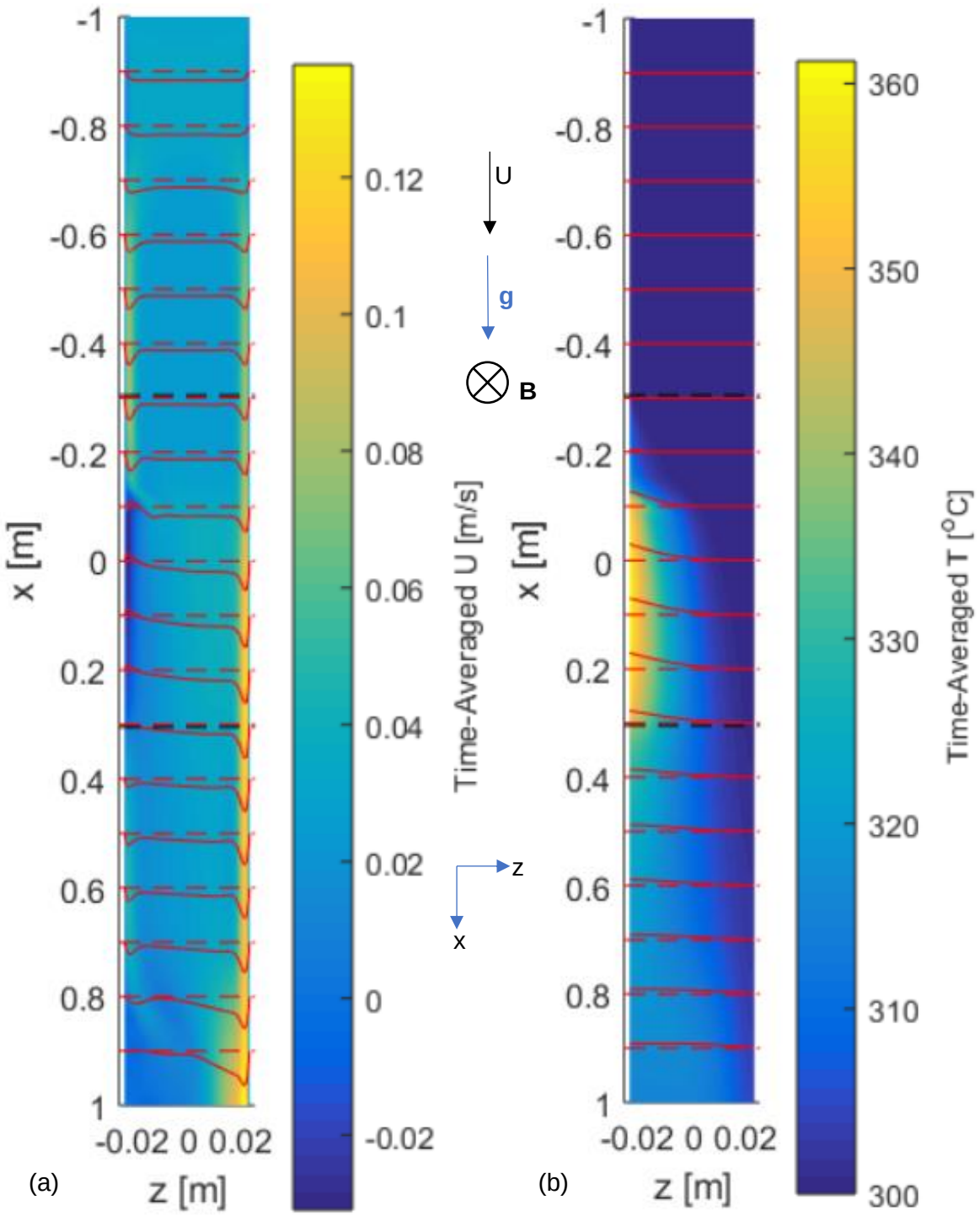

FIG. 118. COMSOL Multiphysics results. (a) Time-averaged velocity contours and profiles on the y=0 center-plane. (b) Time-averaged temperature contours and profiles on the y=0 center-plane. Downward flow with surface heating. B_o=0.5 T, U=0.03 m/s, q_o"=0.04 MW/m^2 (Ha=220, Re=3041, Gr=2.88x10^7). c_w=0.12. The z-axis is stretched compared to the x-axis by a factor of 5 to more easily view the entire flow field. The dashed, red lines spaced every 0.1m are the zero lines for the profiles which are solid red lines. The dashed, black lines mark the bounds of the heated region.

The time-averaged axial velocity profiles at six axial locations x=-0.25m, -0.15m, -0.05m, 0.05m, 0.15m, and 0.25m at y=0 are shown in Fig. 119, including results from both HIMAG and COMSOL.

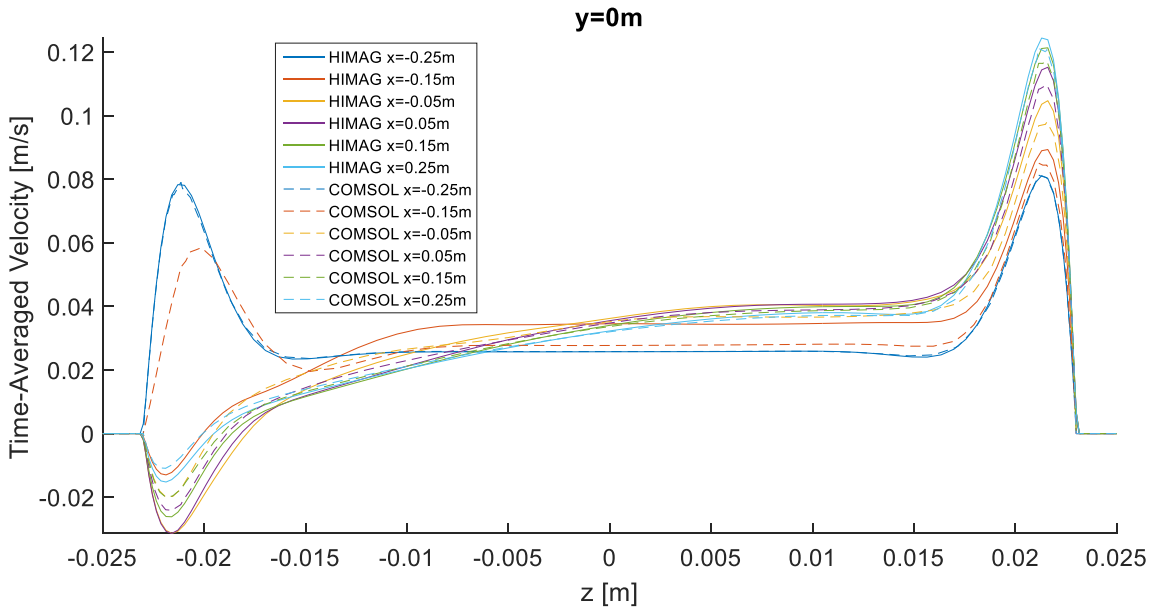

FIG. 119. Time-averaged velocity at y=0m, x= -0.25 m, -0.15 m, -0.05 m, 0.05 m, 0.15 m, and 0.25 m. Downward flow with surface heating. B_o=0.5 T, U=0.03 m/s, q_o"=0.04 MW/m^2 (Ha=220, Re=3041, Gr=2.88x10^7). c_w=0.12. Results from HIMAG are solid lines while results from COMSOL are dashed lines.

The codes show excellent agreement at x=-0.25 m but poor agreement at x=-0.15 m which is upstream the boundary layer separation for the COMSOL results and downstream for the HIMAG results. The results for x≥-0.5 m feature differences in the maximum reverse flow velocity and maximum forward flow velocity but otherwise have the same shape. The maximum reverse flow velocity varies between results by 37%, 23%, 23%, and 28% for x=-0.5 m, 0.05 m, 0.15 m and 0.25 m respectively.

The time-averaged temperature profiles at six axial locations x=-0.25 m, -0.15 m, -0.05 m, 0.05 m, 0.15 m, and 0.25 m at y=0 are shown in Fig. 120, including results from both HIMAG and COMSOL.

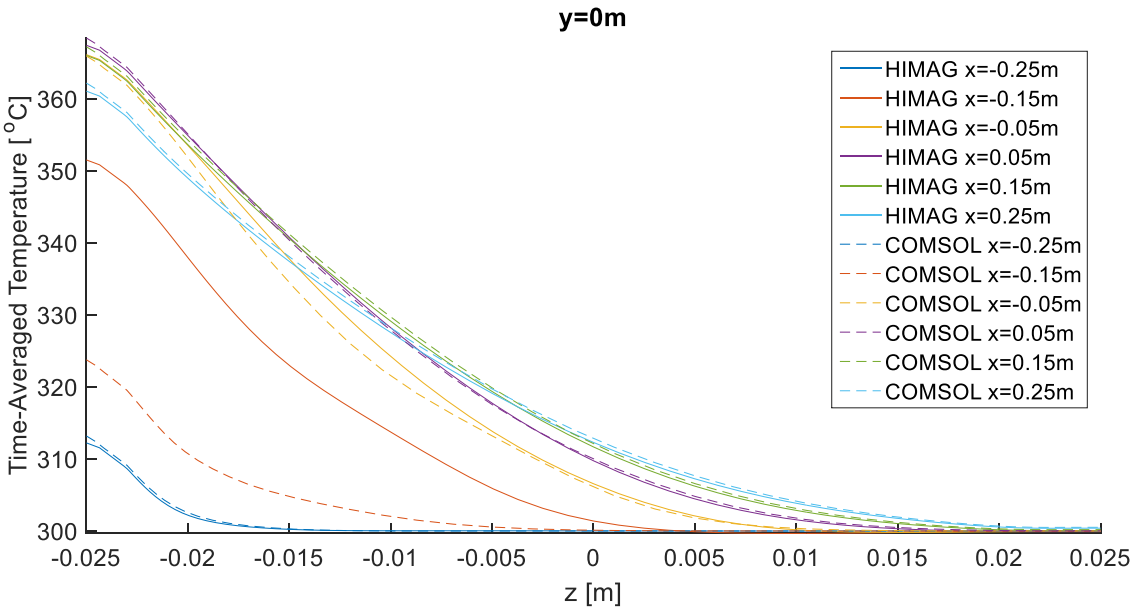

FIG. 120. Time-averaged temperature at y=0m, x= -0.25 m, -0.15 m, -0.05 m, 0.05 m, 0.15 m, and 0.25 m. Downward flow with surface heating. B_o=0.5 T, U=0.03 m/s, q_o"=0.04 MW/m^2 (Ha=220, Re=3041, Gr=2.88x10^7). c_w=0.12. Results from HIMAG are solid lines while results from COMSOL are dashed lines.

As with the time-averaged axial velocity, the two codes show excellent agreement at x=-0.25 m but poor agreement at x=-0.15 m which is upstream the boundary layer separation for the COMSOL results and downstream for the HIMAG results. The results for x≥-0.5 m feature good agreement with only small differences in the bulk region at x=-0.5 m, z<-0.005 m, where the flow is generally hotter in the HIMAG results by ~4°C.

The differences between the results from HIMAG and COMSOL mostly seem to be caused by differences in the location of the boundary layer separation. Still, the flow phenomena observed in the results of both codes are mostly the same (i.e. asymmetric velocity profiles with jets attached to the sidewalls, flow reversal in the heated region, and temperature increase inside the flow reversal). These similarities support the use of both codes in studying MHD mixed convection flows in vertical ducts. Future studies will address the cause of the reported differences to better inform on the selection of future numerical tools.

Chapter 7: Conclusions and Future Studies for MHD Duct Flows with Buoyancy Effects

In Part II of this dissertation, HIMAG was used to simulate the 3D flow of liquid metal through vertical, square ducts (Fig. 27) to explore the MHD mixed convection phenomena which may occur in breeder blankets of fusion power reactors. A fringing, transverse magnetic field provided an 80 cm region of uniform field which was centered on a 60.96 cm region of applied, one-sided heating that the pressure driven liquid metal was made to flow through.

MHD mixed convection phenomena were described in an overview of the flow behavior given PbLi with U=0.02 m/s, B_o=0.5 T, and q_o''=0.2 MW/m^2 (Re=2027, Ha=220, and Gr=1.44x10^8) for the case of applied surface heating at a sidewall. The flow orientation was varied (upward/downward) and the electrical conductivity of the duct walls was varied (c_w=1.2x10^{-9} or 0.12) to provide 4 scenarios to study. The upward, buoyancy assisted flows in the overview featured relatively stable flows with strong jets attached to the hot wall and almost no flow carried by the bulk. The downward, buoyancy opposed flows featured flow reversal, higher temperatures, and flow instabilities in the heated region.

A parametric study was performed for upwards and downwards flows in electrically conducting ducts with applied surface heating for Ha ranging from 110 to 880, Re from 2027 to 20270, and two choices of Gr =1.44x10^8, 3.6x10^8. As expected, increasing Re decreased buoyant effects, going as far as to change the flow regime from that of MHD mixed convection (Re=2027) to that of MHD forced flow ($Re \geq 15201$). Predictably, increasing Gr increased buoyant effects while increasing Ha had a more subtle influence on buoyant effects: increasing Ha reduced the reverse flow velocity near the hot sidewall while also causing the temperature there to increase due to improved stability and thus reduced advection heat transfer normal to the wall.

The pressure distribution and balance of axial forces were analyzed for upwards and downwards duct flows with conducting and nonconducting walls and surface heating on one sidewall given PbLi with U=0.02 m/s, B_o=0.5 T, and q_o''=0.2 MW/m^2 (Re=2027, Ha=220, and Gr=1.44x10^8). The pressure distribution is shown to mostly balance the mean buoyant force, though there is some contribution from Lorentz force in the case of electrically conducting walls. Note that the static pressure distribution is omitted from the presented data as the static pressure drop ($\Delta p_{static} = 186\ \mathrm{kPa}$) is much larger than the pressure drop due to forces other than weight which are on the order of 1 kPa for the given parameters. In flows with much higher Ha, as in breeder blankets, the MHD pressure drop (balanced by viscous drag and net Lorentz force) may dominate instead of gravity based (i.e. buoyant and static) pressure drops. This is especially likely in self-cooled blanket concepts as a high flowrate of LM coupled with a lack of FCI would result in significant MHD pressure drops that scale with σUB^2. The analysis of axial forces concludes with some indication that the core flow is not guaranteed to be inertialess nor two-dimensional in MHD mixed convection flows.

A novel metric for evaluating the velocity nonuniformity along the magnetic field direction was presented and applied to 4 flow scenarios with either upward or downward flow through conducting or nonconducting ducts with applied surface heating on one sidewall given PbLi with U=0.02 m/s, B_o=0.5 T, and q_o''=0.2 MW/m^2 (Re=2027, Ha=220, and Gr=1.44x10^8). The metric, along with plots of kinetic energy, was useful in investigating the flow's departure from quasi-2D behavior in particular circumstances. The analysis yielded 3 major conclusions:

(1) In downward flow cases, feedback between the temperature and the velocity fields promoted lasting asymmetry in both fields along the magnetic field direction. It was found that the temperature of the Hartmann walls would differ, in the time-averaged sense, by ~60^{o}C in electrically conducting downward flow. In upward flows, this feedback mechanism promotes uniformity along the magnetic field direction instead. Interestingly, such asymmetry was not

observed in cases with relatively weaker buoyancy effects as in the case of downward flow in a conducting duct at Ha=220, Re=3041, Gr=2.88x10^7. This implies that a stability threshold exists for this effect, one that is likely characterized by the competition of buoyant effects with stabilizing electromagnetic effects and diffusion.

(2) By promoting inertial transfers of momentum, the buoyancy generally erodes the velocity uniformity along the magnetic field direction. This effect is strongest in downward flows where boundary layer separation occurs. In the cases presented, the boundary layer separation cooccurred with significant three-dimensionality of the flow.

(3) While the buoyant force diminishes uniformity along the magnetic field direction, Joule dissipation is still present, and the resulting behavior of the combined effects is a turbulent flow which has velocity fluctuations in 3D, though the fluctuations parallel to the magnetic field are ~1 order of magnitude smaller, in terms of kinetic energy, than fluctuations which are perpendicular to the magnetic field.

Future work should characterize the instability/feedback mechanism in (1) with respect to Ha, Re, Gr, and c_w. Additionally, Q2D formulations remain as powerful tools for investigating MHD mixed convection flows at higher parameters as they significantly reduce the cost of computations compared to fully 3D formulations. While it is likely that buoyancy assisted flow problems will be tractable for Q2D codes at fusion-relevant parameters, it seems that significant deviations from realistic results may occur in buoyancy opposed flows. Future efforts should directly compare results of 3D and Q2D formulations to see exactly how these deviations may occur as it is likely that Q2D formulations will still be useful for buoyancy opposed flows (e.g. for estimating the time-averaged heat and mass transfer properties).

8 cases consisting of 2 volumetric heating curves (nuclear heating given by a neutronics code or an exponential heating curve which is somewhat steeper but has the same total heat flux) for

each of 4 flow scenarios with different combinations of flow orientation (up/down) and wall conductivity (c_w=0.12 or ~0) were simulated to explore the effect of varying the volumetric heating distribution in MHD mixed convection flows. Despite having the same material properties (PbLi), U=0.02 m/s, B_o=0.5 T, ΔT=381°C (Re=2027, Ha=220, Gr=1.57x10^8), and total heating Q=0.0061 MW, the steeper exponential heating case featured markedly stronger buoyant effects compared to the nuclear heating case in all 4 scenarios due to higher concentration of heating near the hot wall. However, the same kinds of phenomena were observed in cases with the same flow orientation and wall conductivity despite differences in heating. This observation also applies to the comparison with surface heating cases of the same total heating, Ha, Re, c_w, and flow orientation, justifying the use of surface heating as a suitable substitute for nuclear heating in experiments that aim to explore the MHD mixed convection phenomena in flows with steep gradients in volumetric heating.

Lastly, results are presented for direct comparison with experiment, namely the MaPLE-U experiment at UCLA. The included results correspond to PbLi flowing with mean velocity of 3 cm/s downward through a 0.5 T transverse magnetic field with applied surface heating q_o''=0.04 MW/m^2 in a stainless-steel square duct (Ha=220, Re=3041, Gr=2.88x10^7, c_w=0.12). Additionally, experimental velocimetry technique is briefly discussed.

The geometry of LM blankets are bound to be more complex than the vertical, straight, square ducts studied here, and more complex geometry will be accompanied by additional physics. For example, if multiple ducts share common conducting walls, the flows in adjacent ducts will become electrically coupled as discussed in [64, 80]. Also, the magnetic field in fusion blankets is not strictly perpendicular to the duct walls and, as a consequence of the plasma confinement scheme, the magnetic field will be unsteady, unlike the steady, transverse field of the present calculations. While some studies have investigated the effect of magnetic field orientation on magneto-buoyant convection, no studies have been carried out for such flows in time-dependent

magnetic fields. The magnetic field in a fusion blanket will also feature special variation which has not been accounted for in any studies. Flow orientation with respect to gravity will also have some effect on MHD mixed convection phenomena and should be investigated as the entire range of orientation is expected to occur in real LM blanket systems. Furthermore, the MHD mixed convection flows of the present work are set in a parameter space which is tractable for both numerical and experimental investigation; however, in fusion power reactor blankets, the *Ha*, *Re, and Gr* numbers will be much higher (i.e. $Gr \sim 10^9$-10^{12}, $Ha \sim 10^4$, $Re \sim 10^4$-10^5 [1, 43]). Reliable prediction of fluid flow behavior in fusion reactor blankets with multiple field effects and interactions in the fusion nuclear environment requires major advances in modelling to simulate simultaneously high Gr and Ha. Thus, future efforts should either extrapolate the conclusions of studies in the current space but ultimately must work to expand our modelling capability. While it is undoubtably important for future work to investigate the behavior of flows in parameters relevant to fusion, the results presented here serve to inform on future experimental results and will be useful in developing improved MHD solvers. Ultimately, the conclusions of the present work significantly expand our understanding of the physics and phenomena of MHD flows with strong buoyancy effects.

References

[1] M. Abdou, N. B. Morley, S. Smolentsev, A. Ying, S. Malang, A. Rowcliffe, M. Ulrickson, Blanket/first wall challenges and required R&D on the pathway to DEMO, Fusion Eng. Des, 100 (2015) 2–43.

[2] S. Smolentsev, R. Moreau, L. Bühler, and C. Mistrangelo, MHD thermofluid issues of liquid-metal blankets: Phenomena and advances, Fusion Eng. and Des., 85(7-9) (2010) 1196-1205.

[3] J. Shercliff, Steady motion of conducting fluids in pipes under transverse magnetic fields, Mathematical Proceedings of the Cambridge Philosophical Society, 49(1953) 136-144.

[4] S. Uflyand, Hartman problem for a circular tube, Soviet Physics-Technical Physics 5.10 (1961) 1194-1196.

[5] C. Chang and T. Lundgren, Duct flow in magnetohydrodynamics, Journal of Applied Mathematics and Physics ZAMP 12.2 (1961) 100-114.

[6] J. Hunt, Magnetohydrodynamic flow in rectangular ducts, J Fluid Mech., 21.04 (1965) 577-590.

[7] J. Hartmann, Hg-. Dynamics, I. Theory of laminar flow of an electrically conductive liquid in a homogeneous magnetic field, Kg 1. Danske Videnskabernes Selskab, Math. Fys. Medd., 15 (1937).

[8] J. Hunt and K. Stewartson, Magnetohydrodynamic flow in rectangular ducts. II, Journal of fluid mechanics 23.3 (1965) 563-581.

[9] G. Branover and O. Lielausis, The characteristics of the transverse magnetic field effect on turbulent flow of liquid metal at different Reynolds numbers (Magnetic field effect on liquid metal turbulent flow through smooth and roughened tubes at various numbers), Soviet Physics-Technical Physics 10 (1965) 191-195.

[10] G. Branover, A. Vasil'ev, and Y. Gel'fgat, Effect of a transverse magnetic field on the flow in a duct at a sudden cross-section enlargement, Magnitnaya Gidrodynamica, 3(3) (1967) 61-65.

[11] Y. Gel'fgat and L. Kit, Investigation of the conditions of occurrence of M-shaped velocity profiles at sudden expansion or contraction of a magnetohydrodynamic flow, Magnetohydrodynamics, 7(1) (1971) 21-25.

[12] R. Holroyd and J. Walker, A theoretical study of the effects of wall conductivity, non-uniform magnetic fields and variable-area ducts on liquid-metal flows at high Hartmann number, Journal of Fluid Mechanics 84.3 (1978) 471-495.

[13] G. Ludford, Inviscid flow past a body at low magnetic Reynolds number, Reviews of Modern Physics 32.4 (1960) 1000.

[14] J. Hunt, and S. Leibovich, Magnetohydrodynamic flow in channels of variable cross-section with strong transverse magnetic fields, J. Fluid Mech., 28(2) (1967) 241-260.

[15] U. Müller, L. Bühler, Magnetohydrodynamics in channels and containers, Springer Science & Business Media, (2001) 83-97.

[16] J. Hunt and G. Ludford, Three-dimensional MHD duct flows with strong transverse magnetic fields Part 1. Obstacles in a constant area channel, Journal of Fluid Mechanics 33.4 (1968) 693-714.

[17] J. Walker, G. Ludford, and J. Hunt, Three-dimensional MHD duct flows with strong transverse magnetic fields. Part 2. Variable-area rectangular ducts with conducting sides, Journal of Fluid Mechanics 46.4 (1971) 657-684.

[18] J. Walker, G. Ludford, and J. Hunt, Three-dimensional MHD duct flows with strong transverse magnetic fields. Part 3. Variable-area rectangular ducts with insulating walls, J. Fluid Mech., 56.01 (1972) 121-141.

[19] T. Aitov, A. Kalyutik, and A. Tananaev, Numerical analysis of three-dimensional MHD flow in channel with abrupt change of cross-section, Magnetohydrodynamics, 19(2) (1983) 223-229.

[20] M. Myasnikov, and A. Kalyutik, Numerical simulation of incompressible MHD flows in channels with a sudden expansion, Magnetohydrodynamics, 33(4) (1997) 342-349.

[21] L. Bühler, Inertialess magnetohydrodynamic flow in expansions and contractions, FZKA, FZKA 6904, (2003).

[22] S. Molokov, Liquid metal flows in manifolds and expansions of insulating rectangular ducts in the plane perpendicular to a strong magnetic field, KfK-5272, Kernforschungszentrum Karlsruhe, (1994).

[23] A. Tsinober and A. Stern A similar stagnation-point magnetohydrodynamic flow, Izvestija Akademii Nauk Latv. SSR, Ser. fiziko-tehnicheskih nauk, 1 (1964) 15-19 (In Russian).

[24] R. Stieglitz, L. Barleon, L. Bühler, and S. Molokov, Magnetohydrodynamic flow in a right-angle bend in a strong magnetic field, J. Fluid Mech., 326 (1996) 91-123.

[25] C. Mistrangelo, Three-dimensional MHD flow in sudden expansions, Diss. FZKA, (2006).

[26] I. Evtushenko, S. Sidorenkov, and A. Shishko, Experimental studies of magnetohydrodynamic processes in slotted channels within a strong magnetic field, Magnetohydrodynamics 28.2 (1993) 182-192.

[27] L. Bühler, S. Horanyi, and E. Arbogast, Experimental investigation of liquid-metal flows through a sudden expansion at fusion-relevant Hartmann numbers, Fusion engineering and Design 82.15-24 (2007) 2239-2245.

[28] K. Messadek, and M. Abdou, Experimental study of MHD flows in a prototypic inlet manifold section of the DCLL test blanket module, Magnetohydrodynamics, 45(2) (2009) 233-238.

[29] C. Mistrangelo, L. Bühler, MHD flow in a prototypical manifold of DCLL blankets, KIT, KIT Scientific Publishing, 7673 (2014).

[30] M. Sawan, E. Marriott, and M. Dagher, Neutronics performance parameters for the US dual coolant lead lithium ITER test blanket module, 2009 23rd IEEE/NPSS Symposium on Fusion Engineering. IEEE, (2009).

[31] L. Bühler, Laminar buoyant magnetohydrodynamic flow in vertical rectangular ducts, Phys. Fluids. 10(1) (1998) 223-236.

[32] C. Mistrangelo, and L. Bühler, Numerical analysis of buoyant-convective liquid metal flow in channels exposed to strong magnetic fields, 2011 IEEE/NPSS 24th Symposium on Fusion Engineering, IEEE, (2011).

[33] O. Zikanov, A. Thess, and J. Sommeria, Turbulent convection driven by an imposed temperature gradient in the presence of a constant vertical magnetic field, Numerical Flow Simulation I, Springer, Berlin, Heidelberg, (1998) 187-199.

[34] I. Melnikov, N. Rasuvanov, V. Sviridov, E. Sviridov, A. Shestakov, An investigation of heat exchange of liquid metal during flow in a vertical tube with non-uniform heating in the transverse magnetic field, Thermal Engineering 60.5 (2013) 355-362.

[35] I. Kirillov, D. Obukhov, L. Genin, V. Sviridov, N. Razuvanov, V. Batenin, I. Belyaev, I. Poddubnyi, and N. Pyatnitskaya, Buoyancy effects in vertical rectangular duct with coplanar magnetic field and single sided heat load, Fus. Eng. Des., 104 (2016) 1-8.

[36] I. Belyaev, P. Frick, N. Razuvanov, E. Sviridov, and V. Sviridov, Temperature fluctuations in a nonisothermal mercury pipe flow affected by a strong transverse magnetic field, International Journal of Heat and Mass Transfer, 127 (2018) 566-572.

[37] G. Sposito, and M. Ciofalo, Fully developed mixed magnetohydrodynamic convection in a vertical square duct, Numerical Heat Transfer, Part A: Applications, 53.9 (2008) 907-924.

[38] S. Smolentsev, R. Moreau, and M. Abdou, Characterization of key magnetohydrodynamic phenomena for PbLi flows for the US DCLL blanket, Fus. Eng. Des. 83 (2008) 771–783.

[39] H. Saleh, and I. Hashim, Flow reversal of fully-developed mixed MHD convection in vertical channels, Chinese Physics Letters 27.2 (2010) 024401.

[40] C. Mistrangelo, and L. Bühler, Numerical study of fundamental magnetoconvection phenomena in electrically conducting ducts, IEEE Transactions on Plasma Science, 40.3 (2012) 584-589.

[41] M. Chutia, and P. Deka, Numerical Study on MHD Mixed Convection Flow in a Vertical Insulated Square Duct with Strong Transverse Magnetic Field, Journal of Applied Fluid Mechanics 8.3 (2015).

[42] X. Zhang and O. Zikanov, Two-dimensional turbulent convection in a toroidal duct of a liquid metal blanket of a fusion reactor, Journal of Fluid Mechanics 779 (2015) 36-52.

[43] X. Zhang, and O. Zikanov, Mixed convection in a downward flow in a vertical duct with strong transverse magnetic field, arXiv preprint arXiv:1804.02659 (2018).

[44] L. Liu, and O. Zikanov, Elevator mode convection in flows with strong magnetic fields, Physics of Fluids 27.4 (2015) 044103.

[45] N. Vetcha, Study of Instability and transition in MHD flows as applied to liquid metal blankets, Diss. UCLA, 2012.

[46] O. Zikanov, and Y. Listratov, Numerical investigation of MHD heat transfer in a vertical round tube affected by transverse magnetic field, Fus. Eng. Des. 113 (2016) 151-161.

[47] Y. Listratov, D. Ognerubov, O. Zikanov, and V. Sviridov, Numerical simulations of mixed convection in liquid metal flow within a horizontal pipe with transverse magnetic field, Fluid Dynamics Research 50.5 (2018) 051407.

[48] S. Smolentsev, N. Morley, M. Abdou, R. Munipalli, R. Moreau, Current approaches to modeling MHD flows in the dual coolant lead lithium blanket, Magnetohydrodynamics, 42.2-3 (2006) 225-236.

[49] M. Ni, R. Munipalli, N. Morley, P. Huang, M. Abdou, A current density conservative scheme for incompressible MHD flows at a low magnetic Reynolds number. Part I: on a rectangular collocated grid system, Journal of Computational Physics 227 (2007) 174-204.

[50] M. Ni, R. Munipalli, P. Huang, N. Morley, M. Abdou, A current density conservative scheme for incompressible MHD flows at a low magnetic Reynolds number. Part II: on an arbitrary collocated mesh, Journal of Computational Physics 227 (2007) 205-228.

[51] R. Munipalli, S. Shankar, M. Ni, N. Morley, Development of a 3-D incompressible free surface MHD computational environment for arbitrary geometries: HIMAG, DOE SBIR phase-ii final report, (2003).

[52] N. Morley, R. Munipalli, P. Huang, and M. Abdou, MHD simulations of liquid metal flow through a toroidally oriented manifold, Fusion Eng. Des., 83(7-9) (2008) 1335-1339.

[53] J. Hunt, and R. Holroyd, Applications of laboratory and theoretical MHD duct flow studies in fusion reactor technology, HM Stationery Office, (1977).

[54] A. Kulikovskii, Slow steady flows of a conducting fluid at large Hartmann numbers, Fluid Dyn., 3(2) (1968) 3-10.

[55] G. Branover, E. Shcherbinin, Magnetohydrodynamic jet flow in a bounded space, Magnitnaya Gidrodinamika, 2 (1966) 55-63.

[56] B. Picologlou, C. Reed, T. Hua, L. Barleon, H. Kreuzinger, J. Walker, MHD flow tailoring in first wall coolant channels of self-cooled blankets, Fusion Eng. Des., 8 (1989) 297-303.

[57] Q. Hua, and B. Picologlou, Magnetohydrodynamic flow in a manifold and multiple rectangular coolant ducts of self-cooled blankets, Fusion Sci. Technol., 19.1 (1991) 102-112.

[58] H. Chen, Z. Meng, J. Feng, Q. He, Effect of electromagnetic coupling on MHD flow in the manifold of fusion liquid metal blanket, Fus. Eng. and Des., 89(7–8) (2014) 1406-1410.

[59] C. Kessel, J. Blanchard, A. Davis, L. El-Guebaly, N. Ghoniem, P. Humrickhouse, et al., The fusion nuclear science facility, the critical step in the pathway to fusion energy, Fusion Sci. Technol., 68 (2015) 225-236.

[60] S. Smolentsev, M. Abdou, N.B. Morley, S. Malang, C. Kessel, R&D needs and approach to measure progress for liquid metal blankets and systems on the pathway from present experimental facilities to FNSF, Fusion Sci. Technol., 68 (2015) 245-250.

[61] S. Smolentsev, T. Rhodes, G. Pulugundla, C. Courtessole, M. Abdou, S. Malang, M. Tillack, C. Kessel, MHD thermohydraulics analysis and supporting R&D for DCLL blanket in the FNSF, Fus. Eng. Des.,135 (2018) 314-323.

[62] T. Rhodes, S. Smolentsev, M. Abdou, Effect of the Length of the Poloidal Ducts on Flow Balancing in a Liquid Metal Blanket, Submitted to Fus. Eng. Des., 2017.

[63] T. Rhodes, S. Smolentsev, M. Abdou, Magnetohydrodynamic pressure drop and flow balancing of liquid metal flow in a prototypic fusion blanket manifold, Physics of Fluids 30(5), (2018) 057101.

[64] C. Mistrangelo, L. Bühler, Electric flow coupling in the HCLL blanket concept, Fusion Eng. Des. 83 (2008) 1232–1237.

[65] S. Smolentsev, N. Vetcha, M. Abdou, Effect of a magnetic field on stability and transitions in liquid breeder flows in a blanket, Fus. Eng. and Des., 88 (2013) 607-610.

[66] U. Burr, L. Barleon, U. Muller, and A. Tsinober, Turbulent transport of momentum and heat in magnetohydrodynamic rectangular duct flow with strong sidewall jets, J Fluid Mech 406 (2000) 247-279.

[67] P. Crapper and W. Baines, Non Boussinesq forced plumes, Atmospheric Environment (1967), 11.5 (1977) 415-420.

[68] D. Gray, and A. Giorgini, The validity of the Boussinesq approximation for liquids and gases, Intl J. Heat Mass Transfer 19(5) (1976) 545–551.

[69] P-E. Roche, Applicability of Boussinesq approximation in a turbulent fluid with constant properties, arXiv preprint arXiv:0710.3497 (2007).

[70] M. Kiyoshi, Rational derivation of the Boussinesq approximation, (2019).

[71] M. De Les Valls, L. Sedano, L. Batet, I. Ricapito, A. Aiello, O. Gastaldi, F. Gabriel, Lead–lithium eutectic material database for nuclear fusion technology, Journal of nuclear materials 376.3 (2008) 353-357.

[72] C. Pant, A. Bhattacharya, A viscous sponge layer formulation for robust large eddy simulation of thermal plumes, Computers and Fluids 134–135 (2016) 177–189.

[73] L. N. Trefethen, Finite Difference and Spectral Methods for Ordinary and Partial Differential Equations, unpublished text, available at http://people.maths.ox.ac.uk/trefethen/pdetext.html, (1996).

[74] L. Kit, D. Peterson, I. Platniek, and A. Tsinober, Magnitn. Gidrodinam., No. 4, 47 (1970).

[75] Zhou, Tao, H. Chen, and Z. Yang, Effect of fringing magnetic field on magnetohydrodynamic flow in rectangular duct, Fusion Engineering and Design, 86.9-11 (2011) 2352-2357.

[76] N. Vetcha, S. Smolentsev, M. Abdou, R. Moreau, Study of instabilities and quasi-two-dimensional turbulence in volumetrically heated MHD flows in a vertical rectangular duct, Phys. Fluids 25 (2013) 024102.

[77] J. Sommeria, R. Moreau, Why, How and When MHD Turbulence Becomes Two Dimensional? J. Fluid Mech. 118 (1982) 507.

[78] M. Riva, C. Di Sanzo, M. Abdou, and M. Youssef, Reducing the Peak-to-Average-Power-Ratio in Fusion Blankets, Fus. Sci. Tech., 72.3 (2017) 469-477.

[79] Y. Yan, personal communication, May 20, (2019).

[80] C. Mistrangelo and L. Bühler, Magneto-convective flows in electrically and thermally coupled channels, Fus. Eng. Des., 88(9) (2013) 2323-2327.

Appendix A: Dimensionless Figures

Some select results from Part II are presented here in dimensionless form. The velocity has been divided by the mean velocity *U*, the lengths have been divided by the duct half width along the magnetic field direction *b,* and the temperatures are reported as a dimensionless temperature increase $\theta = (\mathrm{T} - T_o)/\Delta T$. ΔT is a characteristic temperature difference calculated using the following formula from Chapter 5:

$$\Delta T = \frac{\mathrm{a}}{k}\int_{-a}^{+a} q'''(z)dz \quad \text{for volumetric heating,} \tag{20a}$$

$$\Delta T = \frac{a}{k} q_o'' \text{ for surface heating.} \tag{20b}$$

Some of the selected results are from simulations which feature volumetric heating as specified in the figure captions. The details of the volumetric heating, including exponential and nuclear heating, can be found in section 6.6. All other simulation details are included in Chapter 5.

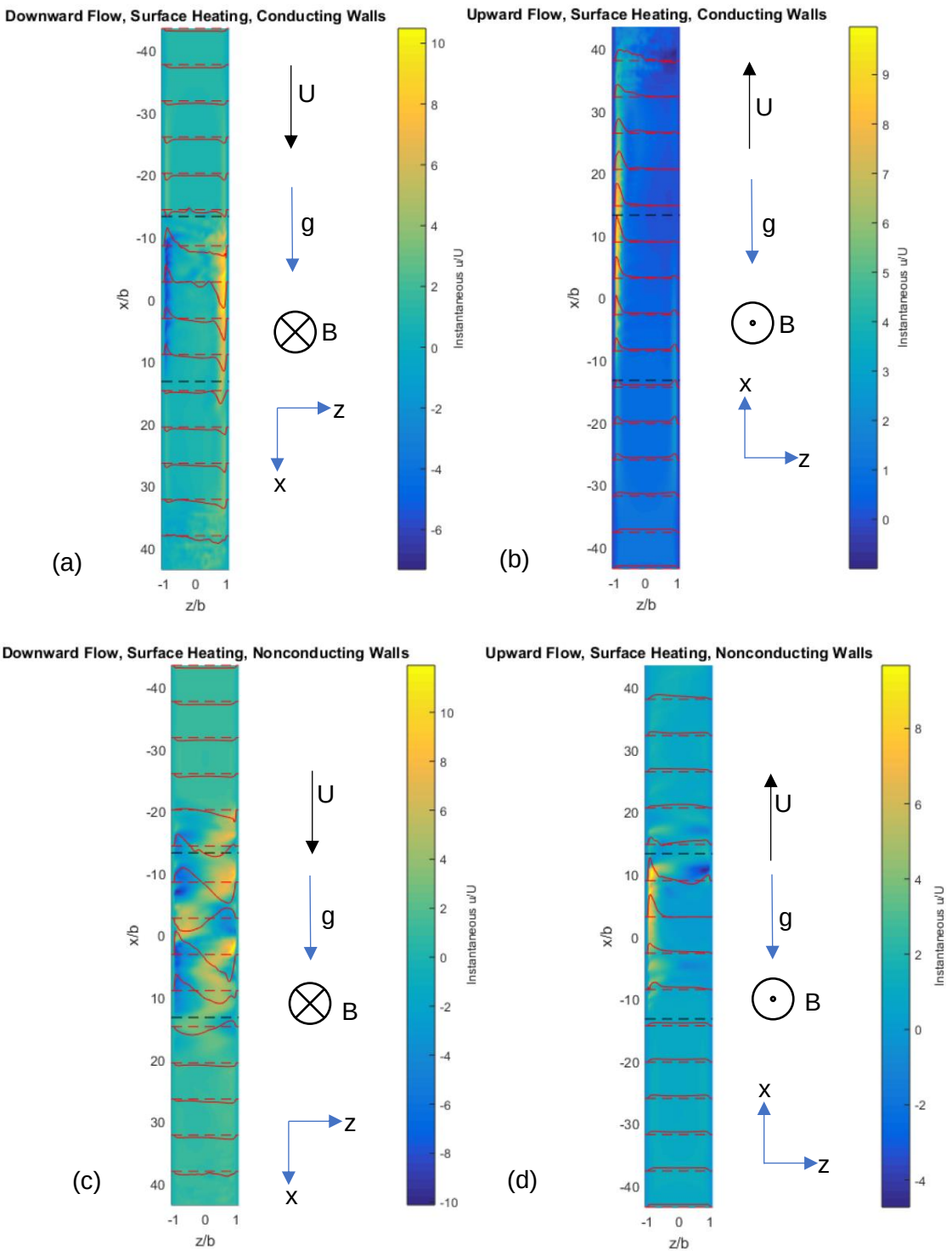

FIG. 121. Instantaneous axial velocity contours and profiles on the y=0 center-plane. Ha=220, Re=2027, Gr=1.44x10^8, surface heating only. (a, b) c_w=0.12, (c, d) c_w~0. (a, c) Downward flow, (b, d) upward flow. The z-axis is stretched compared to the x-axis by a factor of 5 to more easily view the entire flow field. The dashed, red lines spaced every 5.78 characteristic lengths are the zero lines for the profiles which are solid red lines. The dashed, black lines mark the bounds of the heated region.

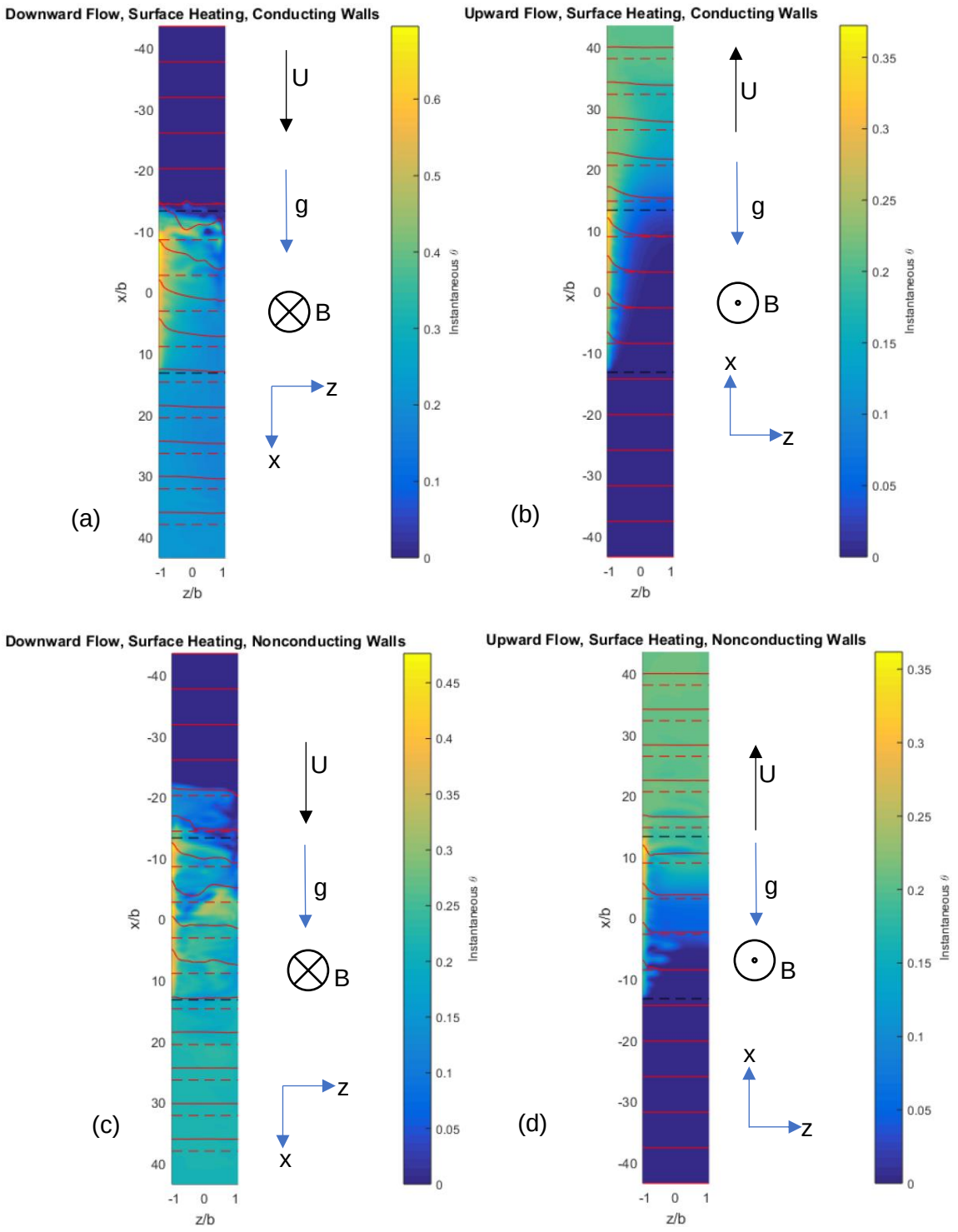

FIG. 122. Instantaneous temperature contours and profiles on the y=0 center-plane. Ha=220, Re=2027, Gr=1.44x10^8, surface heating only. (a, b) c_w=0.12, (c, d) c_w~0. (a, c) Downward flow, (b, d) upward flow. The z-axis is stretched compared to the x-axis by a factor of 5 to more easily view the entire flow field. The dashed, red lines spaced every

5.78 characteristic lengths are the zero lines for the profiles which are solid red lines. The dashed, black lines mark the bounds of the heated region.

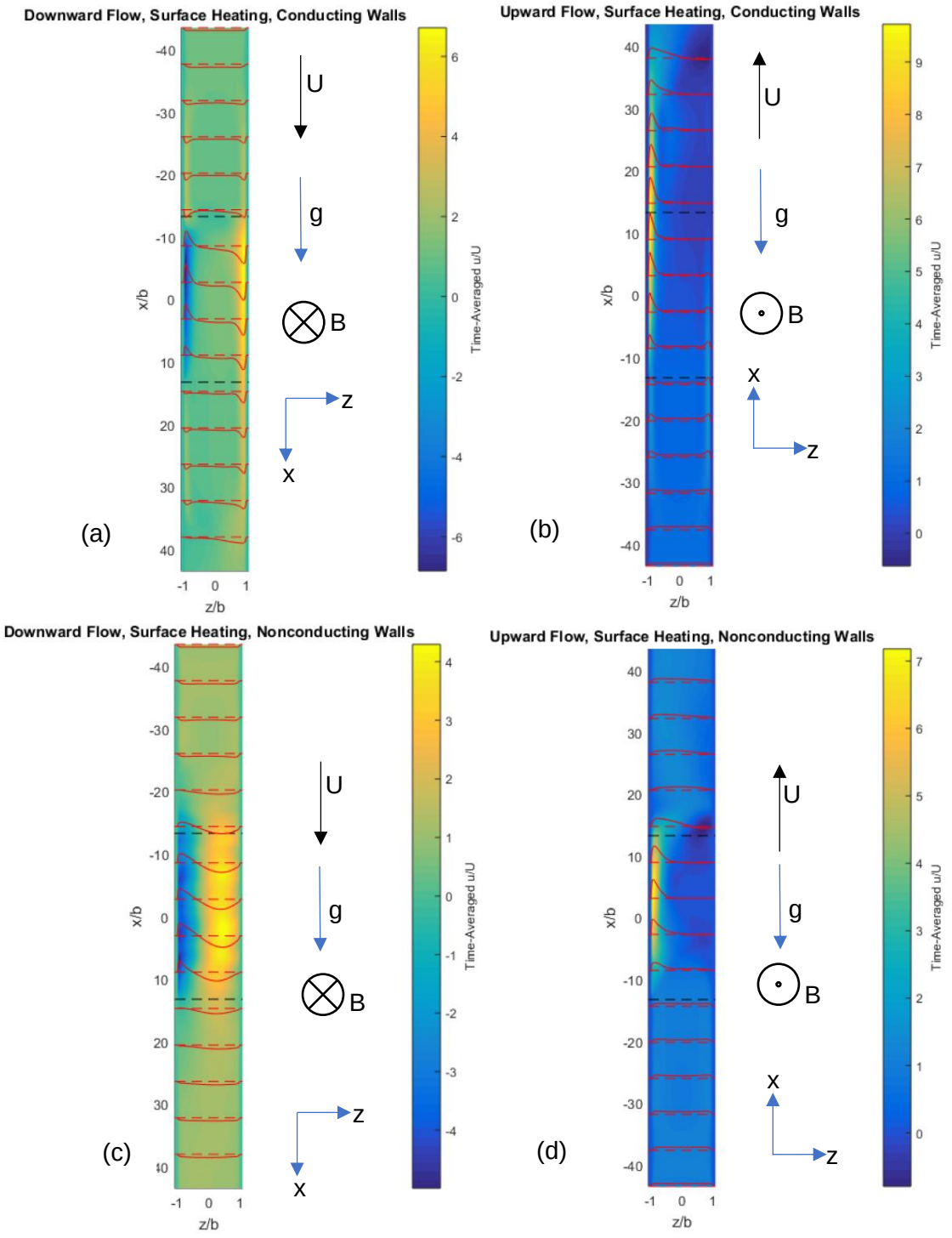

FIG. 123. Time-averaged axial velocity contours and profiles on the y=0 center-plane. Ha=220, Re=2027, Gr=1.44x10^8, surface heating only. (a, b) c_w=0.12, (c, d) c_w~0. (a, c) Downward flow, (b, d) upward flow. The z-axis is stretched compared to the x-axis by a factor of 5 to more easily view the entire flow field. The dashed, red lines spaced every

5.78 characteristic lengths are the zero lines for the profiles which are solid red lines. The dashed, black lines mark the bounds of the heated region.

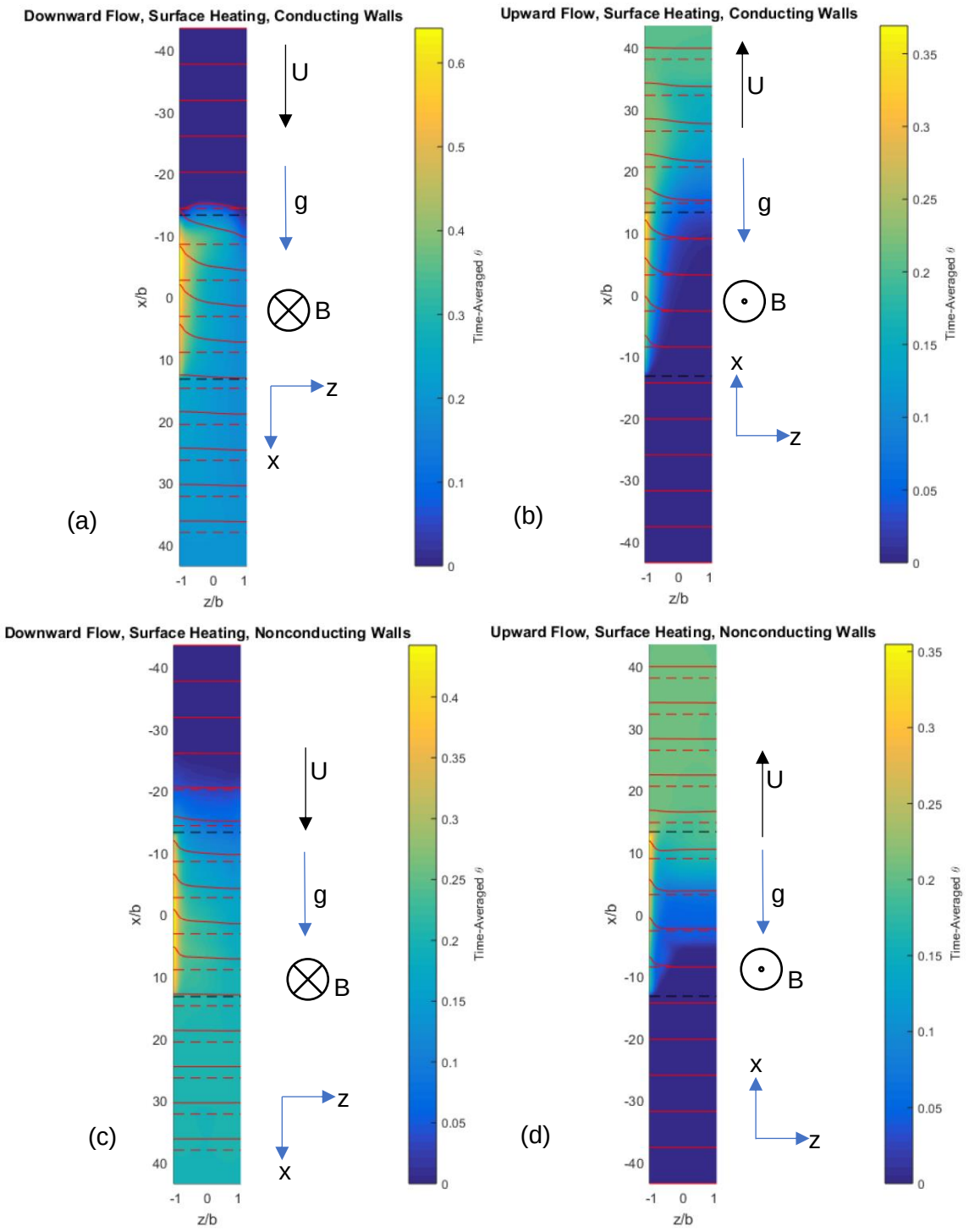

FIG. 124. Time-averaged temperature contours and profiles on the y=0 center-plane. Ha=220, Re=2027, Gr=1.44x10^8, surface heating only. (a, b) c_w=0.12, (c, d) c_w~0. (a, c) Downward flow, (b, d) upward flow. The z-axis is stretched compared to the x-axis by a factor of 5 to more easily view the entire flow field. The dashed, red lines spaced every

5.78 characteristic lengths are the zero lines for the profiles which are solid red lines. The dashed, black lines mark the bounds of the heated region.

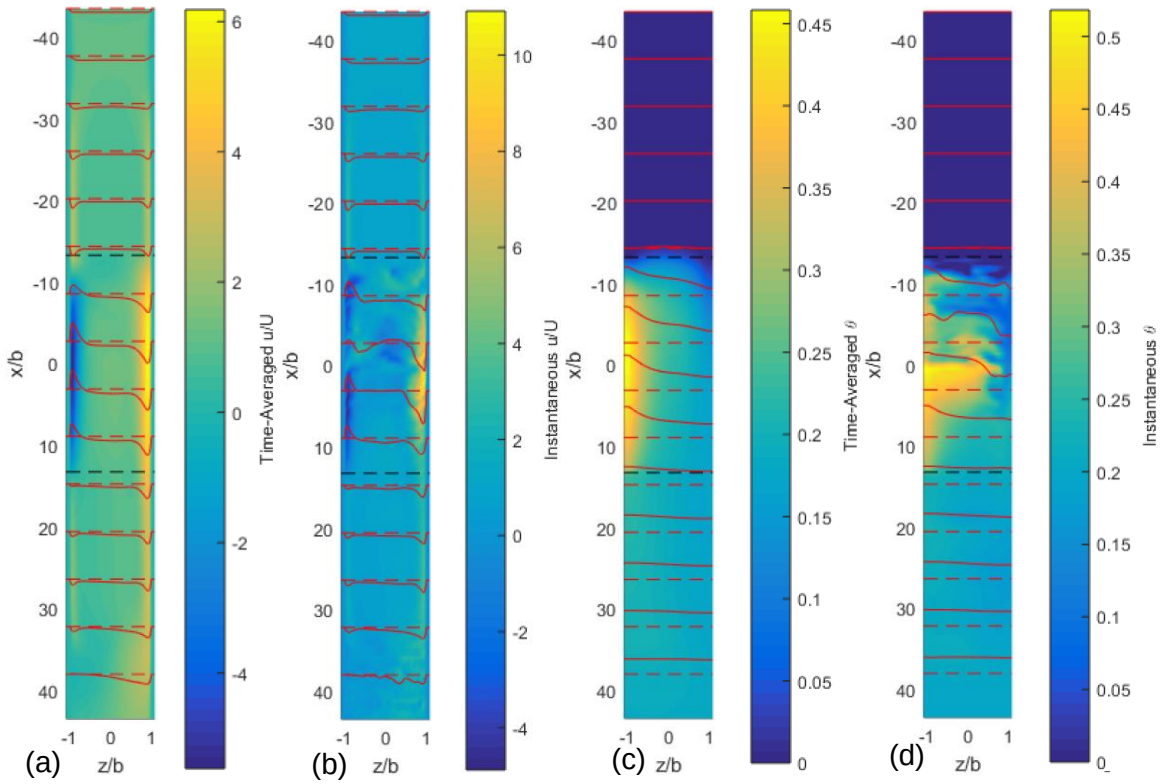

FIG. 125. (a) Time-averaged axial velocity, (b) instantaneous axial velocity, (c) time-averaged temperature, and (d) instantaneous temperature contours and profiles on the y=0 center-plane. Ha=220, Re=2027, Gr=1.57x10^8, c_w=0.12, downward flow with exponential heating. The flow enters from the top in the direction of gravity. The z-axis is stretched compared to the x-axis by a factor of 5 to more easily view the entire flow field. The dashed, red lines spaced every 5.78 characteristic lengths are the zero lines for the profiles which are solid red lines. The dashed, black lines mark the bounds of the heated region.

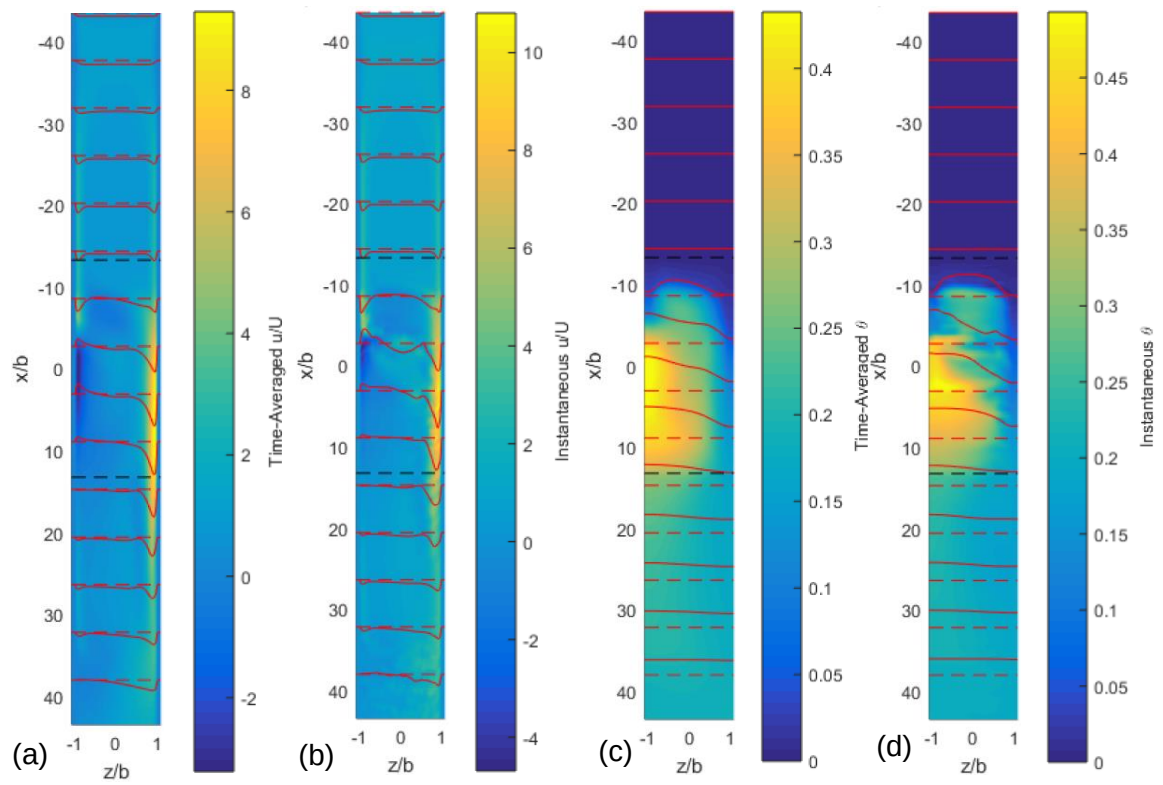

FIG. 126. (a) Time-averaged axial velocity, (b) instantaneous axial velocity, (c) time-averaged temperature, and (d) instantaneous temperature contours and profiles on the y=0 center-plane. Ha=220, Re=2027, Gr=1.57x10^8, c_w=0.12, downward flow with nuclear heating. The flow enters from the top in the direction of gravity. The z-axis is stretched compared to the x-axis by a factor of 5 to more easily view the entire flow field. The dashed, red lines spaced every 5.78 characteristic lengths are the zero lines for the profiles which are solid red lines. The dashed, black lines mark the bounds of the heated region.

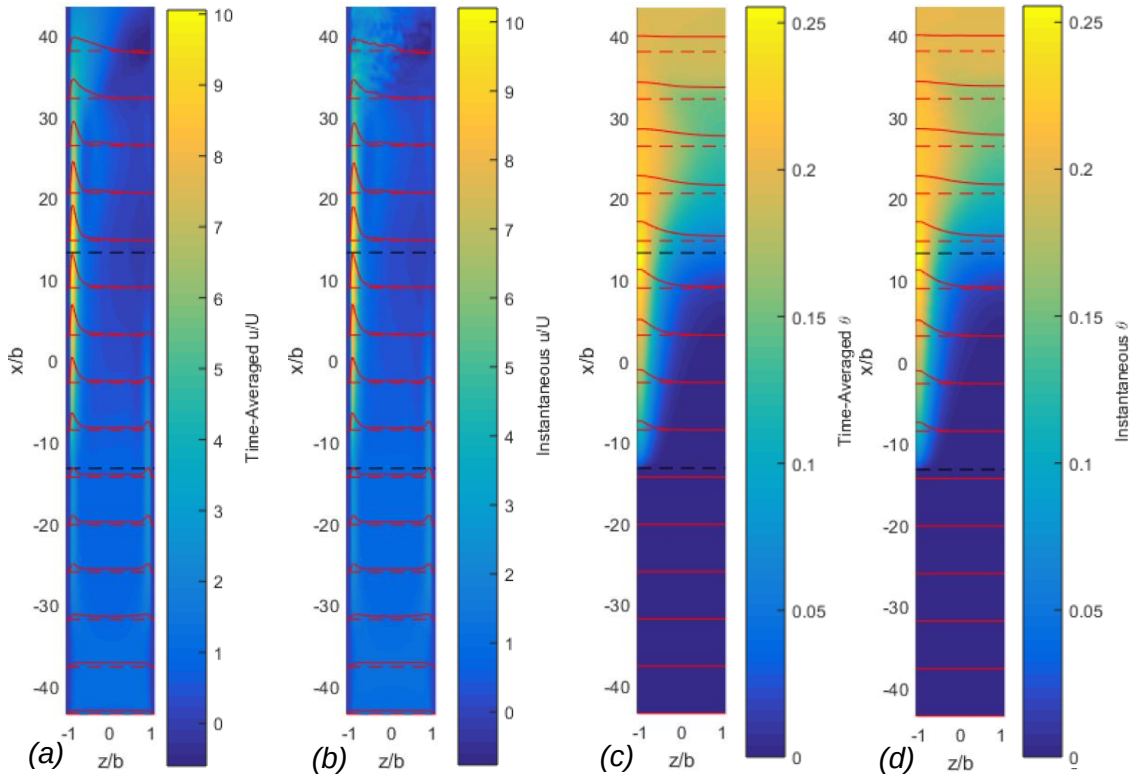

FIG. 127. (a) Time-averaged axial velocity, (b) instantaneous axial velocity, (c) time-averaged temperature, and (d) instantaneous temperature contours and profiles on the y=0 center-plane. Ha=220, Re=2027, Gr=1.57x10^8, c_w=0.12, upward flow with exponential heating. The flow enters from the bottom opposite the direction of gravity. The z-axis is stretched compared to the x-axis by a factor of 5 to more easily view the entire flow field. The dashed, red lines spaced every 5.78 characteristic lengths are the zero lines for the profiles which are solid red lines. The dashed, black lines mark the bounds of the heated region.

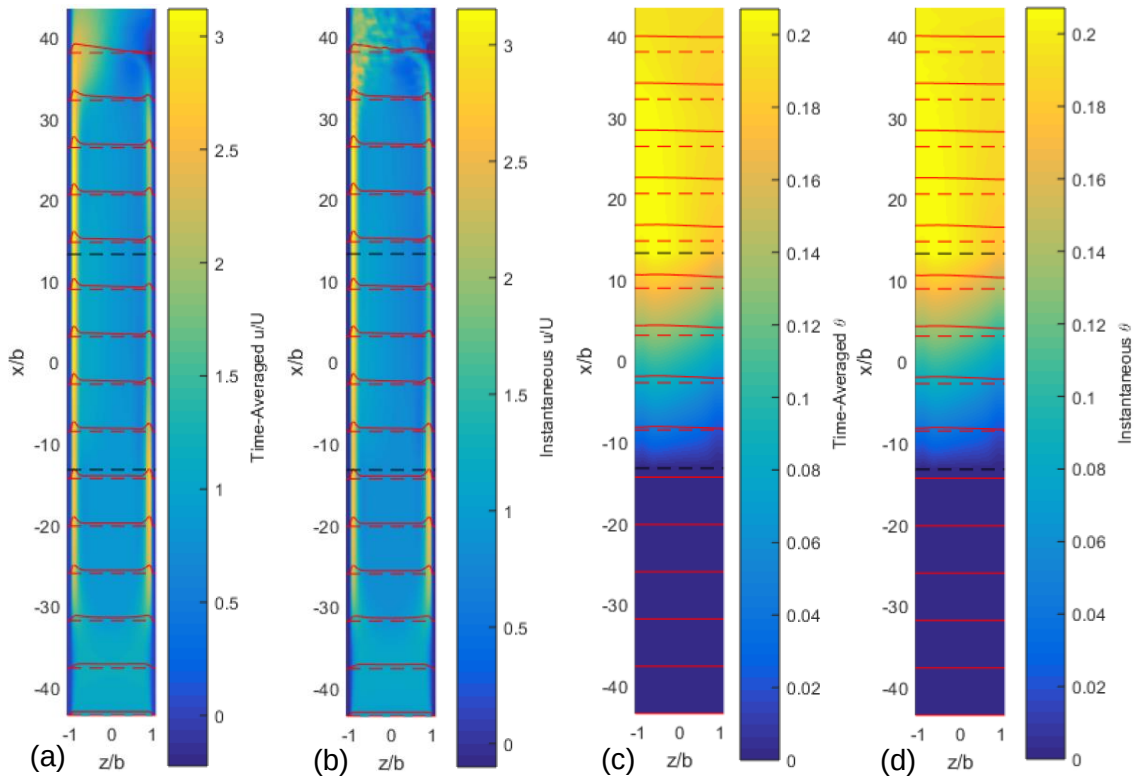

FIG. 128. (a) Time-averaged axial velocity, (b) instantaneous axial velocity, (c) time-averaged temperature, and (d) instantaneous temperature contours and profiles on the y=0 center-plane. Ha=220, Re=2027, Gr=1.57x10^8, c_w=0.12, upward flow with nuclear heating. The flow enters from the bottom opposite the direction of gravity. The z-axis is stretched compared to the x-axis by a factor of 5 to more easily view the entire flow field. The dashed, red lines spaced every 5.78 characteristic lengths are the zero lines for the profiles which are solid red lines. The dashed, black lines mark the bounds of the heated region.

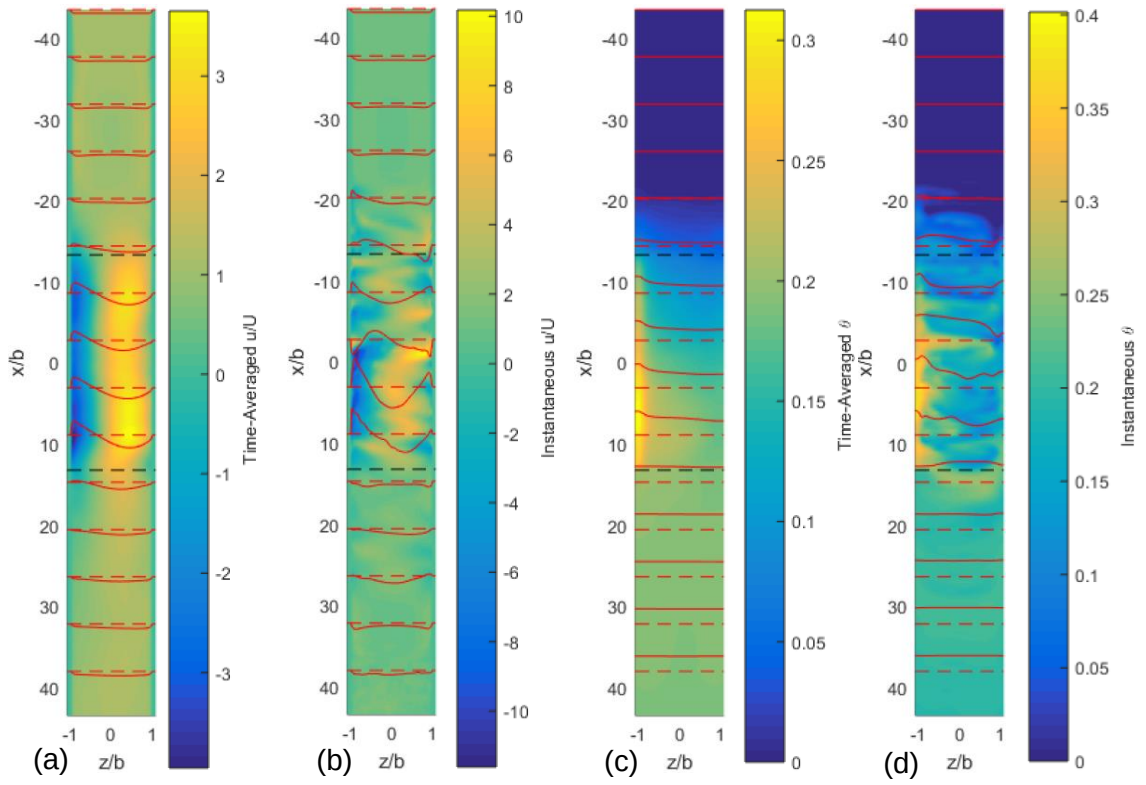

FIG. 129. (a) Time-averaged axial velocity, (b) instantaneous axial velocity, (c) time-averaged temperature, and (d) instantaneous temperature contours and profiles on the y=0 center-plane. Ha=220, Re=2027, Gr=1.57x10^8, c_w~0, downward flow with exponential heating. The flow enters from the top in the direction of gravity. The z-axis is stretched compared to the x-axis by a factor of 5 to more easily view the entire flow field. The dashed, red lines spaced every 5.78 characteristic lengths are the zero lines for the profiles which are solid red lines. The dashed, black lines mark the bounds of the heated region.

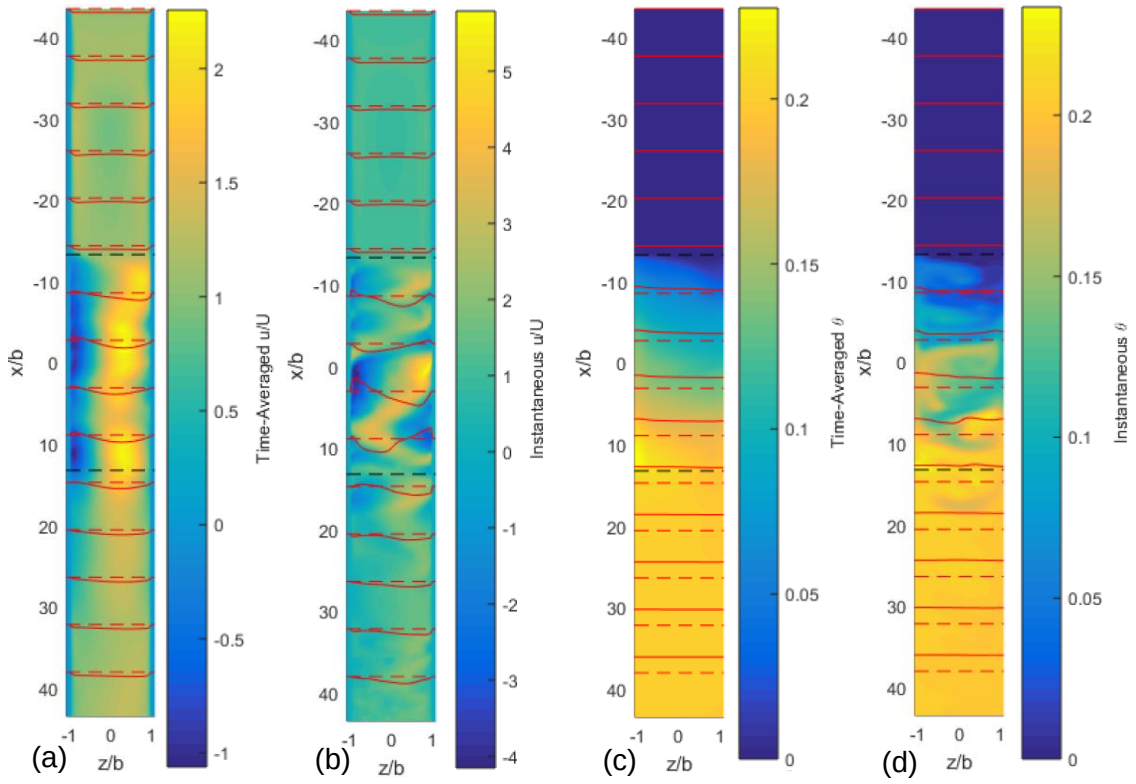

FIG. 130. (a) Time-averaged axial velocity, (b) instantaneous axial velocity, (c) time-averaged temperature, and (d) instantaneous temperature contours and profiles on the y=0 center-plane. Ha=220, Re=2027, Gr=1.57x10^8, c_w~0, downward flow with nuclear heating. The flow enters from the top in the direction of gravity. The z-axis is stretched compared to the x-axis by a factor of 5 to more easily view the entire flow field. The dashed, red lines spaced every 5.78 characteristic lengths are the zero lines for the profiles which are solid red lines. The dashed, black lines mark the bounds of the heated region.

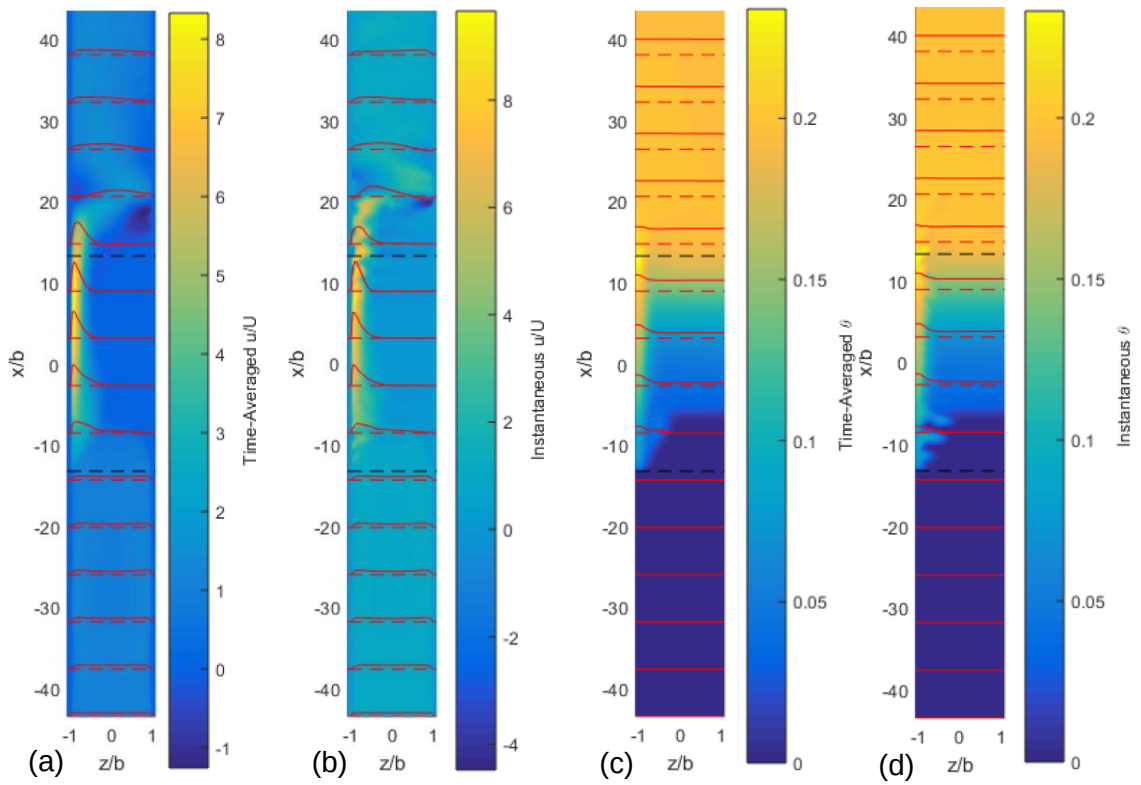

FIG. 131. (a) Time-averaged axial velocity, (b) instantaneous axial velocity, (c) time-averaged temperature, and (d) instantaneous temperature contours and profiles on the y=0 center-plane. Ha=220, Re=2027, Gr=1.57x10^8, c_w~0, upward flow with exponential heating. The flow enters from the bottom opposite the direction of gravity. The z-axis is stretched compared to the x-axis by a factor of 5 to more easily view the entire flow field. The dashed, red lines spaced every 5.78 characteristic lengths are the zero lines for the profiles which are solid red lines. The dashed, black lines mark the bounds of the heated region.

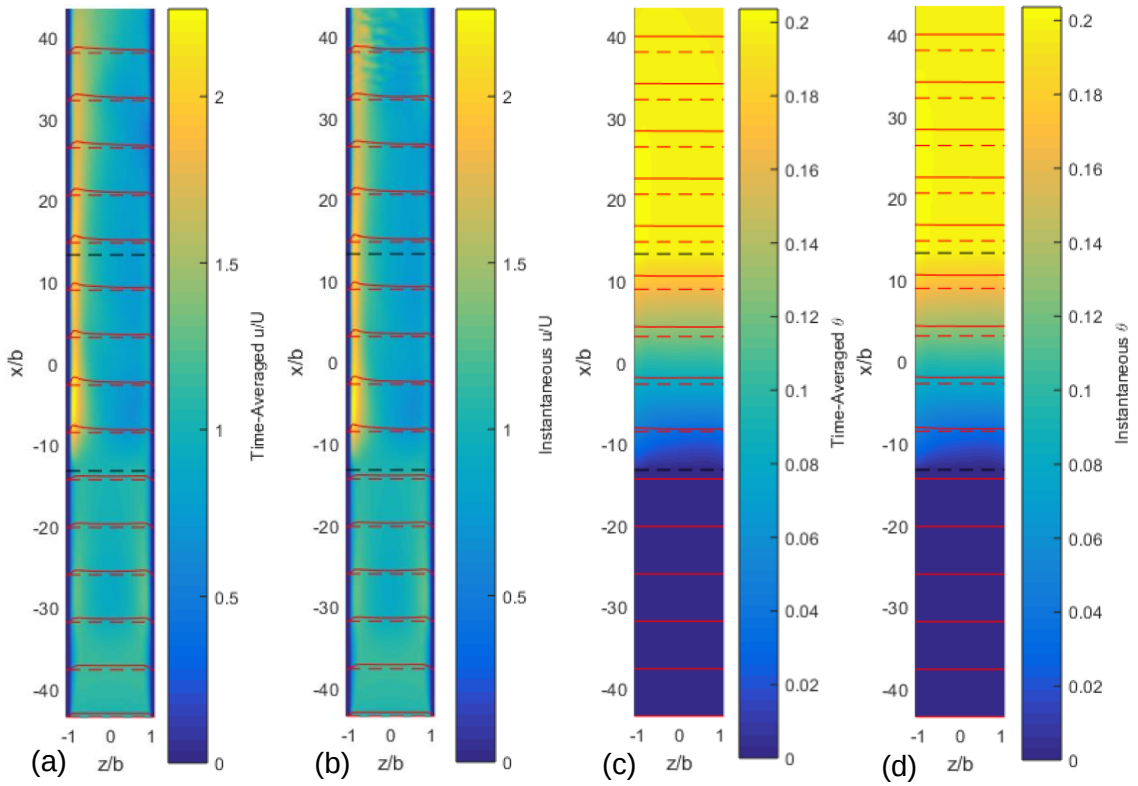

FIG. 132. (a) Time-averaged axial velocity, (b) instantaneous axial velocity, (c) time-averaged temperature, and (d) instantaneous temperature contours and profiles on the y=0 center-plane. Ha=220, Re=2027, Gr=1.57x10^8, c_w~0, upward flow with exponential heating. The flow enters from the bottom opposite the direction of gravity. The z-axis is stretched compared to the x-axis by a factor of 5 to more easily view the entire flow field. The dashed, red lines spaced every 5.78 characteristic lengths are the zero lines for the profiles which are solid red lines. The dashed, black lines mark the bounds of the heated region.